

JAERI - M
94-080

PARAMETRIC ANALYSIS AND OPERATIONAL PERFORMANCE
OF EDA-ITER

June 1994

Yoshiki MURAKAMI*, Hirobumi FUJIEDA**
and Toshihide TSUNEMATSU

JAERI-Mレポートは、日本原子力研究所が不定期に公刊している研究報告書です。
入手の問い合わせは、日本原子力研究所技術情報部情報資料課（〒319-11茨城県那珂郡東海村）あて、お申しこしください。なお、このほかに財団法人原子力弘済会資料センター（〒319-11茨城県那珂郡東海村日本原子力研究所内）で複写による実費頒布をおこなっております。

JAERI-M reports are issued irregularly.

Inquiries about availability of the reports should be addressed to Information Division
Department of Technical Information, Japan Atomic Energy Research Institute, Tokai-
mura, Naka-gun, Ibaraki-ken 319-11, Japan.

©Japan Atomic Energy Research Institute, 1994

編集兼発行 日本原子力研究所
印 刷 いばらき印刷機

Parametric Analysis and Operational Performance of EDA-ITER

Yoshiki MURAKAMI*, Hirobumi FUJIEDA** and Toshihide TSUNEMATSU

Department of ITER Project
Naka Fusion Research Establishment
Japan Atomic Energy Research Institute
Naka-machi, Naka-gun, Ibaraki-ken

(Received March 31, 1994)

Confinement capability of EDA-ITER is investigated by using a 0-D model based on CDA physics design guidelines. Confinement enhancement factor (H-factor) is evaluated and required fusion power (P_{FUS}) for the ignition is calculated. It is found that ignition is possible in H-mode plasma ($H=2$) when helium accumulation (He) is 10% and $P_{FUS} \geq 1$ GW. For Rebut-Lallia scaling law, L-mode ($H=1$) ignition is possible when $P_{FUS} \geq 3$ GW. The required fusion power is, however, more than 4 GW even in H-mode plasmas when the helium accumulation is 20%. Therefore, it is an important future work to study how much helium accumulates in a burning plasma. Capability of steady-state mode operation is also investigated. Required current-drive power for H-mode plasma is about 140 MW when He=10% and the fusion gain Q is more than 5. If the enhanced confinement ($H \sim 3$) in high safety factor region ($q \sim 5$) can be adoptable, steady-state operation with $Q > 10$ is possible and the required current-drive power is about 60 MW. In spite of the larger fusion power, the divertor heat load of EDA-ITER calculated by scaling models is comparable or smaller than that of CDA-ITER due to the longer connection length. Thermal instability of EDA-ITER is also investigated. The growth time is about 15 s for ITER89 power scaling law. Fusion power excursion is investigated in very preliminary way. It is found that the power rises from 1.5 GW to 3 GW in about 100 s if there

* On loan from Toshiba Corporation

** Atomic Data Service

is no control. Although this instability could be stabilized by beta limit or helium accumulation effect, it is an important future work since it may cause severe problem.

Keywords: Operation Region, Confinement Capability, ITER, EDA, Ignition, Steady-state Operation

EDA-I T E Rの運転条件および運転パラメーターの検討

日本原子力研究所那珂研究所 I T E R開発室

村上 好樹*・藤枝 浩文**・常松 俊秀

(1994年 3月31日受理)

国際熱核融合実験炉(I T E R)の工学設計活動(EDA)において、共同中央チームよりEDA版 I T E Rの概念が提案された。ここでは、CDAの物理ガイドラインである0次元のプラズマ・モデルを用いてEDA版 I T E Rの性能評価を行った。核融合炉心プラズマの閉じ込め性能は自己点火に必要なエネルギー閉じ込め時間と現在の大型トカマク実験から外挿されるLモード比例則による閉じ込め時間の比である閉じ込め改善係数(Hファクター)で評価される。EDA版 I T E Rではヘリウム灰の蓄積率が10%の場合に、核融合出力が1 GW以上で $H \leq 2$ (Hモードで自己点火可能)であることがわかった。また、レブー・ラリア比例則に従うと仮定すると出力が約3 GW以上で $H \leq 1$ (Lモードで自己点火可能)であることもわかった。しかし、ヘリウム灰の蓄積率を20%としたときには、Hモードを仮定しても自己点火するためには約4 GW以上の核融合出力が必要であることがわかった。従って、核燃焼プラズマでヘリウム灰がどの程度まで蓄積するかを調べるのが今後の重要な課題である。一方、定常運転モードに対する検討結果によるとCDAと同じ物理的仮定で核融合利得Qが5以上の定常運転を行なうには140MWの電流駆動パワーが必要である。MHD安全係数qが大きな($q \sim 5$)プラズマで $H = 3$ 程度の高効率閉じ込めを仮定すると約60MWの電流駆動パワーで $Q > 10$ の定常運転が可能である。CDAのモデルを使ったダイバート熱負荷の評価では、EDA版 I T E Rでは核融合出力が大きいにもかかわらず結合長の長さ等のためにダイバート熱負荷はCDA版 I T E Rと同程度か小さいこともわかった。本レポートでは熱的な不安定性の成長時間および運転点の時間変化に対する検討も行った。EDA版 I T E Rの自己点火運転点は熱的に不安定であり、不安定性の成長時間は約15秒であることがわかった。また適当な制御を行なわないと100秒程度で1.5 GWから3 GWに出力が増加することが示された。この不安定性はベータ値限界などによる閉じ込めの劣化やヘリウム灰の蓄積による安定化も期待されるが、炉の健全性に与える影響が大きいので、今後十分な検討が必要であろう。

那珂研究所：〒311-01 茨城県那珂郡那珂町大字向山801-1

* (株) 東芝より出向中

** 原子力資料サービス

目 次

1. 序 論	1
2. 自己点火運転	3
2.1 CDA-ITERとEDA-ITERの比較	3
2.2 1.5次元輸送コードと0次元計算の比較	6
2.3 自己点火のために必要な核融合出力	10
2.4 ヘリウム蓄積と運転領域	11
2.5 高 q_p 運転の特徴	12
2.6 短時間の自己点火運転	14
2.7 不純物の種類の効果	15
2.8 粒子および熱負荷	17
3. 定常運転	19
3.1 概 要	19
3.2 定常運転領域	20
3.3 核融合出力と到達可能Q値	23
3.4 高 q_p 運転時の高閉じ込め特性	25
3.5 ダイバータ熱負荷の検討	27
3.6 小 a_p 運転の可能性	29
4. 熱的不安定性と0次元動特性	31
5. 結 論	33
謝 辞	34
参考文献	35

Contents

1. Introduction	1
2. Ignition Mode Operation	3
2.1 Comparison between CDA-ITER and EDA-ITER	3
2.2 Comparison between 1.5-D Transport Analysis and 0-D Calculations	6
2.3 Required Fusion Power for Ignition	10
2.4 Helium Accumulation and Operation Region	11
2.5 Characteristics of High- q_{Ψ} Operation	12
2.6 Possibility of Short-time Ignition	14
2.7 Effect of Impurity Species	15
2.8 Particle and Heat Load	17
3. Steady-state Mode Operation	19
3.1 General Remarks	19
3.2 Steady-state Operation Region	20
3.3 Fusion Power and Achievable Q-value	23
3.4 Enhanced Confinement Plasma with High- q_{Ψ}	25
3.5 Divertor Heat Load	27
3.6 Small- a_p Operation	29
4. Thermal Instability and 0-D Transient Analysis	31
5. Conclusion	33
Acknowledgements	34
References	35

1. Introduction

Engineering Design Activity (EDA) of International Thermonuclear Experimental Reactor (ITER) has been started in July 1992. In EDA, plasma parameters which are different from those of Conceptual Design Activity (CDA) are proposed [1] by using a self-consistent plasma model [2]. In this report, for a comparison with empirical scaling laws, the operational performance is assessed by using a 0-D model based on physics design guidelines of CDA [3].

Operation points of ITER are analyzed by using a 0-D Tokamak Plasma Power Balance Calculation (TPC) code [4]. TPC code solves the power balance of a tokamak plasma including 0-D profile effects and calculates beta values, Troyon coefficient, energy confinement time, neutron wall load, divertor heat load, etc. The divertor heat load is evaluated by using simplified scaling models [5]. In EDA-ITER, beryllium is assumed as a main impurity, which is not considered in CDA-ITER. In CDA-ITER, the impurity species and fractions are given by physics design guidelines depending on the plasma density. In EDA-ITER, the impurity fractions, which are the important factor for the ignition capability, have been remained uncertain. Therefore, we calculate various cases of impurity assumptions. Other parameters are following to private communications with JCT and a publication by P-H. Rebut [1].

In Chap.2, we investigate the ignition capability of EDA-ITER. Major parameters of EDA-ITER are assessed and compared to those of CDA-ITER. Comparison is made between 0-D analyses and 1.5-D transport analyses which are reported by JCT. Required fusion power

for the ignition is evaluated for various assumptions of impurities. Effect of helium accumulation and beryllium fraction on the operation region is also discussed. The required confinement enhancement factor is evaluated for the plasma with high MHD safety factor value since the high performance in a plasma with low plasma current and high poloidal beta value has been reported in the present machine [6]. The plasma with very low helium accumulation is also investigated taking account of the capability for the ignition in a short burn time.

In Chap.3, steady-state operation performance is investigated to obtain required current-drive power and achievable fusion gain. Possibility of steady-state operation with enhanced confinement in high MHD safety factor region is also considered. Divertor heat load for the steady-state plasma is estimated by several scaling models. Characteristics of the plasma with small minor radius are also investigated.

In Chap.4, a thermal instability of EDA-ITER is investigated by assuming the confinement scaling law. Analysis of 0-D transient property is also reported in very preliminary way.

Conclusions of our analyses are described in Chap.5.

2. Ignition Mode Operation

2.1 Comparison between CDA-ITER and EDA-ITER

In EDA-ITER, the plasma major radius R_p is increased from 6 m to 7.75 m and the minor radius a_p is increased from 2.15 m to 2.8 m. Plasma elongation κ is decreased from 2.0 to 1.6 in order to reduce the requirements of the controllability for the positional instability. The plasma volume increases from 1070 m³ to 1910 m³ consequently. Due to the increase of the first wall area (from 920 m² to 1380 m²), the fusion output power P_{FUS} is increased from 1 GW to 1.5 GW in order to achieve the same neutron wall load as that of CDA-ITER. An operation with $P_{FUS}=3$ GW is also considered to secure the ignition capability since the helium accumulation of 20% is concerned (10% in CDA guidelines [3]). In this section, the machine parameters and the operation points of EDA-ITER are evaluated by using 0-D power balance calculation code (TPC code [3]).

Confinement capability is described by using the enhancement factor (H-factor) of the required energy confinement time over L-mode energy confinement time based on empirical scaling laws in the present machine. In general, H-factor becomes smaller as the fusion power increases, though the predicted confinement time decreases with the heating power. The fusion power increases with the plasma elongation κ when the average neutron wall load is fixed. Therefore, the confinement capability is better for the plasma with larger- κ . The controllability against the positional instability, however, degrades as κ increases. In EDA-ITER, the plasma is stabilized by a passive stabilization effect of the vacuum vessel since

the growth rate of the instability for low- κ plasma is relatively small. On the other hand, the stability is maintained by using in-vessel coils in CDA-ITER. The stored energy of PF-coil system is much larger for the double null plasma than that for the single null plasma when κ is small. Therefore, the single null divertor configuration is chosen in EDA-ITER. Another important motivation of the change is to acquire the larger magnetic flux to achieve the long burn time of more than 1000 s by increasing center solenoid (CS) coil radius. Since the neutron shield width must be increased due to the higher fusion power, the plasma major radius increases more than the increase of CS-coil radius.

Figure 2.1 shows the relation between the machine parameters of CDA-ITER and those of EDA-ITER. Contour line plots of Troyon coefficient g , H-factor (the enhancement factor over L-mode energy confinement scaling law) and burn time are shown in R_p - a_p space when the neutron wall loading P_{WAL} is 0.85 MW/m². Here, ignition plasma ($Q=\infty$) is assumed and the fusion power is calculated for the given R_p and a_p . $H(IP)$ and $H(RL)$ denote H-factors for ITER89 power scaling law and Rebut-Lallia scaling law, respectively. The maximum toroidal field B_{TMAX} and the gap δ_{TF} between the toroidal field (TF) coil and the plasma inner edge are fixed in the figure. The toroidal field B_T at the plasma center is calculated for the given R_p and a_p . MHD safety factor q_ψ is also fixed on the figure and the plasma current I_p is determined by B_T , R_p and a_p . Here, we assume that $q_\psi=2.8$, $B_{TMAX}=13.0$ T, $\delta_{TF}=1.2$ m, $\kappa=1.7$ and $\delta=0$ in order that CDA-ITER and EDA-ITER are shown in the same plane. The burn time is calculated by CS-coil radius $R_{OH}=R_p-a_p-\delta_{TF}-0.9$ m and the maximum

poloidal field $B_{P_{MAX}}=13.2$ [5]. We also assume that the electron temperature T_e is 10 keV and helium accumulation rate (ratio of helium density to electron density) is 10%. Points C1 and E1 represent the machines with similar parameters to CDA-ITER and EDA-ITER, respectively. The reason why the burn time of the machine at E1 point is longer than 1000 s is that the shield width ($\delta_{TF}+0.9$) is same as that of CDA-ITER. Dashed line ($A=2.8$) in the figure denotes the machines with the same aspect ratio as CDA-ITER. It is seen that CDA-ITER (C1) is the machine with the smallest major radius when $g \leq 2$, $H(IP) \leq 2$ and $H(RL) \leq 2$. It is not necessary to increase the major radius up to 7.75 m in order to extend the burn time from 400 s to 1000 s. The burn time of 1000 s is possible when the major radius is increased by 0.2 m along the contour line $H(IP)=2$. Increase of 0.7 m in the major radius is enough for the burn time of 1000 s when the aspect ratio is kept constant along the dashed line ($A=2.8$). Note that the shield width of EDA-ITER is thicker than that of CDA-ITER by 0.41 m ($R_{OH}=2.85$ m by our assumption while $R_{OH}=2.44$ m by EDA design). Therefore, we must include the difference in the estimation of major radius.

On the other hand, H-factor at E1 point is much smaller than that at C1 point for both scaling laws. This margin is indispensable for the ignition capability as is discussed later.

Table 2.1 shows the major parameters of EDA-ITER together with those of CDA-ITER. Recently, slight change of plasma size parameters was made. The new parameters are also shown in the table (EDA'). In this report, we adopted the old version of EDA-ITER in stead of the new version unless it is specified.

In old version of EDA-ITER, MHD safety factor (q_ψ) value calculated by CDA formula [3] is lower than 3. According to CDA physics guidelines, q_ψ must be larger than 3 in order to avoid the MHD instabilities. However, we leave it as it is since q_ψ value depends on the calculation formula and the precise value should be evaluated by the equilibrium calculation. Consequently, the bootstrap current fraction may be underestimated in our analyses and the overestimation of the ohmic current may result in the shorter burn time. Calculation formula and the various definition of the safety factor are shown in Figs. 2.2, 2.3 and 2.4.

2.2 Comparison between 1.5-D Transport Analysis and 0-D Calculations

Some operation scenarios have been proposed by using 1.5-D transport simulation code [1]. In this section, we compare 0-D results with the results by JCT. Table 2.2 shows the plasma parameters calculated by JCT [1]. The electron temperature is not described in the report by P-H. Rebut [1]. However, we can calculate the electron temperature from the fusion power and plasma stored energy which can be seen from Fig.2 of Ref [1]. Estimated electron temperatures are also shown in Table 2.2. It should be noted that the radiation power is included in the estimated confinement time in 1.5-D results for the following definition; τ_E^* . It is easily confirmed that the confinement time in Table 2.2 is the quotient of the plasma stored energy W_p divided by the alpha heating power P_α . When this definition is used, we designate the confinement time and the

enhancement factor by superscript *. That is,

$$\begin{aligned}\tau_E &= \frac{W_P}{P_\alpha - P_{RAD}}, & H_{IP} &= \tau_E / \tau_E^{IP}, \\ \tau_E^* &= \frac{W_P}{P_\alpha}, & H_{IP}^* &= \tau_E^* / \tau_E^{IP},\end{aligned}$$

where τ_E^{IP} is the confinement time estimated by the L-mode scaling law and P_{RAD} is the total radiation power. Therefore, H_{IP}^* is always smaller than H_{IP} .

Although the ion temperature is higher than the electron temperature in case of 1.5-D calculations, we assume that the ion temperature is equal to the electron temperature in 0-D calculations for the simplicity. Generally, the confinement of the ion is better than that of the electron. Therefore, our estimation is more pessimistic than that by JCT since the larger part of plasma energy is stored in the particles with better confinement in JCT assumption. The profiles of 0-D calculations do not completely coincide with those of 1.5-D calculations. In our calculation, electron temperature and density profiles are given by

$$\begin{aligned}T_e(r) &= T_e(0) \left\{ 1 - (r/a_p)^2 \right\}^{A_T}, \\ n_e(r) &= n_e(0) \left\{ 1 - (r/a_p)^2 \right\}^{A_N}.\end{aligned}$$

Here, A_T and A_N are the profile coefficients for the electron temperature and electron density, respectively. In this section, we assume that $A_T = A_N = 1.0$ (parabolic profile) for the simplicity. The profile of 1.5-D calculations nearly corresponds to $A_T = 1.7$ and $A_N = 0.2$. While CDA-ITER assumes that $A_T = 1.0$ and $A_N = 0.5$. In 0-D calculations, the plasma stored energy and fusion power are adjusted to those of 1.5-D calculations in order to estimate the confinement time properly. Therefore, the difference of assumption in the ion

temperature is compensated by the difference of the profiles.

Table 2.3 shows the calculated parameters of EDA-ITER. In this case, only carbon is assumed as an impurity. Figures designated by the superscript * are the values which are different from those of Table 2.2. The difference in the bootstrap current is due to the profile effect. Consequently, it causes a discrepancy in the loop voltage (and the burn time). The difference in Troyon g comes from the difference in beta value. This is possibly due to the difference in the ion density, which is the result of the different impurity assumptions. For subscripts of H-factor, IP, IO, GS, RL and SO represent ITER89 power scaling, ITER89 offset-linear scaling, Goldston scaling, Rebut-Lallia scaling and Shimomura-Odajima scaling laws, respectively. It is seen that H-factor evaluated by Rebut-Lallia scaling law is smaller than 2 for all cases. In case of ITER89 power scaling law, however, H-mode ignition is possible only for case 4. Other offset-linear scaling laws (H_{IO} and H_{SO}) require more than 3 GW for H-mode ignition.

In Table 2.4, the confinement enhancement factors are rewritten in terms of the JCT definition. It is seen that H-factor in all scaling laws are smaller than 2 even in Case 1. H-factor evaluated by Rebut-Lallia scaling law is smaller than the unity when the fusion power is larger than 3 GW. This implies that L-mode ignition is possible in Cases 3 and 4.

Table 2.5 shows the H-factor for the same cases when the helium accumulation is 10 %. Table 2.6 is the calculation result when the impurity assumption follows CDA physics guidelines and helium accumulation rate is given by JCT results. In this case, we assume

that $A_T=1.0$ and $A_N=1.2$ since there is no solution for $A_N=1.0$.

Figure 2.5 is a simulated plasma operation parameter contour (POPCON) plot referred from TAC-3 Physics Report [7]. Alphabetic letters in the figure are added by the authors. The operation parameters at these points are listed in Table 2.7. In the table, *1 and *2 denote the results of 1.5-D simulations and 0-D calculations, respectively. The discrepancy in the table is due to the profile effect since the impurity condition coincides in both cases. It is seen that the estimated H-factors at these points are smaller than 2.

Figure 2.6 shows the relation between Troyon coefficient g and the fusion power P_{FUS} for various helium accumulations when $Be=1\%$. It shows that the fusion power varies very much with helium accumulation rate for the same beta value.

Figures 2.7 and 2.8 show POPCON plots for EDA-ITER. Upper graphs in these figures are referred from Fig.2 in Ref. [7]. Lower graphs are 0-D calculation results when $He=12\%$ and $Be=1\%$. It is assumed that $H(IP)=1.5$ in Fig.2.7 and $H(RL)=1.1$ in Fig.2.8, respectively. The difference is very large in high- T_e and high- n_e region in both cases. It is because the helium accumulation rate depends on both T_e and n_e in upper graphs. Figures 2.9 and 2.10 show the 0-D calculation results when the helium accumulation depends on T_e and n_e . Upper graphs show the POPCON plots and lower graphs show the corresponding helium accumulation rate. We assume that $Be=1\%$ and $He = 12 \times (T_e/10keV) \times (n_e/10^{20})^{0.15} \%$ in Fig.2.9 and $He = 12 \times (T_e/10keV)^{1.5} \times (n_e/10^{20})^{0.3} \%$ in Fig.2.10. These graphs are similar to the upper graphs of Figs. 2.7 and 2.8 relatively well.

2.3 Required Fusion Power for Ignition

Figure 2.11 shows the relation between the fusion power P_{FUS} and H-factor in EDA-ITER plasma ($R_p=7.75$ m, $a_p=2.8$ m, $\kappa=1.6$, $\delta=0.05$) for various kinds of scaling laws. Here, we assume that $Q=\infty$, $q_\psi=2.7$, $I_p=25$ MA, $B_T=6$ T and $T_e=10$ keV. In this case, helium accumulation rate is 10% and the impurity fractions are given by CDA physics guidelines [3]. Here, $H(\text{IP})$, $H(\text{IO})$ and $H(\text{RL})$ denote H-factors for ITER89 power scaling law, ITER89 offset-linear scaling law and Rebut-Lallia scaling law, respectively. It is seen that H-factors for all scaling laws are smaller than 2 (ignition is possible in H-mode plasma) when $P_{\text{FUS}}=1$ GW. H-factor for Rebut-Lallia scaling law decreases down to the unity (ignition is possible in L-mode plasma) when $P_{\text{FUS}}=3$ GW. H-factor for ITER89 power scaling law, however, is still more than 1 when $P_{\text{FUS}}=5$ GW. The operation parameters are listed in Table 2.8.

Figure 2.12 shows the relation between the fusion power P_{FUS} and H-factor in EDA-ITER plasma with $Q=\infty$ when the helium accumulation rate is 20%. In this case, more than 4 GW of fusion power is required to achieve the ignition in H-mode plasmas for all scaling laws. When $P_{\text{FUS}}=5$ GW, there is the large uncertainty that $H(\text{RL})=1$ while $H(\text{IP})=2$. The operation parameters for these cases are listed in Table 2.9.

Table 2.10 shows the operation parameters when He=10% and the effective ion charge is fixed to 2.0. In these cases, only carbon is assumed for the impurity.

Figure 2.13 shows the operation region in T_e - n_e space. Solid lines and dashed lines denote H-factor required for the ignition and the fusion power, respectively. Here, $Q=\infty$, He=10% and other impurity fractions are assumed based on CDA physics guidelines. The figure shows that H-factor decreases with the fusion power when the electron temperature is fixed.

Figure 2.14 shows the achievable fusion power for various H-factor and Troyon g values. The required minimum fusion power for the given H-factor increases as the helium fraction increases while the fusion power is limited by the beta limit.

2.4 Helium Accumulation and Operation Region

The Rebut-Lallia-Watkins model used for EDA-ITER suggests a large amount of helium accumulation [7]. In this section, we discuss the effect of the helium accumulation.

Figure 2.15 shows the possible operation region of EDA-ITER when $H(IP) \leq 2$ and Troyon $g \leq 3$. The vertical axis denotes the fusion power and the horizontal axis denotes the helium accumulation rate, respectively. The effective ion charge Z_{eff} is calculated by CDA guidelines [3]. In this case, $Z_{eff} = 2.04$ when $H(IP) = 2$ and He=10%, and $Z_{eff} = 1.76$ when $H(IP) = 2$ and He=20%. Troyon g becomes large and H-factor becomes small as P_{FUS} increases. Therefore, the operation with $Q=\infty$ is achievable in the hatched region in the figure. It is seen that the minimum fusion power required for the ignition increases and the operation region becomes small as the helium accumulation rate

increases. Required fusion power for the ignition is about 4 GW when $\text{He}=20\%$. This ignition characteristics change very much for different scaling law and the permissible H-factor.

Figure 2.16 shows the possible operation region of EDA-ITER when $H(\text{RL}) \leq 1$ and $\text{Troyon } g \leq 3$. In this case, about 5 GW is required for the ignition when $\text{He}=20\%$. Troyon g , however, exceeds the critical value ($g=3$) for this fusion power. Therefore, the maximum allowable helium accumulation rate is about 18 % for this case.

Figure 2.17 shows the required fusion power for the ignition in EDA-ITER when the effective ion charge Z_{eff} is fixed. Here, the condition that $H(\text{IP})=2$ is assumed. It is seen that the required fusion power is very sensitive to Z_{eff} . When $\text{He}=20\%$ and $Z_{\text{eff}}=1.8$, the required fusion power for the ignition is 5.5 GW. When $\text{He}=20\%$ and $Z_{\text{eff}}=1.6$, the required fusion power is reduced to 2 GW. When $\text{He}=20\%$ and $Z_{\text{eff}}=2.0$, it is almost impossible to achieve the ignition.

Figure 2.18 shows the required fusion power in EDA-ITER when $Q=20$, $H(\text{IP}) \leq 2$ and $g \leq 3$. It is seen that the required fusion power is about 1.5 GW when $\text{He}=20\%$.

2.5 Characteristics of High- q_ψ Operation

In the previous sections, we assumed that the plasma current $I_p=25$ MA. In this section, we describe the operation region for high- q_ψ ($I_p < 25$ MA) plasma. High performance of a plasma in high- q_ψ region is reported in the present large tokamak [6]. According to Fig.8 of Ref.[7], the ignition operation is possible for the plasma with

lower- I_p when P_{FUS} is small. This implies that the plasma confinement is better in low- I_p (high- q_ψ) region for the model used in the study. If we can assume the enhanced confinement ($H > 2$) in high- q_ψ region, the requirement in the plasma current can be reduced. Here, we consider only beryllium as an impurity following to JCT study.

Tables 2.11, 2.12 and 2.13 list the operation parameters for the ignition plasma when the fusion power $P_{FUS} = 1.5$ GW and He=10%. Table 2.11 is corresponding to the case when $I_p = 25$ MA ($q_\psi = 2.7$). Table 2.12 is corresponding to the case when $I_p = 20$ MA ($q_\psi = 3.4$). Table 2.13 is corresponding to the case when $I_p = 15$ MA ($q_\psi = 4.5$). The column marked by a symbol, -, means no solution, that is, ignition is possible only for unrealistic H-factors. This is because the radiation power is too large to keep the power balance. Figure 2.19 shows the contour line plot of H-factor evaluated by ITER89 power scaling law in I_p -Be space when He=10%. Figures 2.20, 2.21 and 2.22 are those for ITER89 offset-linear scaling, Rebut-Lallia scaling and Goldston scaling laws, respectively. It is suggested that the H-factor is larger in high-Be and low- I_p region for all scaling laws.

Tables 2.14, 2.15 and 2.16 list the operation parameters for the ignition plasma when the fusion power $P_{FUS} = 1.5$ GW and He=20%. Figure 2.23 shows the contour line plot of H-factor evaluated by ITER89 power scaling law in I_p -Be space when He=20%.

Figure 2.24 shows the contour lines of H-factor and Troyon g in I_p - P_{FUS} plane when He=10% and Be=1%. H-factor is evaluated by ITER89 power scaling law in Fig.2.23-a) and by Rebut-Lallia scaling law in Fig.2.23-b). Figure 2.25 shows the contour lines of H-factor and

Troyon g in I_p - P_{FUS} plane when He=10% and Be=6%. Figure 2.26 shows the contour lines of H-factor and Troyon g in I_p - P_{FUS} plane when He=15% and Be=1%. Figure 2.27 shows the contour lines of H-factor and Troyon g in I_p - P_{FUS} plane when He=15% and Be=3.5%.

Operation region for various beryllium fractions are shown in Fig.2.28 when He=5%, $H \leq 2$ and $g \leq 3$. Figures 2.29 and 2.30 are corresponding to those for helium fractions of 10% and 15%. These graphs are corresponding to Fig.9 in TAC-3 Physics Report [7].

Figure 2.31 shows the operation region for various helium accumulation rates when Be=1%, $H \leq 2$ and $g \leq 3$.

Figures 2.32 and 2.33 show the contour line plots of the required H-factor for the ignition in He-Be space when $I_p=25$ MA. The H-factor is evaluated by ITER89 power scaling law in Fig.2.32 and by Rebut-Lallia scaling law in Fig.2.33, respectively. In both figures, a) is corresponding to the case of 1.5 GW and b) to the case of 3 GW.

2.6 Possibility of Short-time Ignition

It is considered that the ignition may be achieved easily in a short period where helium accumulation is relatively small. In this section, we investigate the burn time and H-factor for EDA-ITER.

Figure 2.34 shows the operation region for the ignition plasma of EDA-ITER when $P_{FUS}=750$ MW and He=10%. Solid lines, short-dashed lines and long dashed lines denote the H-factor, burn time and Troyon g , respectively. The burn time is calculated by the assumptions same as CDA [5]. In this section, we assume that

$B_{P_{MAX}}=12$ T. In Fig.2.34-a), H-factor is evaluated by ITER89 power scaling law. In Fig.2.34-b), H-factor is evaluated by ITER89 offset-linear scaling law. Figure 2.35 shows the operation region for the ignition plasma when $P_{FUS}=1.5$ GW and He=10%. Figure 2.36 shows the operation region for the ignition plasma when $P_{FUS}=3$ GW and He=10%. It is seen that the H-factor is smaller in high- I_p and low- T_e region where the burn time is shorter. If the operation with $q_\psi \leq 3$ is possible, the required H-factor can be reduced. H-factor can be reduced as well as the enhancement of the burn time by increasing the fusion power for the same T_e and I_p . The operation parameters at 10 keV and 25 MA in the above mentioned figures are listed in Table 2.17 (I_1 , I_2 and I_3).

Figures 2.37, 2.38 and 2.39 show the operation region when He=0%. The operation parameters at 10 keV and 25 MA are also listed in Table 2.17 (H_1 , H_2 and H_3). It is seen that $H(LR) \leq 1$ (L-mode ignition is possible) when $P_{FUS}=1.5$ GW. This implies that the plasma may ignite in a short time until helium ash accumulates (e.g. several tens second).

Figures 2.40, 2.41 and 2.42 show the operation region when He=10% and H-factor is calculated by using τ_E^* (See Sec.2.2). The operation parameters at 10 keV and 25 MA are listed in Table 2.18 (I_1' , I_2' and I_3').

2.7 Effect of Impurity Species

In EDA-ITER, only beryllium (Be) is assumed as an impurity other than helium, while carbon, oxygen and iron are assumed in CDA-

ITER. In case of CDA-ITER, the line radiation loss from the main plasma and the radiation losses in the edge region are calculated according to CDA guidelines [3]. In this report, because of uncertainty in the line radiation loss of beryllium, we consider only bremsstrahlung loss power in EDA-ITER. In CDA-ITER, the effective ion charge Z_{eff} is calculated by the electron density n_e because the fractions of impurities are given as functions of n_e . We follow CDA guidelines in calculations of EDA-ITER except the case we assume the specific value of effective ion charge. It is useful to know the relation

$$\begin{aligned} Z_{\text{eff}} &= 1 + \sum_j (Z_j^2 - Z_j) f_j, \\ &= 1 + 2 f_{\text{He}} + 12 f_{\text{Be}} + 30 f_{\text{C}} + 56 f_{\text{Ox}} + 650 f_{\text{Fe}}, \end{aligned}$$

where f_j is a fraction of i -th impurity of which charge number is Z_j .

The bremsstrahlung loss power depends only on Z_{eff} and n_e . Therefore, the difference in impurity species affect only on the dilution effect. The dilution effect of Be is so large that the confinement capability is greatly degraded compared to the case with other impurities.

Figure 2.43 shows the required H-factor for the ignition operation of EDA-ITER when $I_p=25$ MA, $T_e=10$ keV and He=20%. Here, $H(\text{IP})$ and $H(\text{RL})$ denote the enhancement factors evaluated by ITER89 power scaling law and Rebut-Lallia scaling law, respectively. Figure 2.43-a) shows the case that He=20%, Be=3% and no other impurity is assumed. Figure 2.43-b) shows the case that He=20%, C=0.64%. For both cases, it is assumed that $Z_{\text{eff}}=1.76$. The required H-factor for the former case is 30 % larger than that for the latter case.

Figures 2.44 and 2.45 show the required H-factor $H(\text{IP})$ of the

ignition mode plasma for various impurity fractions when $P_{FUS}=1.5$ GW and He=10%. Figure 2.44 shows the case that only beryllium is assumed as the impurity and Fig.2.45 shows the case that carbon is assumed. In both cases, the upper graph is a plot as a function of the impurity fraction and the lower graph is a plot as a function of the effective ion charge (Z_{eff}). The carbon fraction of 2.5% is corresponding to the beryllium fraction of 4% in the view point of the confinement capability (See the operation point of H=2).

Figures 2.46 and 2.47 show the same relationship when He=20%. The fraction, 1.25% of C, is corresponding to 2% of Be, which is the same ratio with the case He=10% (See the operation point of H=3). The ratio of Be fraction to C fraction for the same H-factor decreases as Z_{eff} increases. It implies that overall effect by beryllium is worse than that by carbon from the view point of the dilution.

2.8 Particle and Heat Load

In this section, particle and heat load are evaluated by using a simplified model. The neutron wall load (W_{NEUT}), radiation wall load (W_{RAD}) and wall load (W_{α}) by the ripple loss of alpha particles are listed in Table 2.19. These wall loads are calculated by

$$\begin{aligned} W_{NEUT} &= (P_{FUS} - P_{\alpha}) / S_{wal} , \\ W_{RAD} &= (P_{MAIN} + P_{EDGE}) / S_{wal} , \\ W_{\alpha} &= P_{\alpha} \times f_{\alpha} \times R_{\alpha} / S_{wal} . \end{aligned}$$

Here, $P_{\text{MAIN}} = P_{\text{BRM}} + P_{\text{SYN}} + P_{\text{LIN}}$ and P_{EDGE} is the radiation from the edge region calculated by CDA physics guidelines [3]. Hence, the impurity species and fractions are following to CDA assumptions (beryllium is not considered). R_{α} and f_{α} are the ripple loss fraction (~3%) of alpha particles and the peaking factor (~50), respectively.

It is considered that the heat removal of the divertor plate is an important R & D issue. Figure 2.48 shows the divertor heat load calculated by 0-D scaling models [5]. Here, we assume only carbon as the impurity. Figure 2.48-a) shows H-factor as a function of carbon fraction. Figure 2.48-b) shows the divertor heat load for the ignition plasma when $I_p=25$ MW, $P_{\text{FUS}}=1.5$ GW and He=10%. Three types of divertor scaling models are compared. The angle of divertor plate to the separatrix field line in the poloidal cross section is assumed to be 90° (15° in CDA-ITER). Therefore, 20 MW/m^2 of this graph is corresponding to 5 MW/m^2 in CDA-ITER since $\sin 15^\circ = 0.26$. In the calculation, we need information about the edge radiation. Therefore, we follow CDA assumptions. In EDA-ITER, the gas target divertor concept [8] is adopted and it is completely different from that for CDA-ITER. Therefore, the further study must be done in this matter.

3. Steady-state Mode Operation

3.1 General Remarks

In this chapter, steady-state operation mode of EDA-ITER is investigated. In this report, we consider only a neutral beam injection (NBI) as the current-driver for the simplicity.

EDA-ITER requires large current-drive power for the steady-state operation since it is originally designed as a pulsed reactor. According to Fig.8 of Ref.[1], steady-state operation in EDA-ITER requires the high current-drive figure of merit (FOM), that is, $\gamma = 0.4 \sim 0.9 \times 10^{20} \text{ AW}^{-1}\text{m}^{-2}$. The current-drive FOM γ is a index which is used to estimate the current-drive efficiency for various kinds of current-drivers by one index and given by

$$\gamma = n_e R_P \eta_{CD}.$$

Here, η_{CD} is current-drive efficiency for NBI in our case. Figure 3.1 shows the current-drive FOM (γ) of NBI as a function of electron temperature. It is seen that the current-drive FOM (γ) is approximately proportional to the electron temperature. It is also seen that γ does not depend much on the effective ion charge (Z_{eff}).

According to CDA formula [3], the NBI current-drive efficiency for EDA-ITER is approximately given by

$$\eta_{CD} [\text{A/W}] = 0.0031 \frac{T_e [\text{keV}]}{n_e [10^{20}/\text{m}^3]}.$$

For Case 1 of the previous chapter (Sec.2.2, Table 2.3), the required driven current is about 21.7 MA. Therefore, the required current-drive power is about 840 MW when $T_e=10 \text{ keV}$ and $n_e=1.1 \times 10^{20} \text{ m}^{-3}$. This value is too large for the equipped heating power. If we can

limit, energy confinement time and available current-drive power. The maximum value of the toroidal beta β_t is proportional to the plasma current I_p . The effect of the pressure anisotropy on the beta limit is not clear. In this report, we assume that all components of the beam beta β_b contribute to β_t . This assumption is more conservative than the case that one third of β_b is included.

Confinement constraints are expressed in terms of the maximum permissible enhancement (H-factor) over L-mode energy confinement scaling laws. Generally, the confinement time increases with I_p . Typical value of H-factor in the present experiments of large tokamaks is smaller than 2.

Another constraint is the available current-drive power P_{NBI} . Since the current-drive efficiency is approximately proportional to the electron temperature T_e , the required power is larger in lower- T_e region (and naturally in higher- I_p region). Fusion gain, or energy multiplication, Q ($= 5 P_\alpha / P_{NBI}$) is another key issue.

For the reasons mentioned above, it is convenient to express the operation region of a steady-state plasma in T_e - I_p space together with the contour lines of Troyon coefficient g , H-factor and P_{NBI} .

Figure 3.2 shows the steady-state operation region for various fusion powers P_{FUS} . Here, H-factor is evaluated by using ITER89 power scaling law. In all figures, solid lines, dashed lines and long dashed lines denote contour lines of H-factor, P_{NBI} and Troyon g , respectively. Upper part of the solid line is corresponding to the area $H \leq 2$ (or $H \leq 2.2$) and lower part of the dashed line to the area $P_{NBI} \leq 120$ MW (or $P_{NBI} \leq 140$ MW). Note that the loop voltage V_{LOOP} is equal to 0 V everywhere and the fusion gain Q is not constant on this T_e - I_p

limit, energy confinement time and available current-drive power. The maximum value of the toroidal beta β_t is proportional to the plasma current I_p . The effect of the pressure anisotropy on the beta limit is not clear. In this report, we assume that all components of the beam beta β_b contribute to β_t . This assumption is more conservative than the case that one third of β_b is included.

Confinement constraints are expressed in terms of the maximum permissible enhancement (H-factor) over L-mode energy confinement scaling laws. Generally, the confinement time increases with I_p . Typical value of H-factor in the present experiments of large tokamaks is smaller than 2.

Another constraint is the available current-drive power P_{NBI} . Since the current-drive efficiency is approximately proportional to the electron temperature T_e , the required power is larger in lower- T_e region (and naturally in higher- I_p region). Fusion gain, or energy multiplication, Q ($= 5 P_\alpha / P_{NBI}$) is another key issue.

For the reasons mentioned above, it is convenient to express the operation region of a steady-state plasma in T_e - I_p space together with the contour lines of Troyon coefficient g , H-factor and P_{NBI} .

Figure 3.2 shows the steady-state operation region for various fusion powers P_{FUS} . Here, H-factor is evaluated by using ITER89 power scaling law. In all figures, solid lines, dashed lines and long dashed lines denote contour lines of H-factor, P_{NBI} and Troyon g , respectively. Upper part of the solid line is corresponding to the area $H \leq 2$ (or $H \leq 2.2$) and lower part of the dashed line to the area $P_{NBI} \leq 120$ MW (or $P_{NBI} \leq 140$ MW). Note that the loop voltage V_{LOOP} is equal to 0 V everywhere and the fusion gain Q is not constant on this T_e - I_p

plane. The MHD safety factor $q_\psi > 3$ is another constraint. Here, $q_\psi = 3$ is corresponding to $I_p = 25$ MA. Therefore, operation is possible in the shaded area of the figures. Points S_1 , S_2 , S_3 , S_4 and S_5 are corresponding to the lowest- T_e operation points. Operation parameters of these points are listed in Table 3.3.

Figure 3.3 shows the steady-state operation region of EDA-ITER when $P_{NBI} \leq 140$ MW and $H \leq 2.1$. For the comparison, we show the operation region of CDA-ITER for the same conditions in Fig.3.4. S_1 , S_3 , C_1 and C_3 are the operation points with the lowest- T_e . Operation parameters of these points are listed in Tables 3.4 and 3.5.

Figure 3.5 shows the operation region in T_e - I_p space for steady-state plasma of EDA-ITER when $P_{FUS} = 500$ MW. Here, H-factor is evaluated by using τ_E^* (See Sec.2.2). ITER89 power (IP) scaling law is used in Fig.3.5-a) and ITER89 offset-linear (IO) scaling law is used in Fig.3.5-b). S_1 is the lowest- T_e operation point when $H(IP) \leq 2$ and $P_{FUS} \leq 120$ MW. S_2 is the lowest- T_e operation point when $H(IO) \leq 1.5$ and $P_{FUS} \leq 120$ MW.

Figure 3.6 shows the operation region when $P_{FUS} = 1000$ MW. Here, H-factor is evaluated by using τ_E^* . S_3 is the lowest- T_e operation point when $H(IP) \leq 2$ and $P_{FUS} \leq 120$ MW. S_4 is the lowest- T_e operation point when $H(IO) \leq 1.5$ and $P_{FUS} \leq 120$ MW. In these case of P_{FUS} , the fusion gain Q is larger than 5 ($Q \sim 8.3$).

It is seen from Figs. 3.5 and 3.6 that 120 MW of P_{NBI} is enough for the steady-state mode operation when the JCT definition of τ_E is adopted. The operation parameters for these points are listed in Table 3.6.

3.3 Fusion Power and Achievable Q-value

In this section, we discuss the achievable Q-value for the steady-state plasma. In the following part, we adopt the original dimensions of EDA-ITER, those are, $R_p=7.75$ m and $a_p=2.8$ m.

Figure 3.7 shows the steady-state operation performance of EDA-ITER when $T_e=10$ keV, He=10% and $H_{RL}=2.0$. Figure 3.7-a) shows the achievable fusion gain Q as a function of P_{FUS} . Figure 3.7-b) shows the bootstrap current fraction I_{BS}/I_P as a function of P_{FUS} . Figure 3.7-c) shows the plasma current I_P as a function of P_{FUS} . Figure 3.7-d) shows the electron density n_e and Troyon coefficient g . It is seen that $Q>15$ ($P_{NBI}<100$ MW) when $P_{FUS}=1500$ MW. In this case, the bootstrap fraction is about 80%.

Figure 3.8 shows the steady-state operation performance of EDA-ITER when $T_e=10$ keV, He=10% and $H_{RL}=1.0$. Figures 3.8-a), 3.8-b), 3.8-c) and 3.8-d) show Q , I_{BS}/I_P , I_P and n_e , respectively. In this case, Q is small ($Q=5\sim6$) even when $P_{FUS}\geq 1500$ MW.

Figure 3.9 shows the steady-state operation performance of EDA-ITER when $T_e=10$ keV, He=5% and $H_{RL}=2.0$. Figures 3.9-a), 3.9-b), 3.9-c) and 3.9-d) show Q , I_{BS}/I_P , I_P and n_e , respectively. In this case, Q is very large ($Q>20$) when $P_{FUS}=1500$ MW. The bootstrap fraction is about 80%.

Figure 3.10 shows the steady-state operation performance of EDA-ITER when $T_e=10$ keV, He=5% and $H_{RL}=1.0$. Figures 3.10-a), 3.10-b), 3.10-c) and 3.10-d) show Q , I_{BS}/I_P , I_P and n_e , respectively. In this case, Q is small ($Q=6\sim8$) even when $P_{FUS}\geq 1500$ MW.

Figure 3.11 shows the steady-state operation of EDA-ITER when $I_p=25$ MA and $H_{RL}=1.0$ for various helium fractions. Figure 3.11-a) shows the achievable fusion gain Q as a function of P_{FUS} . Figure 3.11-b) shows the required current-drive power P_{NBI} as a function of P_{FUS} .

Figure 3.12 shows the steady-state operation of EDA-ITER when $T_e=10$ keV and $H_{RL}=1.0$ for various helium fractions.

Figure 3.13 shows the steady-state operation of EDA-ITER when $Z_{eff}=2.0$, $I_p=25$ MA and $H_{RL}=1.0$ for various helium fractions.

Figure 3.14 shows the steady-state operation of EDA-ITER when $Z_{eff}=2.0$, $T_e=10$ keV and $H_{RL}=1.0$ for various helium fractions.

In conclusion, it is very difficult to operate L-mode ($H_{RL}=1$) EDA plasma in steady-state even when He=5%. In H-mode ($H_{RL}=2$) plasma, high- Q steady-state operation is possible both for He=5% and He=10% if Rebut-Lallia scaling law is adoptable. In this case, more than 1.5 GW operation is preferable.

Figure 3.15 shows the steady-state operation of EDA-ITER when $I_p=25$ MA and $P_{FUS}=1200$ MW for various helium fractions. Figure 3.15-a) shows the achievable fusion gain Q as a function of H-factor. Figure 3.15-b) shows the required current-drive power P_{NBI} .

Figure 3.16 shows the steady-state operation of EDA-ITER when $T_e=10$ keV and $P_{FUS}=1200$ MW for various helium fractions. It is seen that the required H-factor is about 2 even for Rebut-Lallia scaling law in order that the current-drive power is small enough to afford.

3.4 Enhanced Confinement Plasma with High- q_ψ

The present large tokamak experiments suggest an enhanced confinement capability in high- q_ψ region [6]. TAC-4 report [9] discussed the performance for high- q_ψ steady-state plasma and proposed some operation points. In TAC-4 report, very high fraction (>90%) of the bootstrap current is assumed [9]. We chose $R_p=8.11$ m, $a_p=3.0$ m, $\kappa=1.53$ and $\delta=0.23$ in this section for investigating a possibility of the operation with a smaller bootstrap fraction by optimizing the fusion power. We also investigate the possibility of decreasing H-factor by increasing the current-drive power P_{NBI} . A pessimistic current-drive efficiency is assumed, that is, 0.6 times smaller than the CDA guidelines [3]. Therefore, it should be noted that 30 MW of P_{NBI} is corresponding to 18 MW for CDA guidelines.

Figures 3.17 shows the operation performance of steady-state plasma when $q_\psi=5.6$, He=14% and $Z_{eff}=2.2$. The impurity fraction is calculated to adjust the plasma parameters to those in Table 7 of Ref.[9] when $P_{FUS}=2.2$ GW. The bootstrap fraction decreases as the fusion power decreases and also by increasing the current-drive power. In this case, the required H-factor decreases in compensation. Figure 3.17-b) shows the corresponding H-factor estimated by ITER89 power scaling law. It is difficult to reduce the fusion power when the current-drive power is small same as that is assumed in TAC-4 report [9]. Therefore, the steady-state operation is not feasible when P_{NBI} is small since the divertor heat load is too large and the margin for the profile control may not be enough for the plasma with large bootstrap current. Figure 3.18 shows more optimistic case with

lower effective ion charge ($Z_{\text{eff}}=1.5$). In this case, the required H-factor is about 4 for Rebut-Lallia scaling law and 5 for ITER89 power scaling law when $P_{\text{NBI}}=30$ MW. Figure 3.19 shows the required H-factor and the bootstrap fraction as a function of He fraction. In these cases, only carbon is assumed as the impurity.

TAC-4 report [9] also investigates the optimized steady-state plasma operation. The plasma with larger- R_p , smaller- a_p and larger- κ is discussed. Figure 3.20 shows the the required H-factor and the bootstrap fraction as a function of the major radius R_p . Here, the plasma minor radius a_p is interpolated linearly between two plasmas listed in Ref.[9]. It is assumed that the toroidal field $B_T=5.7$ T, the fusion power $P_{\text{FUS}}=2200$ MW and the current-drive power $P_{\text{NBI}}=30$ MW for the simplicity. In these cases, we assume beryllium only as the impurity. We also assume that $\kappa=1.53$, $\delta=0.23$ since the required H-factor does not greatly depend on κ and δ if the fusion power is fixed. It is seen that the required H-factor increases with the plasma major radius. However, the decrease of H-factor due to the lower helium fraction dominates the increase of H-factor due to the larger major radius. The decrease of MHD safety factor q_ψ also leads to the reduction of H-factor because of the larger plasma current. Finally, we obtain the good performance plasma with larger- R_p when $q_\psi=4.7$. In Table 7 of Ref.[9], the toroidal field B_T is 4.34 T and MHD safety factor q_ψ is 4.22 which are smaller than our assumption. The elongation k for our calculation is smaller than that for Ref.[9]. Consequently, the plasma current I_p is not much different for each case.

Operation parameters for these cases are summarized in Tables 3.7 and 3.8. Table 3.7 shows the initial operation point given by Ref.[9] and our reconstructions of it. The difference in the impurity assumption affects the electron density and H-factor because of the dilution effect (Compare S_1 and S_2 in the table). Note that the case S_2 is not a realistic case since the bootstrap fraction is too large. Case S_3 is the best reconstruction by 0-D model. Table 3.8 shows the optimized operation point given by Ref.[9] and our reconstructions of it. Note that the case S_4 is not a steady-state case since the bootstrap fraction is too small. Case S_5 is the best reconstruction by 0-D model. S_6 is the case with the same κ and δ as the initial plasma.

Details of the comparison between the normal plasma and the plasma with a small minor radius are discussed in Chap.3.6.

3.5 Divertor Heat Load

In this section, we investigate the divertor heat load for the steady-state operation of EDA-ITER ($R_p=8$ m, $a_p=3$ m). Here, optimistic assumption that $H_{IP}=3$ is assumed. As an impurity, carbon is considered. The angle of divertor plate to the separatrix field line in the poloidal cross section is assumed to be 90° (15° in CDA-ITER). Therefore, 20 MW/m² of our estimation is corresponding to 5 MW/m² in CDA-ITER (See Chap.2.8).

Figures 3.21 shows the divertor heat load of steady-state plasma when $P_{FUS}=500$ MW, He=10% and $Z_{eff}=1.95$. The divertor heat load W_{div} decreases as the current-drive power, P_{NBI} , increases. It is

because the electron temperature at the operation point decreases with the increase of P_{NBI} and the decrease of plasma current consequently. It should be noted that the divertor heat load has a positive dependence on the plasma current [5], which is also shown in Fig.3.21. Figures 3.22 shows the divertor heat load of steady-state plasma when $P_{FUS}=750$ MW, He=10% and $Z_{eff}=1.95$. Figures 3.23 shows the divertor heat load of steady-state plasma when $P_{FUS}=1000$ MW, He=10% and $Z_{eff}=1.95$.

The particle load and heat load for the steady-state plasma are summarized in Tables 3.9 and 3.10 when the fusion power P_{FUS} is 750 MW and 1500 MW. In Table 3.9, the plasma current I_p is fixed to be 25 MA and the electron temperature is optimized. In Table 3.10, the electron temperature T_e is fixed to be 10 keV and the plasma current is optimized. Here, the impurity fractions are calculated by using CDA guidelines [3]. W_{NEUT} , W_{RAD} and W_{α} denote the neutron wall load, radiation wall load and alpha particle ripple loss local wall load, respectively (See Chap.2.8 for the detail).

At the next step, the fusion gain, Q , is optimized in the view point of the electron temperature T_e . Here, cases with He=10% and He=20% are investigated.

Figures 3.24 shows the operation performance of steady-state plasma when $P_{FUS}=500$ MW and $Z_{eff}=1.7$. Figure 3.24-a) shows the achievable fusion gain, Q , as a function of electron temperature T_e . Figure 3.24-b) shows the required current-drive power P_{NBI} . Figures c), d), e) and f) show Troyon g , q_{ψ} , I_{BS}/I_p and n_e , respectively. Figure 3.24-g) shows the divertor heat load W_{div}^{HK} for Constant- χ model [5]. Figure 3.24-h) shows the divertor heat load W_{div}^{JT60} for JT-60U model [5].

Figures 3.25, 3.26 and 3.27 show the operation performance of steady-state plasma for $P_{\text{FUS}}=500$ MW and $Z_{\text{eff}}=1.95$, for $P_{\text{FUS}}=1000$ MW and $Z_{\text{eff}}=1.7$, and $P_{\text{FUS}}=1000$ MW and $Z_{\text{eff}}=1.95$, respectively.

In each figure, a) shows the fusion gain Q , b) shows the required current-drive power P_{NBI} , c) shows Troyon g , d) shows MHD safety factor q_{Ψ} , e) shows the bootstrap current fraction, f) shows the average electron density n_e , g) shows the divertor heat load calculated by Constant- χ model and h) shows the divertor heat load calculated by JT-60U model, respectively. In all cases, the optimum temperature for Q value is about 16 keV. Operation parameters and the divertor heat load are summarized in Table 3.11.

3.6 Small- a_p Operation

In this section, we discuss the specific operation for plasmas with a smaller minor radius a_p . We assume that the major radius R_p is 7.8 m in both normal plasmas and plasmas with a small- a_p . The minor radius of the normal plasma is chosen to be 2.8 m. Here, we choose the radius of $a_p=2.0$ m as an example of a small minor radius plasma. In this case, the plasma stored energy becomes small and consequently the required confinement time decreases. Therefore, it is expected that the required plasma current becomes small for the same H-factor and the required current-drive power P_{NBI} decreases.

Figure 3.28 denotes the operation region for the normal case and the small- a_p case. Solid line, short-dashed line and long-dashed line denote the contour lines for H-factor evaluated by ITER89 power

scaling law, $P_{\text{NBI}}=120$ MW (and 140 MW) and Troyon factor $g=3$, respectively. The operation region is shown by a shaded area. Point SS denotes the operation point with the lowest electron temperature for the plasma with small- a_p . The plasma parameters at this point are described in Table 3.12 as well as those for the normal operation point. In case of the normal plasma, there is no operation region when $P_{\text{FUS}}=750$ MW and $P_{\text{NBI}} \leq 120$ MW, while there appears an operation region for small- a_p plasma. There is an operation region even when $P_{\text{FUS}}=500$ MW. It is because the fraction of the bootstrap current is larger than that of the normal plasma (See Table 3.12). According to the simplified estimation [10] for a circular cross section, the bootstrap fraction is given by

$$I_{\text{BS}} / I_{\text{P}} = 0.65 \beta_{\text{P}}^* / A^{0.5}.$$

Here, β_{P}^* is a poloidal beta value estimated by the plasma current and given by

$$\beta_{\text{P}}^* = \frac{\kappa}{20 f(\kappa, \delta) h(A)} A q_{\Psi} g,$$

where $f(\kappa, \delta)$ is the shaping coefficient (f_8 of Fig.2.2) and $h(A)$ is the toroidal effect (f_9 of Fig.2.2). For $\kappa=1.7$ and $\delta=0.15$, $f(\kappa, \delta)=2.0$.

Function $h(A)$ has a weak dependence on A and it takes $1.1 < h < 1.2$ for $A > 3$. Then, we obtain $\beta_{\text{P}}^* \sim 0.036 A q_{\Psi} g$. Finally, we obtain

$$I_{\text{BS}} / I_{\text{P}} \sim 0.023 A^{0.5} q_{\Psi} g.$$

At Point SS, $A=3.9$, $q_{\Psi}=3.2$ and $g=3$, while in case of the normal plasma, $A=2.89$, $q_{\Psi}=4.3$ and $g=2.3$ (Point S4 of Fig.3.28-a). Therefore, the effect of high- g is compensated by that of low- q_{Ψ} and the bootstrap fraction dominantly depends on A . In ITER physics guidelines [3], $I_{\text{BS}} / I_{\text{P}} \propto q_{\Psi}^{0.8} g^{1.3}$ and the high- g effect is not completely cancelled by low- q_{Ψ} . When this relation holds, there is some advantage for a small- a_p operation in the present device.

4. Thermal Instability and 0-D Transient Analysis

It is well known that a fusion plasma can be unstable against temperature perturbations [11]. This instability is called "thermal instability". Although the fusion power excursion would be limited by other instabilities, it is important to examine the thermal characteristics of the plasma for zero order approximation. In this section, we show the preliminary results for the thermal instability and 0-D transient behavior of EDA-ITER. Here, we assume that the plasma reported in TAC-4 [9] (major radius R_p is 8.11 m and a small radius a_p is 3.0 m).

Figure 4.1 shows the plasma operation parameter contour (POPCON) plot for the EDA-ITER. Solid lines denote the required heating power when $H(IP)=1.8$. Here, $H(IP)$ is the H-factor estimated by ITER89 power scaling law. Effective ion charge Z_{eff} is assumed to be 1.5 (He=10% and C=1%). Contour lines of the growth rate for the thermal instability are also shown in the figure. It is seen that the growth time is about 15 s for this case. Note that the growth time is greatly dependent on energy confinement scaling laws. For example, the growth time is about 4 s for ITER89 offset-linear scaling law. An ignition operation point of ITER is also shown in the figure where the electron temperature T_e and the electron density n_e are 10 keV and $0.98 \times 10^{20} \text{ m}^{-3}$, respectively. The fusion power P_{FUS} is 1.5 GW and Troyon coefficient is 1.8 at this point. This is an equilibrium point of a static plasma power balance. According to a linear theory, this equilibrium is unstable, i.e., a small temperature rise increases the

fusion reaction rate and the temperature will continue to rise until the plasma reaches the other stable equilibrium point.

Figure 4.2 shows the time development of the electron temperature T_e and the fusion power P_{FUS} for the reference operation point of EDA-ITER when the small perturbation in the electron temperature occurs. Here, we assume that the electron density is constant (by proper fuelling). If the helium accumulation is included, the excursion may be stabilized. This effect, however, depends on the fuelling and pumping assumptions and includes the uncertainty. Therefore, we neglect the helium accumulation effect for the simplicity. It is seen from Fig.4.2 that the electron temperature increases from 10 keV to 16 keV and the fusion power increases to about 3.2 GW. This process occurs in the direction of the arrow in Fig.4.1. If the instability is not suppressed properly, severe problem will occur in the plasma facing component etc. One possible scheme is to select the higher- T_e and lower- n_e operation point where is the thermally stable region. In this case, however, the divertor condition becomes worse. The control method is under investigation.

5. Conclusion

The major radius of EDA-ITER is large enough to achieve the burn time of 1000 s. In the viewpoint of confinement, the large major radius is essential for the ignition for high helium accumulation. The required fusion power for the ignition greatly depends on the scaling law and the helium accumulation rate. EDA-ITER has enough capability of ignition when the helium accumulation rate is 10 %. The ignition can be achieved in H-mode plasma when $P_{FUS}=1$ GW. There is a possibility of L-mode ignition when $P_{FUS}=3$ GW. In case of high accumulation of helium, however, very large fusion power might be required. It is found that about 4 GW is required for the ignition when $He=20$ %, $H(IP)\leq 2$ and Troyon $g\leq 3$. For Rebut-Lallia scaling law, the required fusion power would be reduced to 1.5 GW. Lower Q-value (~ 20) can be achieved for 1.5 GW and for ITER89 power scaling law. The results suggest that the helium accumulation and impurity inflow to the plasma are key issues for the plasma performance.

The divertor heat load estimated by CDA model is comparable to or smaller than CDA-ITER ignition mode if the divertor plate like CDA could be designed. It is because the electron density is not much larger than that of CDA-ITER and the connection length ($L=R_p q_\psi$) is longer than that of CDA-ITER. Heat loading for the advanced divertor concept is left for the future study.

Steady-state operation is also investigated extensively. Required current-drive power P_{NBI} for the steady-state operation with $Q>5$ is about 140 MW when $I_p=25$ MA and $H_{IP}=2.0$. If the enhanced confinement ($H_{IP}=3$) in high- q_ψ region is feasible, the required

current-drive power is about 60 MW when $P_{\text{FUS}}=1000$ MA, He=10% and $Z_{\text{eff}}=1.7$. The required current-drive power is about 110 MW when $P_{\text{FUS}}=1000$ MA, He=20% and $Z_{\text{eff}}=1.7$.

The divertor heat load for the steady-state operation is also investigated for CDA divertor model. It is found that the heat load for the steady-state operation is comparable to that for the ignition mode. However, it depends greatly on the impurity assumptions and the edge radiation by beryllium has not been evaluated. Estimation of the divertor heat load for the plasma with beryllium impurity is the subject of the future study. Heat load for the gas target divertor is out of the scope of this study.

Thermal instability and 0-D transient behavior of EDA-ITER is investigated. The growth time is about 15 s when ITER89 power scaling law is assumed. The fusion power increases to 3.2 GW nonlinearly in about 100 s. The growth time is greatly dependent on the energy confinement scaling law. The growth time is about 4 s if ITER89 offset-linear scaling law is used. Further study should be done in this subject.

Acknowledgements

The authors are grateful to Dr. S. Matsuda for his continuous support and encouragement.

current-drive power is about 60 MW when $P_{\text{FUS}}=1000$ MA, He=10% and $Z_{\text{eff}}=1.7$. The required current-drive power is about 110 MW when $P_{\text{FUS}}=1000$ MA, He=20% and $Z_{\text{eff}}=1.7$.

The divertor heat load for the steady-state operation is also investigated for CDA divertor model. It is found that the heat load for the steady-state operation is comparable to that for the ignition mode. However, it depends greatly on the impurity assumptions and the edge radiation by beryllium has not been evaluated. Estimation of the divertor heat load for the plasma with beryllium impurity is the subject of the future study. Heat load for the gas target divertor is out of the scope of this study.

Thermal instability and 0-D transient behavior of EDA-ITER is investigated. The growth time is about 15 s when ITER89 power scaling law is assumed. The fusion power increases to 3.2 GW nonlinearly in about 100 s. The growth time is greatly dependent on the energy confinement scaling law. The growth time is about 4 s if ITER89 offset-linear scaling law is used. Further study should be done in this subject.

Acknowledgements

The authors are grateful to Dr. S. Matsuda for his continuous support and encouragement.

References

- [1] P-H. Rebut *et. al.*, "A Fusion Reactor: Continuous or Semi-continuous?", JET-P (92) 65.
- [2] P-H. Rebut *et. al.*, in *Plasma Physics and Controlled Nuclear Fusion Research 1988* (IAEA, Vienna, 1989) Vol.2, p2209.
- [3] N. A. Uckan and ITER Physics Group, "ITER document series, No. 10", IAEA/ITER/DS/10, IAEA, Vienna (1990).
- [4] H. Fujieda, Y. Murakami and M. Sugihara, "Tokamak Plasma Power Balance Calculation Code (TPC Code) Outline and Operation Manual", JAERI-M 92-178 (1992) [in Japanese].
- [5] Y. Murakami and M. Sugihara, "Optimization of Steady-state and Hybrid Operations in a Tokamak Fusion Reactor by Using Divertor Scaling Models", *Fusion Technology*, **24** (1993) 375.
- [6] D. Meade *et. al.*, in *Plasma Physics and Controlled Nuclear Fusion Research 1990* (IAEA, Vienna, 1991) Vol.1, p9.
- [7] ITER TAC-3-03 Report, "ITER Physics and Plasma Operation Studies" (September 1993).
- [8] M. L. Watkins and P-H. Rebut, in *Controlled Fusion and Plasma Heating* (Proc. 19th Eur. Conf., Innsbruck 1992) Vol.16C, Part II, European Physical Society (1992) 731.
- [9] ITER TAC-4-03 Report, "Physics and Plasma Operation Studies" (January 1994).
- [10] J. D. Cordey *et. al.*, *Plasma Phys. Contr. Fusion* **30** (1988) 1625.
- [11] H. Yamato, M. Ohta and S. Mori, "Thermal Stability of a Spatially Non-uniform Plasma in a D-T fusion Reactor", *Nucl. Fusion*, **12** (1972) 604.

Table 2.1 Major parameters of CDA-ITER and EDA-ITER.

			CDA	EDA	EDA'
Major radius	R_P	(m)	6.0	7.75	8.0
Minor radius	a_P	(m)	2.15	2.8	3.0
Aspect ratio	A		2.79	2.77	2.67
Elongation	κ_{95}		2.0	1.6	←
Triangularity	δ_{95}		0.35	0.05	←
Elongation at separatrix	κ_x		2.22	1.96	←
Triangularity at separatrix	δ_x		0.52	0.16	←
Plasma volume	V_P	(m ³)	1072	1908	2261
Plasma surface area	S_P	(m ²)	877	1335	1476
First wall surface area	S_{wal}	(m ²)	918	1382	1525
Plasma current	I_P	(MA)	22	25	24
MHD safety factor	q_Ψ		3.02	2.68	3.05
Cylindrical q	q_{cyl}		2.45	2.17	2.43
Engineering q	q_I		2.12	2.16	2.42
Plasma self-inductance	L_P	(μH)	9.24	14.1	←
Toroidal field on axis	B_T	(T)	4.85	6.0	5.81
Maximum toroidal field	B_{TMAX}	(T)	11.2	13.2	13.0
Position of maximum field	R_{TFC}	(m)	2.72	3.7	3.75
Fusion power	P_{FUS}	(GW)	1.08	1.5	←
Loop voltage	V_{LOOP}	(V)	0.11	0.13	0.11
Maximum poloidal field	B_{PMAX}	(T)	13.4	13.0	13.0
Position of OH coils	R_{OH}	(m)	1.725	2.44	2.49
Total flux	Φ_{TOTAL}	(Vs)	325	600	630
Flux for current-rise	Φ_{RAMP}	(Vs)	270	450	440
Flux for burn	Φ_{BURN}	(Vs)	45	140	180
Burn time	T_{BURN}	(s)	400	1100	1600

Table 2.2 Major plasma parameters given by Ref. [1].

			Case 1	Case 2	Case 3	Case 4
Alpha power	P_{α}	(MW)	216	427	637	850
Ion temperature	$T_i(0)$	(keV)	19	23	21	16
Average electron density	$\langle n_e \rangle$	($10^{20}/\text{m}^3$)	1.1	1.6	2.1	2.6
Energy confinement time	τ_E^*	(s)	4.0	3.4	2.8	2.1
Bootstrap current	I_{BS}	(MA)	2.7	4.8	6.6	7.1
Helium accumulation	n_{He}/n_e	(%)	19	24	24	20
Loop voltage	V_{LOOP}	(V)	0.15	0.10	0.10	0.11
Troyon coefficient	g		1.40	2.34	2.86	2.97
Plasma stored energy	W_P	(MJ)	870	1440	1760	1800
Electron temperature (Center)	$T_e(0)$	(keV)	15	18	16	13
Electron temperature (Average)	T_e	(keV)	10	12	11	9

Table 2.3 Operation parameters calculated by 0-D model for EDA-ITER. W_p , P_{fus} , n_e and He ratio are given by Ref. [1]. Carbon fraction and T_e are determined to adjust the above parameters.

	Case 1	Case 2	Case 3	Case 4
I_P (MA)	25.0	←	←	←
q_Ψ	2.7	←	←	←
P_{FUS} (MW)	1080	2135	3185	4250
P_{RAD} (MW)	92	189	283	364
P_α (MW)	216	427	637	850
W_P (MJ)	870	1440	1760	1800
Q	∞	←	←	←
$\langle T_e \rangle$ (keV)	10.0	11.4	10.6	8.5
$\langle n_e \rangle$ ($10^{20} m^{-3}$)	1.1	1.6	2.1	2.6
He (%)	19	24	24	20
Z_{eff}	1.6	1.7	1.7	1.6
Troyon g	1.5 *	2.5 *	3.0 *	3.1 *
β_t (%)	2.2	3.7	4.5	4.6
β_α (%)	0.13	0.17	0.19	0.19
β_p	0.58	0.96	1.2	1.2
I_{BS} (MA)	3.3 *	6.2 *	8.0 *	8.2 *
V_{LOOP} (V)	0.12 *	0.09 *	0.10	0.12 *
T_{BURN} (s)	820	1200	1250	1000
τ_E (s)	6.8	6.0	4.9	3.7
τ_E^* (s)	4.0	3.4	2.8	2.1
H_{IP}	2.1	2.5	2.4	2.0
H_{IO}	2.3	2.2	1.9	1.5
H_{GS}	2.2	2.6	2.6	2.2
H_{RL}	1.8	1.8	1.5	1.1
H_{SO}	2.2	2.3	2.0	1.6

Note : $\tau_E^* = W_P / P_\alpha$

Table 2.4 Operation parameters calculated by 0-D model for EDA-ITER. W_p , P_{FUS} , n_e and He ratio are given by Ref. [1]. Carbon fraction and T_e are determined to adjust the above parameters. H-factors are calculated by τ_E^* .

	Case 1	Case 2	Case 3	Case 4
I_p (MA)	25.0	←	←	←
q_Ψ	2.7	←	←	←
P_{FUS} (MW)	1080	2135	3185	4250
P_{RAD} (MW)	92	188	283	364
P_α (MW)	216	427	637	850
W_p (MJ)	870	1440	1760	1800
Q	∞	←	←	←
$\langle T_e \rangle$ (keV)	10.0	11.4	10.6	8.5
$\langle n_e \rangle$ ($10^{20} m^{-3}$)	1.1	1.6	2.1	2.6
He (%)	19	24	24	20
Z_{eff}	1.6	1.7	1.7	1.6
Troyon g	1.5	2.5	3.0	3.1
β_t (%)	2.2	3.7	4.5	4.6
β_α (%)	0.13	0.17	0.19	0.19
β_p	0.59	0.96	1.2	1.2
I_{BS} (MA)	3.3	6.3	8.1	8.3
V_{LOOP} (V)	0.12	0.09	0.09	0.12
T_{BURN} (s)	820	1200	1250	1000
τ_E (s)	6.8	6.0	4.9	3.7
τ_E^* (s)	4.0	3.4	2.8	2.1
H_{IP}^*	1.6	1.8	1.7	1.5
H_{IO}^*	1.5	1.4	1.2	0.9
H_{GS}^*	1.6	1.9	1.9	1.7
H_{RL}^*	1.2	1.1	0.9	0.7
H_{SO}^*	1.5	1.5	1.3	1.0

Note : $\tau_E^* = W_p / P_\alpha$

Table 2.4 Operation parameters calculated by 0-D model for EDA-ITER. W_p , P_{FUS} , n_e and He ratio are given by Ref. [1]. Carbon fraction and T_e are determined to adjust the above parameters. H-factors are calculated by τ_E^* .

	Case 1	Case 2	Case 3	Case 4
I_p (MA)	25.0	←	←	←
q_Ψ	2.7	←	←	←
P_{FUS} (MW)	1080	2135	3185	4250
P_{RAD} (MW)	92	188	283	364
P_α (MW)	216	427	637	850
W_p (MJ)	870	1440	1760	1800
Q	∞	←	←	←
$\langle T_e \rangle$ (keV)	10.0	11.4	10.6	8.5
$\langle n_e \rangle$ ($10^{20} m^{-3}$)	1.1	1.6	2.1	2.6
He (%)	19	24	24	20
Z_{eff}	1.6	1.7	1.7	1.6
Troyon g	1.5	2.5	3.0	3.1
β_t (%)	2.2	3.7	4.5	4.6
β_α (%)	0.13	0.17	0.19	0.19
β_p	0.59	0.96	1.2	1.2
I_{BS} (MA)	3.3	6.3	8.1	8.3
V_{LOOP} (V)	0.12	0.09	0.09	0.12
T_{BURN} (s)	820	1200	1250	1000
τ_E (s)	6.8	6.0	4.9	3.7
τ_E^* (s)	4.0	3.4	2.8	2.1
H_{IP}^*	1.6	1.8	1.7	1.5
H_{IO}^*	1.5	1.4	1.2	0.9
H_{GS}^*	1.6	1.9	1.9	1.7
H_{RL}^*	1.2	1.1	0.9	0.7
H_{SO}^*	1.5	1.5	1.3	1.0

Note : $\tau_E^* = W_p / P_\alpha$

Table 2.5 $T_e=10$ keV, He=10% and other impurities are given by CDA guidelines.

	Case 1	Case 2	Case 3	Case 4
I_P (MA)	25.0	←	←	←
q_Ψ	2.7	←	←	←
P_{FUS} (MW)	1080	2135	3185	4250
P_{RAD} (MW)	81	121	160	197
P_α (MW)	216	427	637	850
W_P (MJ)	722	1001	1217	1403
Q	∞	←	←	←
$\langle T_e \rangle$ (keV)	10.0	←	←	←
$\langle n_e \rangle$ (10^{20}m^{-3})	0.86	1.2	1.4	1.7
He (%)	10	←	←	←
Z_{eff}	1.8	1.7	1.6	1.6
Troyon g	1.3	1.8	2.2	2.5
β_t (%)	1.9	2.7	3.3	3.8
β_α (%)	0.16	0.23	0.29	0.34
β_p	0.50	0.70	0.85	0.98
I_{BS} (MA)	2.7	4.1	5.3	6.4
V_{LOOP} (V)	0.14	0.12	0.11	0.10
T_{BURN} (s)	700	860	980	1100
τ_E (s)	5.2	3.2	2.5	2.1
τ_E^* (s)	3.3	2.3	1.9	1.7
H_{IP}^*	1.3	1.3	1.2	1.2
H_{IO}^*	1.3	1.0	0.8	0.7
H_{GS}^*	1.3	1.3	1.3	1.3
H_{RL}^*	1.1	0.8	0.7	0.6
H_{SO}^*	1.3	1.1	0.9	0.8

Note : $\tau_E^* = W_P / P_\alpha$

Table 2.6 W_p , P_{FUS} , n_e and He ratio are given by Ref. [1]. Carbon and iron fractions are given by CDA guidelines. Oxygen fraction and T_e are determined to adjust the above parameters.

	Case 1	Case 2	Case 3	Case 4
I_p (MA)	25.0	←	←	←
$q\psi$	2.7	←	←	←
P_{FUS} (MW)	1080	2135	3185	4250
P_{RAD} (MW)	116	220	326	421
P_α (MW)	216	427	637	850
W_p (MJ)	870	1440	1760	1800
Q	∞	←	←	←
$\langle T_e \rangle$ (keV)	10.0	11.5	10.7	8.7
$\langle n_e \rangle$ ($10^{20} m^{-3}$)	1.1	1.6	2.1	2.6
He (%)	19	24	24	20
Z_{eff}	1.8	1.9	1.9	1.8
Troyon g	1.5	2.5	3.0	3.1
β_t (%)	2.2	3.7	4.5	4.6
β_α (%)	0.12	0.16	0.18	0.18
β_p	0.58	0.96	1.2	1.2
I_{BS} (MA)	3.3	6.2	8.0	8.3
V_{LOOP} (V)	0.14	0.10	0.10	0.13
T_{BURN} (s)	720	1120	1170	920
τ_E (s)	8.4	6.9	5.6	4.2
τ_E^* (s)	4.0	3.4	2.8	2.1
H_{IP}^*	1.6	1.8	1.7	1.5
H_{IO}^*	1.5	1.4	1.2	0.9
H_{GS}^*	1.6	1.9	1.9	1.7
H_{RL}^*	1.2	1.1	1.0	0.7
H_{SO}^*	1.5	1.5	1.3	1.0

Note : $\tau_E^* = W_p / P_\alpha$

Table 2.7 Comparison between 1.5-D results and 0-D calculations. Here, $R_p=7.75$ m, $a_p=2.8$ m, $\kappa=1.6$, $I_p=25$ MA, $B_T=6$ T, $Be=1\%$ and $Q=\infty$.

		A	B	C	D	E	F	G
T_e	(keV)	9.6	10.8	12.5	12.7	12.0	10.1	8.5
n_e	($10^{20}/m^3$)	1.00	1.19	1.33	1.50	1.79	2.09	2.50
He	(%)	17	19	21	22	21	20	19
P_α^{*1}	(GW)	0.21	0.32	0.43	0.53	0.64	0.76	0.86
P_{RAD}^{*1}	(GW)	0.08	0.13	0.17	0.21	0.24	0.28	0.32
W_P^{*1}	(GJ)	0.89	1.2	1.5	1.7	1.8	1.9	2.0
P_α^{*2}	(GW)	0.20	0.32	0.46	0.56	0.77	0.81	0.84
P_{RAD}^{*2}	(GW)	0.07	0.11	0.15	0.19	0.25	0.30	0.38
W_P^{*2}	(GJ)	0.79	1.0	1.3	1.5	1.7	1.7	1.7
H_{IP}^{*2}		1.9	1.9	2.0	2.1	2.0	1.9	2.0
H_{RL}^{*2}		1.6	1.4	1.3	1.3	1.1	1.1	1.1

*1) 1.5-D results (Fig.1 & Fig.3 in TAC-3 Physics Report [7])

*2) 0-D calculations

Table 2.8 Operation parameters of EDA-ITER. Here, $Q=\infty$, He=10% and other impurity fractions are given by CDA physics guidelines.

		(I ₁)	(I ₂)	(I ₃)	(I ₄)	(I ₅)
P _{FUS}	(MW)	1000	2000	3000	4000	5000
I _P	(MA)	25.0	←	←	←	←
q _ψ		2.7	←	←	←	←
Q		∞	←	←	←	←
<T _e >	(keV)	10.0	←	←	←	←
<n _e >	(10 ²⁰ /m ³)	0.83	1.15	1.40	1.61	1.80
He	(%)	10	←	←	←	←
Z _{eff}		1.9	1.7	1.6	1.6	1.6
Troyon g		1.2	1.7	2.1	2.5	2.7
β _t	(%)	1.9	2.6	3.2	3.6	4.1
β _p		0.48	0.68	0.83	0.95	1.1
I _{BS} /I _P	(%)	10	16	20	25	28
P _{RAD}	(MW)	78	116	153	188	223
W _P	(MJ)	697	970	1182	1361	1520
τ _E	(s)	5.5	3.4	2.6	2.2	1.9
H _{IP}		1.8	1.5	1.5	1.4	1.4
H _{IO}		1.9	1.4	1.1	0.97	0.87
H _{RL}		1.6	1.1	0.87	0.75	0.67
V _{LOOP}	(V)	0.15	0.12	0.11	0.11	0.10
T _{BURN}	(s)	680	840	960	1100	1200

Table 2.8 Operation parameters of EDA-ITER. Here, $Q=\infty$, He=10% and other impurity fractions are given by CDA physics guidelines.

		(I ₁)	(I ₂)	(I ₃)	(I ₄)	(I ₅)
P _{FUS}	(MW)	1000	2000	3000	4000	5000
I _P	(MA)	25.0	←	←	←	←
q _ψ		2.7	←	←	←	←
Q		∞	←	←	←	←
<T _e >	(keV)	10.0	←	←	←	←
<n _e >	(10 ²⁰ /m ³)	0.83	1.15	1.40	1.61	1.80
He	(%)	10	←	←	←	←
Z _{eff}		1.9	1.7	1.6	1.6	1.6
Troyon g		1.2	1.7	2.1	2.5	2.7
β _t	(%)	1.9	2.6	3.2	3.6	4.1
β _p		0.48	0.68	0.83	0.95	1.1
I _{BS} /I _P	(%)	10	16	20	25	28
P _{RAD}	(MW)	78	116	153	188	223
W _P	(MJ)	697	970	1182	1361	1520
τ _E	(s)	5.5	3.4	2.6	2.2	1.9
H _{IP}		1.8	1.5	1.5	1.4	1.4
H _{IO}		1.9	1.4	1.1	0.97	0.87
H _{RL}		1.6	1.1	0.87	0.75	0.67
V _{LOOP}	(V)	0.15	0.12	0.11	0.11	0.10
T _{BURN}	(s)	680	840	960	1100	1200

Table 2.9 Operation parameters of EDA-ITER. Here, $Q=\infty$, He=20% and other impurity fractions are given by CDA physics guidelines.

		(I ₁)	(I ₂)	(I ₃)	(I ₄)	(I ₅)
P _{FUS}	(MW)	1000	2000	3000	4000	5000
I _P	(MA)	25.0	←	←	←	←
q _ψ		2.7	←	←	←	←
Q		∞	←	←	←	←
<T _e >	(keV)	10.0	←	←	←	←
<n _e >	(10 ²⁰ /m ³)	1.13	1.57	1.91	2.20	2.46
He	(%)	20	←	←	←	←
Z _{eff}		1.9	1.8	1.8	1.8	1.8
Troyon g		1.5	2.2	2.6	3.0	3.4
β _t	(%)	2.3	3.2	3.9	4.5	5.1
β _p		0.60	0.84	1.03	1.18	1.32
I _{BS} /I _P	(%)	14	21	27	33	38
P _{RAD}	(MW)	123	195	261	324	384
W _P	(MJ)	897	1253	1530	1764	1970
τ _E	(s)	11.1	6.0	4.5	3.7	3.2
H _{IP}		2.8	2.3	2.1	2.0	2.0
H _{IO}		3.2	2.2	1.8	1.5	1.4
H _{RL}		2.6	1.8	1.4	1.2	1.1
V _{LOOP}	(V)	0.14	0.12	0.11	0.10	0.10
T _{BURN}	(s)	710	870	1000	1100	1300

Table 2.10 Operation parameters of EDA-ITER. Here, $Q=\infty$, He=10% and $Z_{eff}=2.0$.

		(I ₁)	(I ₂)	(I ₃)	(I ₄)	(I ₅)
P _{FUS}	(MW)	1000	2000	3000	4000	5000
I _P	(MA)	25.0	←	←	←	←
q _ψ		2.7	←	←	←	←
Q		∞	←	←	←	←
<T _e >	(keV)	10.0	←	←	←	←
<n _e >	(10 ²⁰ /m ³)	0.92	1.3	1.6	1.8	2.1
He	(%)	10	←	←	←	←
Z _{eff}		2.0	←	←	←	←
Troyon g		1.3	1.9	2.3	2.6	2.9
β _t	(%)	2.0	2.8	3.4	3.9	4.4
β _p		0.51	0.72	0.88	1.0	1.1
I _{BS} /I _P	(%)	11	17	22	27	31
P _{RAD}	(MW)	90	153	212	267	320
W _P	(MJ)	747	1056	1293	1493	1669
τ _E	(s)	6.5	4.2	3.3	2.8	2.4
H _{IP}		2.0	1.8	1.7	1.6	1.6
H _{IO}		2.2	1.6	1.4	1.2	1.1
H _{RL}		1.8	1.4	1.1	1.0	0.9
V _{LOOP}	(V)	0.16	0.15	0.14	0.13	0.12
T _{BURN}	(s)	640	730	810	890	970

Table 2.10 Operation parameters of EDA-ITER. Here, $Q=\infty$, He=10% and $Z_{eff}=2.0$.

		(I ₁)	(I ₂)	(I ₃)	(I ₄)	(I ₅)
P _{FUS}	(MW)	1000	2000	3000	4000	5000
I _P	(MA)	25.0	←	←	←	←
q _ψ		2.7	←	←	←	←
Q		∞	←	←	←	←
<T _e >	(keV)	10.0	←	←	←	←
<n _e >	(10 ²⁰ /m ³)	0.92	1.3	1.6	1.8	2.1
He	(%)	10	←	←	←	←
Z _{eff}		2.0	←	←	←	←
Troyon g		1.3	1.9	2.3	2.6	2.9
β _t	(%)	2.0	2.8	3.4	3.9	4.4
β _p		0.51	0.72	0.88	1.0	1.1
I _{BS} /I _P	(%)	11	17	22	27	31
P _{RAD}	(MW)	90	153	212	267	320
W _P	(MJ)	747	1056	1293	1493	1669
τ _E	(s)	6.5	4.2	3.3	2.8	2.4
H _{IP}		2.0	1.8	1.7	1.6	1.6
H _{IO}		2.2	1.6	1.4	1.2	1.1
H _{RL}		1.8	1.4	1.1	1.0	0.9
V _{LOOP}	(V)	0.16	0.15	0.14	0.13	0.12
T _{BURN}	(s)	640	730	810	890	970

Table 2.11 Required H-factor for various beryllium fractions when $I_p=25$ MA.
 Here, $R_p=7.75$ m, $a_p=2.8$ m, $\kappa=1.6$, $\delta=0.05$ and $B_T=6$ T, respectively.

		(B ₁₁)	(B ₁₂)	(B ₁₃)	(B ₁₄)	(B ₁₅)	(B ₁₆)
Be	(%)	1	4	6	7	10	12
He	(%)	10	←	←	←	←	←
Z _{eff}		1.32	1.68	1.92	2.04	2.40	2.64
I _p	(MA)	25.0	←	←	←	←	←
q _ψ		2.7	←	←	←	←	←
T _e	(keV)	10.0	←	←	←	←	←
P _{FUS}	(GW)	1.5	←	←	←	←	←
Q		∞	←	←	←	←	←
Troyon g		1.48	1.62	1.76	1.85	2.23	2.66
n _e	(10 ²⁰ /m ³)	0.95	1.13	1.29	1.39	1.81	2.26
n _D	(10 ²⁰ /m ³)	0.36	←	←	←	←	←
β _i	(%)	2.20	2.41	2.62	2.75	3.33	3.96
β _p		0.57	0.63	0.68	0.72	0.87	1.03
P _α	(MW)	300	←	←	←	←	←
P _{RAD}	(MW)	61	102	148	180	348	590
P _{CNV}	(MW)	242	201	156	124	<0	<0
τ _E	(s)	3.37	4.57	6.53	8.69	-	-
W _{th}	(MJ)	815	921	1017	1076	1325	1594
H _{IP}		1.44	1.76	2.21	2.63	-	-
H _{IO}		1.35	1.72	2.25	2.75	-	-
H _{RL}		0.99	1.38	1.86	2.29	-	-
H _{GS}		1.45	1.81	2.29	2.75	-	-
T _{burn}	(s)	1463	1185	1068	1025	950	958

Table 2.12 Required H-factor for various beryllium fractions when $I_P=20$ MA.
 Here, $R_p=7.75$ m, $a_p=2.8$ m, $\kappa=1.6$, $\delta=0.05$ and $B_T=6$ T, respectively.

		(B ₂₁)	(B ₂₂)	(B ₂₃)	(B ₂₄)	(B ₂₅)	(B ₂₆)
Be	(%)	1	4	6	7	10	12
He	(%)	10	←	←	←	←	←
Z _{eff}		1.32	1.68	1.92	2.04	2.40	2.64
I _P	(MA)	20.0	←	←	←	←	←
q _ψ		3.4	←	←	←	←	←
T _e	(keV)	10.0	←	←	←	←	←
P _{FUS}	(GW)	1.5	←	←	←	←	←
Q		∞	←	←	←	←	←
Troyon g		1.85	2.03	2.20	2.31	2.79	3.33
n _e	(10 ²⁰ /m ³)	0.95	1.13	1.29	1.39	1.81	2.26
n _D	(10 ²⁰ /m ³)	0.36	←	←	←	←	←
β _t	(%)	2.20	2.41	2.62	2.75	3.33	3.96
β _p		0.90	0.98	1.07	1.12	1.36	1.62
P _α	(MW)	300	←	←	←	←	←
P _{RAD}	(MW)	61	102	148	180	348	590
P _{CNV}	(MW)	241	200	154	122	<0	<0
τ _E	(s)	3.38	4.61	6.60	8.82	-	-
W _{th}	(MJ)	815	921	1017	1076	1325	1594
H _{IP}		1.74	2.14	2.68	3.20	-	-
H _{IO}		1.53	1.97	2.59	3.18	-	-
H _{RL}		1.22	1.68	2.26	2.76	-	-
H _{GS}		1.81	2.26	2.87	3.45	-	-
T _{burn}	(s)	3070	2518	2301	2228	2165	2340

Table 2.13 Required H-factor for various beryllium fractions when $I_P=15$ MA.
 Here, $R_p=7.75$ m, $a_p=2.8$ m, $\kappa=1.6$, $\delta=0.05$ and $B_T=6$ T, respectively.

		(B ₃₁)	(B ₃₂)	(B ₃₃)	(B ₃₄)	(B ₃₅)	(B ₃₆)
Be	(%)	1	4	6	7	10	12
He	(%)	10	←	←	←	←	←
Z _{eff}		1.32	1.68	1.92	2.04	2.40	2.64
I _P	(MA)	15.0	←	←	←	←	←
q _ψ		4.5	←	←	←	←	←
T _e	(keV)	10.0	←	←	←	←	←
P _{FUS}	(GW)	1.5	←	←	←	←	←
Q		∞	←	←	←	←	←
Troyon g		2.46	2.70	2.94	3.09	3.72	4.43
n _e	(10 ²⁰ /m ³)	0.95	1.13	1.29	1.39	1.81	2.26
n _D	(10 ²⁰ /m ³)	0.36	←	←	←	←	←
β _t	(%)	2.20	2.41	2.62	2.75	3.33	3.96
β _p		1.59	1.75	1.90	2.00	2.41	2.87
P _α	(MW)	300	←	←	←	←	←
P _{RAD}	(MW)	61	102	148	180	348	590
P _{CNV}	(MW)	240	199	153	121	<0	<0
τ _E	(s)	3.39	4.63	6.65	8.91	-	-
W _{th}	(MJ)	815	921	1017	1076	1325	1594
H _{IP}		2.23	2.74	3.44	4.11	-	-
H _{IO}		1.80	2.33	3.08	3.81	-	-
H _{RL}		1.58	2.17	2.87	3.48	-	-
H _{GS}		2.41	3.02	3.83	4.62	-	-
T _{burn}	(s)	7062	6071	5844	5873	7086	3.37 h

Table 2.14 Required H-factor for various beryllium fractions when $I_P=25$ MA and He=20%. Here, $R_p=7.75$ m, $a_p=2.8$ m, $\kappa=1.6$, $\delta=0.05$ and $B_T=6$ T, respectively.

		(B ₄₁)	(B ₄₂)	(B ₄₃)	(B ₄₄)	(B ₄₅)	(B ₄₆)
Be	(%)	1	2	3	4	5	7
He	(%)	20	←	←	←	←	←
Z_{eff}		1.52	1.64	1.76	1.88	2.00	2.24
I_P	(MA)	25.0	←	←	←	←	←
q_ψ		2.7	←	←	←	←	←
T_e	(keV)	10.0	←	←	←	←	←
P_{FUS}	(GW)	1.5	←	←	←	←	←
Q		∞	←	←	←	←	←
Troyon g		1.81	1.91	2.02	2.15	2.30	2.75
n_e	($10^{20}/\text{m}^3$)	1.29	1.39	1.50	1.64	1.81	2.26
n_D	($10^{20}/\text{m}^3$)	0.36	←	←	←	←	←
β_t	(%)	2.70	2.84	3.00	3.19	3.43	4.09
β_P		0.71	0.74	0.78	0.83	0.90	1.07
P_α	(MW)	300	←	←	←	←	←
P_{RAD}	(MW)	120	147	183	230	292	503
P_{CNV}	(MW)	184	156	121	74	11	<0
τ_E	(s)	5.70	7.10	9.78	17.09	121.9	-
W_{th}	(MJ)	1047	1108	1180	1264	1366	1646
H_{IP}		2.08	2.39	2.90	4.07	15.39	-
H_{IO}		2.06	2.42	3.02	4.27	12.94	-
H_{RL}		1.59	1.91	2.42	3.43	10.05	-
H_{GS}		2.16	2.50	3.06	4.34	16.86	-
T_{burn}	(s)	1364	1290	1231	1188	1158	1154

Table 2.14 Required H-factor for various beryllium fractions when $I_P=25$ MA and He=20%. Here, $R_p=7.75$ m, $a_p=2.8$ m, $\kappa=1.6$, $\delta=0.05$ and $B_T=6$ T, respectively.

		(B ₄₁)	(B ₄₂)	(B ₄₃)	(B ₄₄)	(B ₄₅)	(B ₄₆)
Be	(%)	1	2	3	4	5	7
He	(%)	20	←	←	←	←	←
Z_{eff}		1.52	1.64	1.76	1.88	2.00	2.24
I_P	(MA)	25.0	←	←	←	←	←
q_ψ		2.7	←	←	←	←	←
T_e	(keV)	10.0	←	←	←	←	←
P_{FUS}	(GW)	1.5	←	←	←	←	←
Q		∞	←	←	←	←	←
Troyon g		1.81	1.91	2.02	2.15	2.30	2.75
n_e	($10^{20}/\text{m}^3$)	1.29	1.39	1.50	1.64	1.81	2.26
n_D	($10^{20}/\text{m}^3$)	0.36	←	←	←	←	←
β_t	(%)	2.70	2.84	3.00	3.19	3.43	4.09
β_P		0.71	0.74	0.78	0.83	0.90	1.07
P_α	(MW)	300	←	←	←	←	←
P_{RAD}	(MW)	120	147	183	230	292	503
P_{CNV}	(MW)	184	156	121	74	11	<0
τ_E	(s)	5.70	7.10	9.78	17.09	121.9	-
W_{th}	(MJ)	1047	1108	1180	1264	1366	1646
H_{IP}		2.08	2.39	2.90	4.07	15.39	-
H_{IO}		2.06	2.42	3.02	4.27	12.94	-
H_{RL}		1.59	1.91	2.42	3.43	10.05	-
H_{GS}		2.16	2.50	3.06	4.34	16.86	-
T_{burn}	(s)	1364	1290	1231	1188	1158	1154

Table 2.15 Required H-factor for various beryllium fractions when $I_P=20$ MA and He=20%. Here, $R_p=7.75$ m, $a_p=2.8$ m, $\kappa=1.6$, $\delta=0.05$ and $B_T=6$ T, respectively.

		(B ₅₁)	(B ₅₂)	(B ₅₃)	(B ₅₄)	(B ₅₅)	(B ₅₆)
Be	(%)	1	2	3	4	5	7
He	(%)	20	←	←	←	←	←
Z _{eff}		1.52	1.64	1.76	1.88	2.00	2.24
I _P	(MA)	20.0	←	←	←	←	←
q _ψ		3.4	←	←	←	←	←
T _e	(keV)	10.0	←	←	←	←	←
P _{FUS}	(GW)	1.5	←	←	←	←	←
Q		∞	←	←	←	←	←
Troyon g		2.27	2.38	2.52	2.68	2.88	3.43
n _e	(10 ²⁰ /m ³)	1.29	1.39	1.50	1.64	1.81	2.26
n _D	(10 ²⁰ /m ³)	0.36	←	←	←	←	←
β _t	(%)	2.70	2.84	3.00	3.19	3.43	4.09
β _p		1.10	1.16	1.22	1.30	1.40	1.67
P _α	(MW)	300	←	←	←	←	←
P _{RAD}	(MW)	120	147	183	230	292	503
P _{CNV}	(MW)	182	155	119	72	9	<0
τ _E	(s)	5.75	7.17	9.91	17.48	144.1	-
W _{th}	(MJ)	1047	1108	1180	1264	1366	1646
H _{IP}		2.53	2.90	3.54	4.98	21.21	-
H _{IO}		2.36	2.78	3.49	5.00	17.04	-
H _{RL}		1.94	2.32	2.92	4.09	12.77	-
H _{GS}		2.70	3.13	3.84	5.47	23.73	-
T _{burn}	(s)	2954	2822	2728	2675	2668	2868

Table 2.16 Required H-factor for various beryllium fractions when $I_p=15$ MA and He=20%. Here, $R_p=7.75$ m, $a_p=2.8$ m, $\kappa=1.6$, $\delta=0.05$ and $B_T=6$ T, respectively.

		(B ₆₁)	(B ₆₂)	(B ₆₃)	(B ₆₄)	(B ₆₅)	(B ₆₆)
Be	(%)	1	2	3	4	5	7
He	(%)	20	←	←	←	←	←
Z _{eff}		1.52	1.64	1.76	1.88	2.00	2.24
I _p	(MA)	15.0	←	←	←	←	←
q _ψ		4.5	←	←	←	←	←
T _e	(keV)	10.0	←	←	←	←	←
P _{FUS}	(GW)	1.5	←	←	←	←	←
Q		∞	←	←	←	←	←
Troyon g		3.02	3.18	3.36	3.58	3.84	4.58
n _e	(10 ²⁰ /m ³)	1.29	1.39	1.50	1.64	1.81	2.26
n _D	(10 ²⁰ /m ³)	0.36	←	←	←	←	←
β _t	(%)	2.70	2.84	3.00	3.19	3.43	4.09
β _p		1.96	2.06	2.18	2.32	2.49	2.97
P _α	(MW)	300	←	←	←	←	←
P _{RAD}	(MW)	120	147	183	230	292	503
P _{CNV}	(MW)	181	154	118	71	8	<0
τ _E	(s)	5.78	7.21	10.00	17.75	163.1	-
W _{th}	(MJ)	1047	1108	1180	1264	1366	1646
H _{IP}		3.24	3.72	4.54	6.42	29.92	-
H _{IO}		2.79	3.31	4.18	6.07	22.93	-
H _{RL}		2.49	2.96	3.68	5.07	16.37	-
H _{GS}		3.60	4.17	5.13	7.33	34.66	-
T _{burn}	(s)	7663	7626	7789	8242	9211	4.84 (h)

Table 2.17 Operation parameters at $T_e=10$ keV and $I_p=25$ MA.

		(I ₁)	(I ₂)	(I ₃)	(H ₁)	(H ₂)	(H ₃)
I _P	(MA)	25.0	←	←	←	←	←
q _ψ		2.7	←	←	←	←	←
P _{FUS}	(MW)	750	1500	3000	750	1500	3000
P _{RAD}	(MW)	68	97	153	50	67	100
P _α	(MW)	150	300	600	150	300	600
W _P	(MJ)	610	844	1182	511	703	982
Q		∞	←	←	←	←	←
⟨T _e ⟩	(keV)	10.0	←	←	←	←	←
⟨n _e ⟩	(10 ²⁰ /m ³)	0.74	1.0	1.4	0.59	0.80	1.1
He	(%)	10	←	←	0.0	←	←
Z _{eff}		2.0	1.7	1.6	2.1	1.7	1.5
Troyon g		1.1	1.5	2.1	0.95	1.3	1.9
β _t	(%)	1.6	2.3	3.2	1.4	2.0	2.8
β _α	(%)	0.13	0.19	0.28	0.17	0.26	0.37
β _p		0.42	0.59	0.83	0.37	0.51	0.72
I _{BS}	(MA)	2.2	3.3	5.1	1.8	2.8	4.3
V _{LOOP}	(V)	0.16	0.13	0.11	0.17	0.13	0.11
T _{BURN}	(s)	610	770	960	560	750	970
τ _E	(s)	7.0	4.1	2.6	4.9	3.0	2.0
H _{IP}		1.9	1.6	1.5	1.5	1.3	1.2
H _{IO}		2.3	1.6	1.1	1.7	1.2	0.86
H _{CS}		1.9	1.6	1.5	1.5	1.3	1.2
H _{RL}		1.9	1.3	0.87	1.5	0.97	0.65
H _{SO}		2.1	1.6	1.2	1.6	1.3	0.95
Figure		2.32	2.33	2.34	2.35	2.36	2.37

Table 2.18 Operation parameters at $T_e=10$ keV and $I_p=25$ MA.
Here, H-factor is calculated by τ_E^* .

		(I ₁ ')	(I ₂ ')	(I ₃ ')
I_p	(MA)	25.0	←	←
q_ψ		2.7	←	←
P_{FUS}	(MW)	750	1500	3000
P_{RAD}	(MW)	68	97	153
P_α	(MW)	150	300	600
W_P	(MJ)	610	844	1182
Q		∞	←	←
$\langle T_e \rangle$	(keV)	10.0	←	←
$\langle n_e \rangle$	($10^{20}/m^3$)	0.74	1.0	1.4
He	(%)	10	←	←
Z_{eff}		2.0	1.7	1.6
Troyon g		1.1	1.5	2.1
β_t	(%)	1.6	2.3	3.2
β_α	(%)	0.13	0.19	0.28
β_p		0.42	0.59	0.83
I_{BS}	(MA)	2.2	3.3	5.1
V_{LOOP}	(V)	0.16	0.13	0.11
T_{BURN}	(s)	610	770	960
τ_E	(s)	7.0	4.1	2.6
τ_E^*	(s)	4.0	2.8	2.0
H_{IP}^*		1.4	1.3	1.2
H_{IO}^*		1.5	1.1	0.9
H_{GS}^*		1.4	1.3	1.3
H_{RL}^*		1.3	0.9	0.7
H_{SO}^*		1.4	1.2	1.0
Figure		2.38	2.39	2.40

Note : $\tau_E^* = W_P / P_\alpha$

Table 2.19 Particle and heat load for the ignition plasma of EDA-ITER. Here, the impurity fractions are calculated by CDA physics guidelines.

		(I ₁)	(I ₂)	(I ₃)	(I ₄)
SOL	(m)	0.2	←	←	←
S _P	(m ²)	1335	←	←	←
V _P	(m ³)	1908	←	←	←
P _{FUS}	(MW)	1500	←	3000	←
He	(%)	10	20	10	20
Z _{eff}		1.7	1.8	1.6	1.8
<T _e >	(keV)	10.0	←	←	←
<n _e >	(10 ²⁰ /m ³)	1.00	1.37	1.40	1.91
W _{NEUT}	(MW/m ²)	0.84	←	1.68	←
W _{RAD}	(MW/m ²)	0.10	0.16	0.15	0.25
W _α	(MW/m ²)	0.32	←	0.63	←
P _{div}	(MW)	155	77	386	252
W _{div} ^{HK}	(MW/m ²)	15	4	47	19
P _{RAD}	(MW)	97	160	153	261
W _P	(MJ)	844	1090	1182	1530
τ _E	(s)	4.1	7.6	2.6	4.5
H _{IP}		1.6	2.5	1.5	2.1
H _{RL}		1.3	2.1	0.9	1.4

Table 3.1 Requirement for the steady-state mode operation.

		Case 1	Case 2	Case 3	Case 4
R_P	(m)	7.75	←	←	←
a_P	(m)	2.8	←	←	←
κ_{95}		1.6	←	←	←
δ_{95}		0.05	←	←	←
V_P	(m ³)	1908	←	←	←
B_T	(T)	6.0	←	←	←
I_P	(MA)	25.0	←	←	←
$q\Psi$		2.7	←	←	←
P_{FUS}	(MW)	1080	2135	3185	4250
P_α	(MW)	216	427	637	850
Q		∞	←	←	←
W_P	(MJ)	870	1440	1760	1800
T_e	(keV)	10.0	11.4	10.6	8.5
n_e	(10 ²⁰ m ⁻³)	1.1	1.6	2.1	2.6
He	(%)	19	24	24	20
T_e	(keV)	10.0	11.4	10.6	8.5
n_e	(10 ²⁰ m ⁻³)	1.1	1.6	2.1	2.6
Troyon g		1.5 (1.4)	2.5 (2.3)	3.0 (2.9)	3.1 (3.0)
I_{BS}	(MA)	3.3 (2.7)	6.2 (4.8)	8.0 (6.6)	8.2 (7.1)
τ_E	(s)	6.8 (4.0)	6.0 (3.4)	4.9 (2.8)	3.7 (2.1)
H_{IP}		2.1	2.5	2.4	2.0
H_{RL}		1.8	1.8	1.5	1.1
<hr/>					
I_{CD}	(MA)	22.3	20.2	18.4	17.9
η_{CD}	(A/W)	0.0265	0.0205	0.0144	0.0091
γ	(10 ²⁰ A/Wm ²)	0.220	0.254	0.236	0.185
P_{CD}	(MW)	842	985	1278	1967
Q		1.3	2.2	2.5	2.2
Required γ (Q=5)		0.86	0.59	0.47	0.43
Required γ (Q=10)		1.7	1.2	0.95	0.86
Required γ (Q=25)		4.3	2.9	2.4	2.1

Table 3.2 Major parameters of EDA-ITER (steady-state mode).

Major radius	R_P	(m)	7.8
Minor radius	a_P	(m)	2.7
Aspect ratio	A		2.89
Elongation	κ_{95}		1.7
Triangularity	δ_{95}		0.15
Elongation at separatrix	κ_x		2.08
Triangularity at separatrix	δ_x		0.34
Plasma volume	V_P	(m ³)	1890
Plasma surface area	S_P	(m ²)	1360
Plasma current	I_P	(MA)	2.5
MHD safety factor	q_Ψ		2.74
Cylindrical q	q_{cyl}		2.25
Engineering q	q_I		2.18
Plasma self-inductance	L_P	(μ H)	14.3
Toroidal field on axis	B_T	(T)	6.0
Maximum toroidal field	B_{TMAX}	(T)	13.2
Position of maximum field	R_{TFC}	(m)	3.7
Maximum poloidal field	B_{PMAX}	(T)	12.0
Position of OH coils	R_{OH}	(m)	2.44

Table 3.3 Operation parameters for steady-state plasma of EDA-ITER.

	S1	S2	S3	S4	S5
P_{FUS} (MW)	500	←	750	←	1000
P_{NBI} (MW)	120	140	120	140	140
H (ITER89-P)	2.2	2.0	2.2	2.0	2.2
Q	4.2	3.6	6.1	5.4	7.0
T_e (keV)	13.4	12.0	16.9	15.0	12.0
n_e ($10^{20}/\text{m}^3$)	0.54	0.58	0.55	0.59	0.77
q_ψ	5.0	5.1	4.1	4.3	5.2
I_P (MA)	13.8	13.5	16.6	16.0	13.3
I_{BS}/I_P	0.33	0.33	0.32	0.32	0.48
I_{NBI}/I_P	0.67	0.67	0.68	0.68	0.52
Troyon g	2.1	2.1	2.3	2.3	2.8
β_t (%)	1.8	1.7	2.4	2.3	2.3
β_p	1.6	1.6	1.4	1.5	2.1
τ_E (s)	3.6	3.1	3.7	3.2	2.9
H (ITER89-OL)	2.0	1.7	1.9	1.7	1.7
H (Rebut-Lallia)	2.3	2.0	2.1	1.8	1.8
He (%)	10	←	←	←	←
Z_{eff}	2.5	2.3	2.4	2.3	1.9

Table 3.4 Operation parameters for steady-state plasma of EDA-ITER.

			S1	S2	S3
Major radius	R_P	(m)	7.8	←	←
Minor radius	a_P	(m)	2.7	←	←
Elongation	κ		1.7	←	←
Toroidal field on axis	B_T	(T)	6.0	←	←
Fusion power	P_{FUS}	(MW)	500	750	1000
Current-drive power	P_{NBI}	(MW)	140	←	←
Radiation loss	P_{RAD}	(MW)	58	66	74
Fusion gain	Q		3.6	5.4	7.2
MHD safety factor	q_ψ		5.5	4.9	4.5
Plasma current	I_P	(MA)	12.4	14.0	15.3
Bootstrap fraction	I_{BS}/I_P		0.37	0.38	0.39
Controllability	I_{NBI}/I_P		0.63	0.62	0.61
Current-drive efficiency	η_{NBI}	(A/W)	0.056	0.062	0.067
Electron temperature	T_e	(keV)	11.0	12.9	14.5
Electron density	n_e	($10^{20}/m^3$)	0.62	0.65	0.67
Troyon g			2.2	2.4	2.6
Toroidal beta	β_t	(%)	1.7	2.1	2.5
Poloidal beta	β_p		1.8	1.8	1.7
Helium fraction	He	(%)	10	←	←
Effective ion charge	Z_{eff}		2.2	2.1	2.1
Confinement time	τ_E	(s)	3.0	3.0	3.0
H-factor (ITER89-P)			2.1	←	←
H-factor (ITER89-OL)			1.8	1.7	1.7
H-factor (Rebut-Lallia)			2.0	1.9	1.8
Divertor heat Load	W_{div}	(MW/m ²)			
Constant- χ model			13	20	27
Bohm- χ model			9	12	15
JT-60U model			9	13	19

Table 3.5 Operation parameters for steady-state plasma of CDA-ITER.

			C1	C2	C3
Major radius	R_p (m)		6.0	←	←
Minor radius	a_p (m)		2.15	←	←
Elongation	κ		2.0	←	←
Toroidal field on axis	B_T (T)		4.85	←	←
Fusion power	P_{FUS} (MW)		500	750	1000
Current-drive power	P_{NBI} (MW)		140	←	←
Radiation loss	P_{RAD} (MW)		4.1	4.6	5.1
Fusion gain	Q		3.6	5.4	7.2
MHD safety factor	q_ψ		5.5	4.8	4.4
Plasma current	I_p (MA)		12.1	13.8	15.0
Bootstrap fraction	I_{BS}/I_p		0.39	0.39	0.41
Controllability	I_{NBI}/I_p		0.61	0.61	0.59
Current-drive efficiency	η_{NBI} (A/W)		0.054	0.061	0.064
Electron temperature	$\langle T_e \rangle$ (keV)		10.7	12.6	14.0
Electron density	$\langle n_e \rangle$ ($10^{20}/m^3$)		0.80	0.84	0.88
Troyon g			2.8	3.1	3.4
Toroidal beta	β_t (%)		3.3	4.1	4.9
Poloidal beta	β_p		1.7	1.6	1.6
Helium fraction	He (%)		1.0	←	←
Effective ion charge	Z_{eff}		1.9	1.9	1.8
Confinement time	τ_E (s)		2.0	2.0	2.0
H-factor (ITER89-P)			2.1	←	←
H-factor (ITER89-OL)			1.6	1.5	1.4
H-factor (Rebut-Lallia)			1.8	1.7	1.5
Divertor heat Load	W_{div} (MW/m ²)				
Constant- χ model			1.0	1.4	1.9
Bohm- χ model			7	9	11
JT-60U model			7	11	15

Table 3.6 Operation parameters for steady-state plasma of EDA-ITER.
Here, H-factor is calculated by τ_E^* .

	S1	S2	S3	S4
P_{FUS} (MW)	500	←	1000	←
P_{NBI} (MW)	120	←	←	←
P_{RAD} (MW)	59	59	74	77
Q	4.2	←	8.3	←
T_e (keV)	10.4	13.5	13.1	11.0
n_e ($10^{20}/m^3$)	0.64	0.54	0.72	0.83
q_ψ	6.1	5.0	5.1	5.8
I_P (MA)	11.2	13.8	13.4	11.8
I_{BS}/I_P	0.46	0.33	0.48	0.59
I_{NBI}/I_P	0.54	0.67	0.52	0.41
Troyon g	2.3	2.1	2.8	3.0
β_t (%)	1.6	1.8	2.3	2.2
β_p	2.1	1.6	2.1	2.5
He (%)	10	←	←	←
Z_{eff}	2.1	2.5	2.0	1.9
W_P (MJ)	547	581	777	753
τ_E^* (s)	2.5	2.6	2.4	2.4
H_{IP}^*	2.0	1.8	2.0	2.1
H_{IO}^*	1.6	1.5	1.4	1.5
H_{GS}^*	2.1	1.8	2.1	2.3
H_{RL}^*	1.8	1.8	1.6	1.7
H_{SO}^*	1.2	1.3	1.2	1.2

Table 3.7 Steady-state operation point reported in Ref. [9] and its reconstructions by 0-D model (Initial point).

		(TAC4)	(S ₁)	(S ₂)	(S ₃)
R _P	(m)	8.11	←	←	←
a _P	(m)	3.0	←	←	←
κ		1.53	←	←	←
δ		0.23	←	←	←
B _T	(T)	5.7	←	←	←
Z _{eff}		?	2.2	←	1.6
He	(%)	20	14	←	20
Be	(%)	?	-	8	1.3
C	(%)	?	3	-	-
P _{FUS}	(MW)	2200	←	←	←
P _{NBI}	(MW)	30	←	←	←
Q		73	←	←	←
P _{RAD}	(MW)	?	220	370	150
q _ψ		5.6	←	←	←
I _P	(MA)	13	12.5	←	←
I _{NBI}	(MA)	?	0.5	0.4	0.5
I _{BS}	(MA)	?	12.0	15.6	12.0
I _{BS} /I _P		0.98	0.96	1.2	0.96
V _{LOOP}	(V)	0	←	←	←
⟨T _e ⟩	(keV)	12.0	←	←	←
⟨n _e ⟩	(10 ²⁰ /m ³)	1.4	1.4	1.8	1.4
Troyon g		4.4 ~ 6.0	5.2	6.3	5.2
β _t	(%)	?	3.8	4.6	3.8
W _P	(MJ)	?	1500	1900	1500
τ _E	(s)	5.7	6.0	18	4.6
H _{IP}		4.4	4.4	8.8	3.9
H _{RL}		?	3.4	6.5	2.5

Table 3.8 Steady-state operation point reported in Ref. [9] and its reconstructions by 0-D model (Optimized point).

		(TAC4')	(S ₄)	(S ₅)	(S ₆)
R _P	(m)	8.46	←	←	←
a _P	(m)	2.68	←	←	←
κ		1.71	←	←	1.53
δ		0.44	←	←	0.23
B _T	(T)	4.34	←	←	←
Z _{eff}		?	1.44	←	←
He	(%)	12 ?	12	←	←
Be	(%)	?	1.7	←	←
P _{FUS}	(MW)	2000	←	←	←
P _{NBI}	(MW)	50	←	←	←
Q		40	←	←	←
P _{RAD}	(MW)	?	93	←	←
q _ψ		4.2	4.3	4.9	3.5
I _P	(MA)	12	12	11	11
I _{NBI}	(MA)	1	0.7	←	0.6
I _{BS}	(MA)	11	8.4	9.8	10
I _{BS} /I _P		0.91	0.69	0.91	0.91
<T _e >	(keV)	10	←	←	←
<n _e >	(10 ²⁰ /m ³)	1.25	←	←	1.33
Troyon g		5.0 / 6.7	5.1	5.8	5.9
β _t	(%)	?	5.3	←	5.7
W _P	(MJ)	?	1140	←	1080
τ _E	(s)	2.6	3.2	←	3.0
H _{IP}		2.6	2.8	3.1	3.0
H _{RL}		?	1.9	2.1	2.1

Table 3.9 Heat load for the steady-state mode of EDA-ITER when $I_p=25$ MA.
Here, the impurity fractions are given by CDA guidelines.

		(S ₁)	(S ₂)	(S ₃)	(S ₄)
P _{FUS}	(MW)	750	←	1500	←
I _P	(MA)	25.0	←	←	←
q _ψ		2.7	←	←	←
Q		5.6	4.0	10.8	7.0
He	(%)	10	20	10	20
SOL	(m)	0.2	←	←	←
<T _e >	(keV)	23.7	21.2	25.1	21.5
<n _e >	(10 ²⁰ /m ³)	0.45	0.60	0.56	0.79
Troyon g		1.9	2.1	2.5	2.7
Z _{eff}		3.0	2.4	2.4	2.1
P _{NBI}	(MW)	135	186	139	214
W _{NEUT}	(MW/m ²)	0.42	←	0.84	←
W _{RAD}	(MW/m ²)	0.09	0.10	0.11	0.12
W _α	(MW/m ²)	0.16	←	0.32	←
P _{DIV}	(MW)	153	192	282	336
W _{DIV}	(MW/m ²)	27	31	59	60
P _{RAD}	(MW)	94	103	117	132
W _P	(MJ)	845	989	1150	1332
τ _E	(s)	4.4	4.2	3.6	3.5
H _{IP}		2.0	←	←	←
H _{IO}		1.9	1.8	1.6	1.5
H _{RL}		1.9	1.7	1.5	1.4
V _{LOOP}	(V)	0.0	←	←	←
T _{BURN}	(s)	∞	←	←	←

Table 3.10 Heat load for the steady-state mode of EDA-ITER when $T_e=10$ keV.
Here, the impurity fractions are given by CDA guidelines.

		(S ₁)	(S ₂)	(S ₃)	(S ₄)
P_{FUS}	(MW)	750	←	1500	←
I_P	(MA)	12.3	14.0	13.0	15.5
q_ψ		5.4	4.8	5.2	4.3
Q		4.3	2.8	7.7	4.3
He	(%)	10	20	10	20
SOL	(m)	0.2	←	←	←
$\langle T_e \rangle$	(keV)	10.0	←	←	←
$\langle n_e \rangle$	($10^{20}/m^3$)	0.74	0.99	1.00	1.37
Troyon g		2.4	2.6	3.1	3.2
Z_{eff}		2.0	1.9	1.7	1.8
P_{NBI}	(MW)	175	269	195	348
W_{NEUT}	(MW/m ²)	0.42	←	0.84	←
W_{RAD}	(MW/m ²)	0.08	0.11	0.10	0.16
W_α	(MW/m ²)	0.16	←	0.32	←
P_{DIV}	(MW)	214	263	347	422
W_{DIV}	(MW/m ²)	23	26	39	45
P_{RAD}	(MW)	68	104	97	160
W_P	(MJ)	610	783	844	1090
τ_E	(s)	2.4	2.5	2.1	2.2
H_{IP}		2.0	←	←	←
H_{IO}		1.5	1.4	1.3	1.2
H_{RL}		1.6	1.5	1.4	1.2
V_{LOOP}	(V)	0.0	←	←	←
T_{BURN}	(s)	∞	←	←	←

Table 3.11 Divertor heat load of the steady-state plasma calculated by CDA models. Here, $H_{1P}=3$ is assumed. Note that the angle of the plate is 90° , while it is 15° in CDA. Therefore, the heat load is 4 times smaller than the value listed for CDA type divertor.

P_{FUS} (GW)	Z_{eff}	He (%)	T_e (KeV)	$n_e / 10^{20}$ (m^{-3})	Q	I_P (MA)	q_Ψ	I_{BS} / I_P	P_{div} (MW)	W_{div} (HK) (MW/ m^2)	W_{div} (JT60) (MW/ m^2)
0.5	1.7	10	10	0.59	6.6	10.3	7.3	0.62	116	13	8
			16	0.40	8.1	13.1	5.8	0.41	111	18	10
		20	14	0.57	5.0	13.7	5.5	0.43	135	19	12
			18	0.48	5.3	16.7	4.5	0.32	127	21	14
	1.95	10	10	0.64	5.4	10.7	7.0	0.58	109	11	7
			16	0.43	7.0	13.7	5.5	0.39	107	16	10
		20	10	0.85	3.3	12.2	6.2	0.54	134	13	9
			18	0.52	4.5	17.8	4.3	0.31	124	20	13
1.0	1.7	10	10	0.84	12.3	11.2	6.7	0.73	181	20	14
			16	0.56	15.8	13.5	5.6	0.57	188	32	20
		20	11	0.99	7.1	13.3	5.7	0.63	217	25	19
			18	0.67	9.1	17.3	4.4	0.45	210	36	25
	1.95	10	10	0.90	9.4	11.8	6.4	0.69	168	17	12
			16	0.60	13.0	14.2	5.3	0.53	179	28	18
		20	10	1.20	5.0	13.7	5.5	0.62	199	19	15
			18	0.74	7.4	18.5	4.1	0.42	203	33	24

Table 3.12 Operation parameters of a steady-state plasma with different minor radius.

			S3	S4	SS
Major radius	R_P	(m)	7.8	←	←
Minor radius	a_P	(m)	2.7	←	2.0
Aspect ratio	A		2.89	←	3.9
Plasma volume	V_P	(m ³)	1890	←	1040
Toroidal field on axis	B_T	(T)	6.0	←	←
Fusion power	P_{FUS}	(MW)	750	←	←
Current-drive power	P_{NBI}	(MW)	120	140	120
Radiation loss	P_{RAD}	(MW)	71	68	47
Fusion gain	Q		6.2	5.4	6.2
MHD safety factor	q_ψ		4.1	4.3	3.2
Plasma current	I_P	(MA)	16.6	16.0	11.0
Bootstrap fraction	I_{BS}/I_P		0.32	0.32	0.48
Controllability	I_{NBI}/I_P		0.68	0.68	0.52
Current-drive efficiency	η_{NBI}	(A/W)	0.092	0.079	0.048
Troyon g			2.3	2.3	3.0
Toroidal beta	β_t	(%)	2.4	2.3	2.8
Poloidal beta	β_p		1.4	1.5	2.1
Electron temperature	T_e	(keV)	16.9	15.0	13.3
Electron density	n_e	(10 ²⁰ /m ³)	0.55	0.59	0.82
Helium fraction	He	(%)	10	←	←
Effective ion charge	Z_{eff}		2.4	2.3	1.9
Impurity seeding			No	←	←
Stored energy	W_P	(MJ)	750	714	494
Confinement time	τ_E	(s)	3.7	3.2	2.2
H-factor (ITER89-P)			2.2	2.0	←
H-factor (ITER89-OL)			2.4	2.3	1.8
H-factor (Rebut-Lallia)			2.1	1.8	2.2

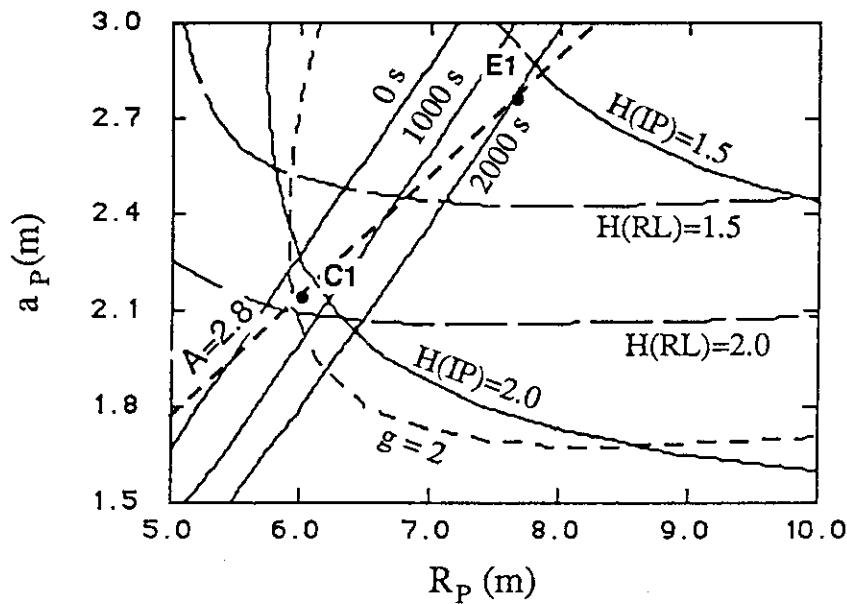


Fig. 2.1 Relation between CDA-ITER and EDA-ITER in R_p - a_p space. Here, $Q=\infty$, $P_{WAL}=0.85 \text{ MW/m}^2$, $q_\Psi=2.8$, $B_{TMAX}=13.0 \text{ T}$, $\delta_{TF}=1.2 \text{ m}$, $\kappa=1.7$, $\delta=0$, $B_{PMAX}=13.2 \text{ T}$, $T_e=10 \text{ keV}$, $\text{He}=10\%$. Points C1 and E1 represent the machines with similar parameters to CDA-ITER and EDA-ITER.

Quit

Plasma Formulary

Version 1.1 YoshiKI MURAKAMI

1 / 6

- Major radius $R_p = \boxed{6}$ m
- Minor radius $a_p = \boxed{2.15}$ m
- Elongation $\kappa = \boxed{2.0}$
- Triangularity $\delta = \boxed{0.35}$

- Toroidal field $B_T = \boxed{4.85}$ T
- Plasma current $I_p = \boxed{22}$ MA
- Troyon $g = \boxed{2.0}$

Calculate

Default

- $A = \boxed{2.7907}$
- $\varepsilon = \boxed{0.3583}$
- $f_7 = \boxed{2.5000}$
- $f_8 = \boxed{2.8871}$
- $f_9 = \boxed{1.2335}$

- $\beta_t = \boxed{4.2196} \%$
- $\beta_p = \boxed{0.4740}$
- $q_I = \boxed{2.1230}$
- $q_{cyl} = \boxed{2.4518}$
- $q_\Psi = \boxed{3.0243}$

$$\begin{aligned}
 q_I &= f_7 q \\
 q_{cyl} &= f_8 q \\
 q_\Psi &= f_8 f_9 q \\
 f_7 &= (1+\kappa^2)/2 \\
 f_8 &= \{1+\kappa^2 (1+2\delta^2 - 1.2\delta^3)\}/2 \\
 f_9 &= (1.17-0.65\varepsilon)/(1-\varepsilon^2)^2 \\
 q &= 5a_p B_T / (A I_p [\text{MA}])
 \end{aligned}$$

Fig. 2.2 Calculation of q_Ψ value for CDA-ITER.

Quit

1 / 6

Plasma Formulary

Version 1.1 Yoshiki MURAKAMI

• Major radius	R _p =	7.75	m	• Toroidal field	B _T =	6	T
• Minor radius	a _p =	2.8	m	• Plasma current	I _p =	25	MA
• Elongation	κ =	1.6		• Troyon g	=	2.0	
• Triangularity	δ =	0.05					

Calculate

Default

• A =	2.7679	• β _t =	2.9762	%
• ε =	0.3613	• β _p =	0.5376	
• f ₇ =	1.7800	• q _I =	2.1608	
• f ₈ =	1.7862	• q _{cyl} =	2.1683	
• f ₉ =	1.2370	• q _ψ =	2.6823	

$$\begin{aligned}
 q_I &= f_7 q \\
 q_{cyl} &= f_8 q \\
 q_\psi &= f_8 f_9 q \\
 f_7 &= (1 + \kappa^2)/2 \\
 f_8 &= \{1 + \kappa^2 (1 + 2\delta^2 - 1.2\delta^3)\}/2 \\
 f_9 &= (1.17 - 0.65\epsilon)/(1 - \epsilon^2)^2 \\
 q &= 5a_p B_T / (A I_p [\text{MA}])
 \end{aligned}$$

←
→

Fig.2.3 Calculation of q_ψ value for EDA-ITER.

Quit

1 / 6

Plasma Formulary

Version 1.1 Yoshiki MURAKAMI

• Major radius	R _p =	8	m	• Toroidal field	B _T =	5.813	T
• Minor radius	a _p =	3	m	• Plasma current	I _p =	24	MA
• Elongation	κ =	1.6		• Troyon g	=	2.0	
• Triangularity	δ =	0.05					

Calculate

Default

• A =	2.6667	• β _t =	2.7525	%
• ε =	0.3750	• β _p =	0.5813	
• f ₇ =	1.7800	• q _I =	2.4251	
• f ₈ =	1.7862	• q _{cyl} =	2.4336	
• f ₉ =	1.2542	• q _ψ =	3.0522	

$$\begin{aligned}
 q_I &= f_7 q \\
 q_{cyl} &= f_8 q \\
 q_\psi &= f_8 f_9 q \\
 f_7 &= (1 + \kappa^2)/2 \\
 f_8 &= \{1 + \kappa^2 (1 + 2\delta^2 - 1.2\delta^3)\}/2 \\
 f_9 &= (1.17 - 0.65\epsilon)/(1 - \epsilon^2)^2 \\
 q &= 5a_p B_T / (A I_p [\text{MA}])
 \end{aligned}$$

←
→

Fig.2.4 Calculation of q_ψ value for EDA-ITER (new version).

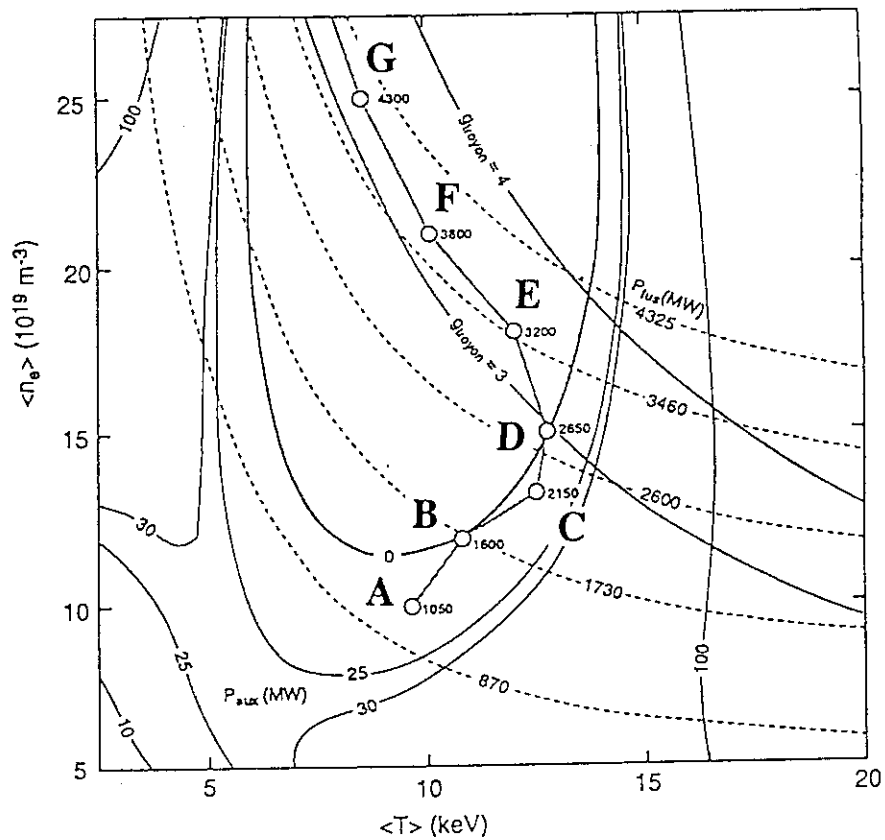


Fig. 2.5 Simulated plasma operation contour map referred from TAC-3 Physics Report [7].

$$R_p = 7.75 \text{ m}, a_p = 2.8 \text{ m}, \kappa = 1.6, \delta = 0.05, \\ Q = \infty, \text{Be} = 1 \%, T_e = 10 \text{ keV}, I_p = 25 \text{ MA}$$

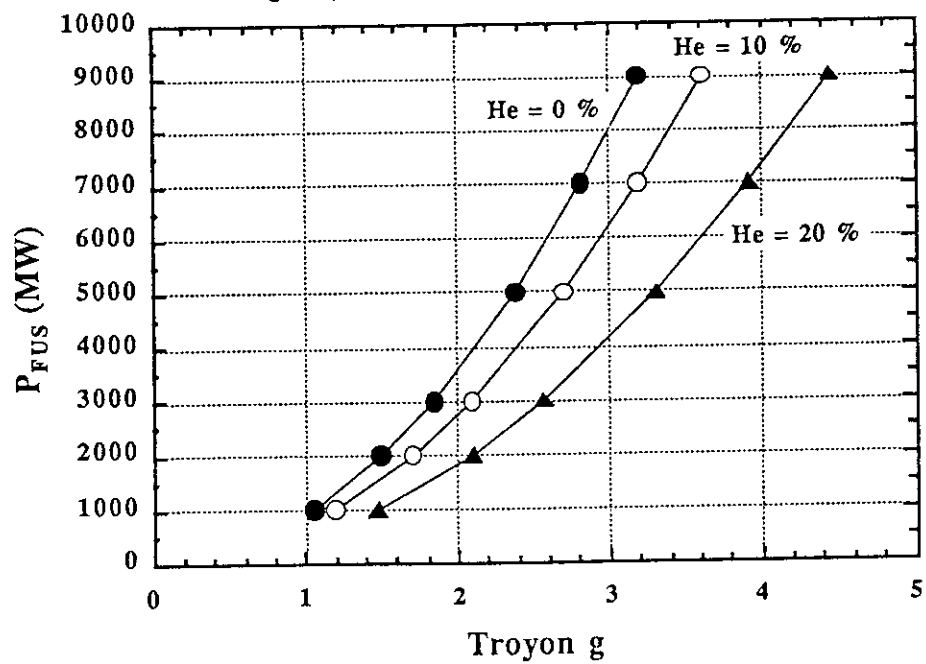


Fig. 2.6 Relation between Troyon coefficient g and the fusion power P_{FUS} for various helium accumulations when $\text{Be}=1\%$.

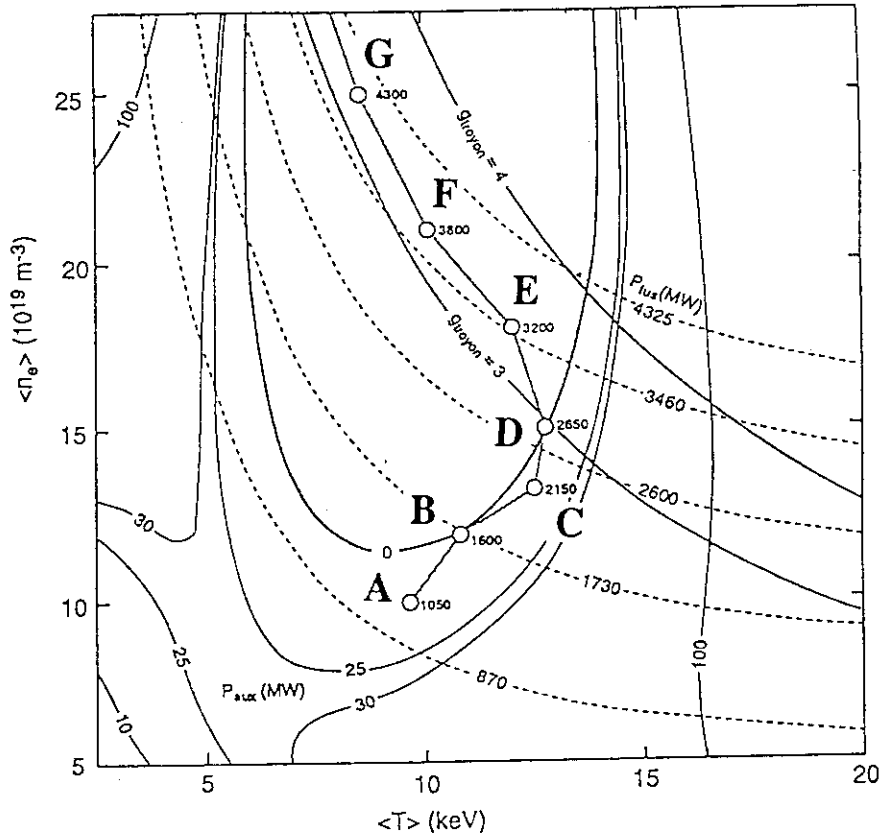


Fig. 2.5 Simulated plasma operation contour map referred from TAC-3 Physics Report [7].

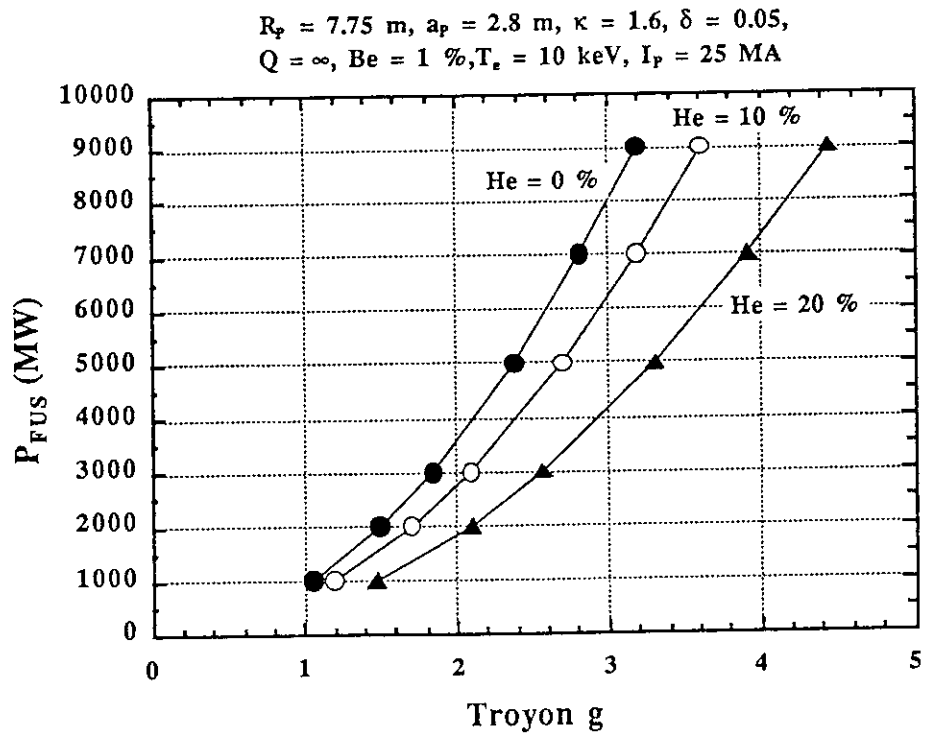
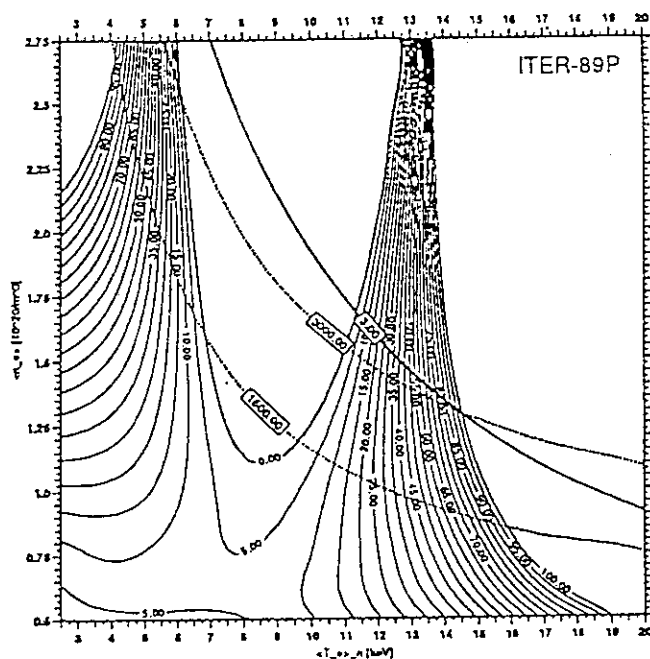


Fig. 2.6 Relation between Troyon coefficient g and the fusion power P_{fus} for various helium accumulations when $Be=1\%$.

a)



b)

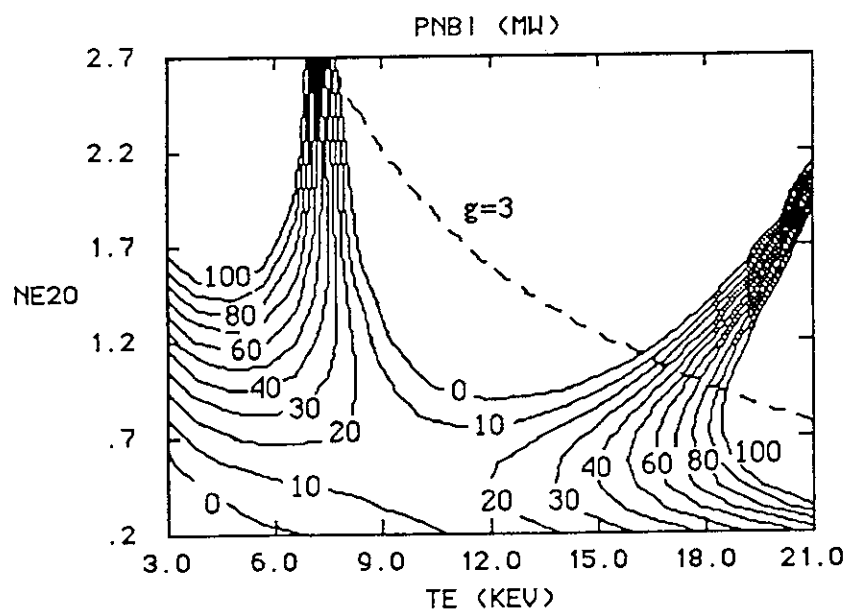
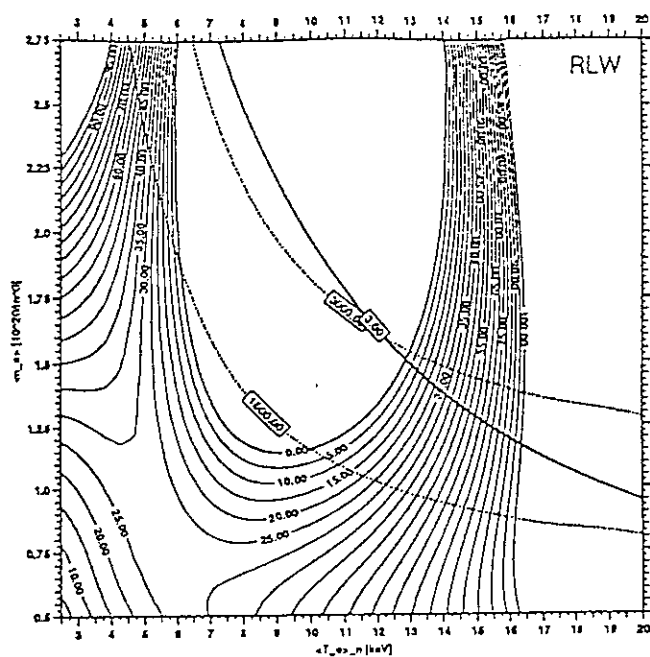


Fig.2.7 POPCON plot for EDA-ITER.

a) Referred from Fig.2 of Ref. [7],

b) 0-D results when H(IP)=1.5, He=12% and Be=1%.

a)



b)

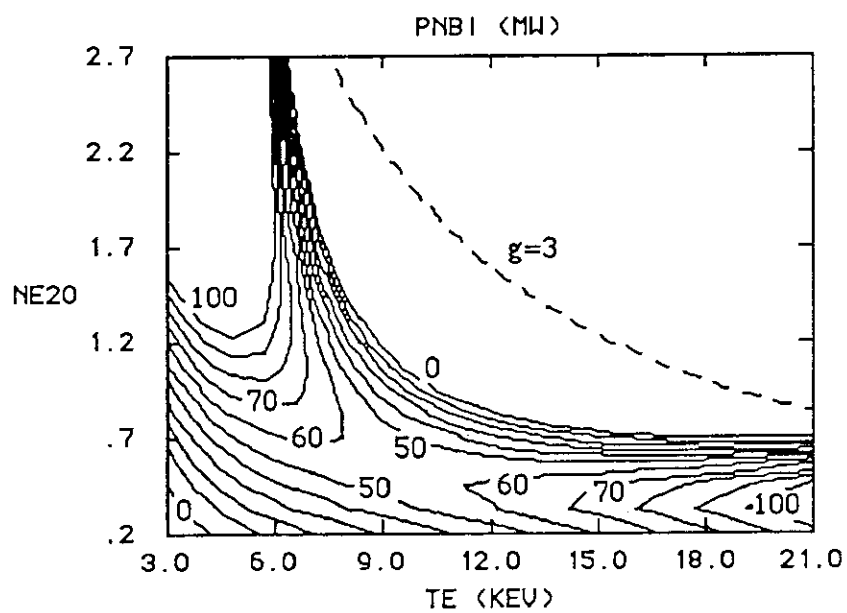


Fig.2.8 POPCON plot for EDA-ITER.

a) Referred from Fig.2 of Ref. [7],

b) 0-D results when $H(RL)=1.1$, $He=12\%$ and $Be=1\%$.

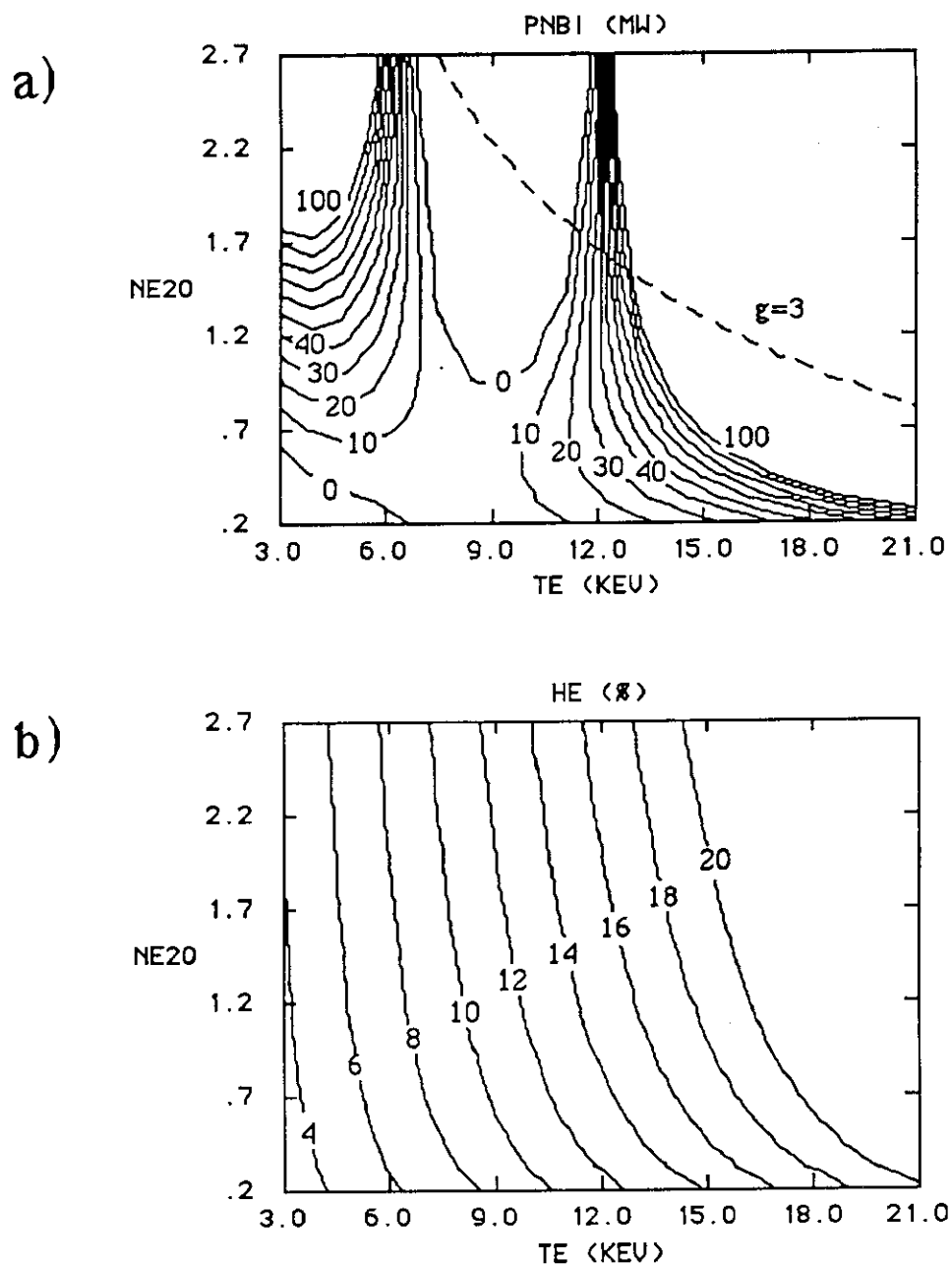


Fig.2.9 O-D calculation results when the helium accumulation depends on T_e and n_e .
 a) POPCON plot when $H(IP)=1.5$,
 b) helium accumulation rate.

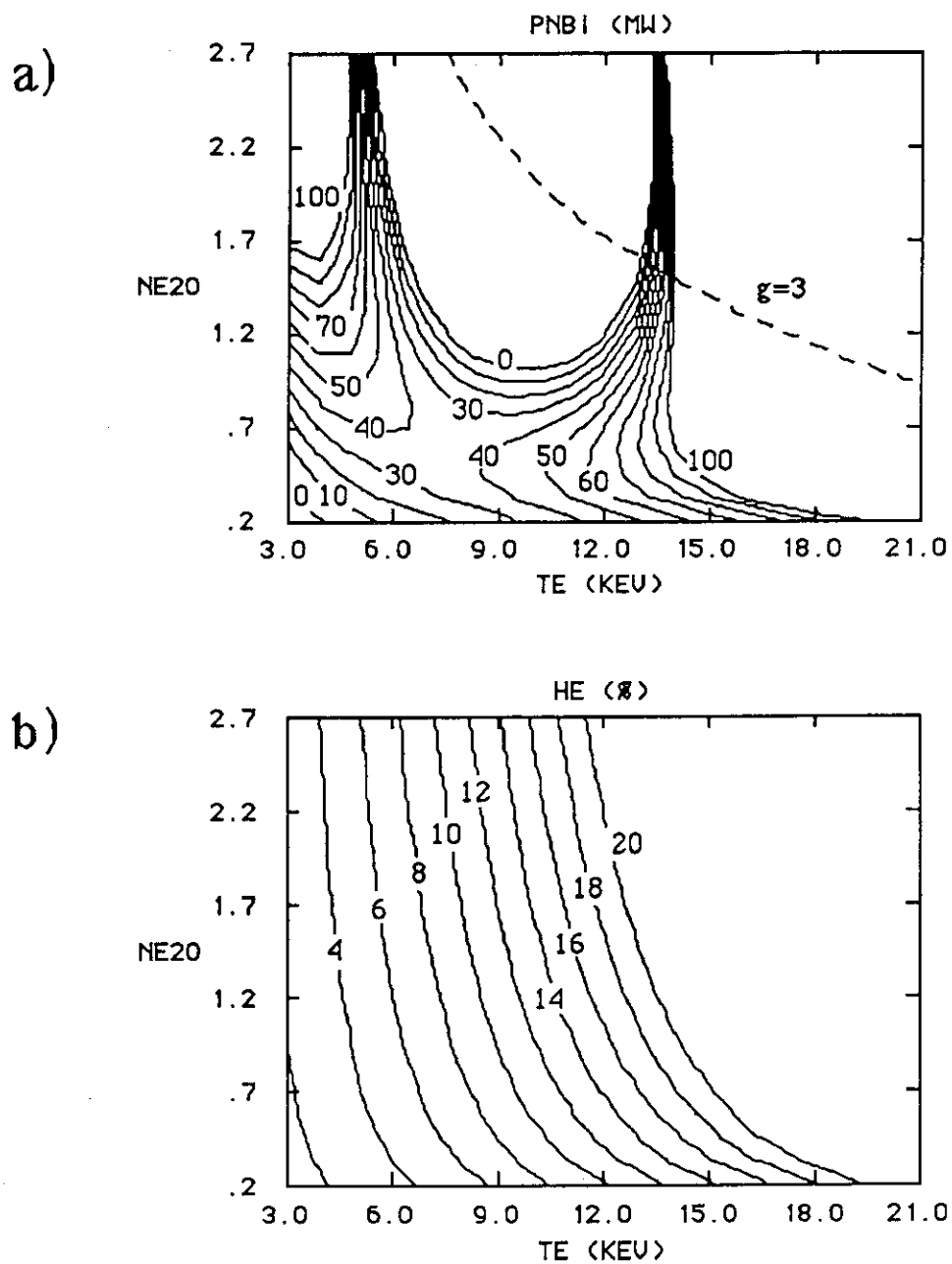


Fig.2.10 O-D calculation results when the helium accumulation depends on T_e and n_e .
 a) POPCON plot when $H(RL)=1.1$,
 b) helium accumulation rate.

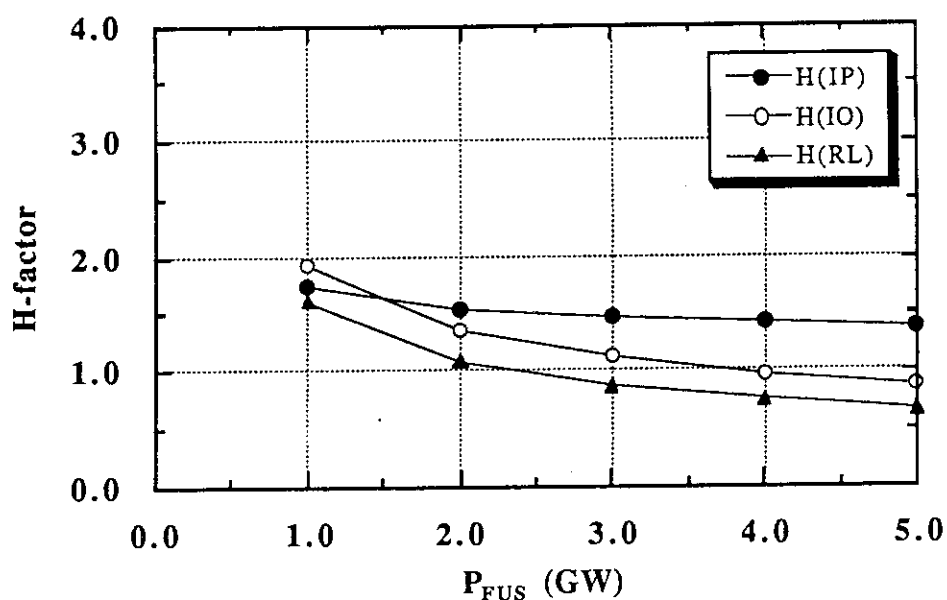


Fig. 2.11 Fusion power (P_{FUS}) and required H-factor for ignition mode operation when $I_P=25$ MA, $T_e=10$ keV and He=10%. Here, H_{IP} , H_{IO} , H_{RL} denote H-factors for ITER89 power scaling law, ITER89 offset-linear scaling law and Rebut-Lallia scaling law, respectively.

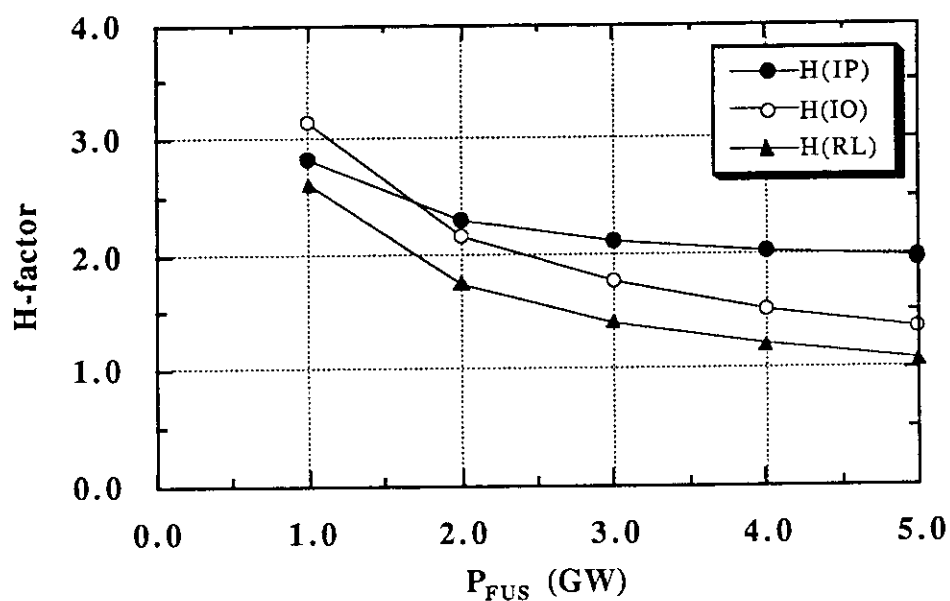


Fig. 2.12 Fusion power (P_{FUS}) and required H-factor for ignition mode operation when $I_P=25$ MA, $T_e=10$ keV and He=20%. Here, H_{IP} , H_{IO} , H_{RL} denote H-factors for ITER89 power scaling law, ITER89 offset-linear scaling law and Rebut-Lallia scaling law, respectively.

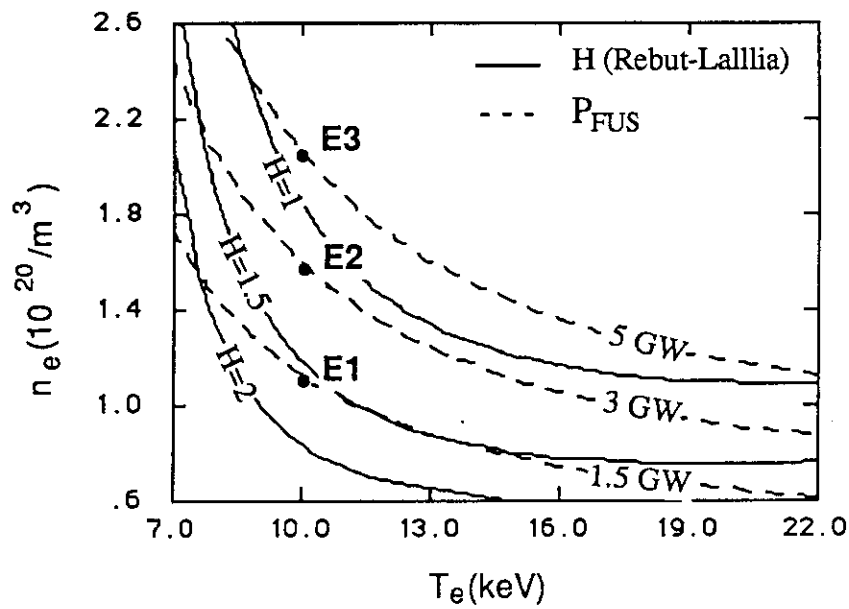


Fig.2.13 Operation region in T_e - n_e space for ignition plasma ($Q=\infty$). Solid lines denote H-factor required for ignition and dashed lines denote the fusion power, respectively.

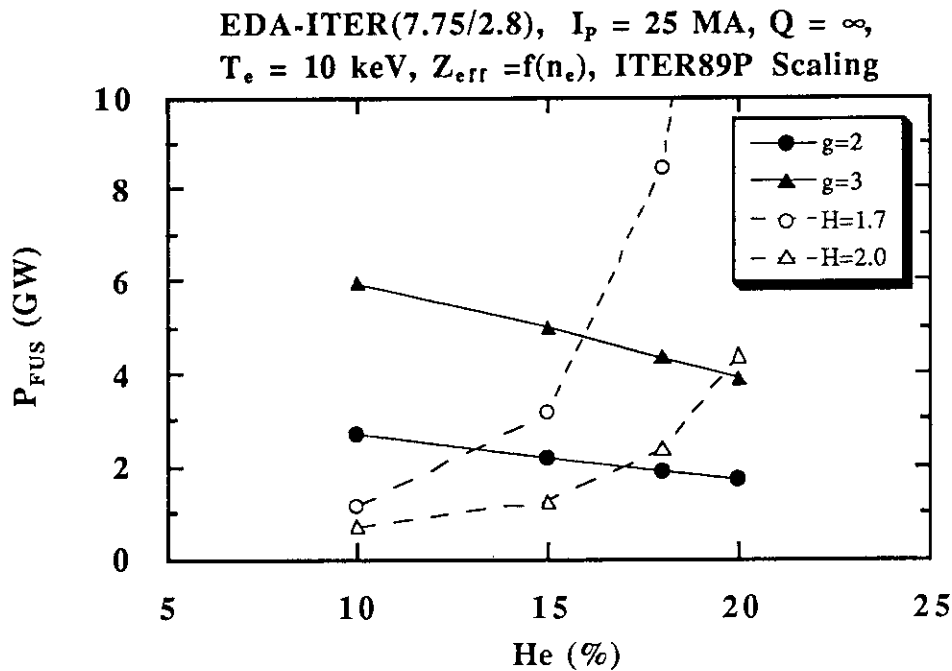


Fig.2.14 Achievable fusion power for various H-factor and Troyon g values.

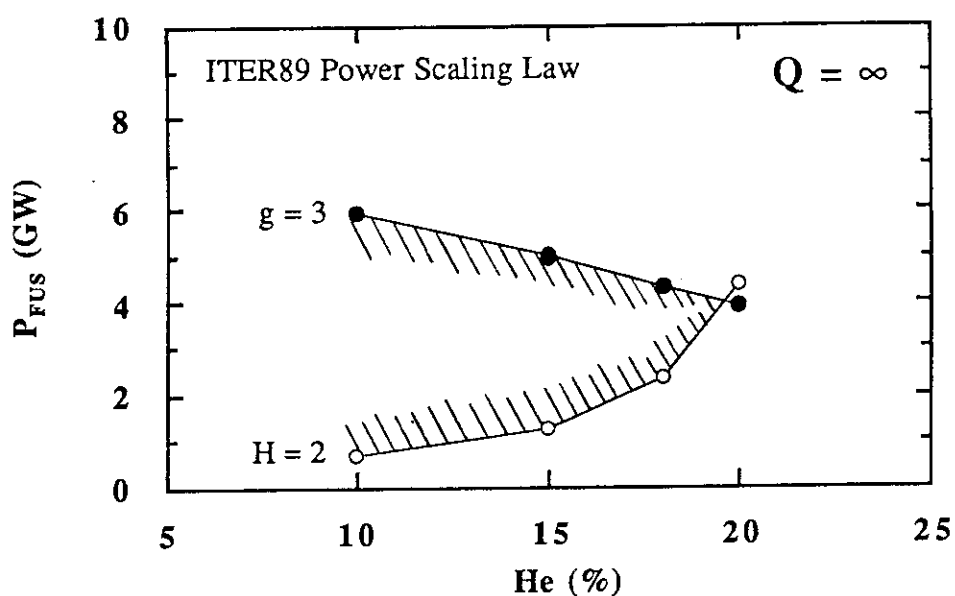


Fig. 2.15 Relation between He accumulation and operation space for ignition mode. Lowest possible fusion power increases and operation region becomes small as He fraction increases. Hatched area denote the operation region where $g \leq 3$ and $H_{IP} \leq 2$.

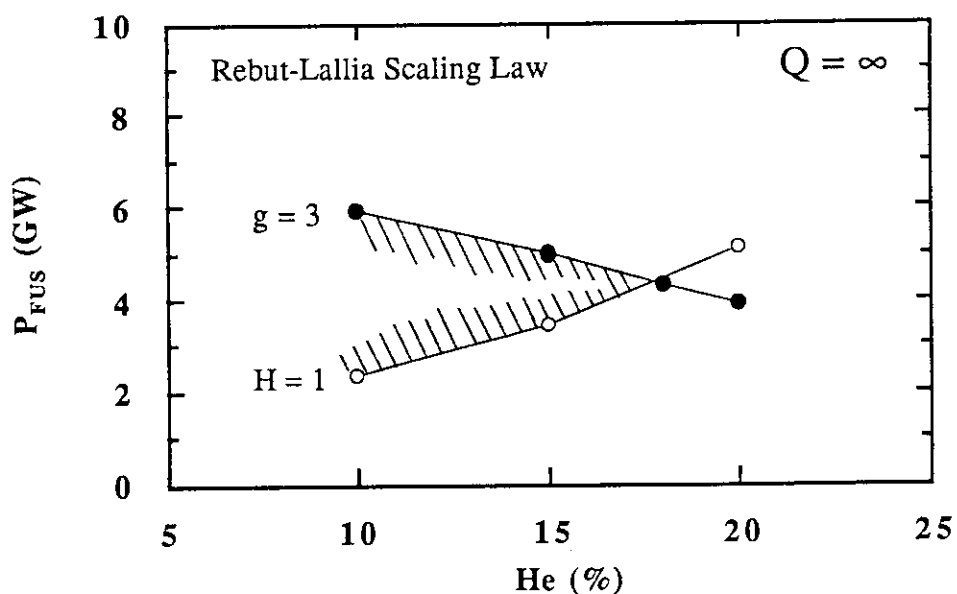


Fig. 2.16 Relation between He accumulation and operation space for ignition mode. Lowest possible fusion power increases and operation region becomes small as He fraction increases. Hatched area denote the operation region where $g \leq 3$ and $H_{RL} \leq 2$.

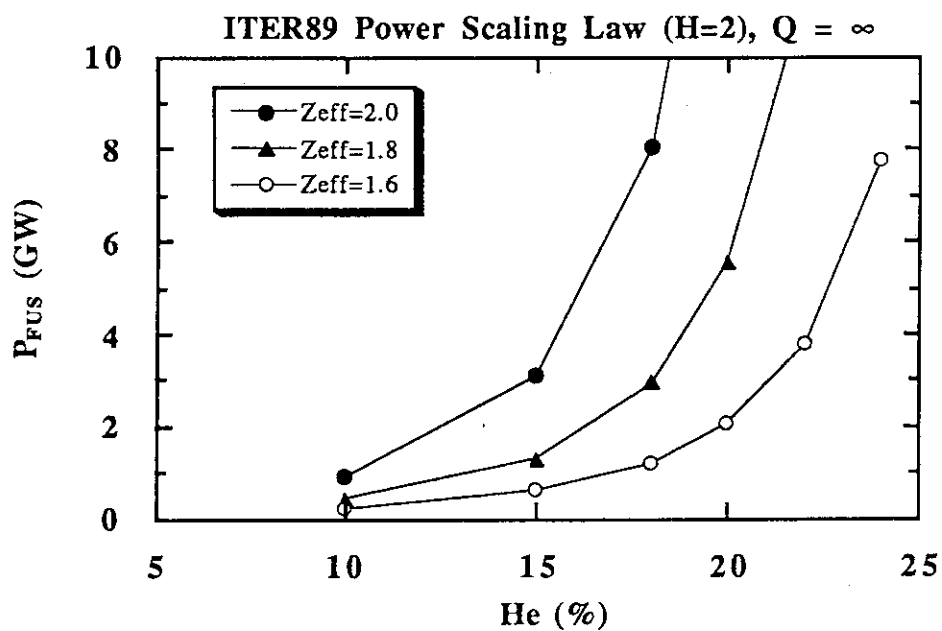


Fig.2.17 Required fusion power for the ignition when the effective ion charge Z_{eff} is fixed. Here, $H(IP)=2$ is assumed.

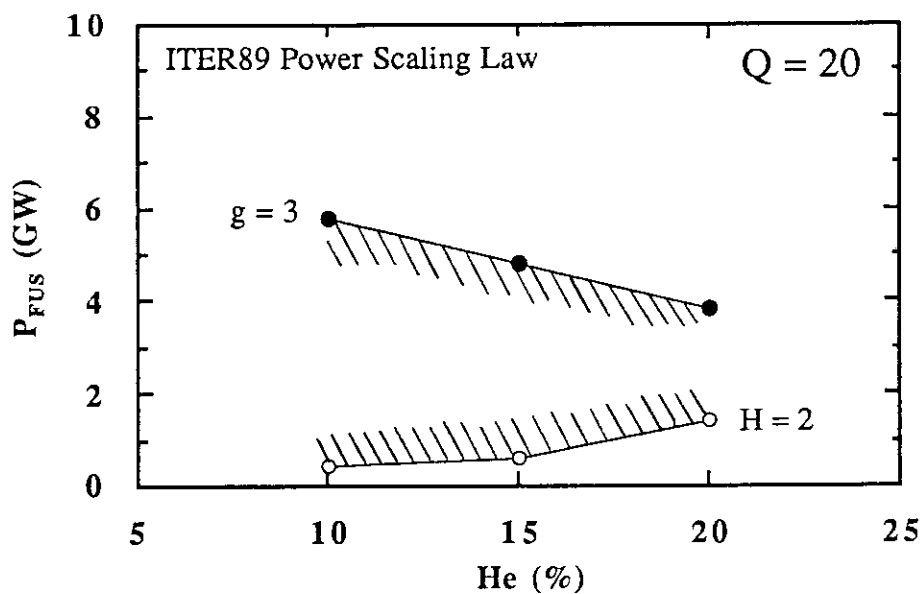


Fig.2.18 Required fusion power when $Q=20$, $H(IP) \leq 2$ and $g \leq 3$.

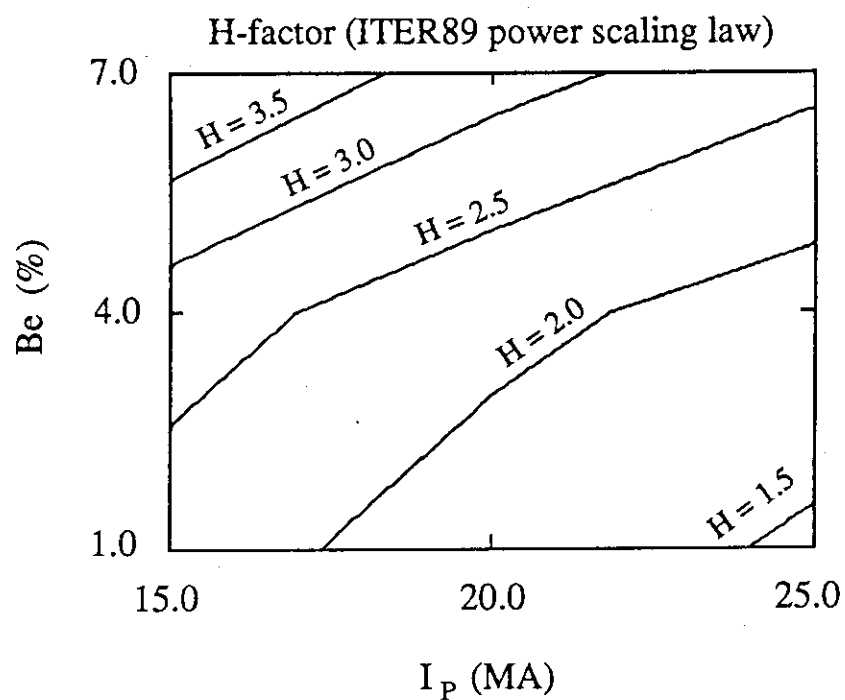


Fig.2.19 Contour line plot of H-factor evaluated by ITER89 power scaling law in I_P -Be space when $P_{FUS}=1.5$ GW and $He=10\%$.

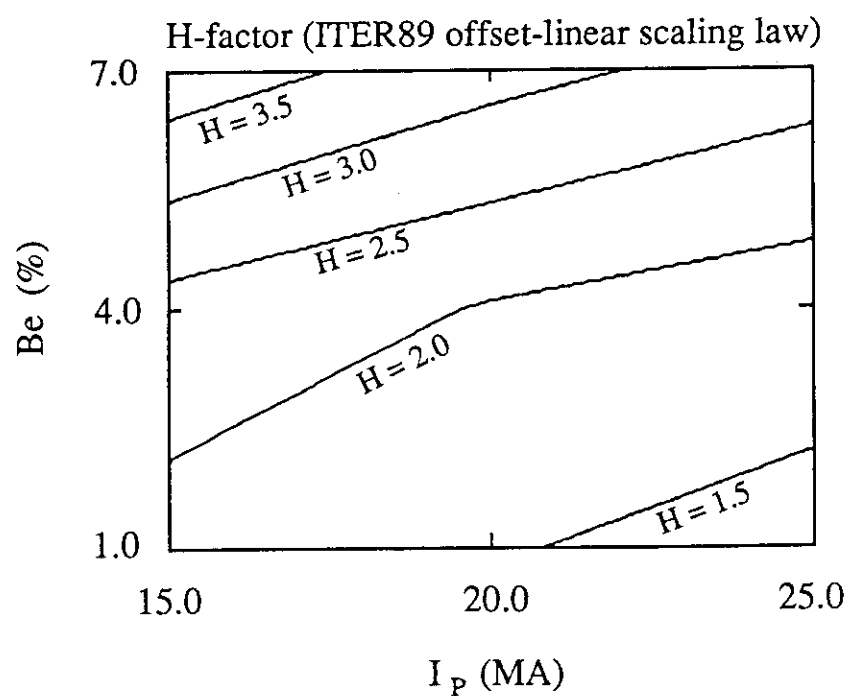


Fig.2.20 Contour line plot of H-factor evaluated by ITER89 offset-linear scaling law in I_P -Be space when $P_{FUS}=1.5$ GW and $He=10\%$.

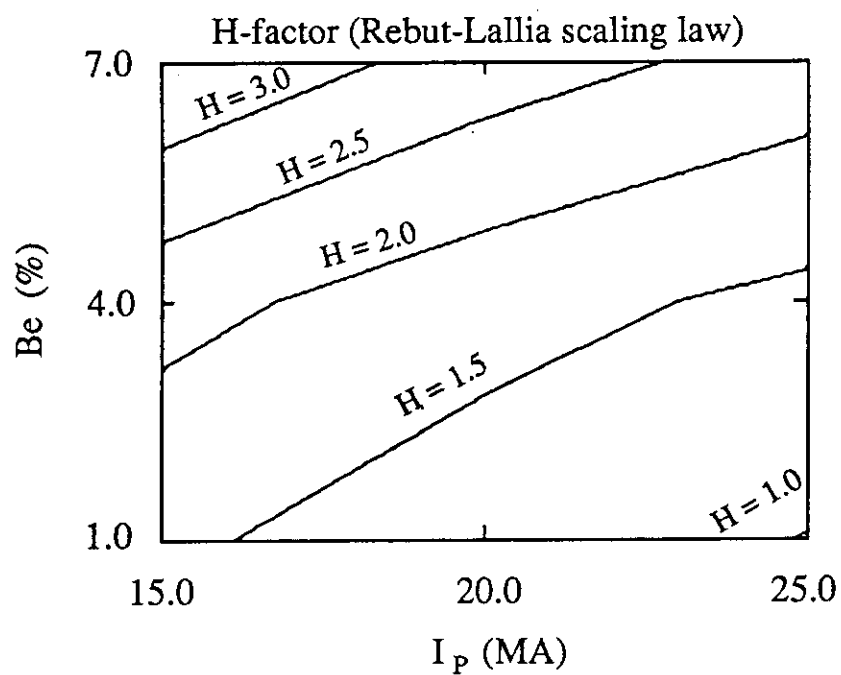


Fig. 2.21 Contour line plot of H-factor evaluated by Rebut-Lallia scaling law in I_P -Be space when $P_{FUS}=1.5$ GW and $He=10\%$.

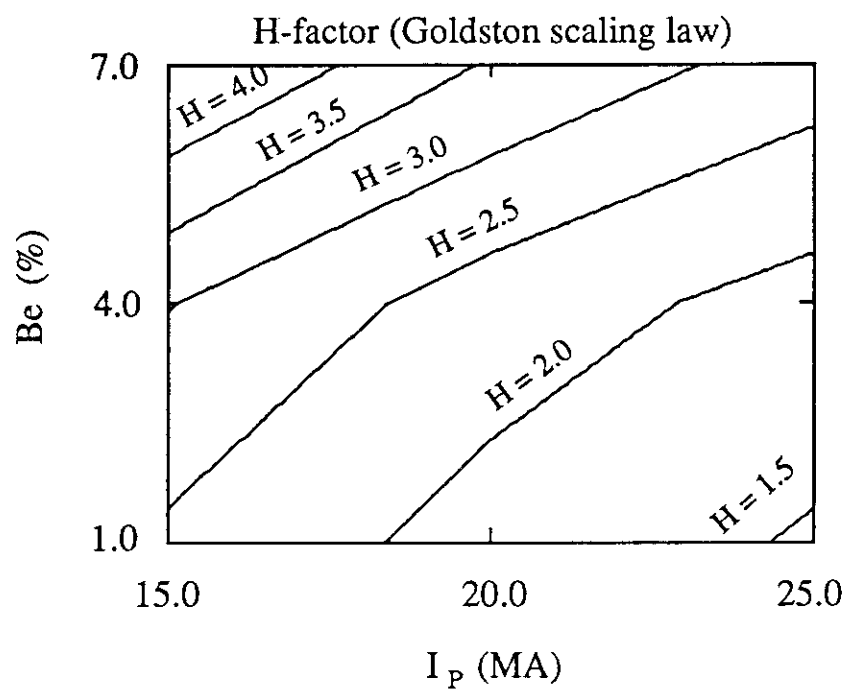


Fig. 2.22 Contour line plot of H-factor evaluated by Goldston scaling law in I_P -Be space when $P_{FUS}=1.5$ GW and $He=10\%$.

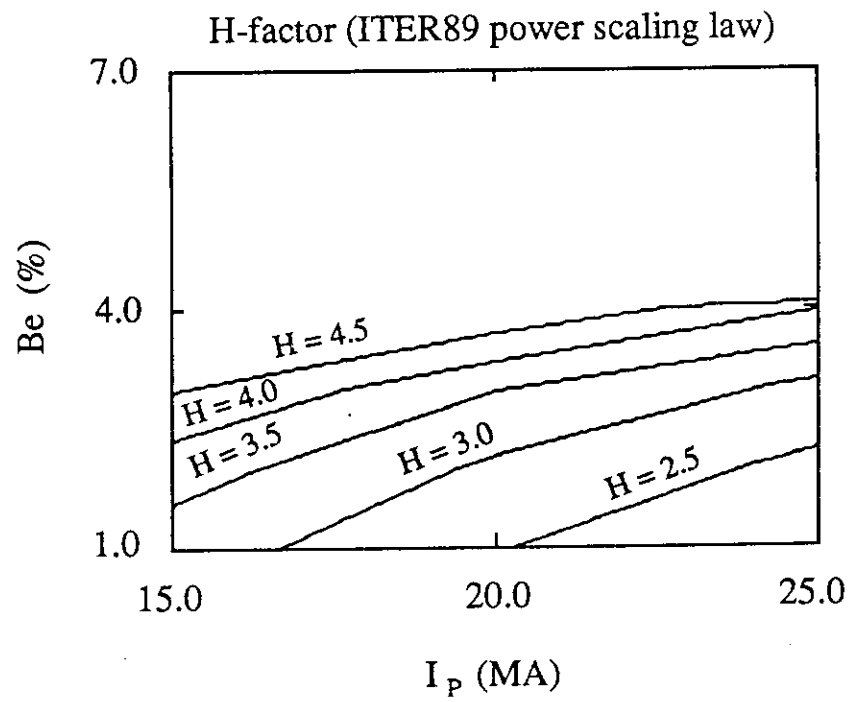
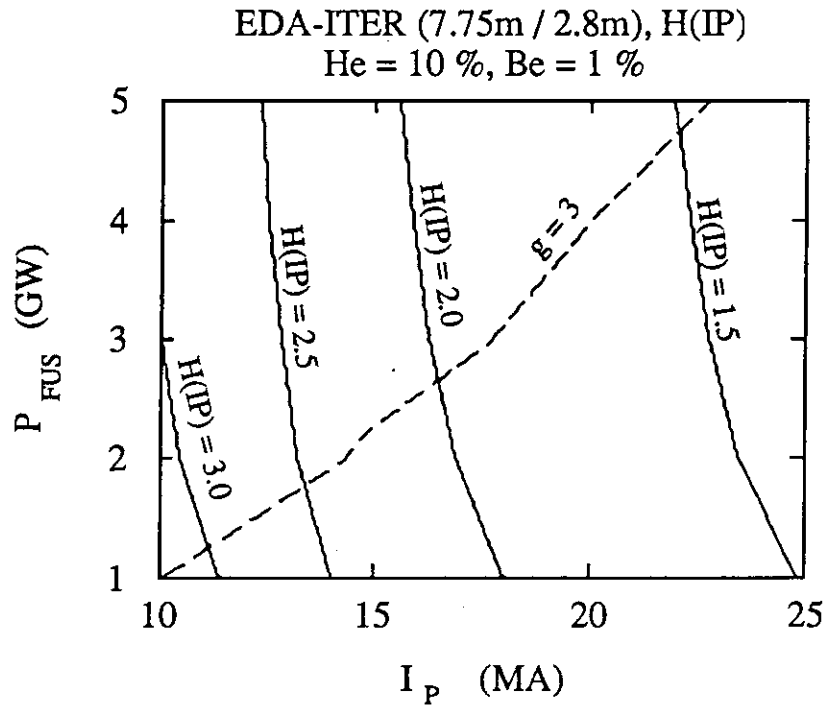


Fig. 2.23 Contour line plot of H-factor evaluated by ITER89 power scaling law in I_p -Be space when $P_{fus}=1.5$ GW and He=20%.

a)



b)

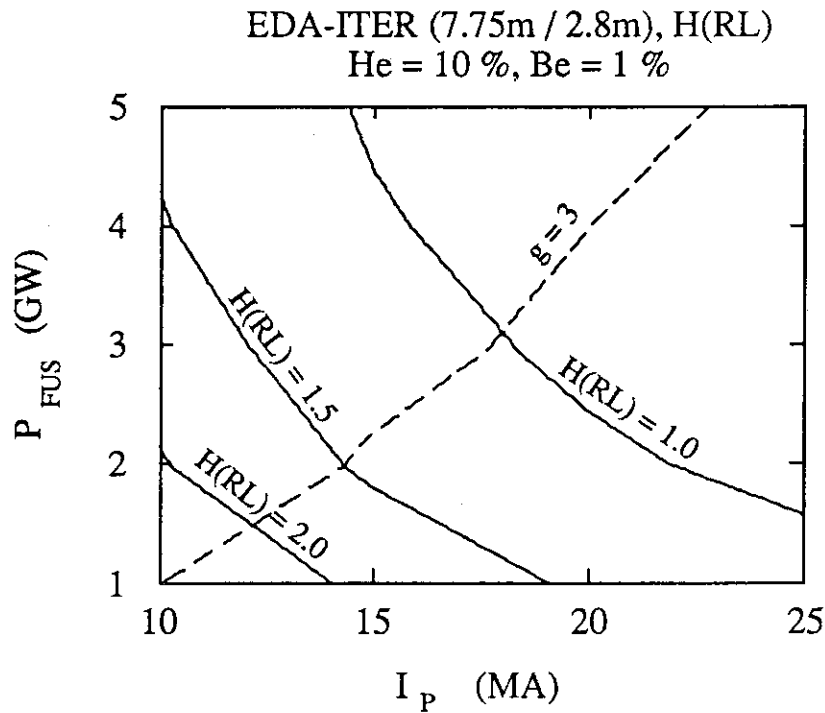
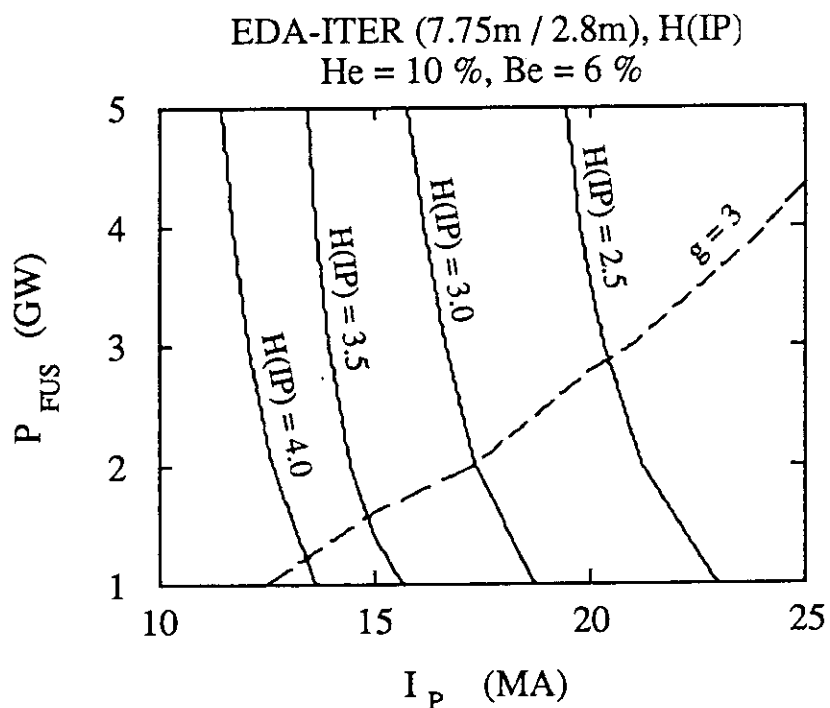


Fig.2.24 Contour lines of H-factor and Troyon q in I_p - P_{FUS} plane when He=10% and Be=1%.

a) H-factor is evaluated by ITER89 power scaling law,
b) H-factor is evaluated by Rebut-Lallia scaling law.

a)



b)

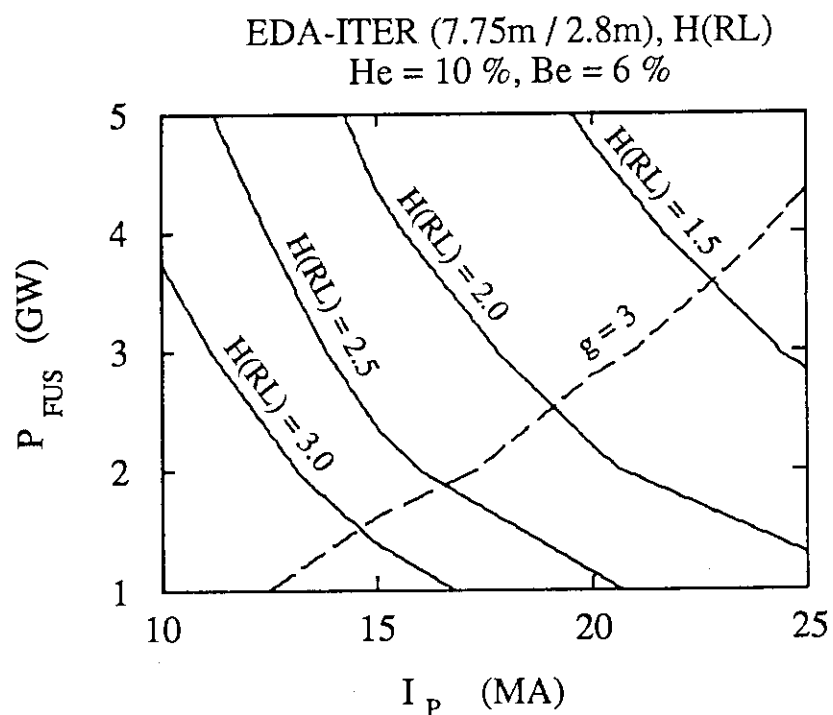
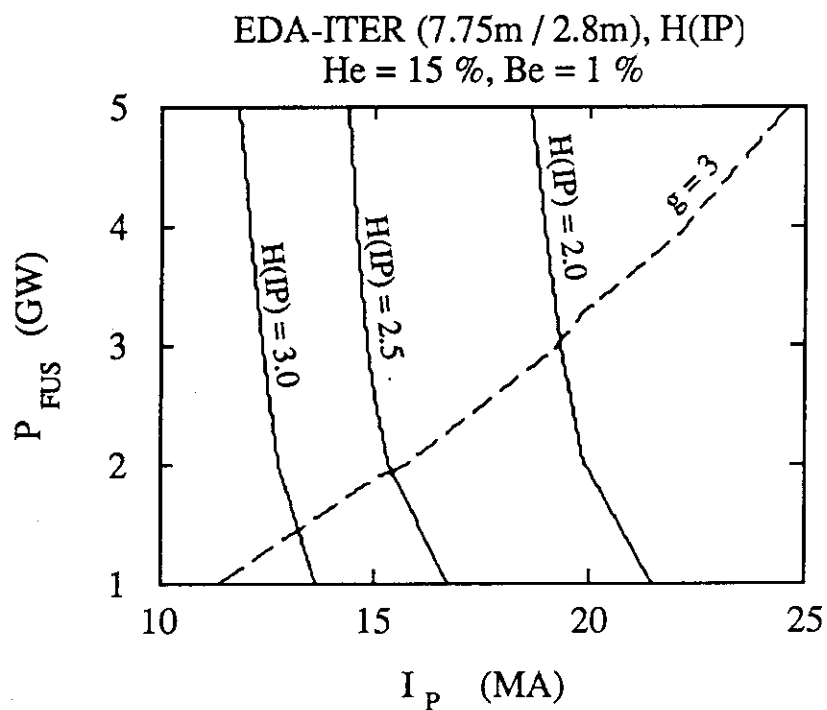


Fig. 2.25 Contour lines of H-factor and Troyon g in I_p - P_{FUS} plane when He=10% and Be=6%.

- a) H-factor is evaluated by ITER89 power scaling law,
b) H-factor is evaluated by Rebut-Lallia scaling law.

a)



b)

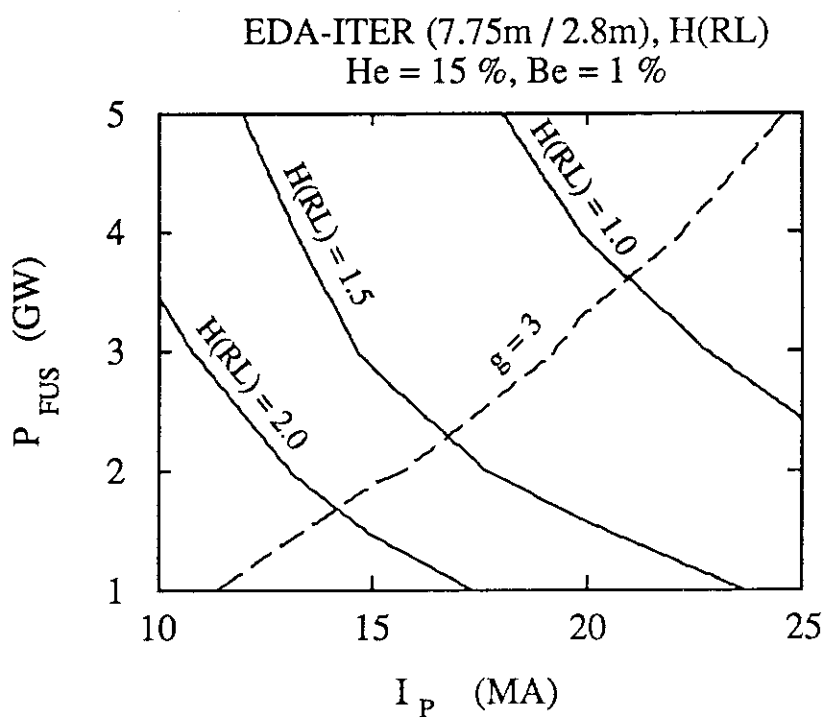
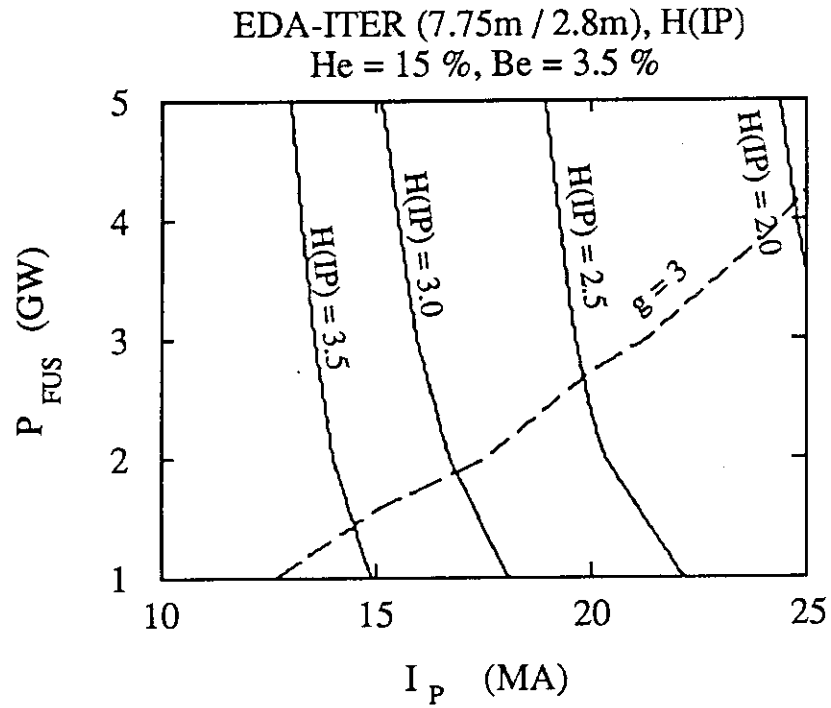


Fig. 2.26 Contour lines of H-factor and Troyon g in I_p - P_{FUS} plane when He=15% and Be=1%.

- a) H-factor is evaluated by ITER89 power scaling law,
b) H-factor is evaluated by Rebut-Lallia scaling law.

a)



b)

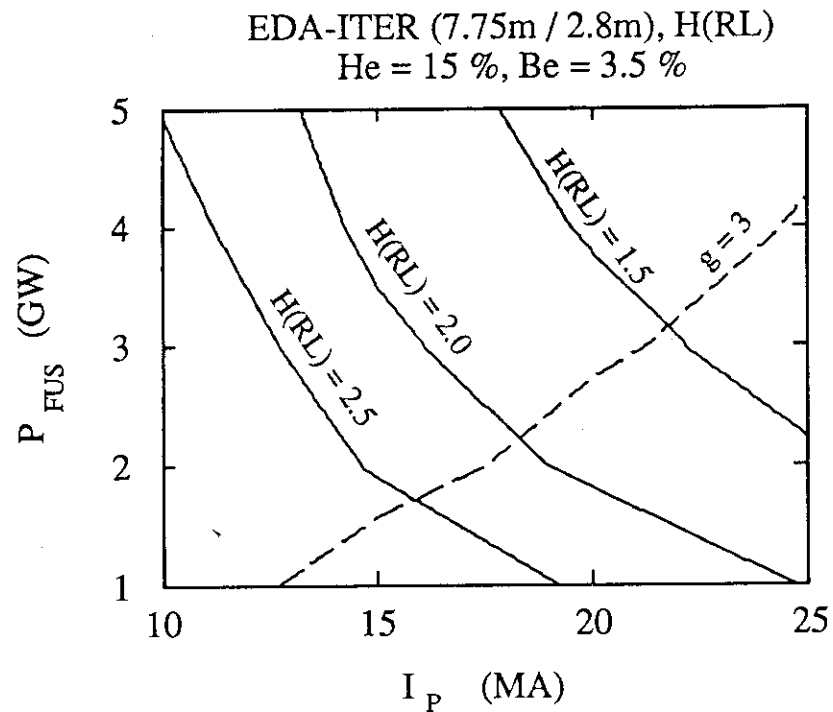
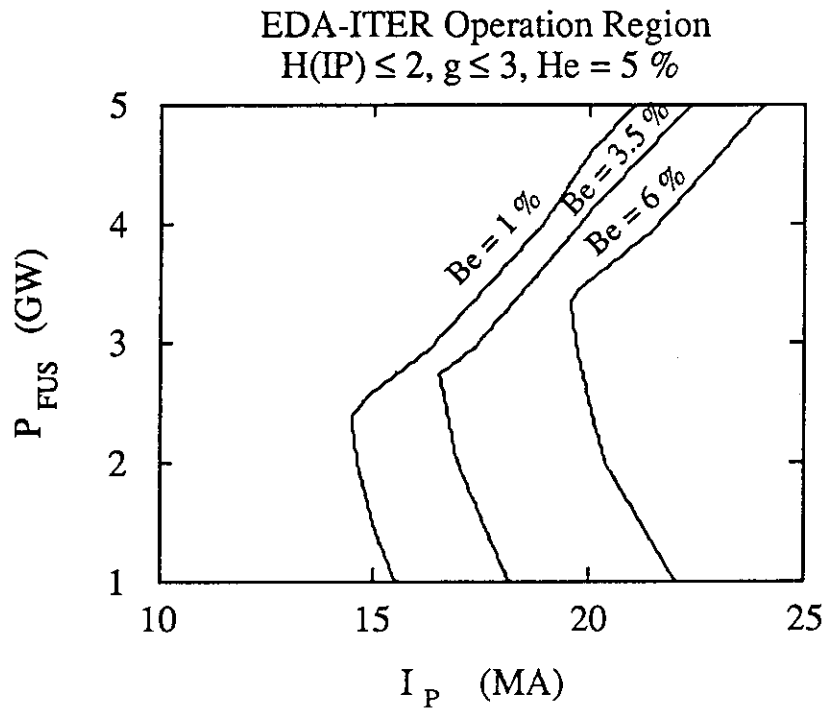


Fig. 2.27 Contour lines of H-factor and Troyon g in I_P - P_{FUS} plane when He=15% and Be=3.5%.

a) H-factor is evaluated by ITER89 power scaling law,
b) H-factor is evaluated by Rebut-Lallia scaling law.

a)



b)

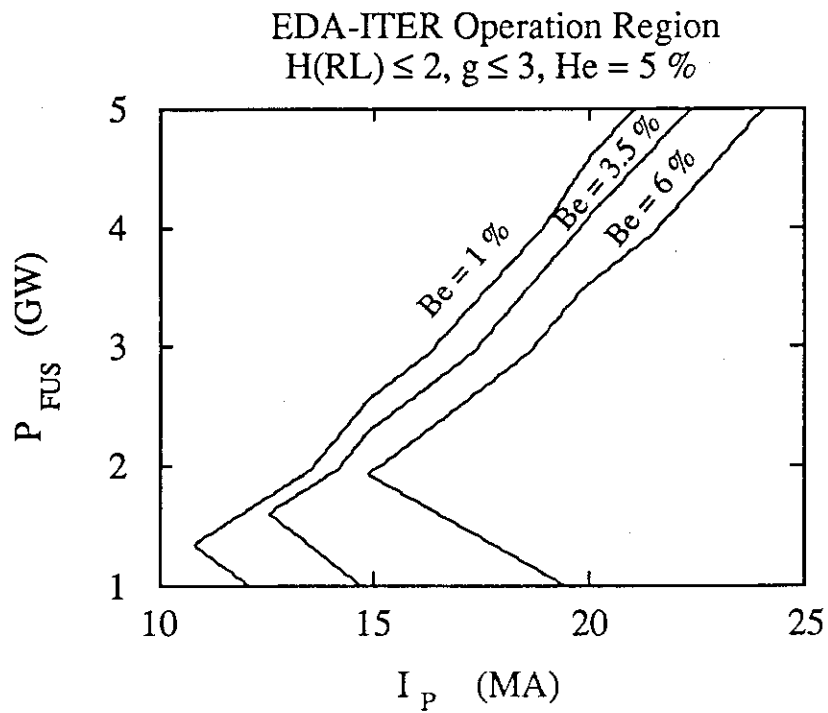
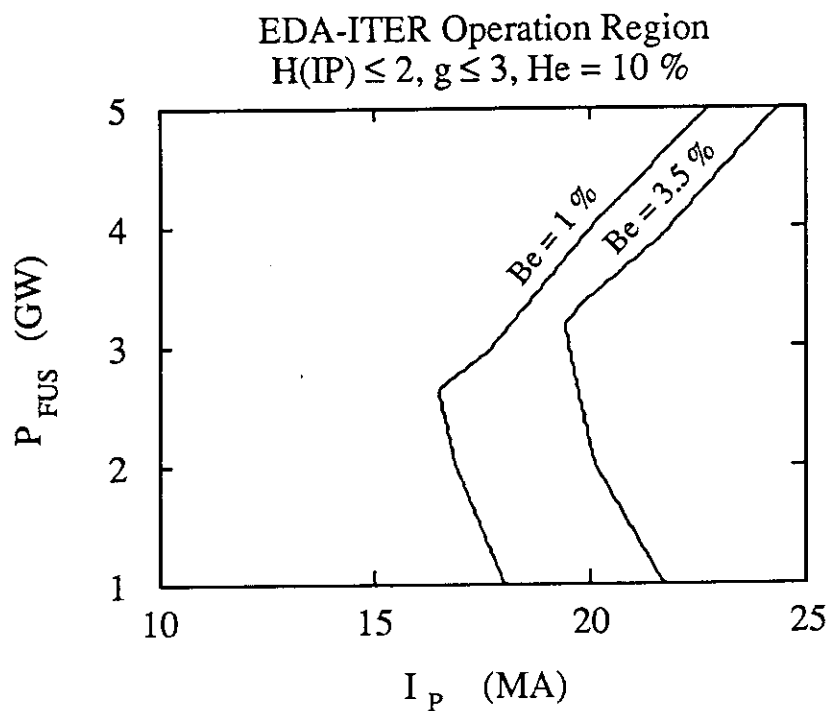


Fig.2.28 Operation region for various beryllium fractions in I_P - P_{FUS} plane when $He=5\%$, $H \leq 2$ and $g \leq 3$.

- a) H-factor is evaluated by ITER89 power scaling law,
 b) H-factor is evaluated by Rebut-Lallia scaling law.

a)



b)

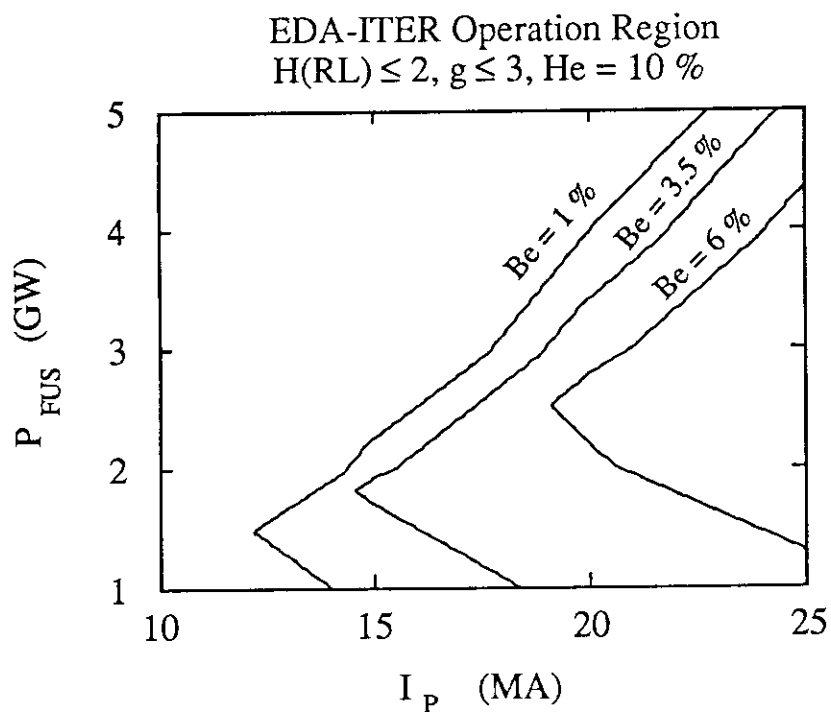
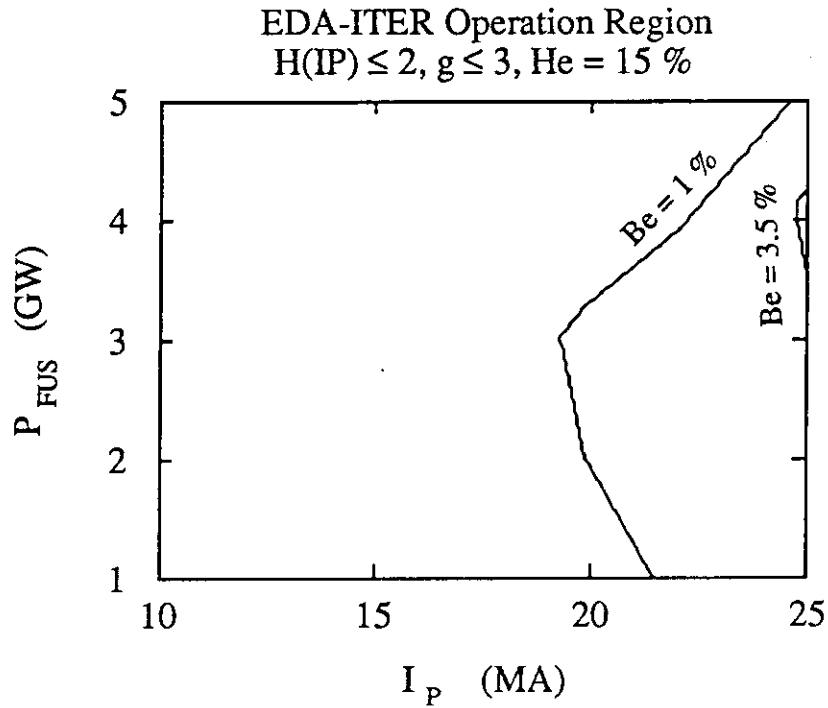


Fig. 2.29 Operation region for various beryllium fractions in I_p - P_{FUS} plane when $He=10\%$, $H \leq 2$ and $g \leq 3$.

a) H-factor is evaluated by ITER89 power scaling law,
 b) H-factor is evaluated by Rebut-Lallia scaling law.

a)



b)

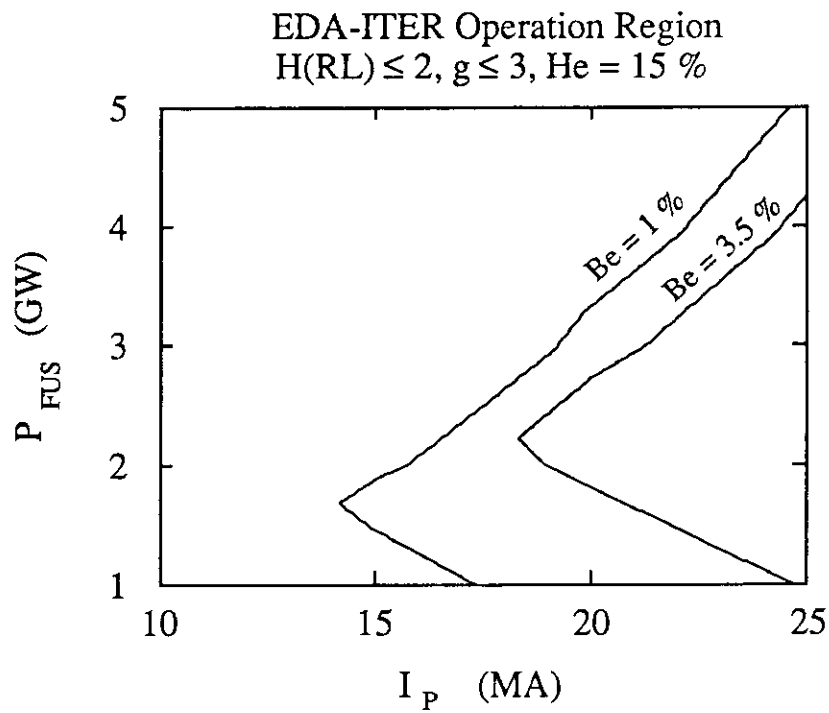
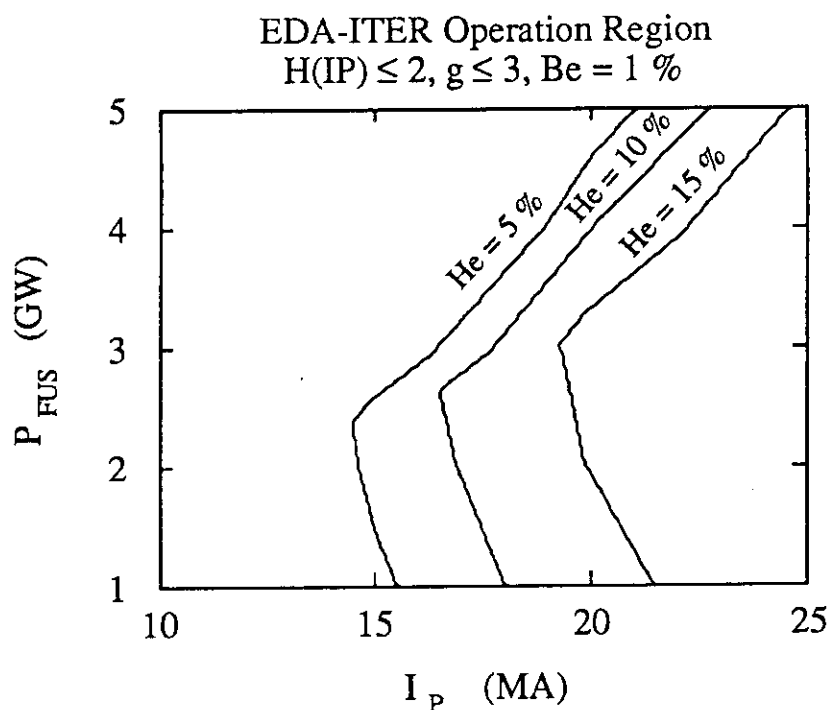


Fig. 2.30 Operation region for various beryllium fractions in I_p - P_{FUS} plane when $He=15\%$, $H \leq 2$ and $g \leq 3$.

- a) H-factor is evaluated by ITER89 power scaling law,
 b) H-factor is evaluated by Rebut-Lallia scaling law.

a)



b)

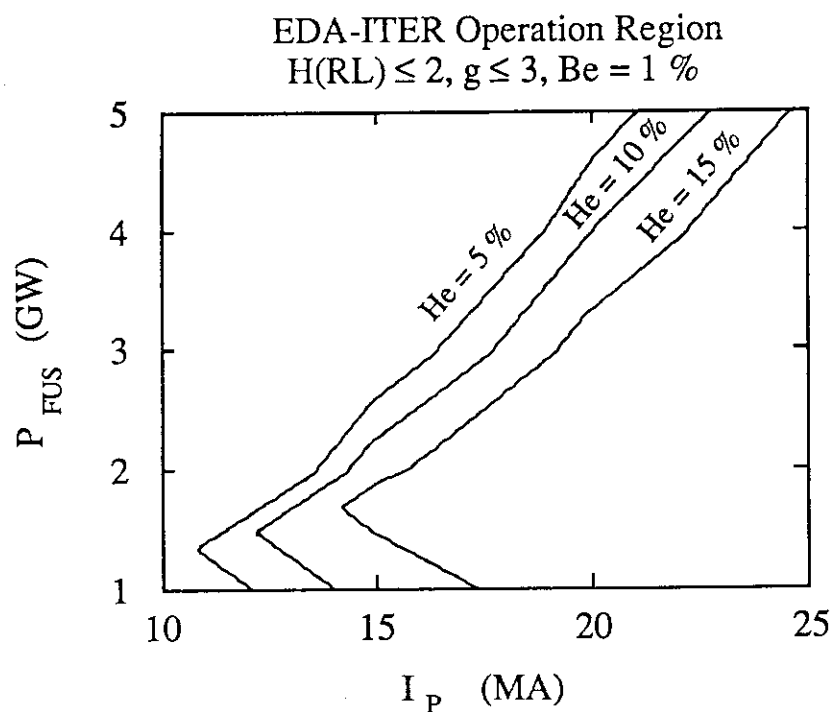


Fig.2.31 Operation region for various helium fractions in I_p - P_{FUS} plane when $Be=1\%$, $H \leq 2$ and $g \leq 3$.

a) H-factor is evaluated by ITER89 power scaling law,
 b) H-factor is evaluated by Rebut-Lallia scaling law.

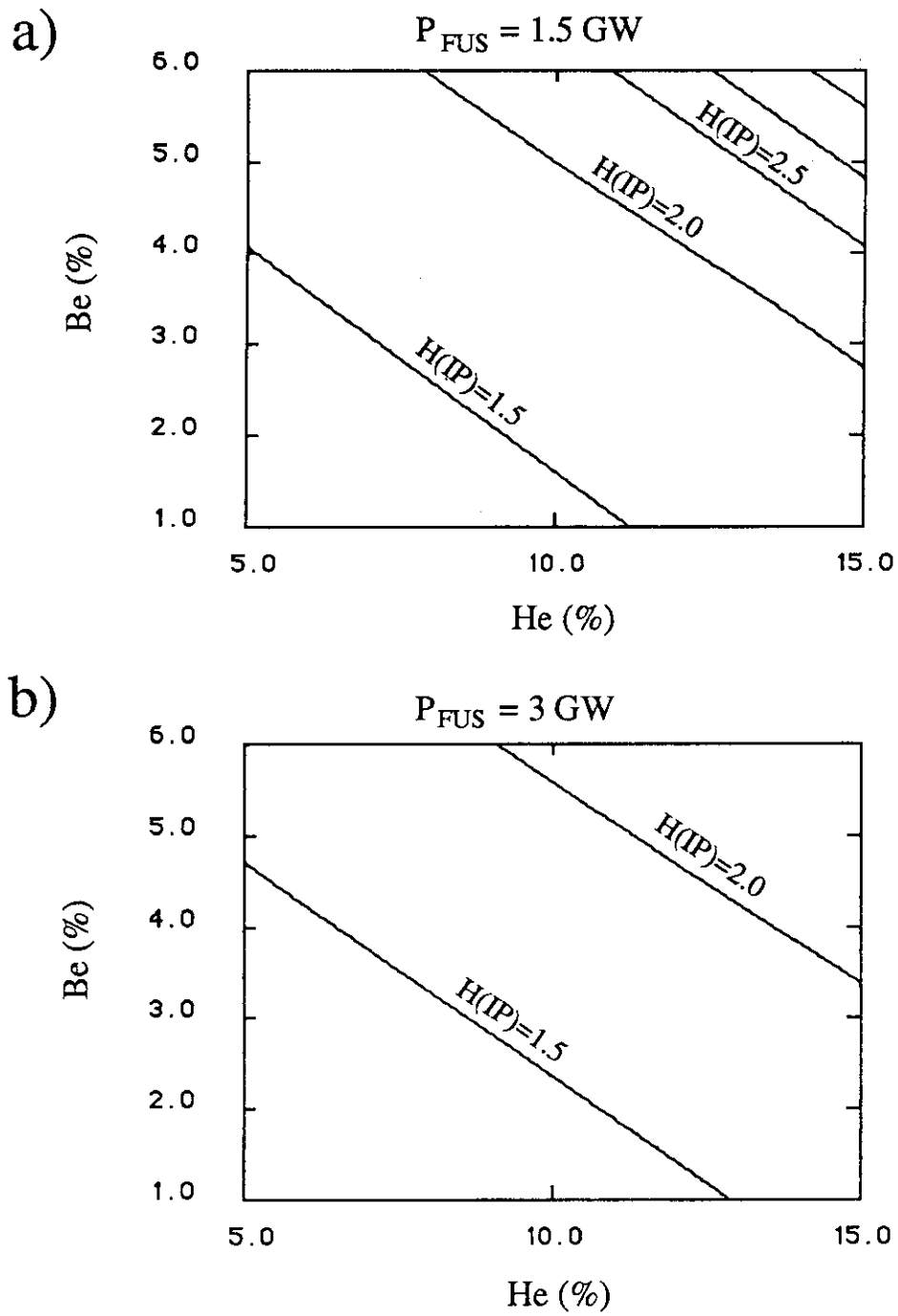


Fig. 2.32 Contour line plot of H-factor required for the ignition when $I_p=25 \text{ MA}$ and $P_{FUS}=1.5 \text{ GW}$ (a) or 3 GW (b). Here, H-factor is evaluated by ITER89 power scaling law.

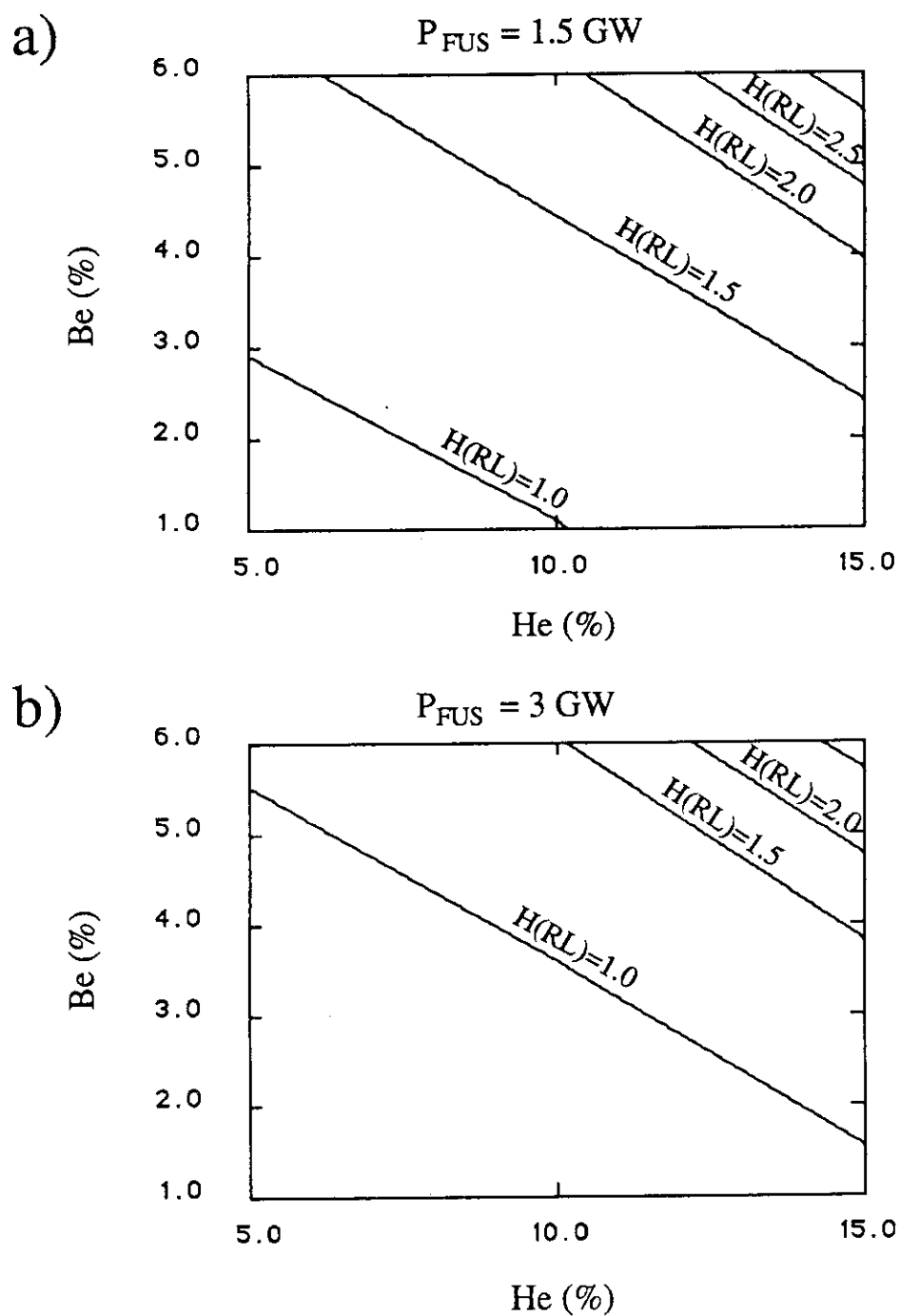


Fig. 2.33 Contour line plot of H-factor required for the ignition when $I_p=25 \text{ MA}$ and $P_{FUS}=1.5 \text{ GW}$ (a) or 3 GW (b). Here, H-factor is evaluated by Rebut-Lallia scaling law.

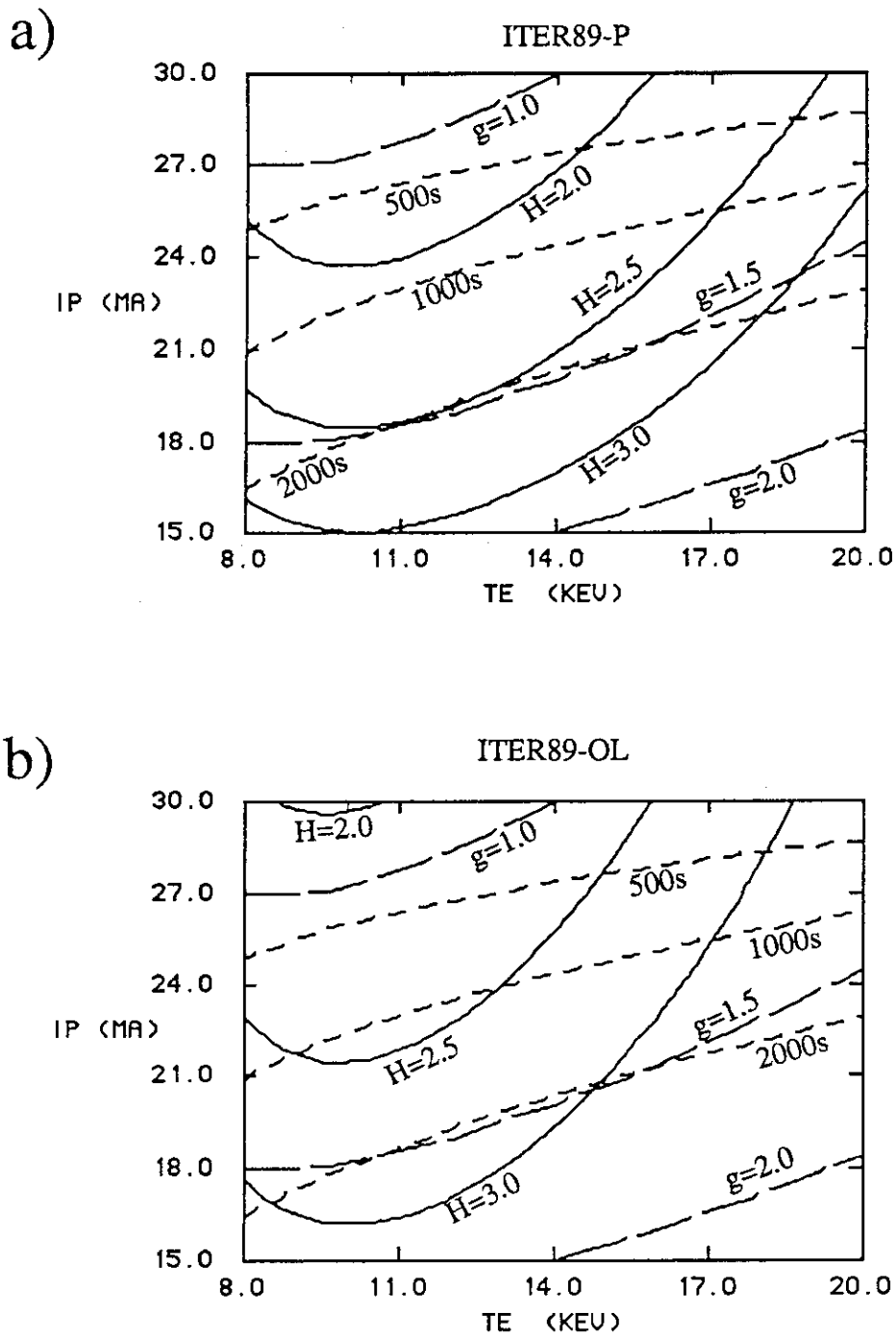


Fig.2.34 Operation region for the ignition plasma in T_e - I_p space when $P_{fus}=0.75$ GW and He=10%.

- a) H-factor is evaluated by ITER89 power scaling law,
 b) H-factor is evaluated by ITER89 offset-linear scaling law.

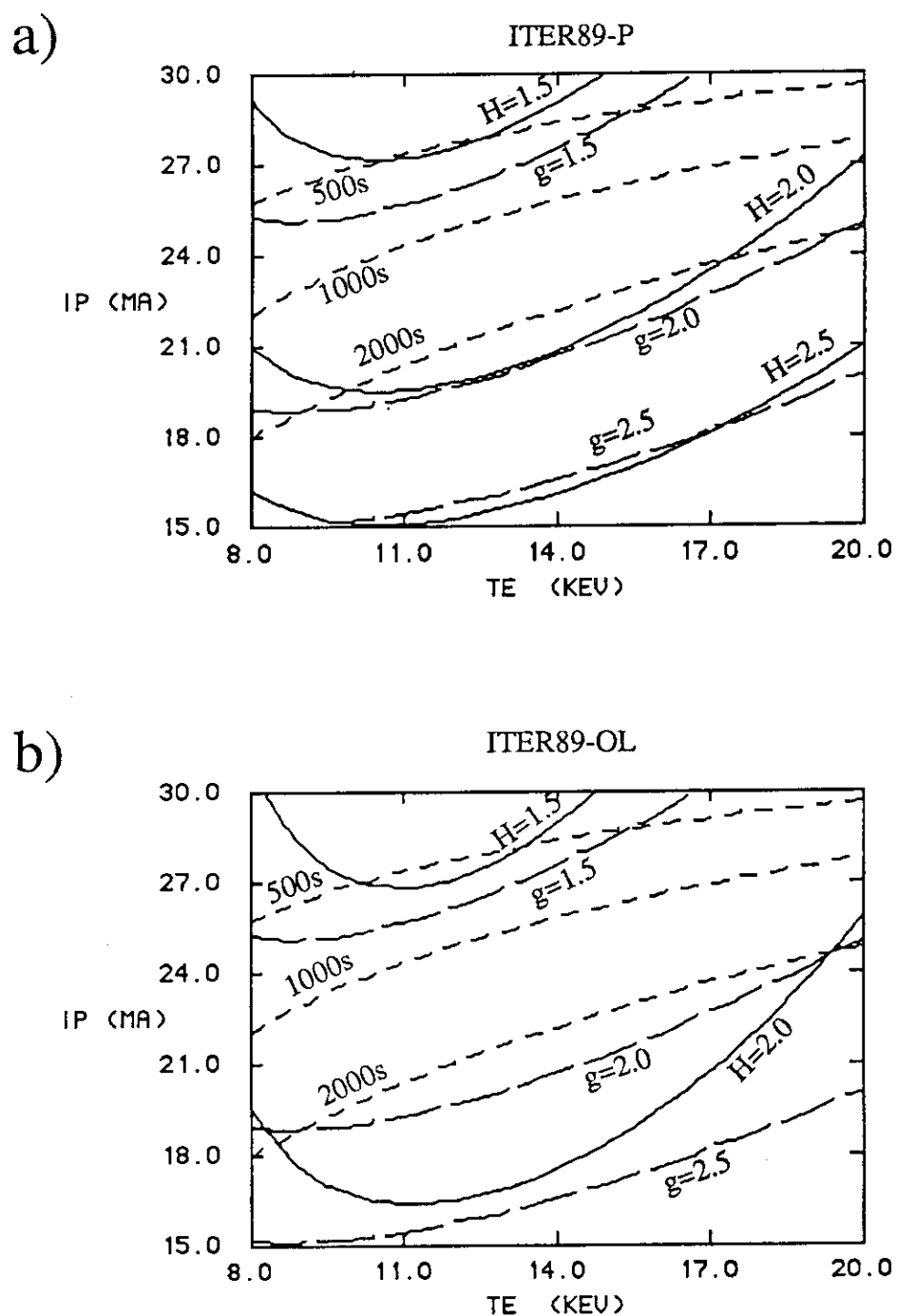
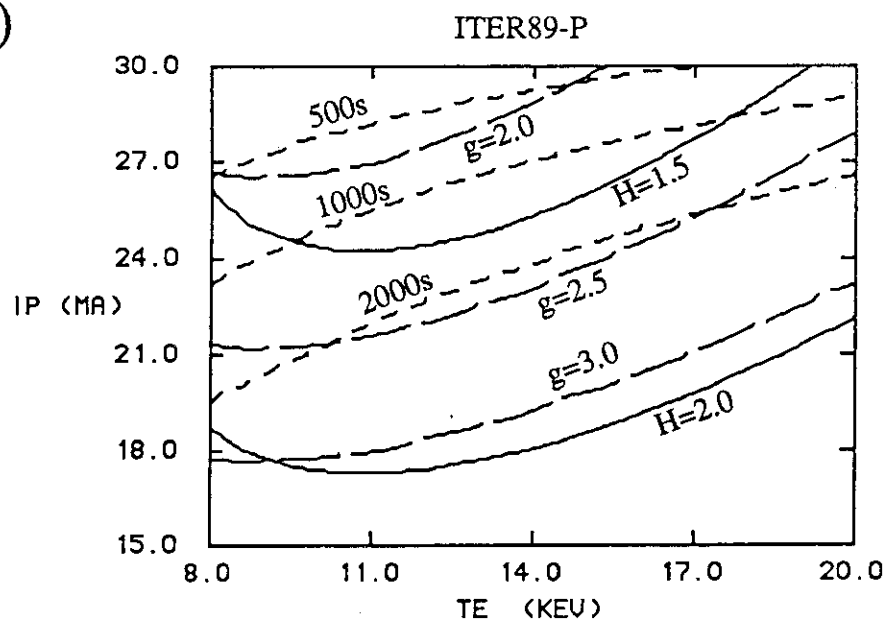


Fig. 2.35 Operation region for the ignition plasma in T_e - I_p space when $P_{fus}=1.5$ GW and He=10%.

a) H-factor is evaluated by ITER89 power scaling law,

b) H-factor is evaluated by ITER89 offset-linear scaling law.

a)



b)

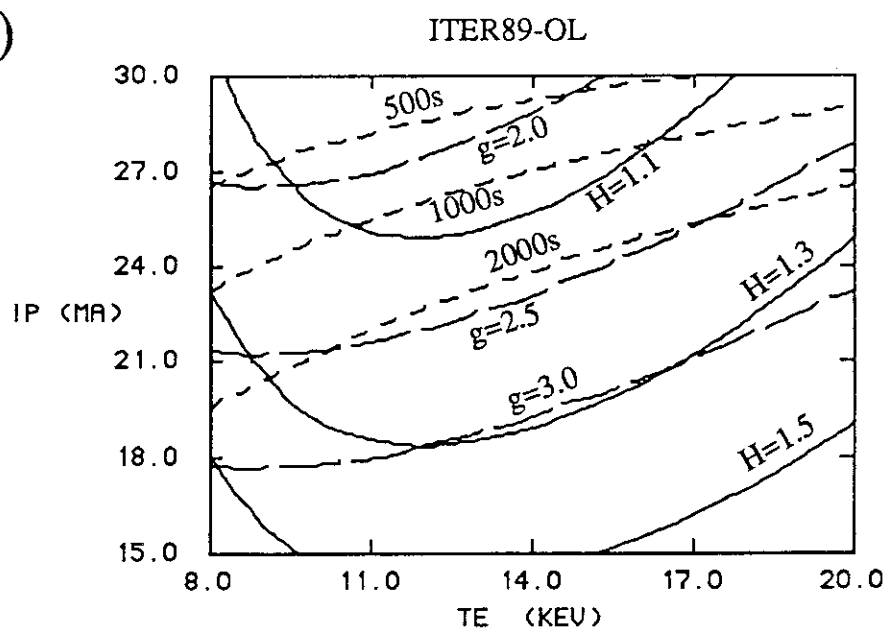


Fig.2.36 Operation region for the ignition plasma in T_e - I_P space when $P_{fus}=3$ GW and $He=10\%$.
 a) H-factor is evaluated by ITER89 power scaling law,
 b) H-factor is evaluated by ITER89 offset-linear scaling law.

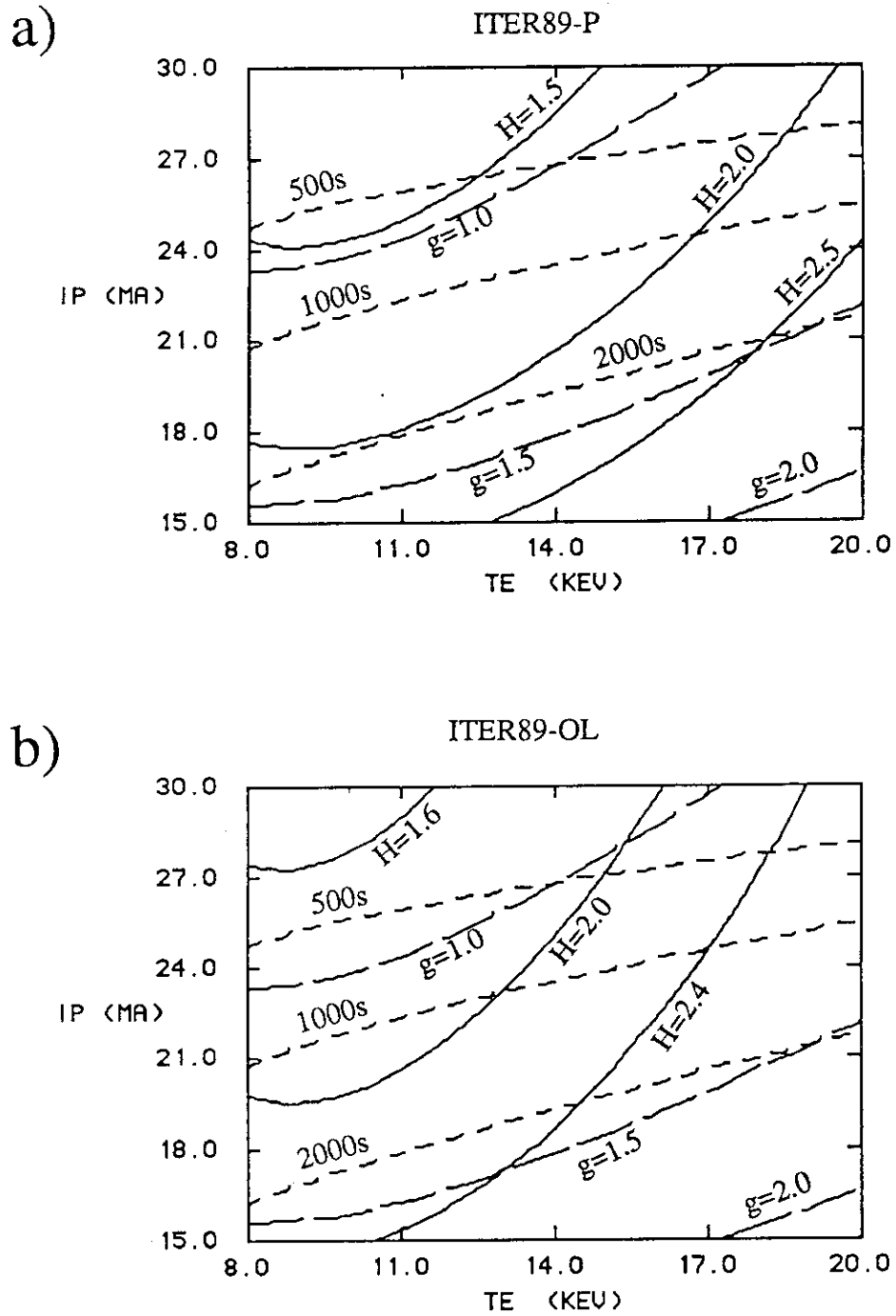
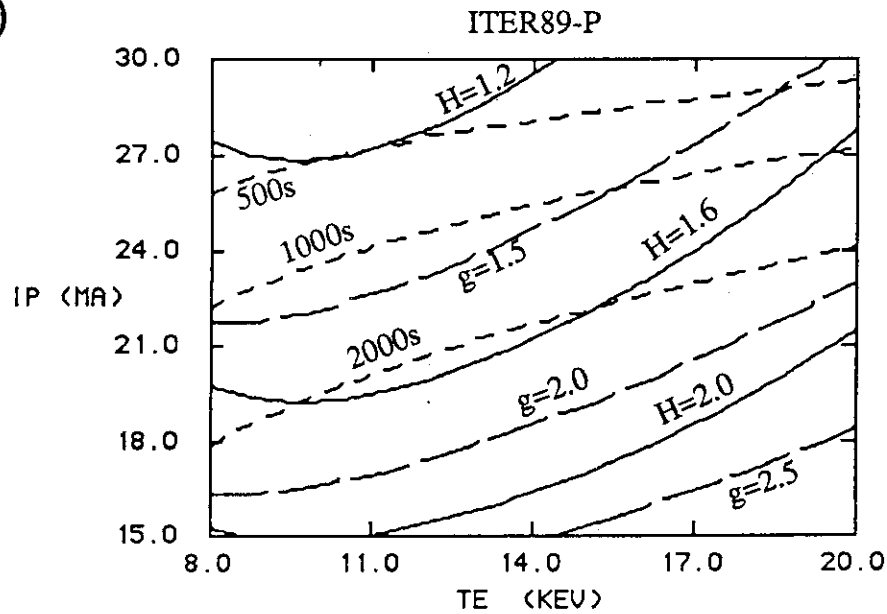


Fig.2.37 Operation region for the ignition plasma in T_e - I_p space when $P_{fus}=0.75$ GW and He=0%.

a) H-factor is evaluated by ITER89 power scaling law,
 b) H-factor is evaluated by ITER89 offset-linear scaling law.

a)



b)

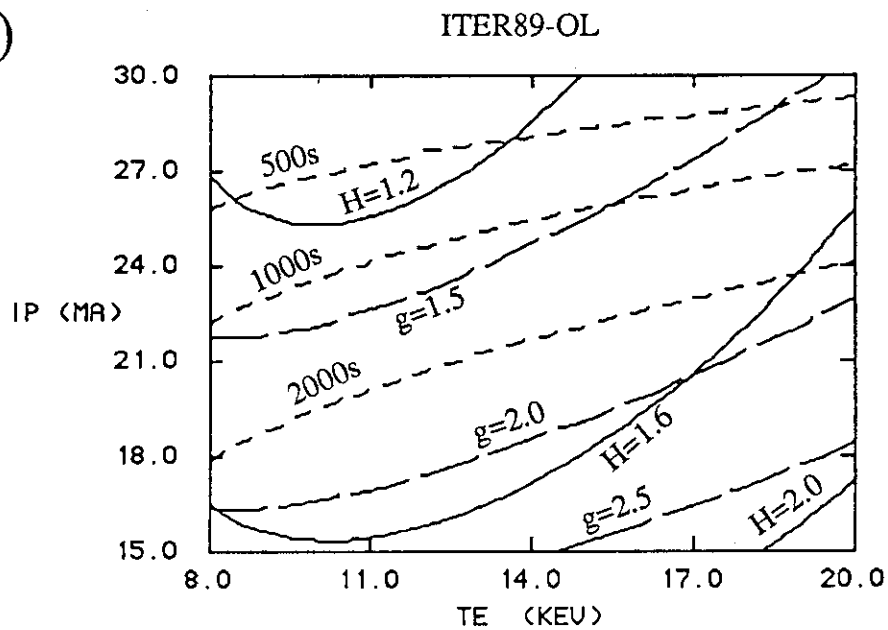
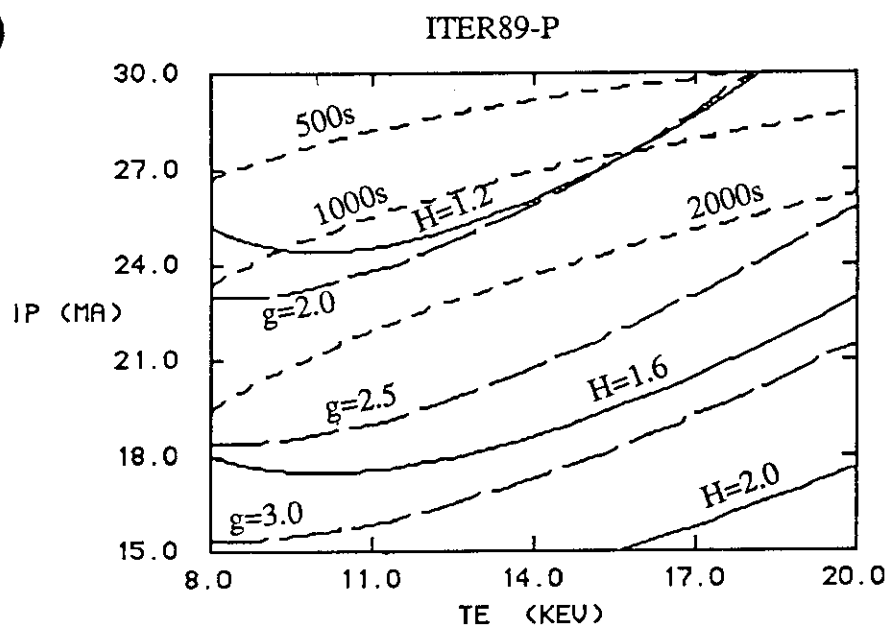


Fig. 2.38 Operation region for the ignition plasma in T_e - I_P space when $P_{fus}=1.5$ GW and He=0%.

a) H-factor is evaluated by ITER89 power scaling law,

b) H-factor is evaluated by ITER89 offset-linear scaling law.

a)



b)

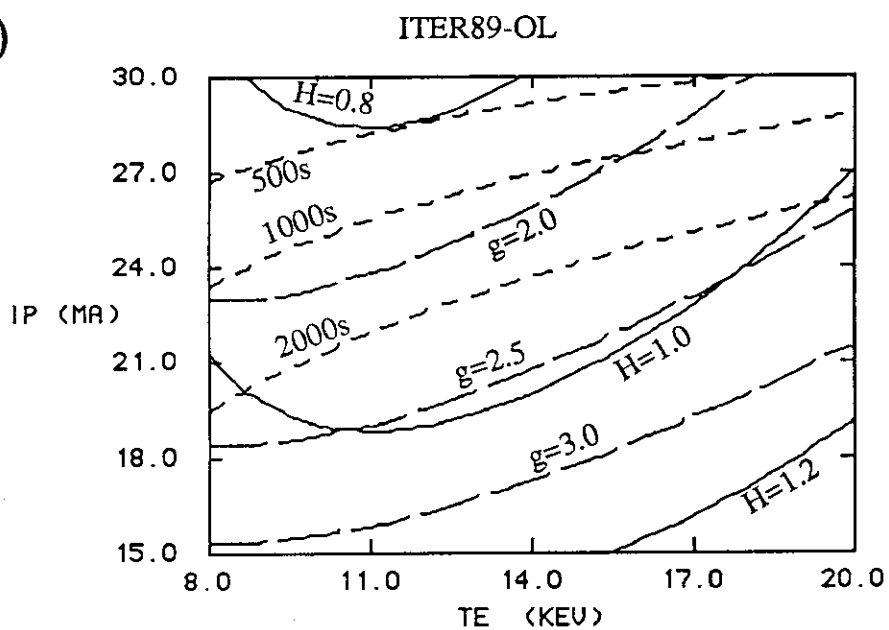
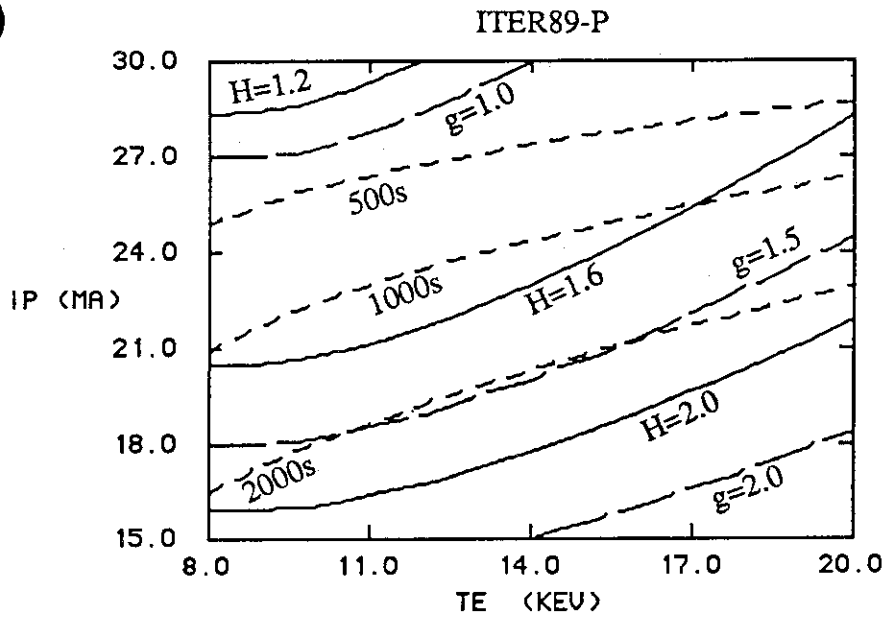


Fig. 2.39 Operation region for the ignition plasma in T_e - I_P space when $P_{FUS}=3$ GW and He=0%.

a) H-factor is evaluated by ITER89 power scaling law,

b) H-factor is evaluated by ITER89 offset-linear scaling law.

a)



b)

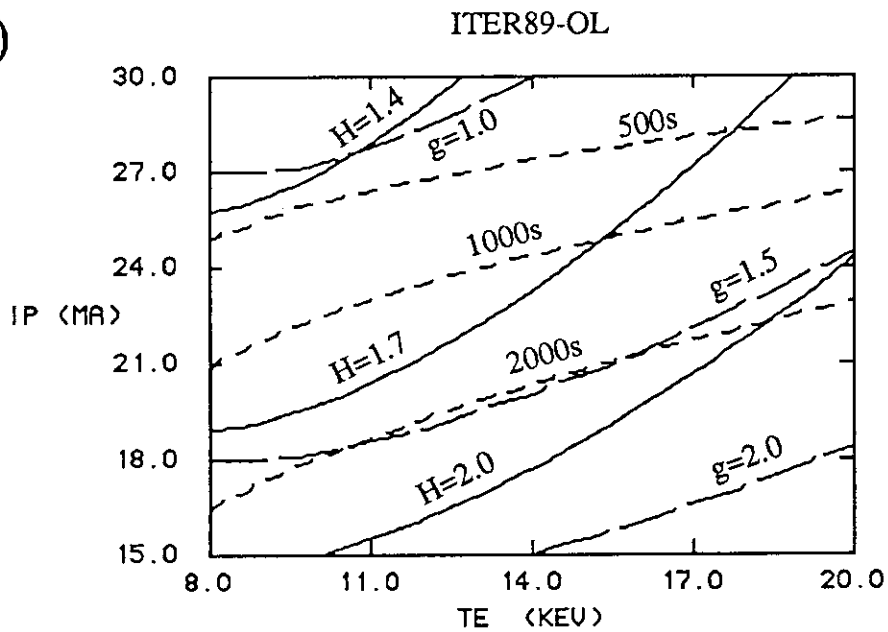
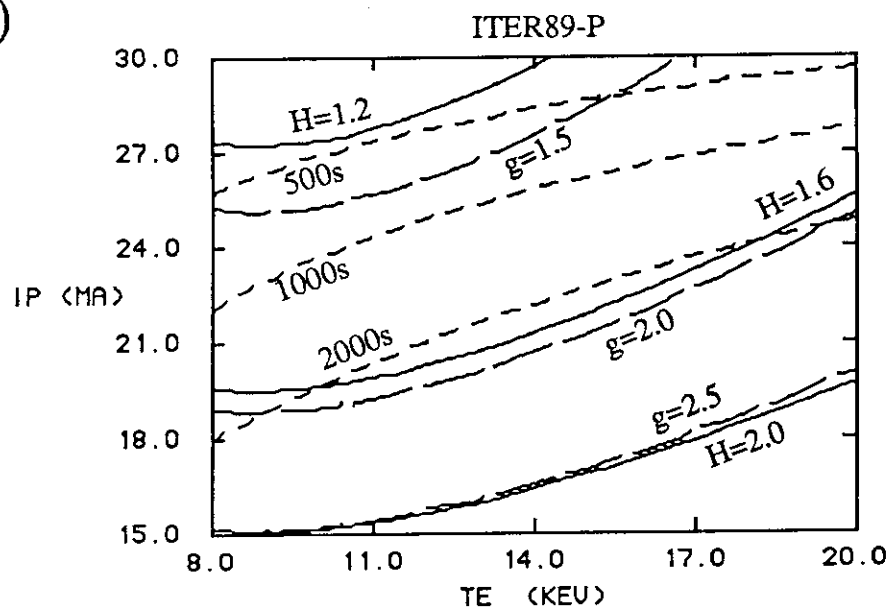


Fig. 2.40 Operation region for the ignition plasma in T_e - I_P space when $P_{FUS}=0.75$ GW and He=10%. Here, τ_E is evaluated by W_F/P_α .
 a) H-factor is evaluated by ITER89 power scaling law,
 b) H-factor is evaluated by ITER89 offset-linear scaling law.

a)



b)

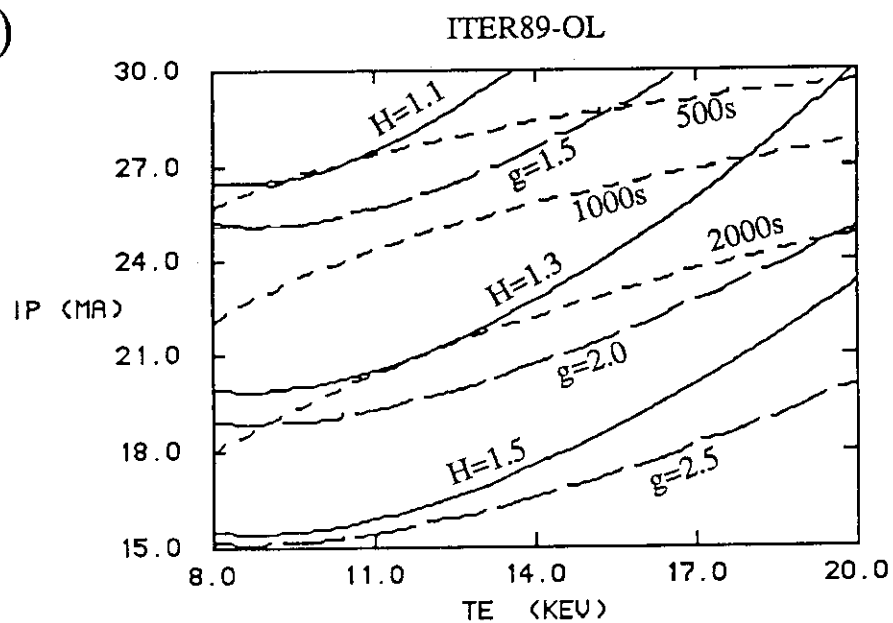


Fig. 2.41 Operation region for the ignition plasma in T_e - I_p space when $P_{FUS}=1.5$ GW and He=10%. Here, τ_E is evaluated by W_p/P_α .
 a) H-factor is evaluated by ITER89 power scaling law,
 b) H-factor is evaluated by ITER89 offset-linear scaling law.

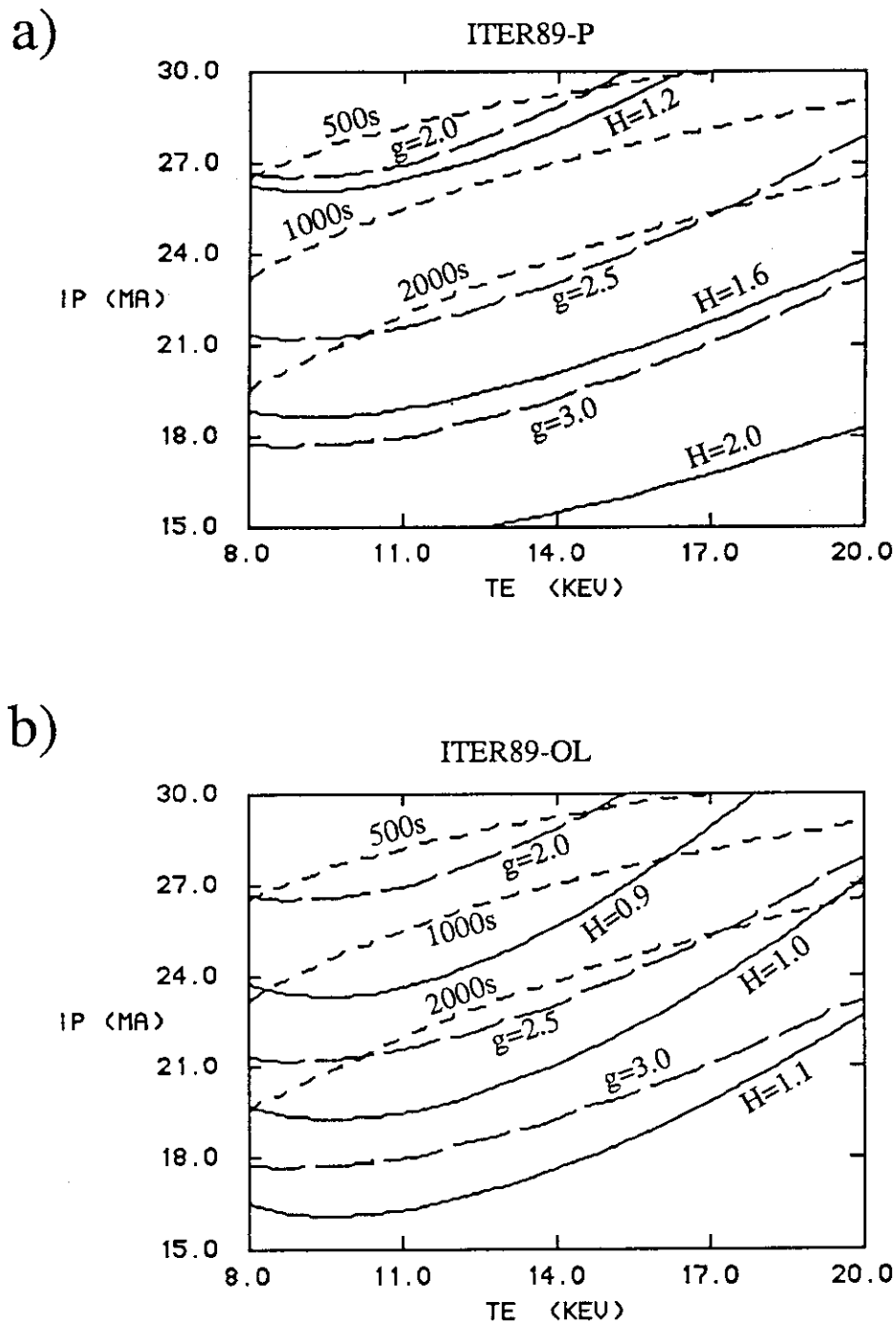
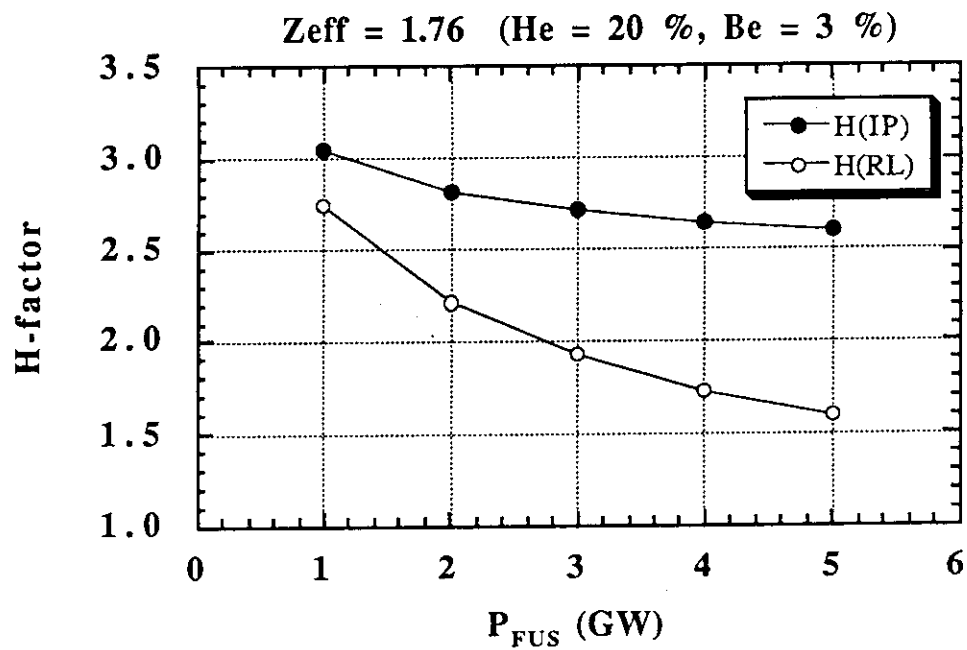


Fig.2.42 Operation region for the ignition plasma in T_e - I_P space when $P_{FUS}=3$ GW and He=10%. Here, τ_E is evaluated by W_P/P_α .
 a) H-factor is evaluated by ITER89 power scaling law,
 b) H-factor is evaluated by ITER89 offset-linear scaling law.

a)



b)

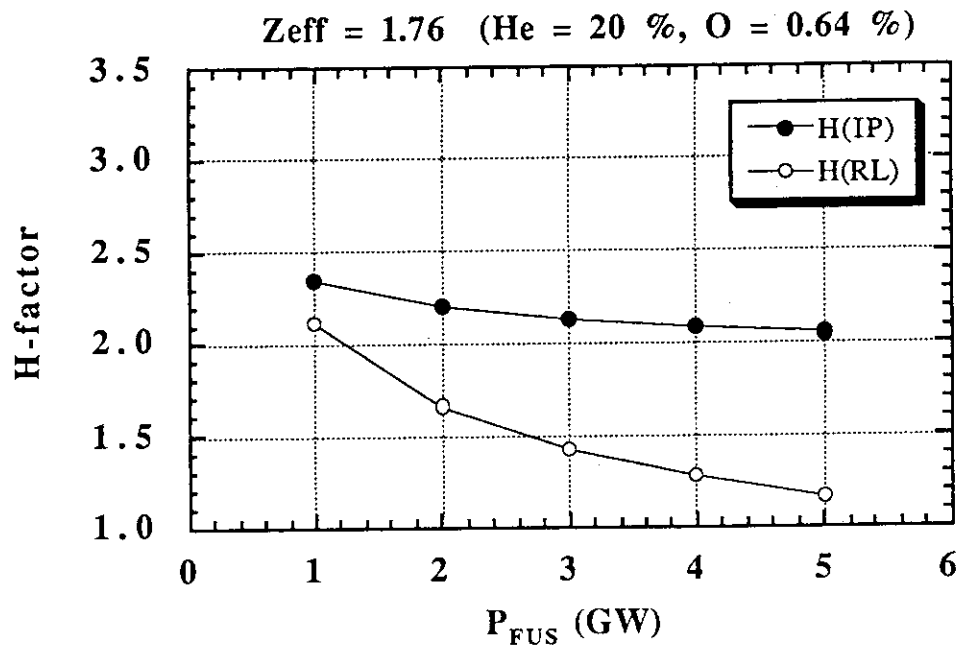
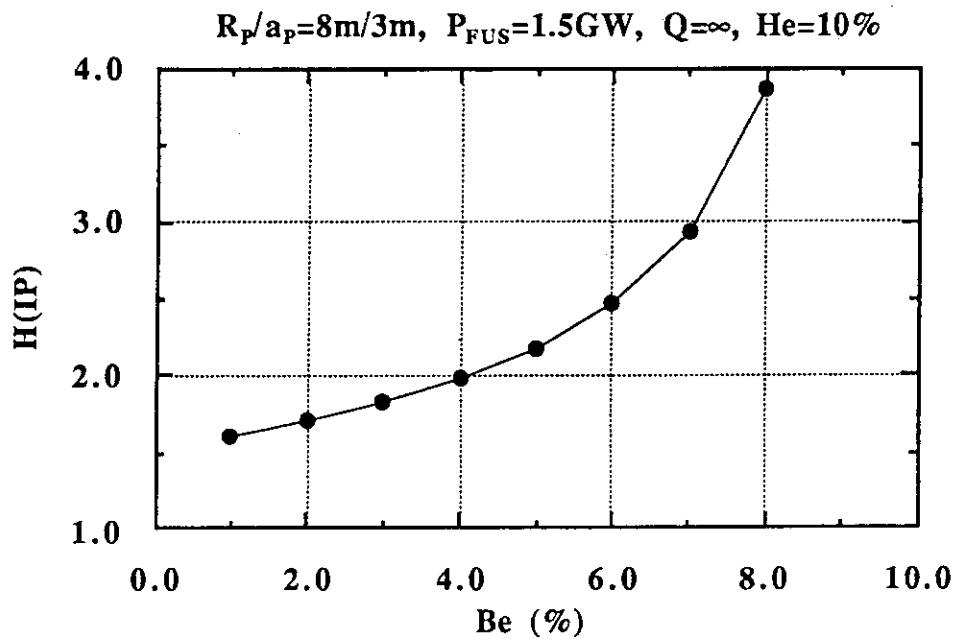


Fig.2.43 Required H-factor for the ignition operation as a function of P_{FUS} when $I_{\text{P}}=25$ MA, $T_{\text{e}}=10$ keV and $Z_{\text{eff}}=1.76$.
 a) He=20% and Be=3%, b) He=20% and O=0.64%.

a)



b)

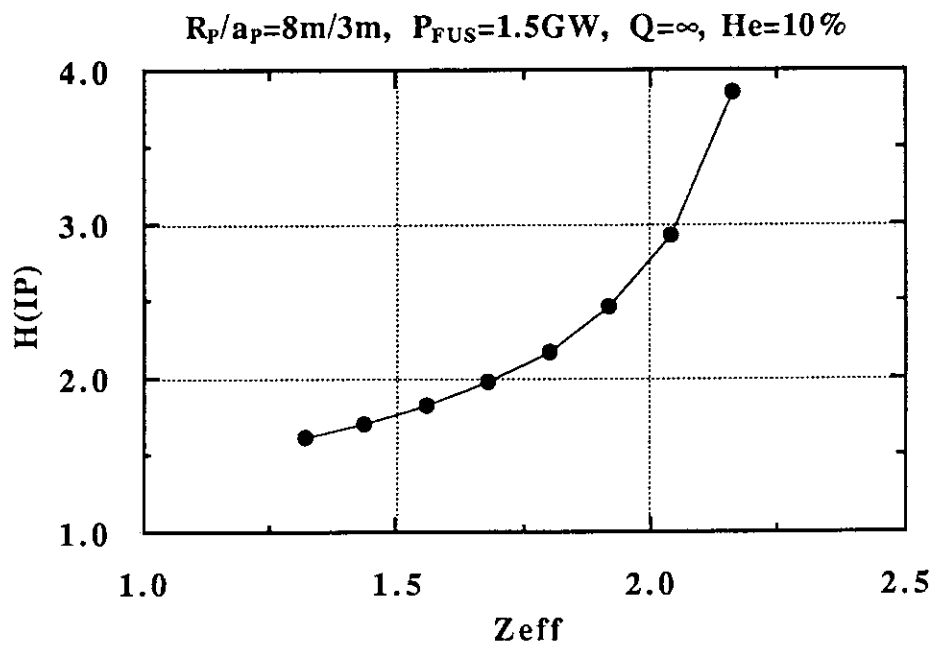
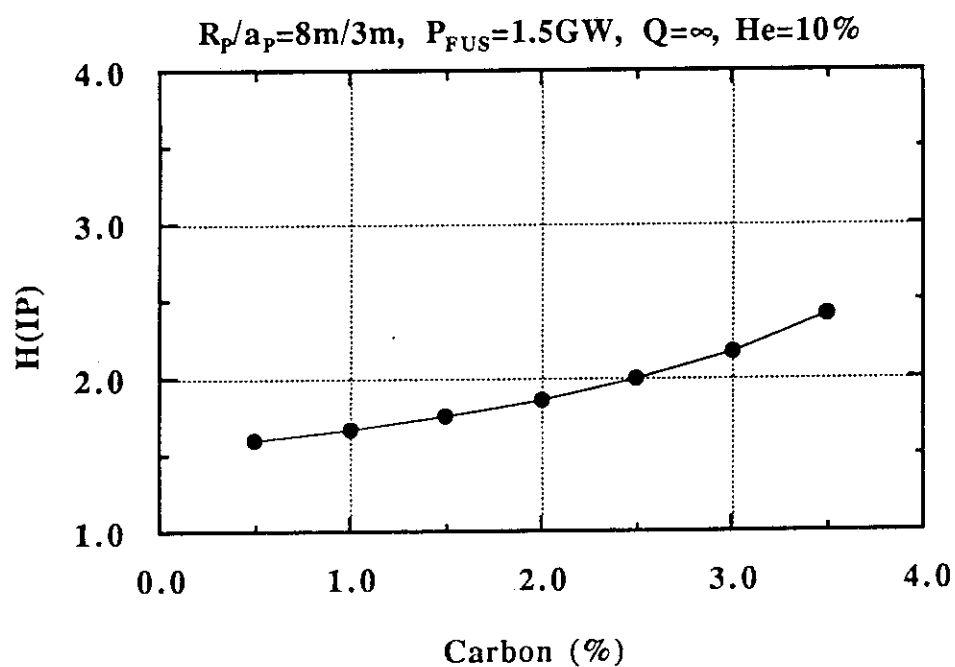


Fig.2.44 Required H-factor for the ignition plasma as a function of beryllium fraction when $P_{FUS}=1.5$ GW and He=10%. Here, H-factor is evaluated by ITER89 power scaling law. Lower graph is the same case as upper one in which abscissa is rewritten by Z_{eff} .

a)



b)

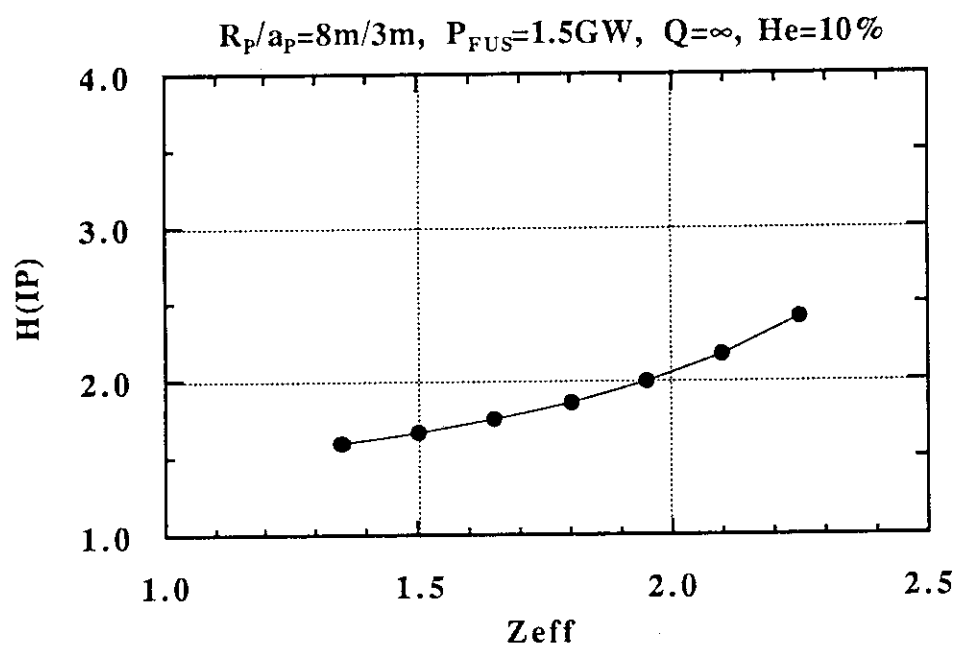
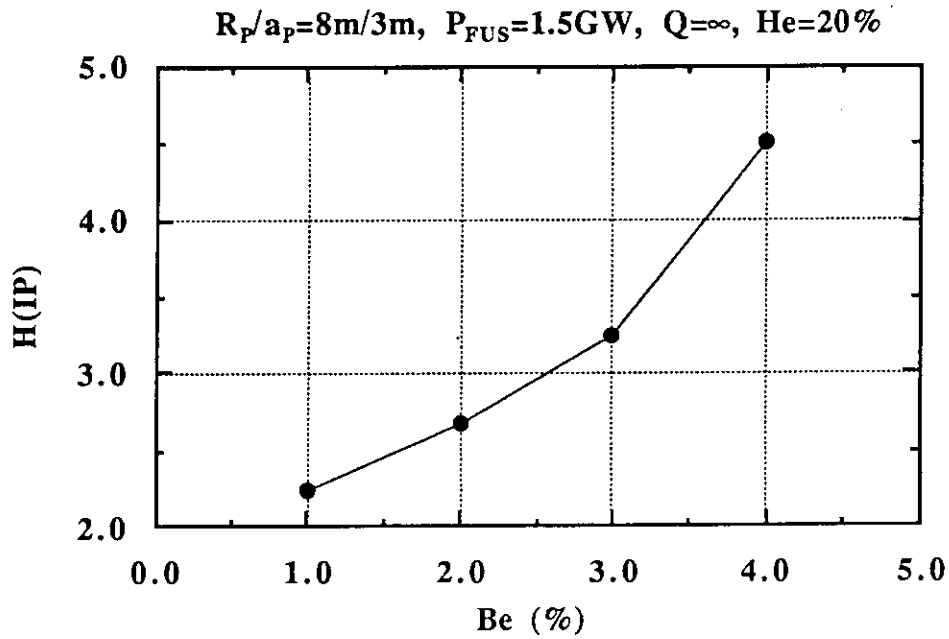


Fig.2.45 Required H-factor for the ignition plasma as a function of carbon fraction when $P_{FUS}=1.5$ GW and He=10%. Here, H-factor is evaluated by ITER89 power scaling law. Lower graph is the same case as upper one in which abscissa is rewritten by Z_{eff} .

a)



b)

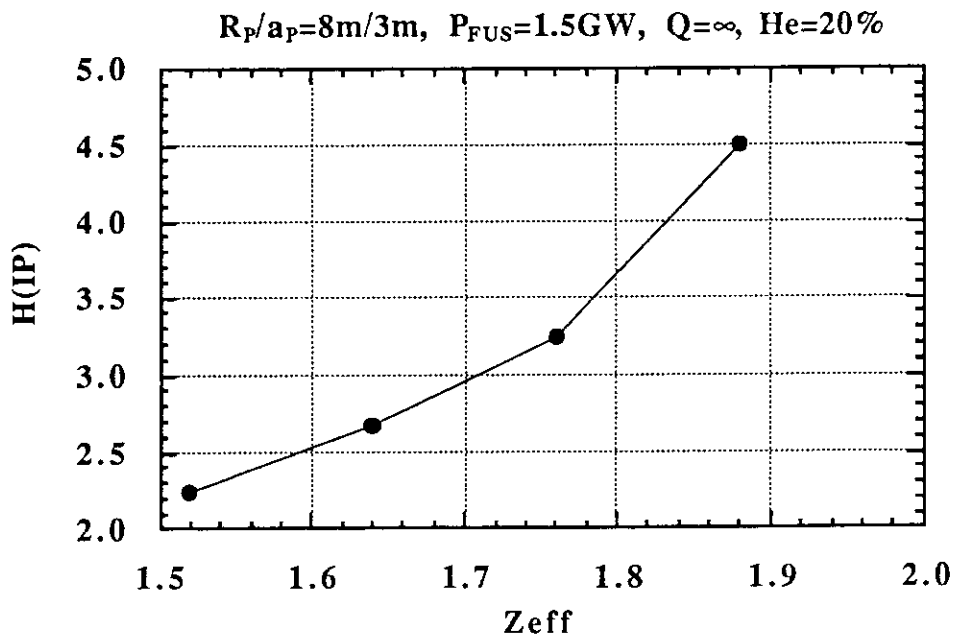
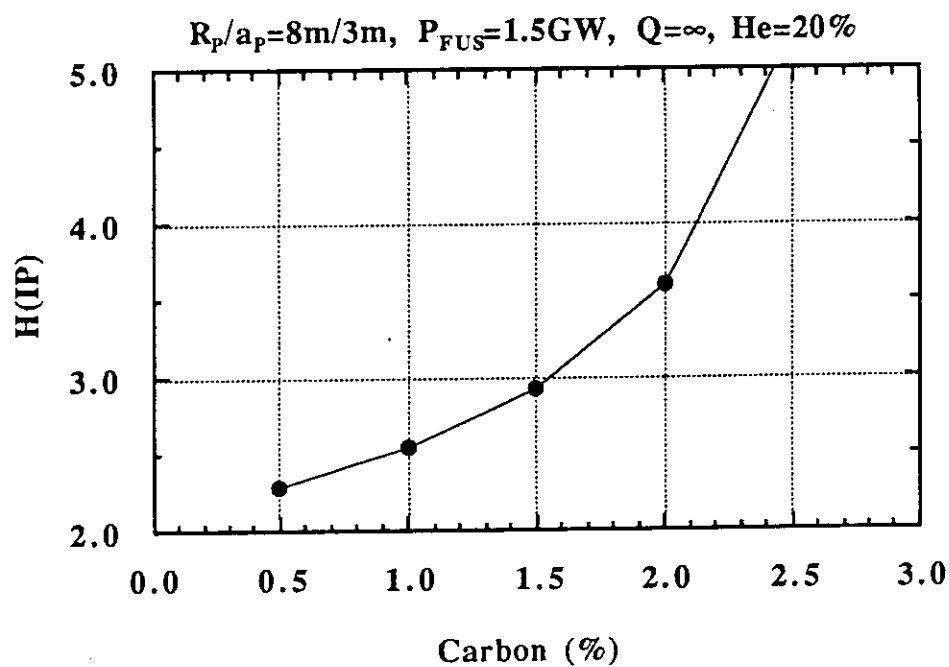


Fig.2.46 Required H-factor for the ignition plasma as a function of beryllium fraction when $P_{FUS}=1.5$ GW and He=20%. Here, H-factor is evaluated by ITER89 power scaling law. Lower graph is the same case as upper one in which abscissa is rewritten by Z_{eff} .

a)



b)

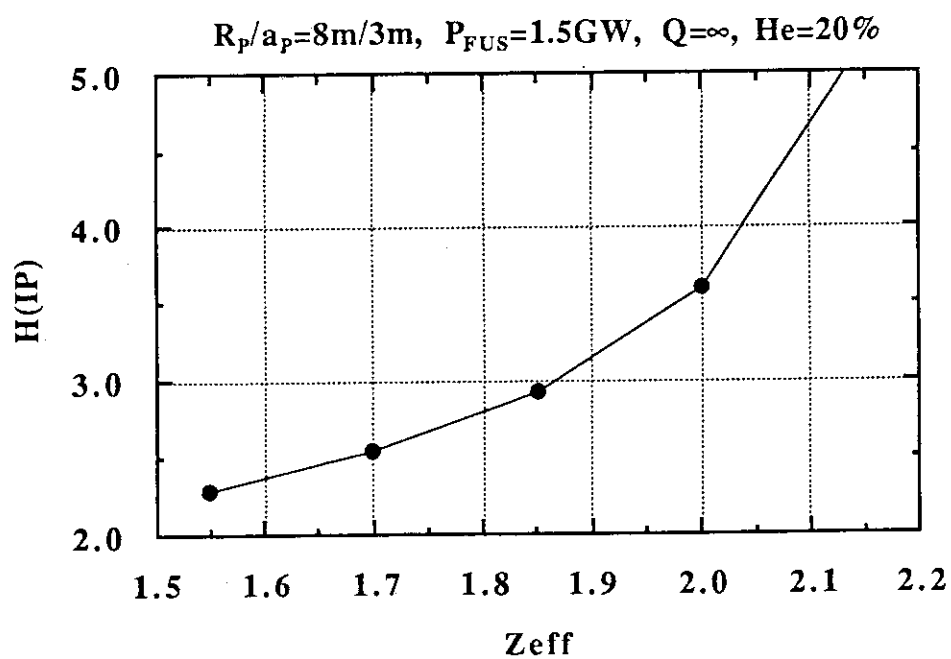
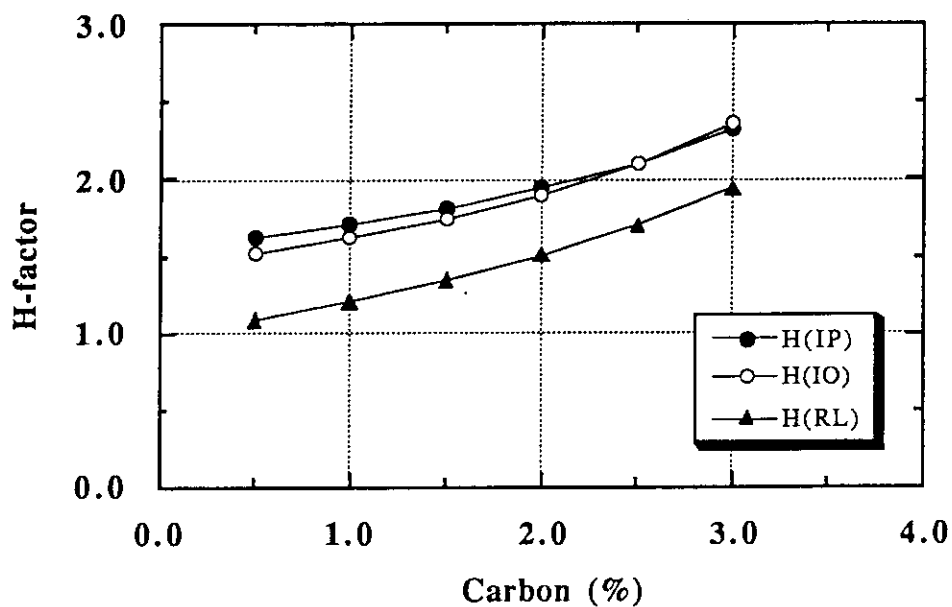


Fig.2.47 Required H-factor for the ignition plasma as a function of carbon fraction when $P_{FUS}=1.5$ GW and $He=20\%$. Here, H-factor is evaluated by ITER89 power scaling law. Lower graph is the same case as upper one in which abscissa is rewritten by Z_{eff} .

a)



b)

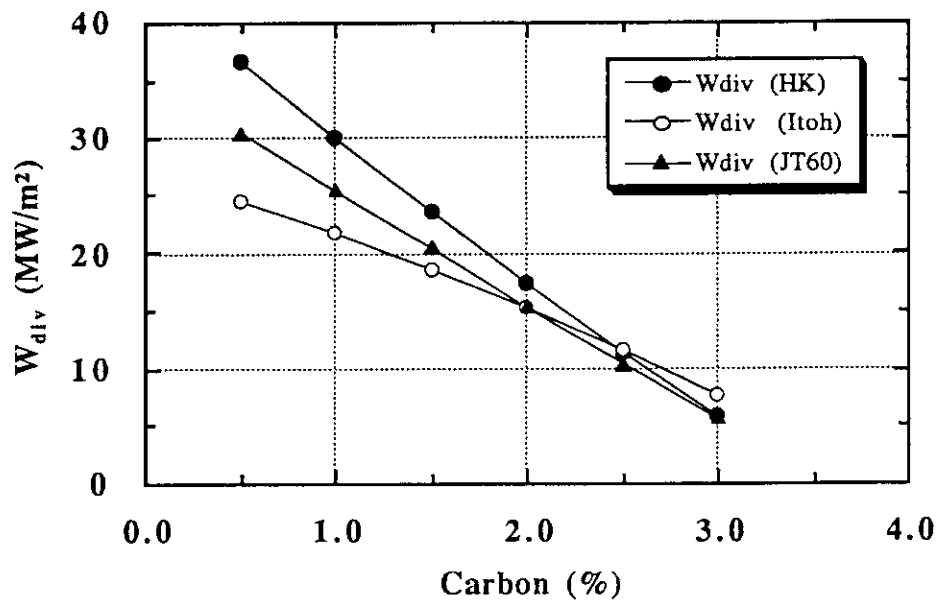


Fig.2.48 a) H-factors for the ignition plasma as a function of carbon fraction when $I_P=25$ MW, $P_{FUS}=1.5$ GW and He=10%.
 b) Divertor heat load calculated by 0-D scaling models. HK, Itoh and JT60 denote Constant- χ model, Bohm-type χ model and JT-60U empirical scaling model, respectively. The angle of the divertor plate to the separatrix field line in the poloidal cross section is assumed to be 90° .

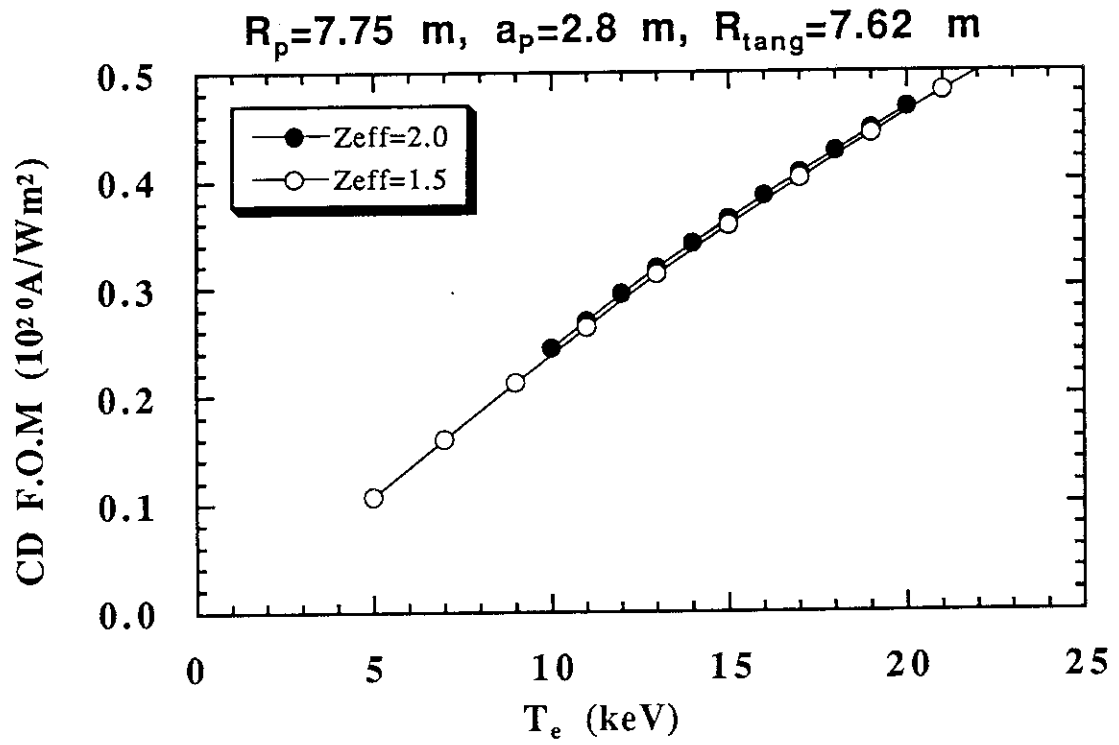


Fig.3.1 Current drive figure of merit (FOM) as a function of the electron temperature.

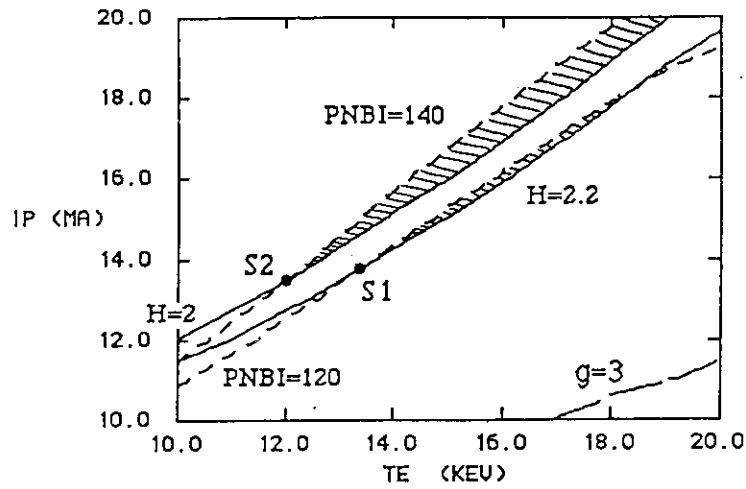
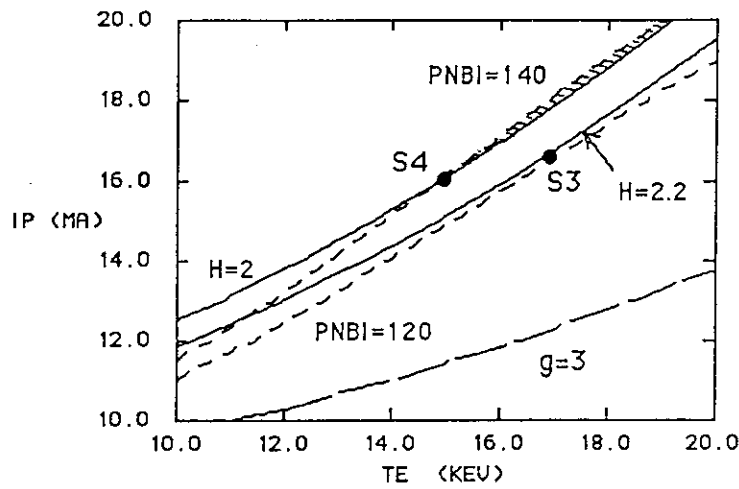
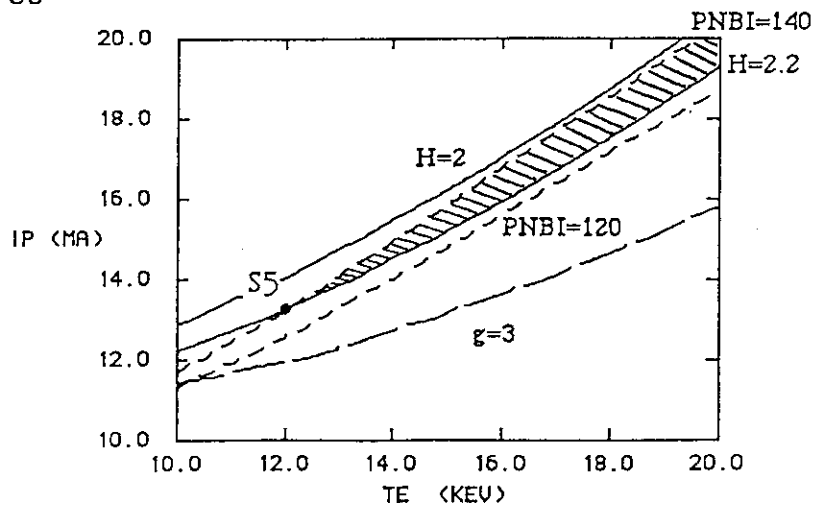
a) $P_{FUS}=500$ MWb) $P_{FUS}=750$ MWc) $P_{FUS}=1000$ MW

Fig. 3.2 Operation region in T_e - I_p space for steady-state plasma of EDA-ITER for various fusion power P_{FUS} . Here, H -factor is evaluated by ITER89 power scaling law.

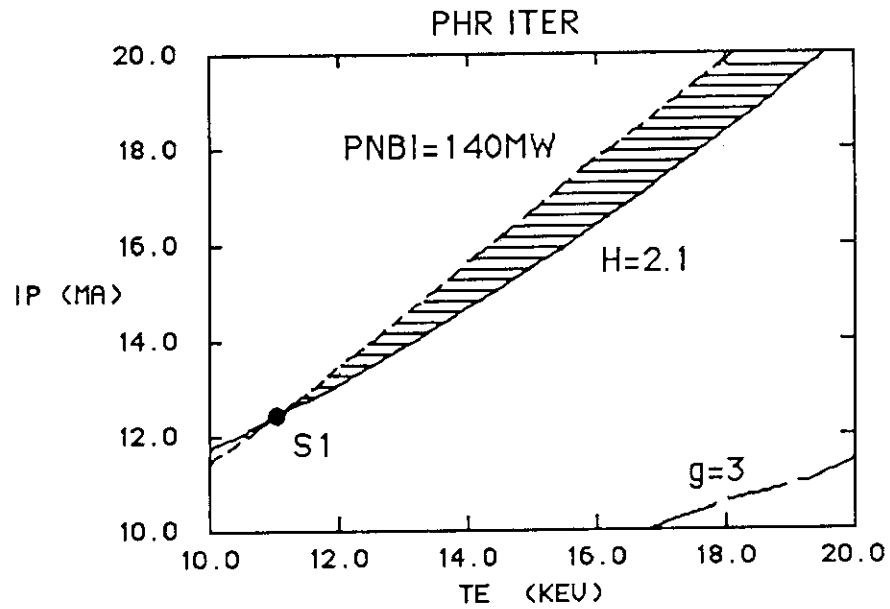
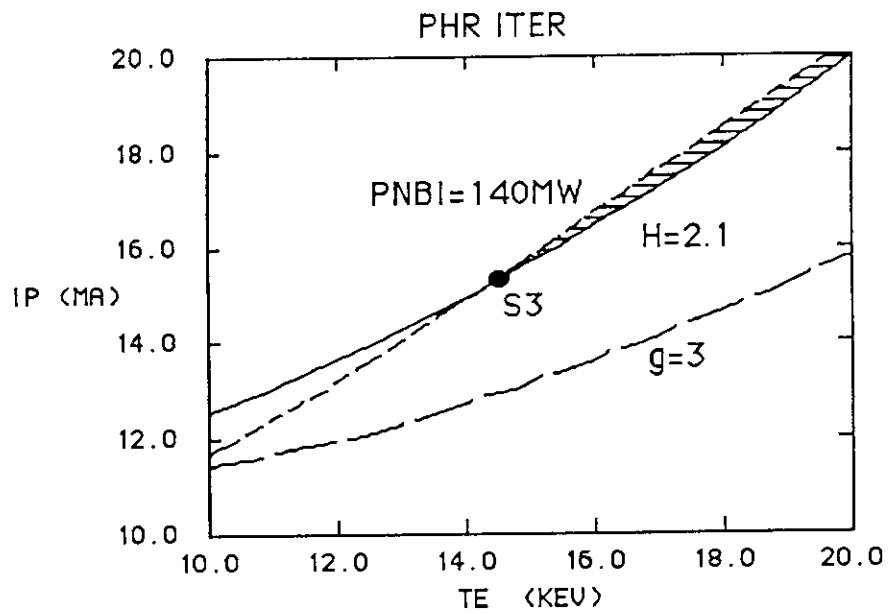
a) $P_{FUS}=500$ MWb) $P_{FUS}=1000$ MW

Fig. 3.3 Operation region in T_e - I_p space for steady-state plasma of EDA-ITER when a) $P_{FUS}=500$ MW and b) $P_{FUS}=1000$ MW.

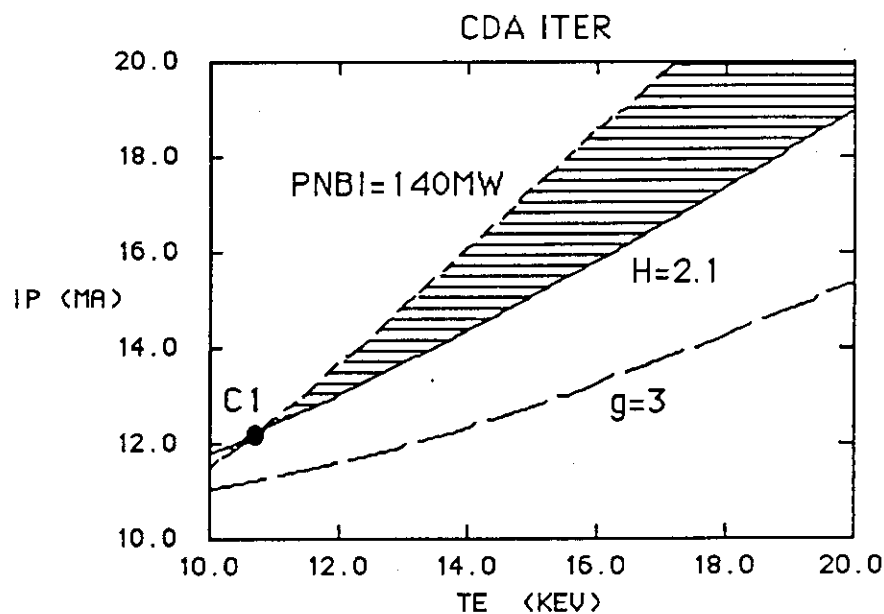
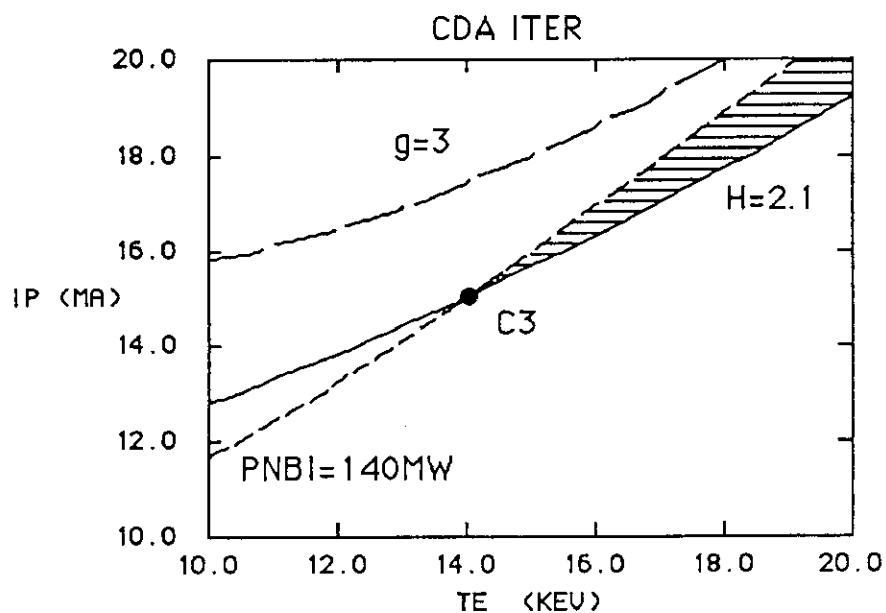
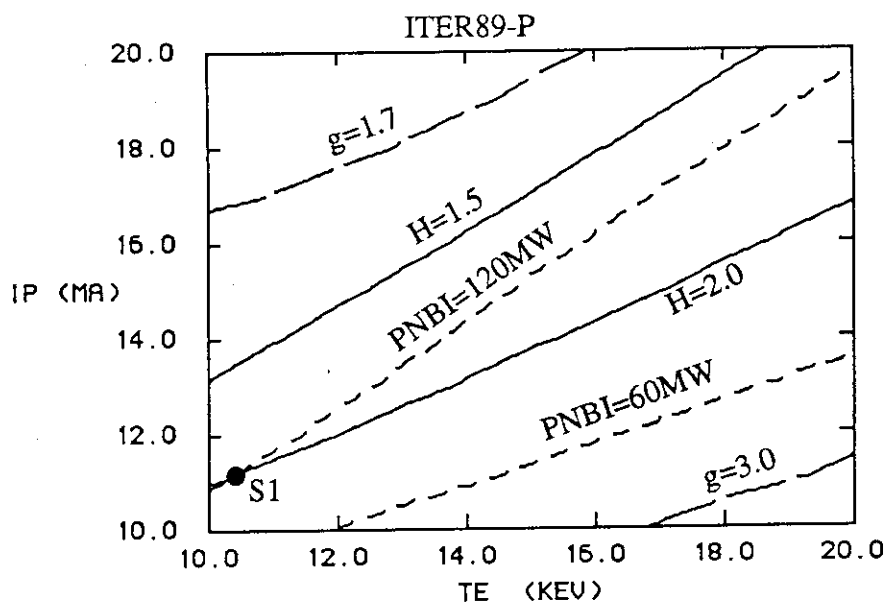
a) $P_{FUS}=500$ MWb) $P_{FUS}=1000$ MW

Fig. 3.4 Operation region in T_e - I_p space for steady-state plasma of CDA-ITER when a) $P_{FUS}=500$ MW and b) $P_{FUS}=1000$ MW.

a)



b)

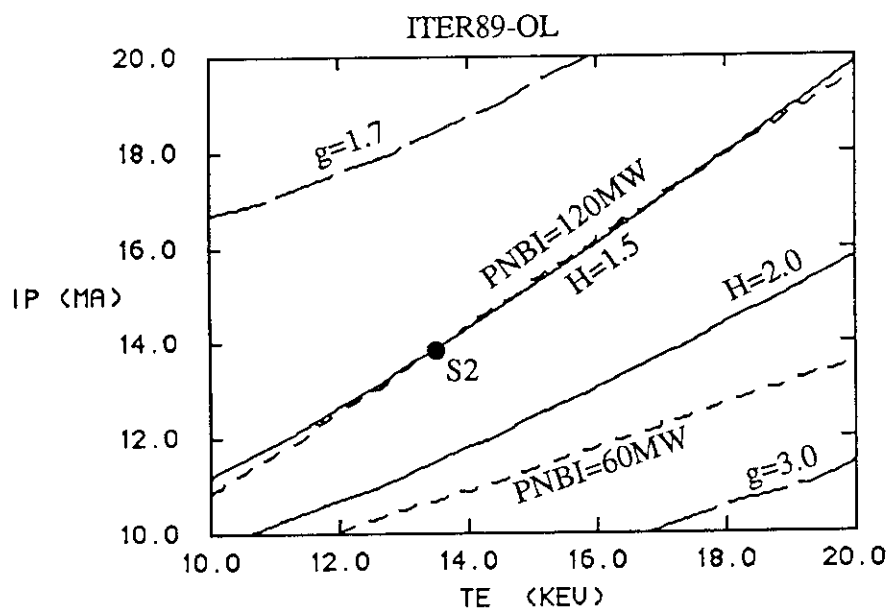
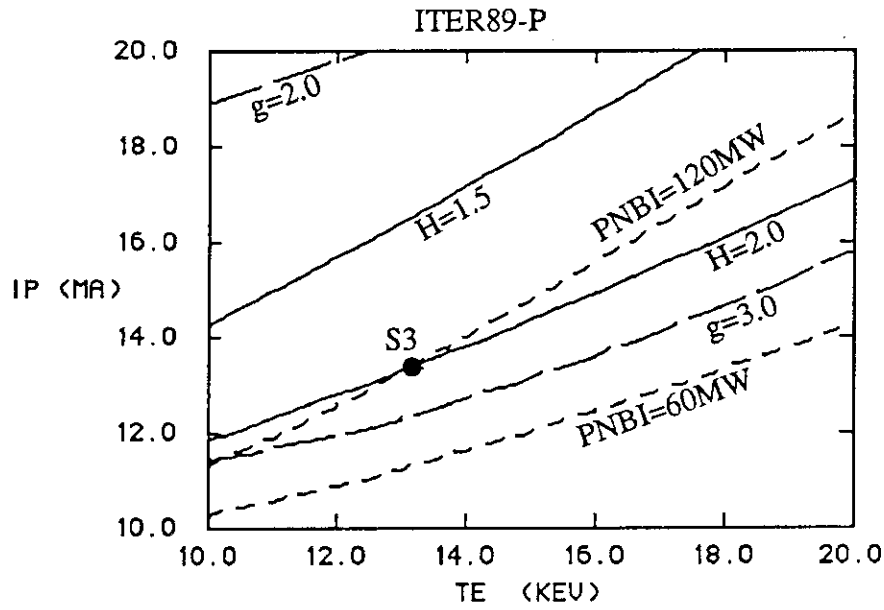


Fig.3.5 Operation region in T_e - I_p space for steady-state plasma of EDA-ITER when $P_{FUS}=500$ MW. Here, H-factor is evaluated by τ_E^* for a) ITER89 power scaling and b) ITER89 offset-linear scaling laws, respectively.

a)



b)

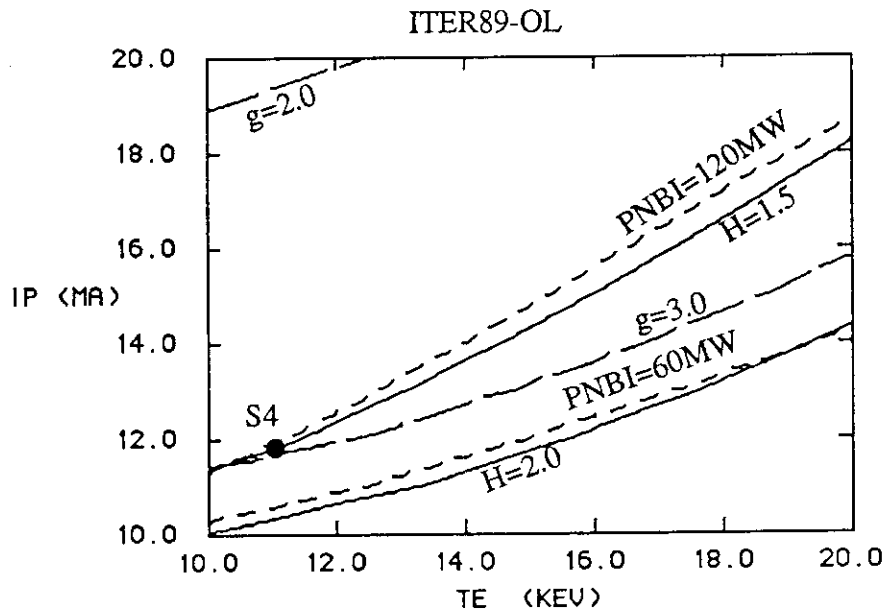
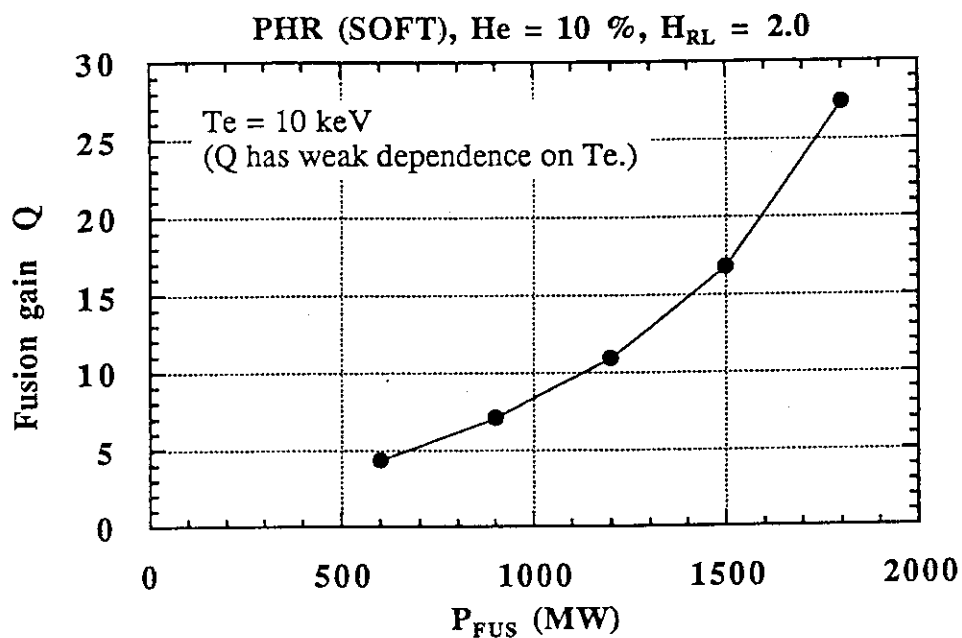


Fig. 3.6 Operation region in T_e - I_p space for steady-state plasma of EDA-ITER when $P_{FUS}=1000$ MW. Here, H-factor is evaluated by τ_E^* for a) ITER89 power scaling and b) ITER89 offset-linear scaling laws, respectively.

a)



b)

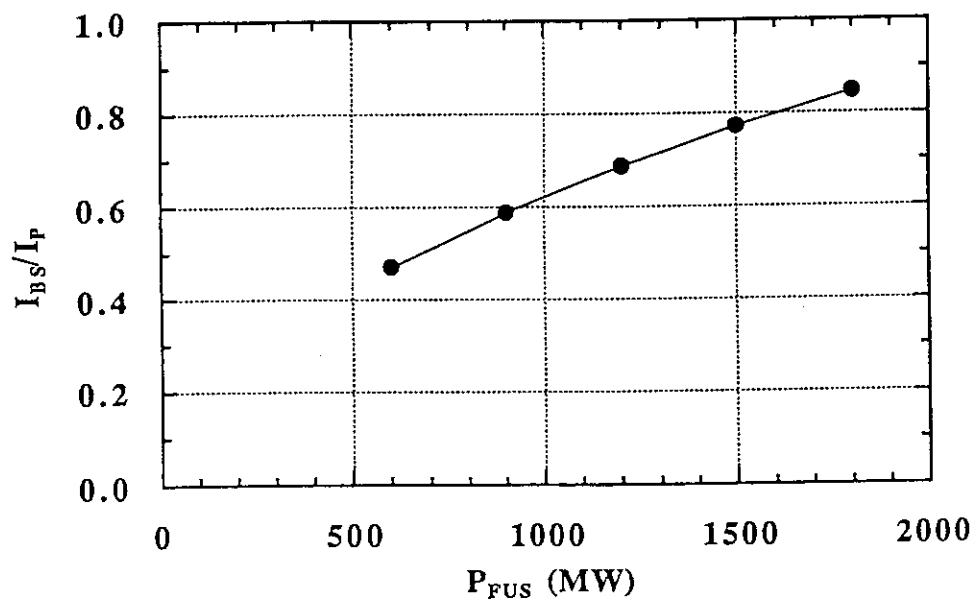
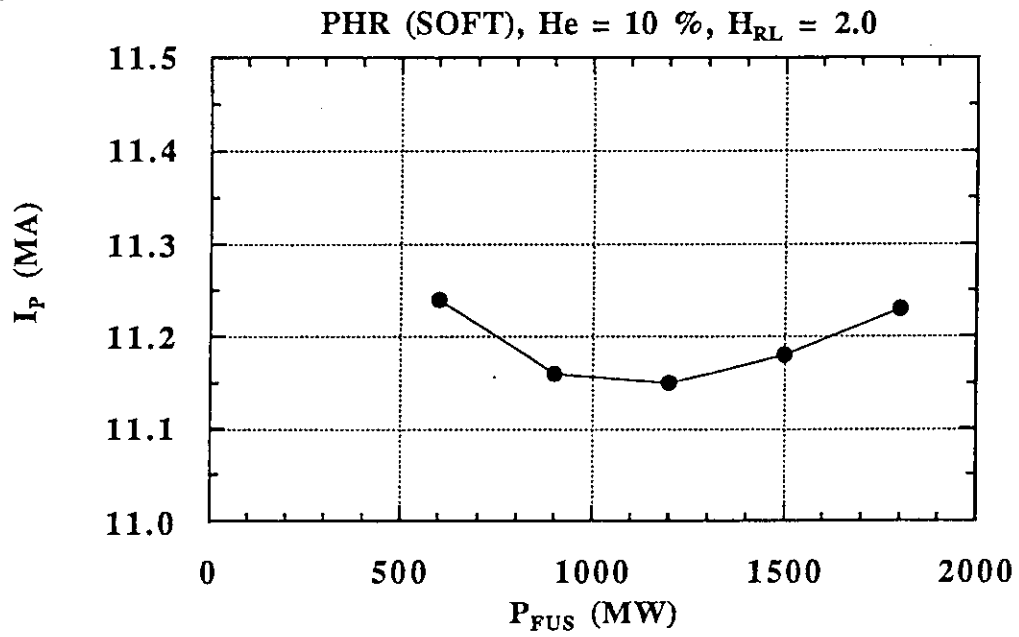


Fig. 3.7 Steady-state operation of EDA-ITER when $T_e=10$ keV, He=10% and $H_{RL}=2.0$.

- a) Achievable fusion gain Q as a function of P_{FUS} .
- b) Bootstrap current fraction I_{BS}/I_P as a function of P_{FUS} .
- c) Plasma current I_P as a function of P_{FUS} .
- d) Electron density n_e and Troyon coefficient g .

c)



d)

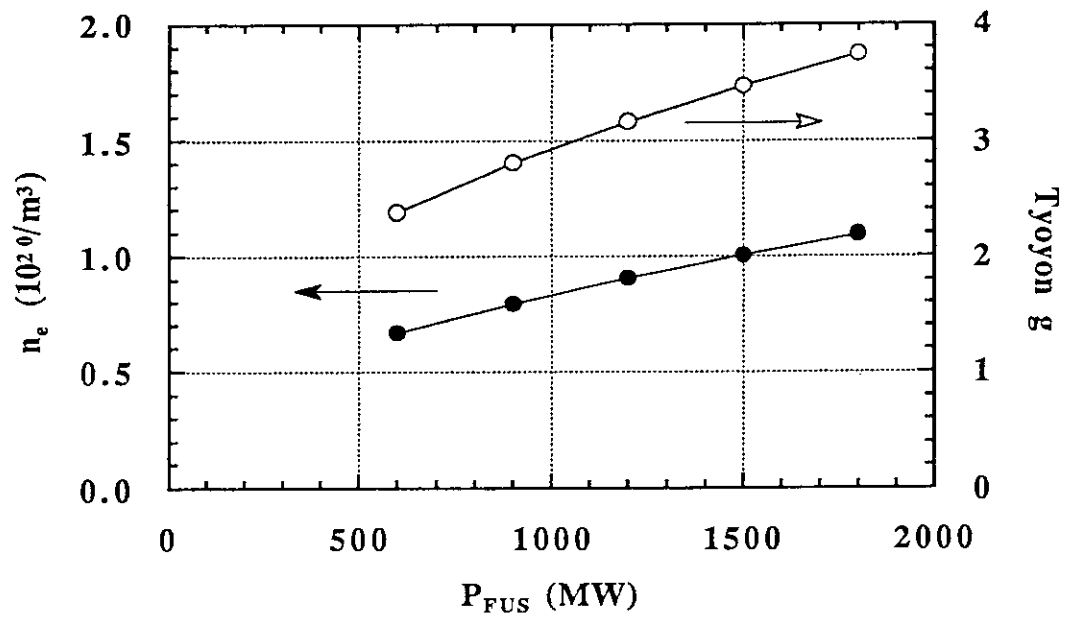
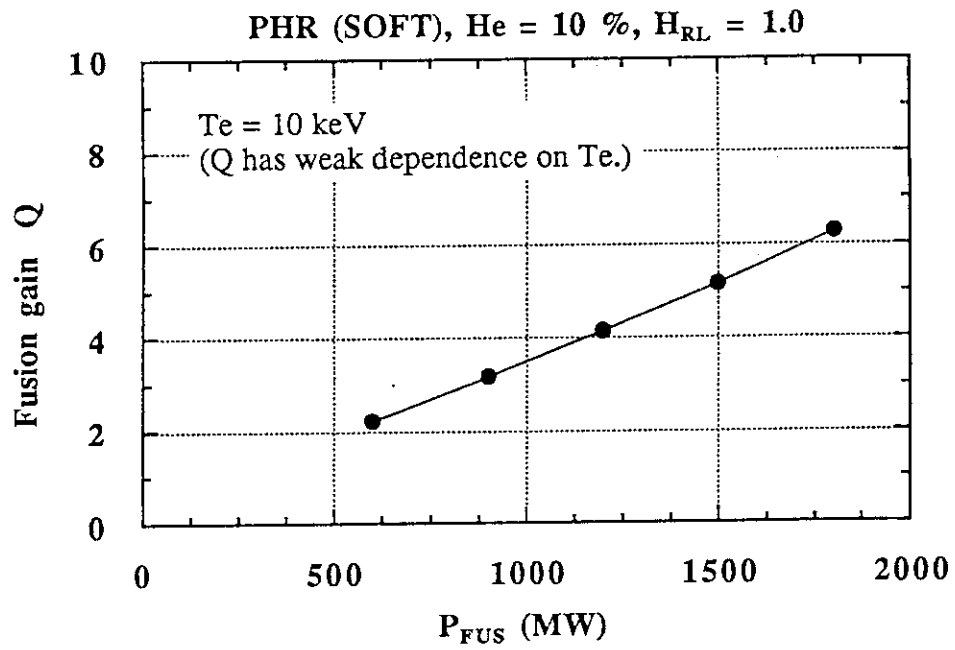


Fig. 3.7 (Continued)

a)



b)

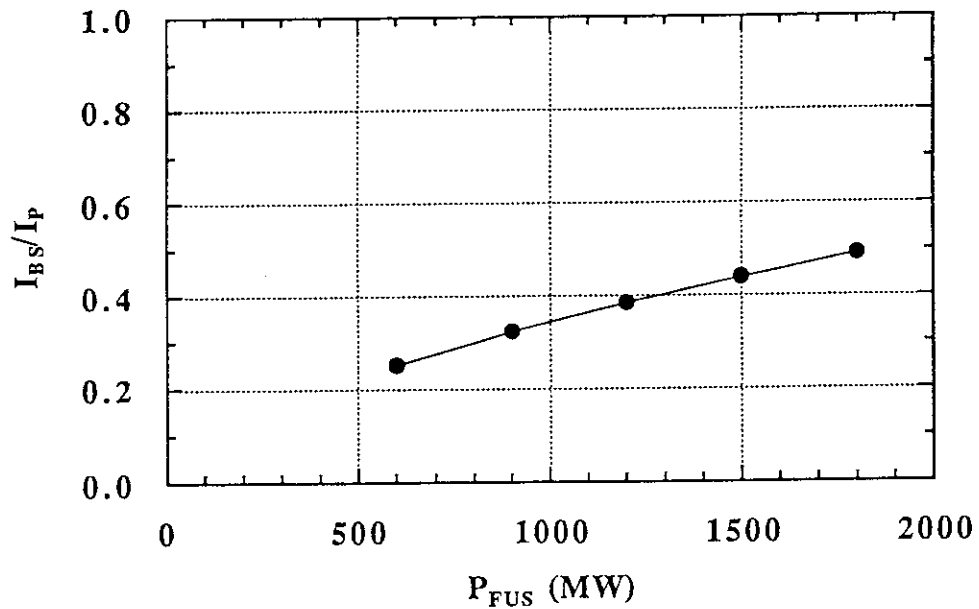
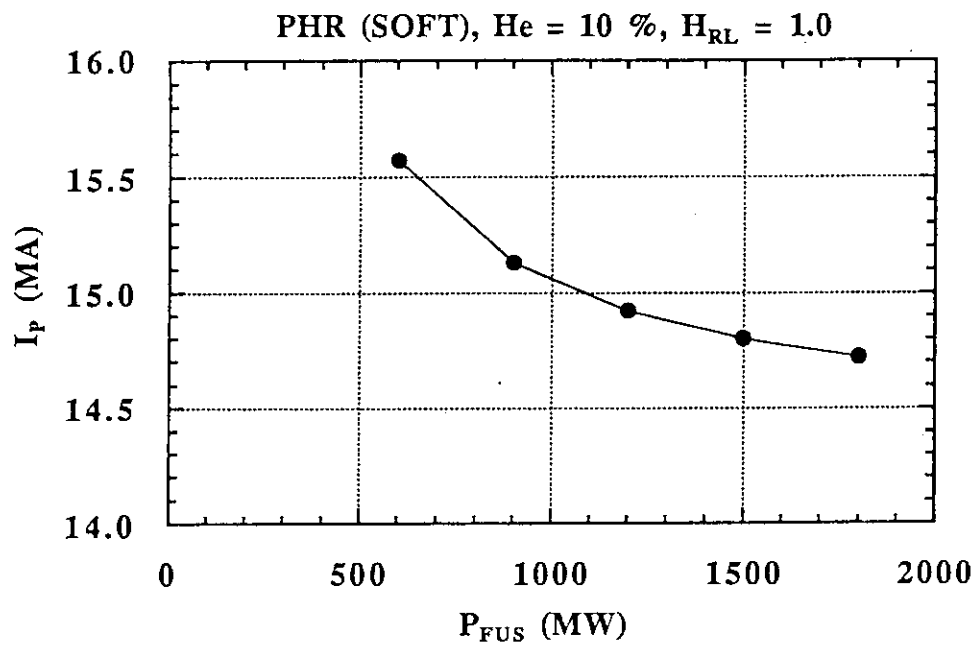


Fig. 3.8 Steady-state operation of EDA-ITER when $T_e=10$ keV, He=10% and $H_{RL}=1.0$.

- a) Achievable fusion gain Q as a function of P_{FUS} .
- b) Bootstrap current fraction I_{BS}/I_P as a function of P_{FUS} .
- c) Plasma current I_P as a function of P_{FUS} .
- d) Electron density n_e and Troyon coefficient g .

c)



d)

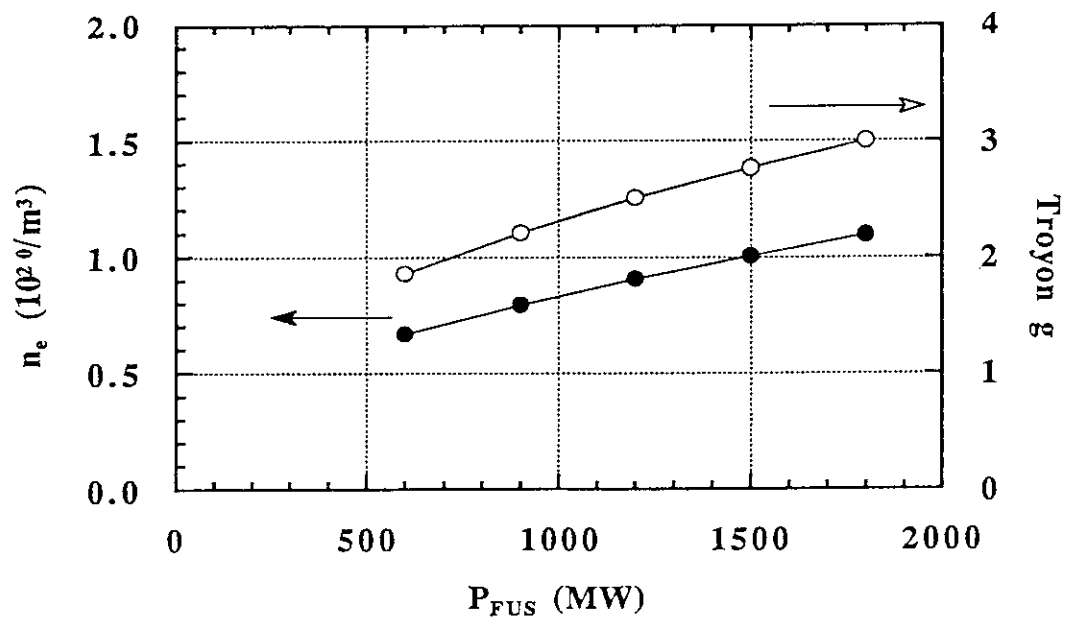
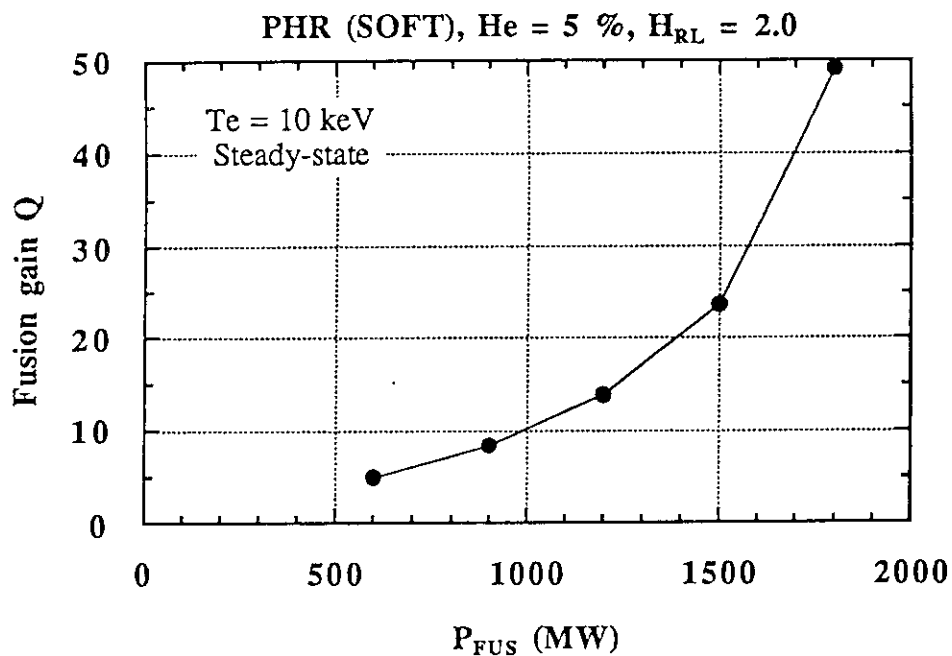


Fig.3.8 (Continued)

a)



b)

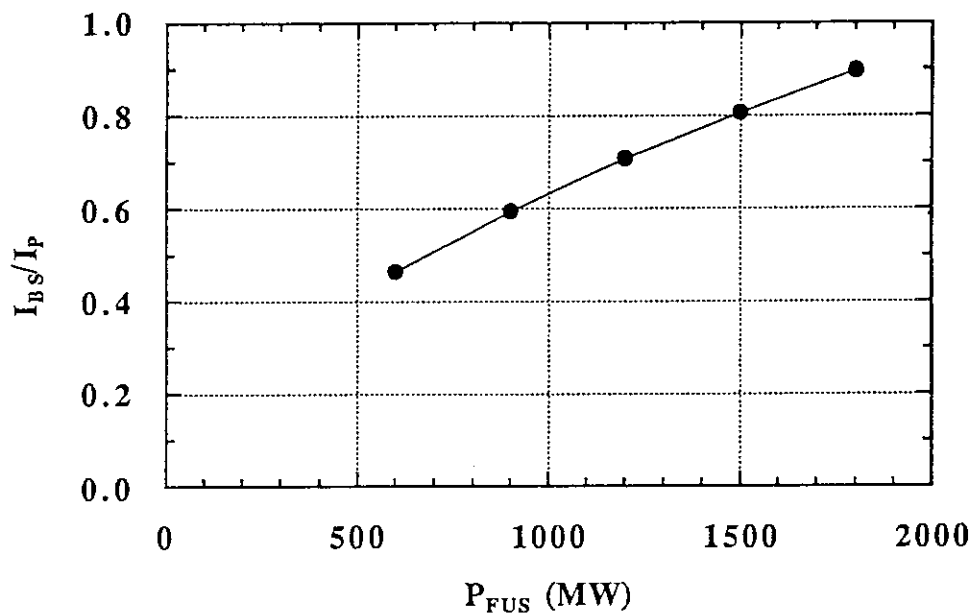
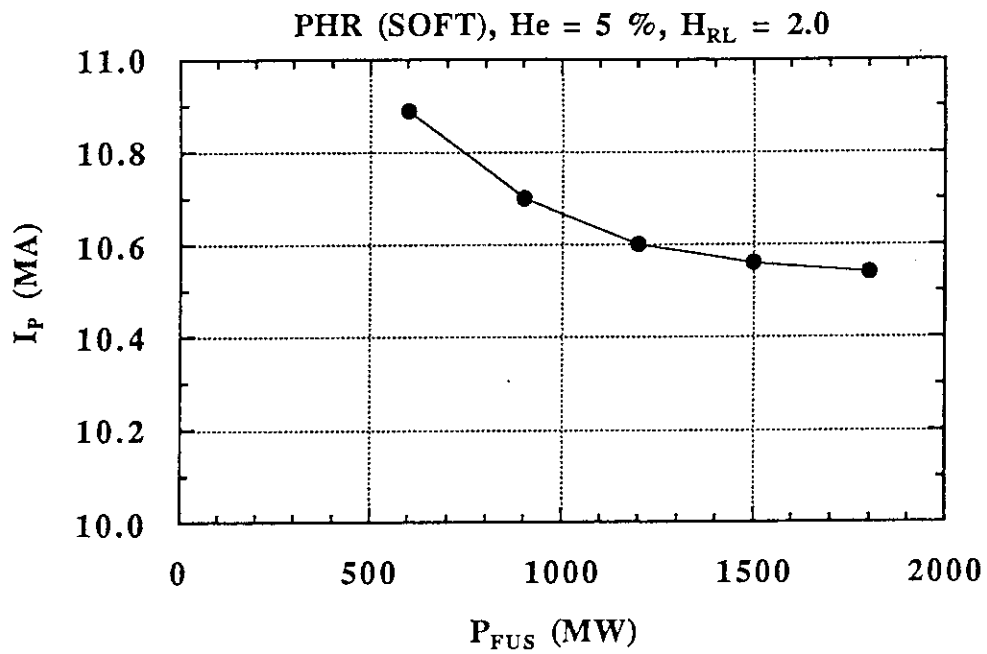


Fig. 3.9 Steady-state operation of EDA-ITER when $T_e=10$ keV, He=5% and $H_{RL}=2.0$.

- a) Achievable fusion gain Q as a function of P_{FUS} .
- b) Bootstrap current fraction I_{BS}/I_P as a function of P_{FUS} .
- c) Plasma current I_P as a function of P_{FUS} .
- d) Electron density n_e and Troyon coefficient g .

c)



d)

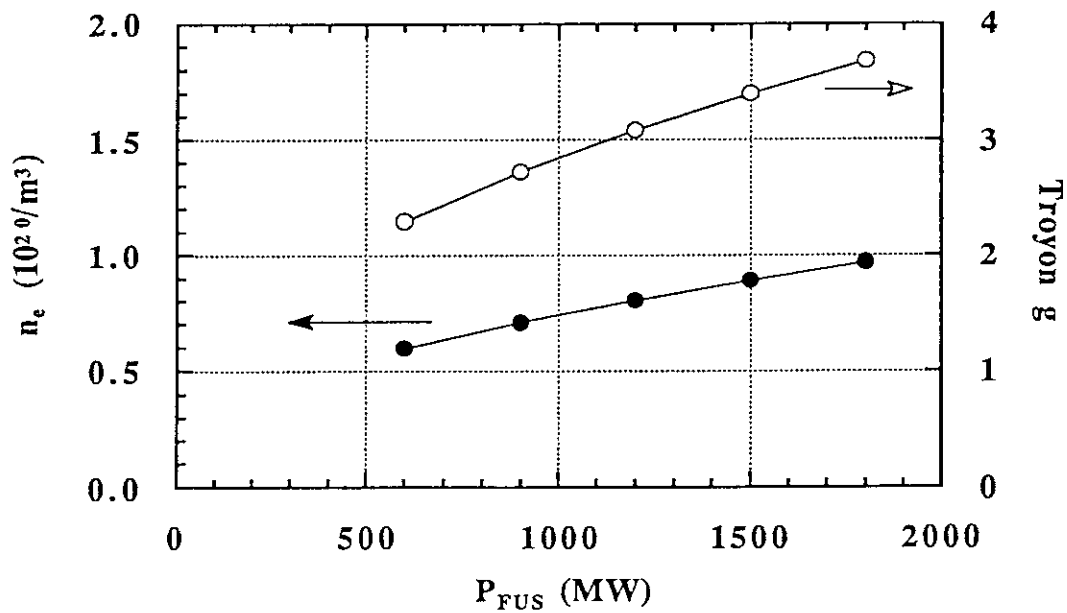
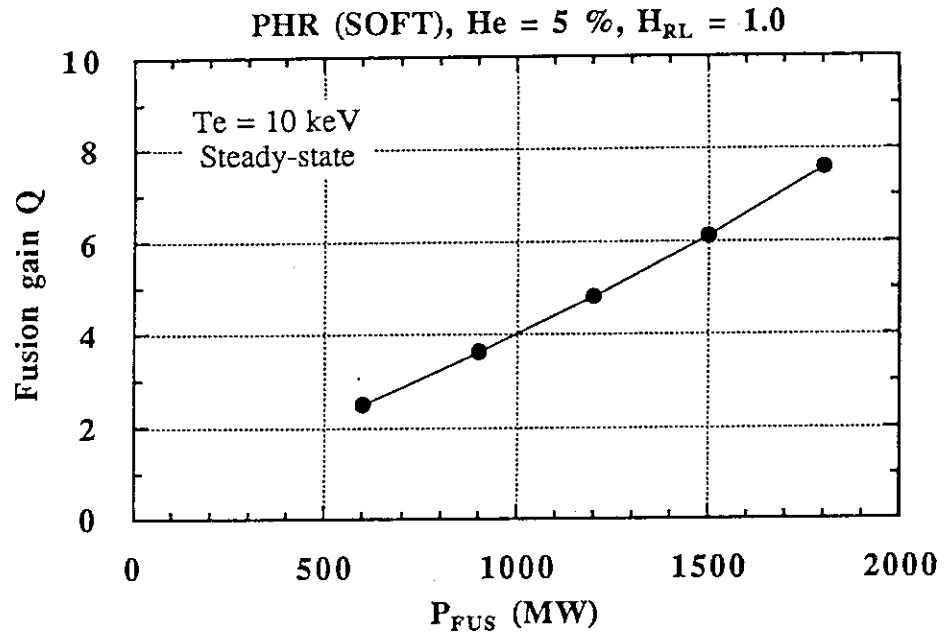


Fig. 3.9 (Continued)

a)



b)

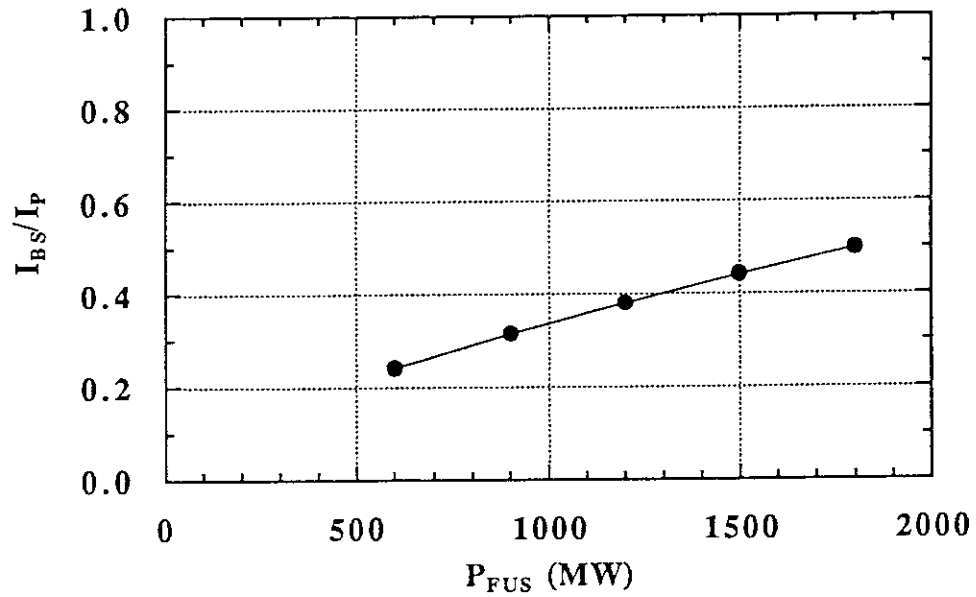


Fig. 3.10 Steady-state operation of EDA-ITER when $T_e=10$ keV, He=5% and $H_{RL}=1.0$.

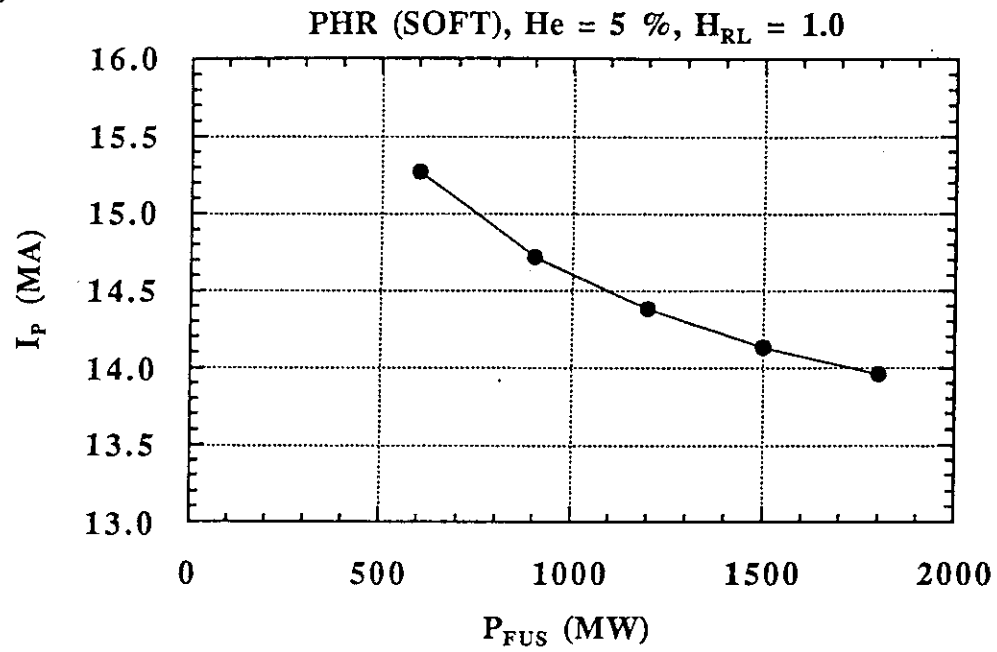
a) Achievable fusion gain Q as a function of P_{FUS} .

b) Bootstrap current fraction I_{BS}/I_P as a function of P_{FUS} .

c) Plasma current I_P as a function of P_{FUS} .

d) Electron density n_e and Troyon coefficient g .

c)



d)

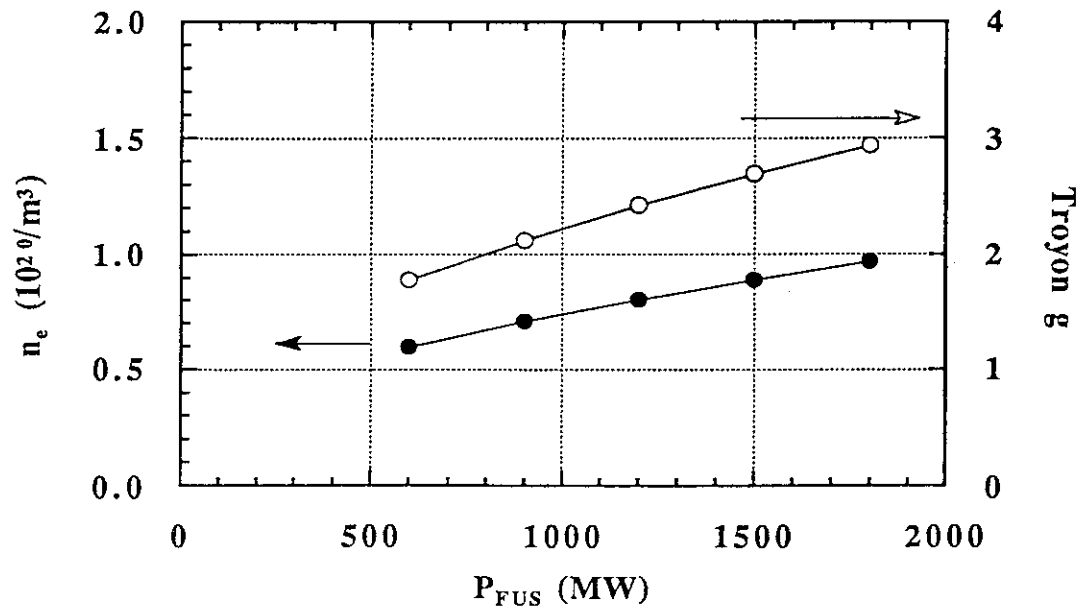
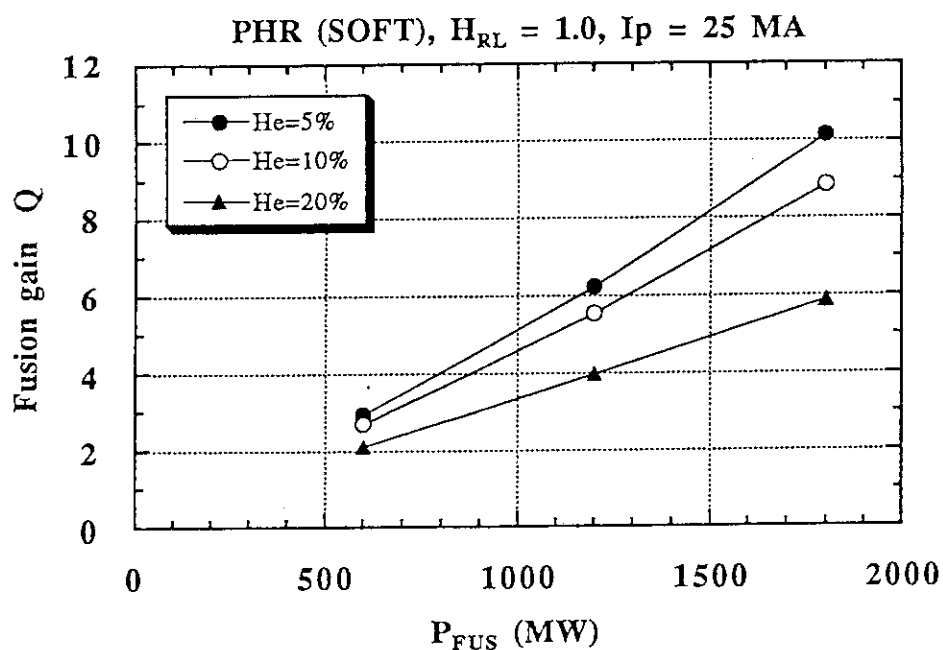


Fig. 3.10 (Continued)

a)



b)

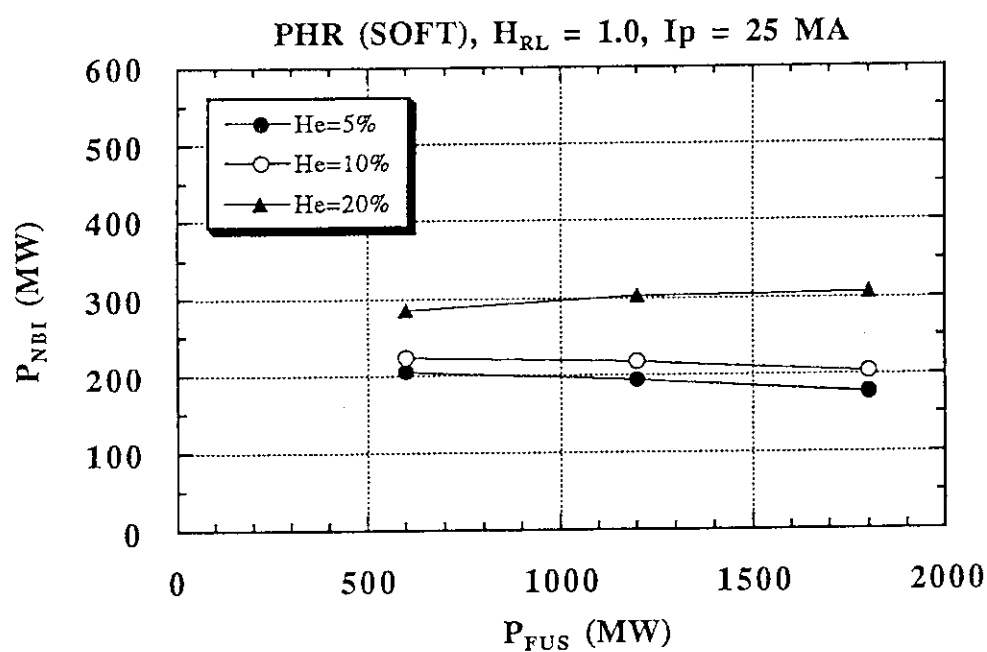
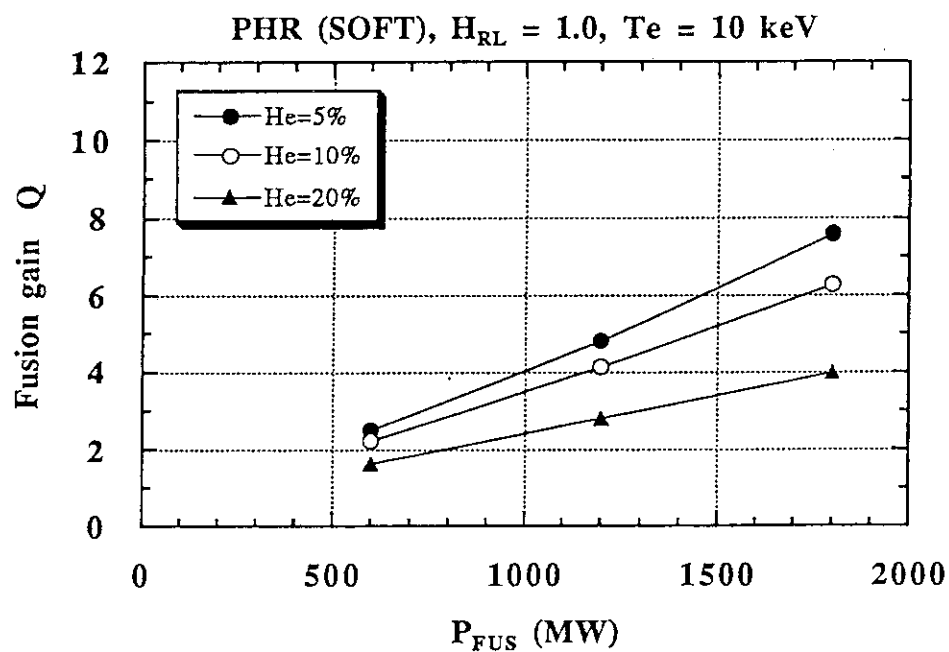


Fig. 3.11 Steady-state operation of EDA-ITER when $I_p=25$ MA and $H_{RL}=1.0$ for various helium fractions.
 a) Achievable fusion gain Q as a function of P_{FUS} .
 b) Required current-drive power P_{NBI} as a function of P_{FUS} .

a)



b)

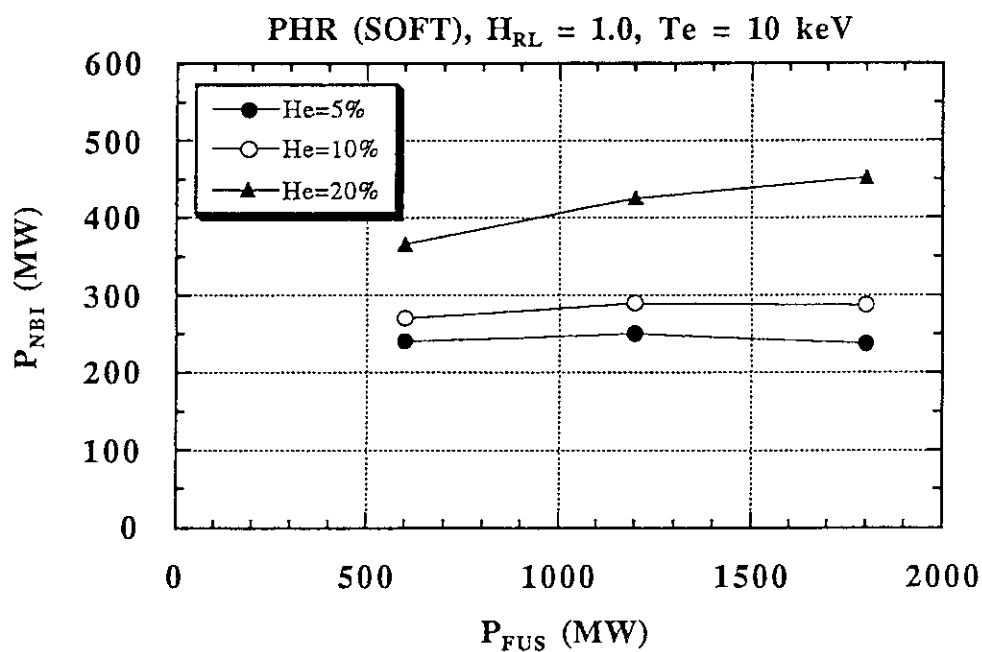
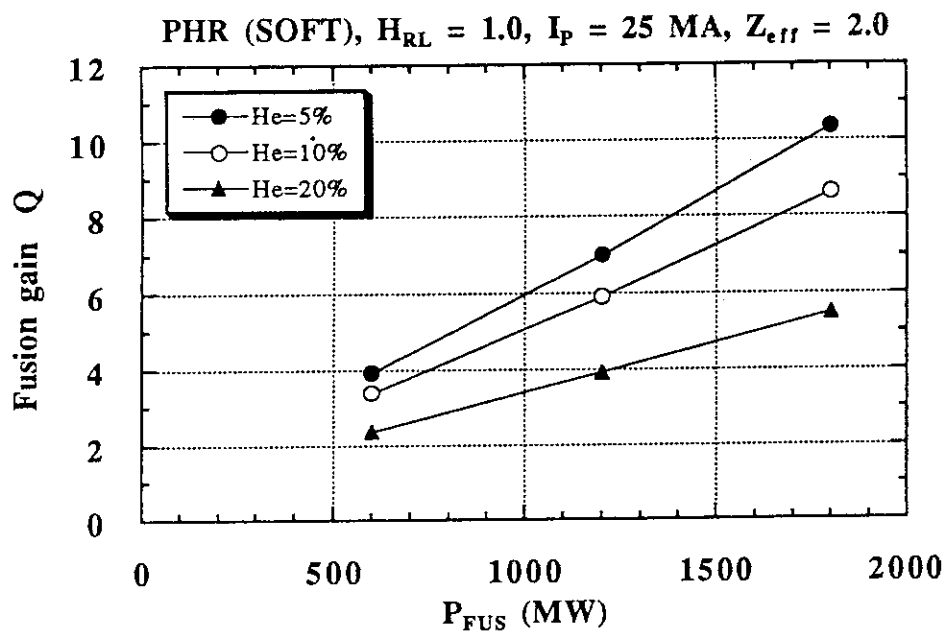


Fig. 3.12 Steady-state operation of EDA-ITER when $T_e=10$ keV and $H_{RL}=1.0$ for various helium fractions.
 a) Achievable fusion gain Q as a function of P_{FUS} .
 b) Required current-drive power P_{NBI} as a function of P_{FUS} .

a)



b)

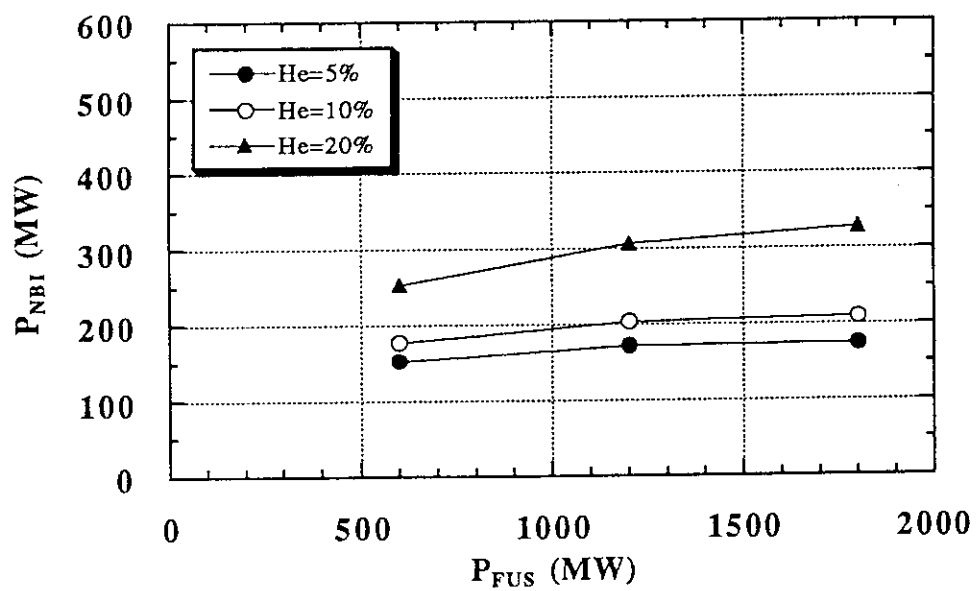
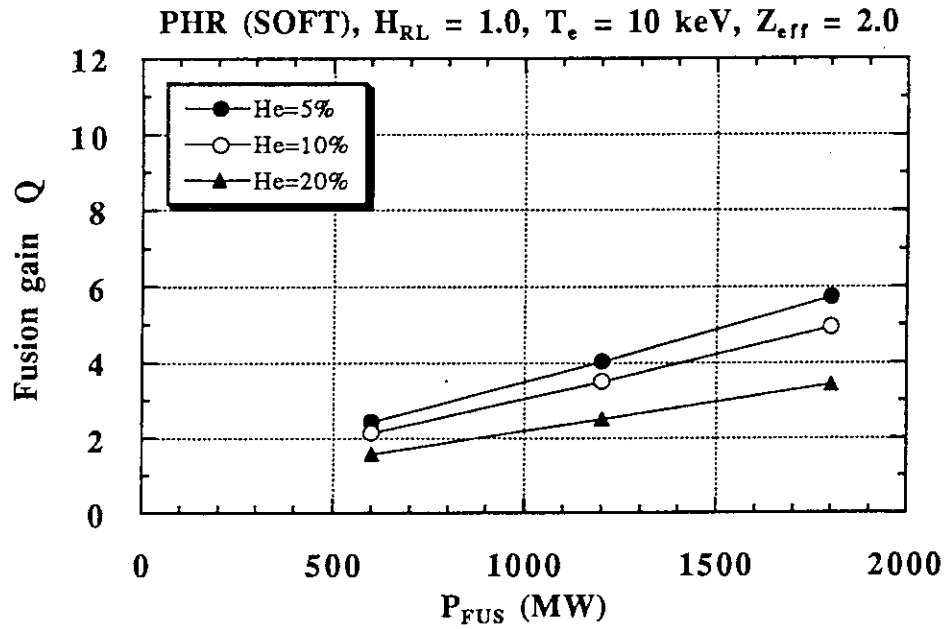


Fig. 3.13 Steady-state operation of EDA-ITER when $I_p=25$ MA, $Z_{eff}=2.0$ and $H_{RL}=1.0$ for various helium fractions.
 a) Achievable fusion gain Q as a function of P_{FUS} .
 b) Required current-drive power P_{NBI} as a function of P_{FUS} .

a)



b)

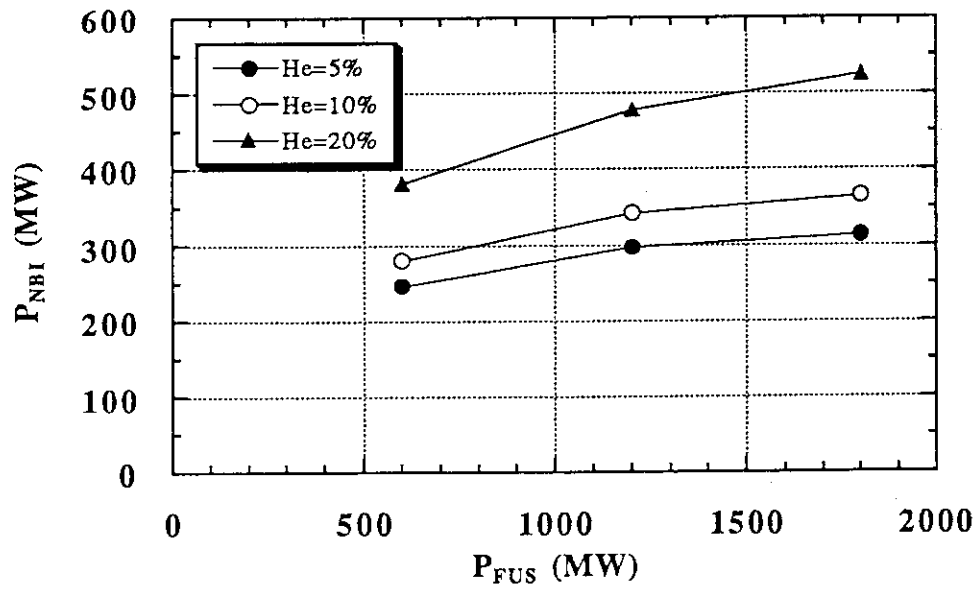
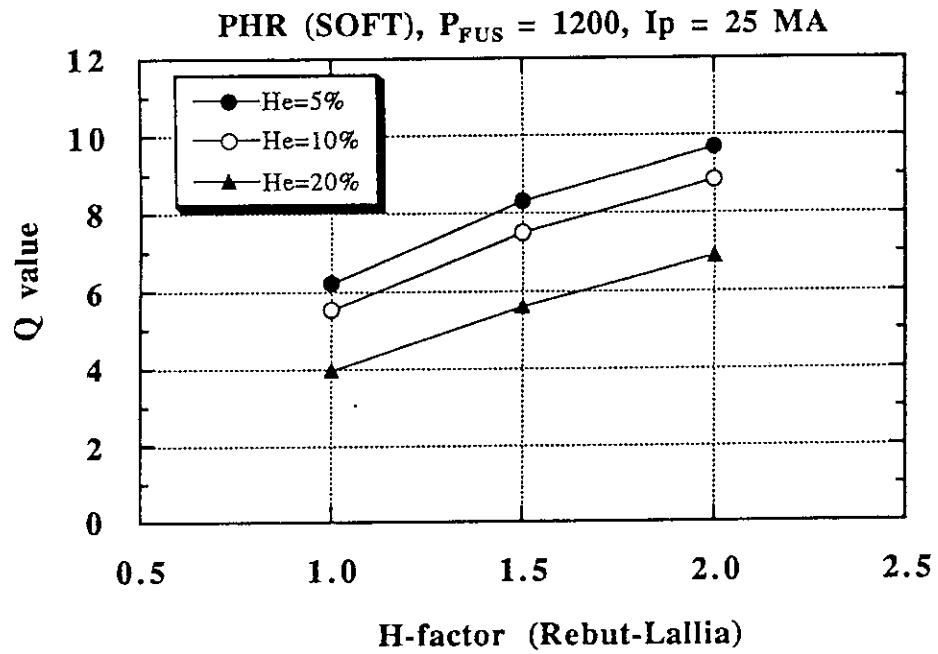


Fig. 3.14 Steady-state operation of EDA-ITER when $T_e=10$ keV, $Z_{eff}=2.0$ and $H_{RL}=1.0$ for various helium fractions.
 a) Achievable fusion gain Q as a function of P_{FUS} .
 b) Required current-drive power P_{NBI} as a function of P_{FUS} .

a)



b)

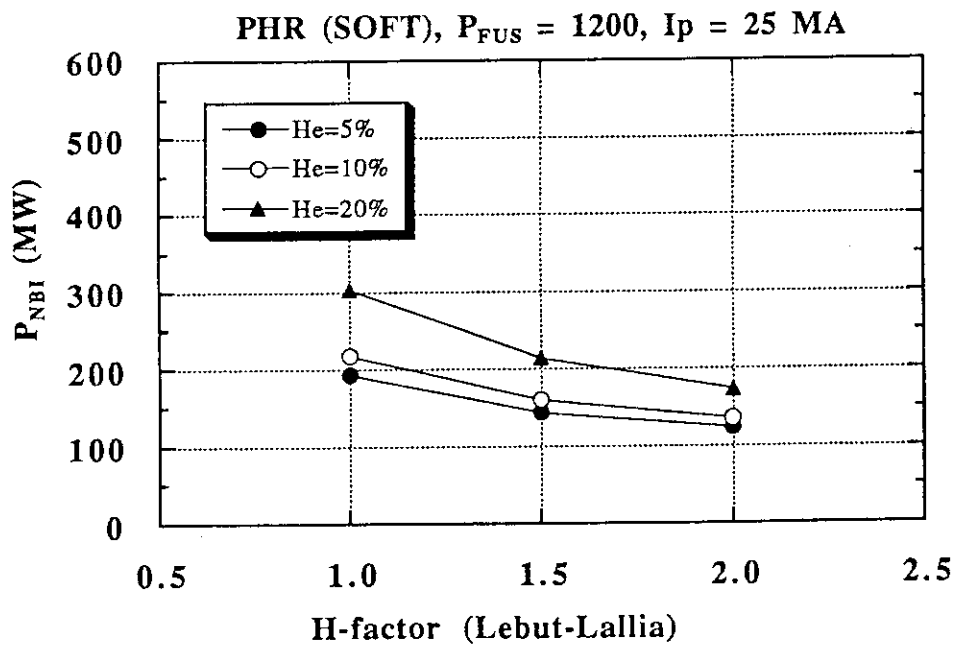
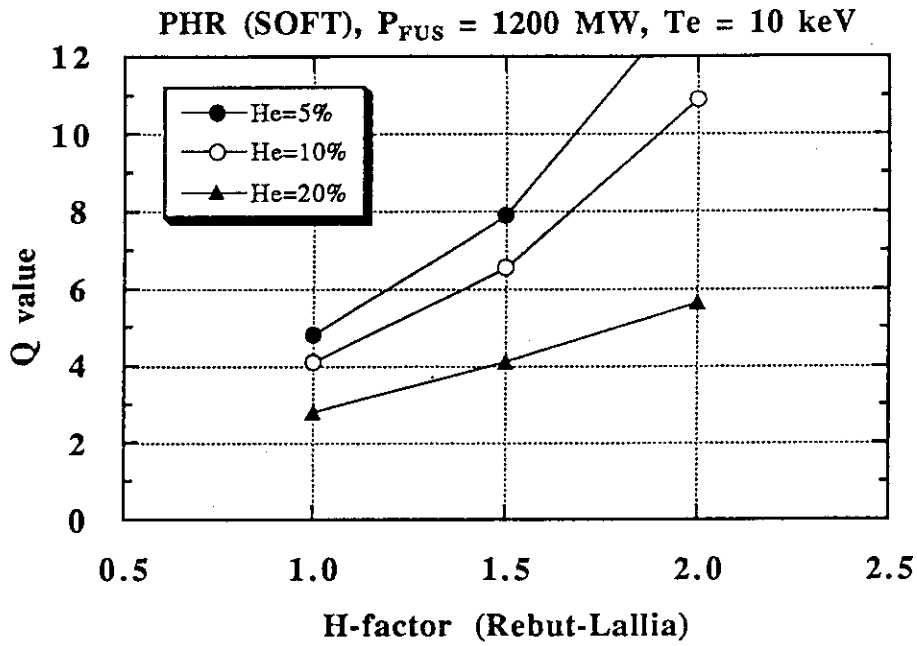


Fig. 3.15 Steady-state operation of EDA-ITER when $I_p=25$ MA and $P_{FUS}=1200$ MW for various helium fractions.
 a) Achievable fusion gain Q as a function of H-factor.
 b) Required current-drive power P_{NBI} .

a)



b)

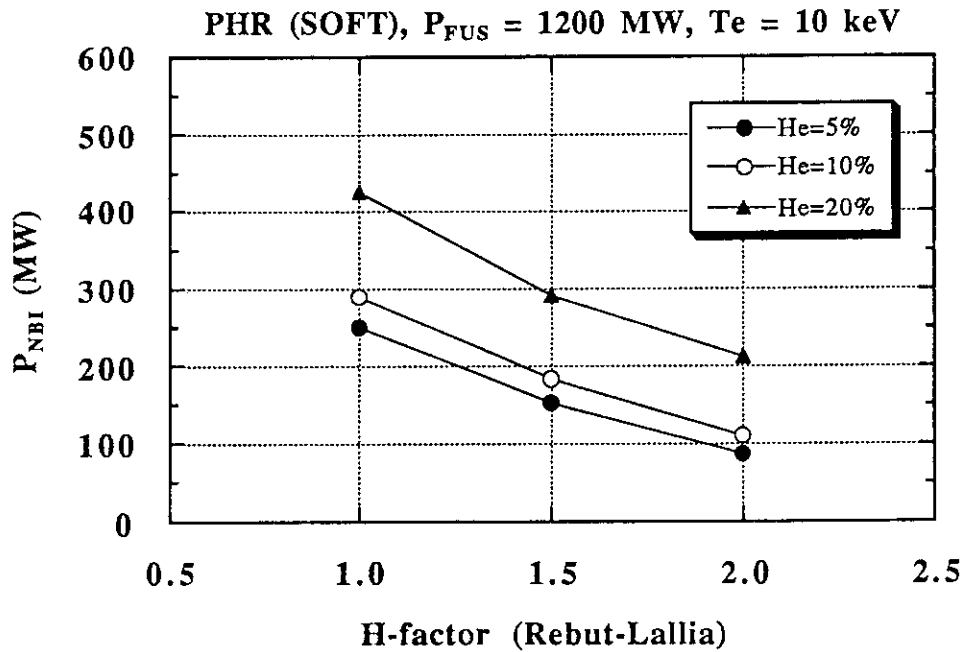
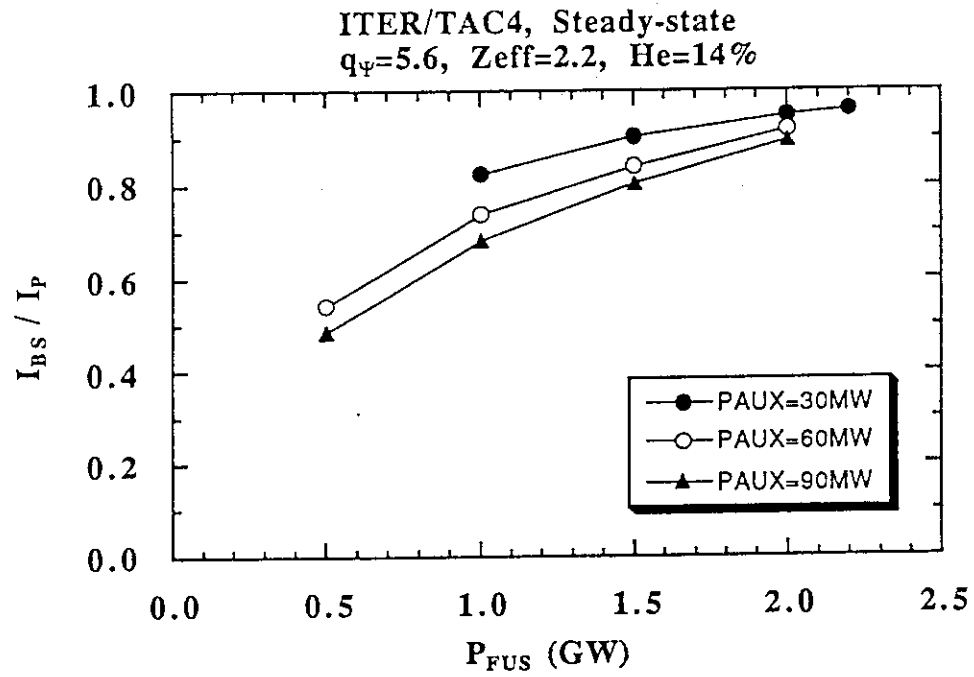


Fig. 3.16 Steady-state operation of EDA-ITER when $T_e=10$ keV and $P_{FUS}=1200$ MW for various helium fractions.
 a) Achievable fusion gain Q as a function of H-factor.
 b) Required current-drive power P_{NBI} .

a)



b)

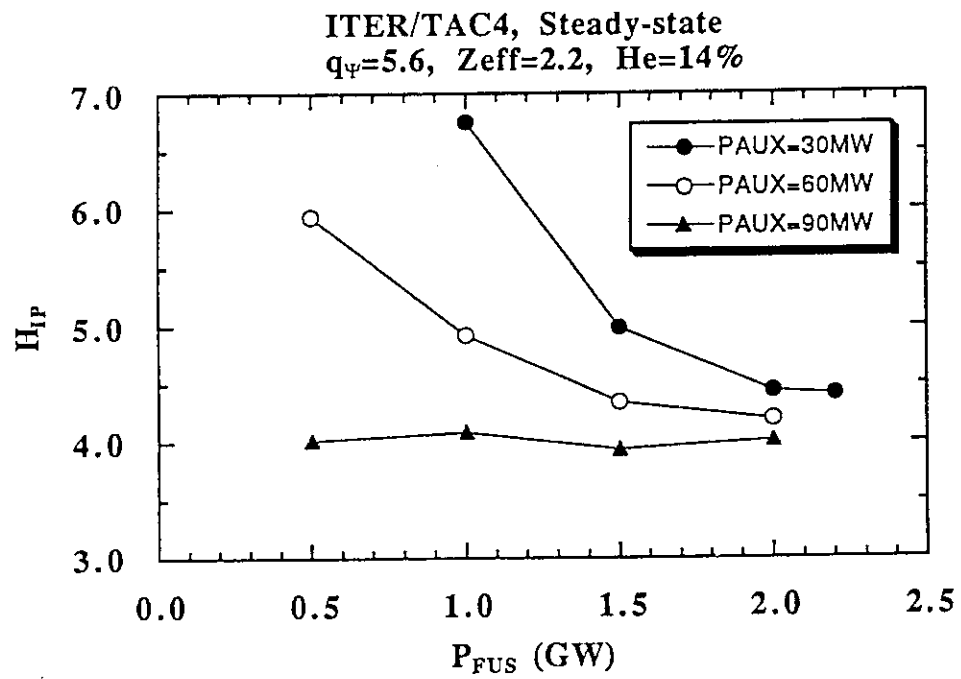
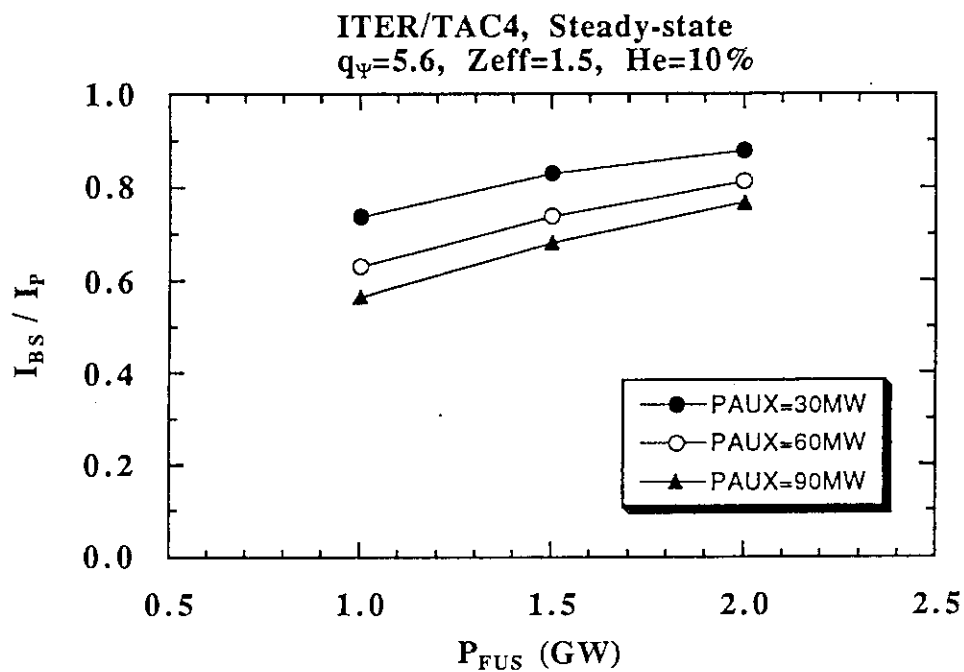


Fig. 3.17 Operation performance of steady-state plasma in high- q_{Ψ} region for various current-drive power P_{NBI} . Here, $q_{\Psi}=5.6$, He=14% and $Z_{eff}=2.2$.
 a) Fraction of the bootstrap current,
 b) Required H-factor evaluated by ITER89 power scaling law.

a)



c)

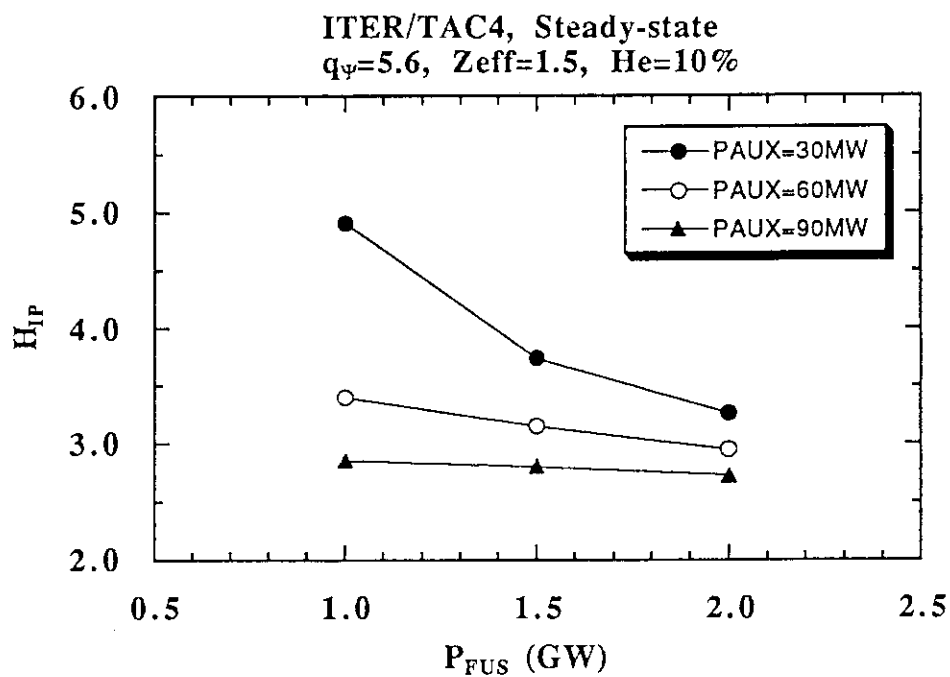
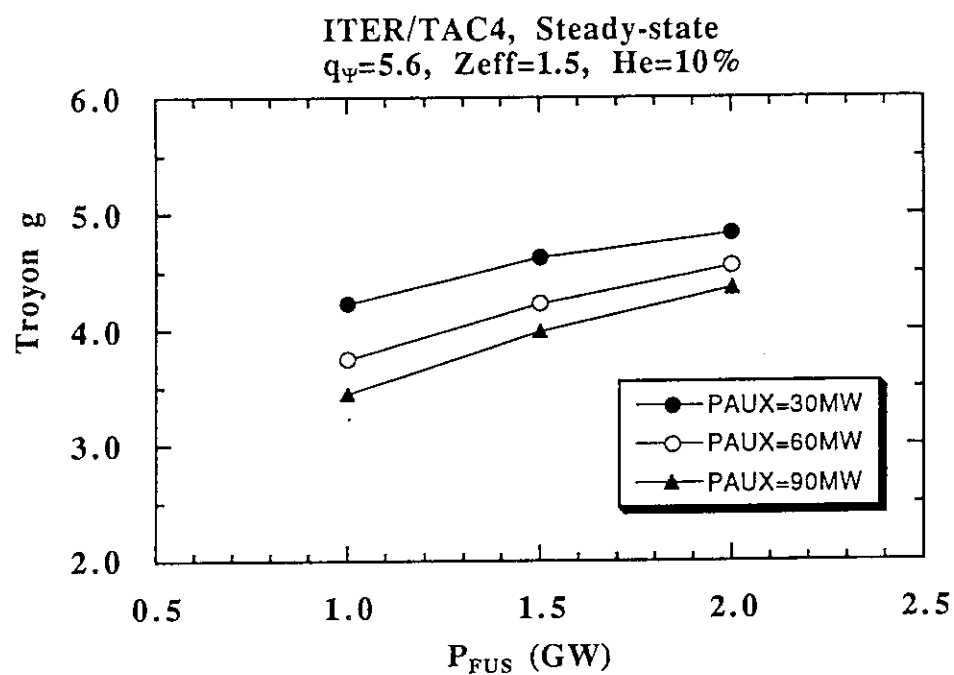


Fig. 3.18 Operation performance of steady-state plasma in high- q_ψ region for various current-drive power P_{NBI} . Here, $q_\psi=5.6$, He=10% and $Z_{eff}=1.5$.
 a) Fraction of the bootstrap current,
 b) Troyon coefficient g ,
 c) Required H-factor evaluated by ITER89 power scaling law,
 d) Required H-factor evaluated by Rebut-Lallia scaling law.

b)



d)

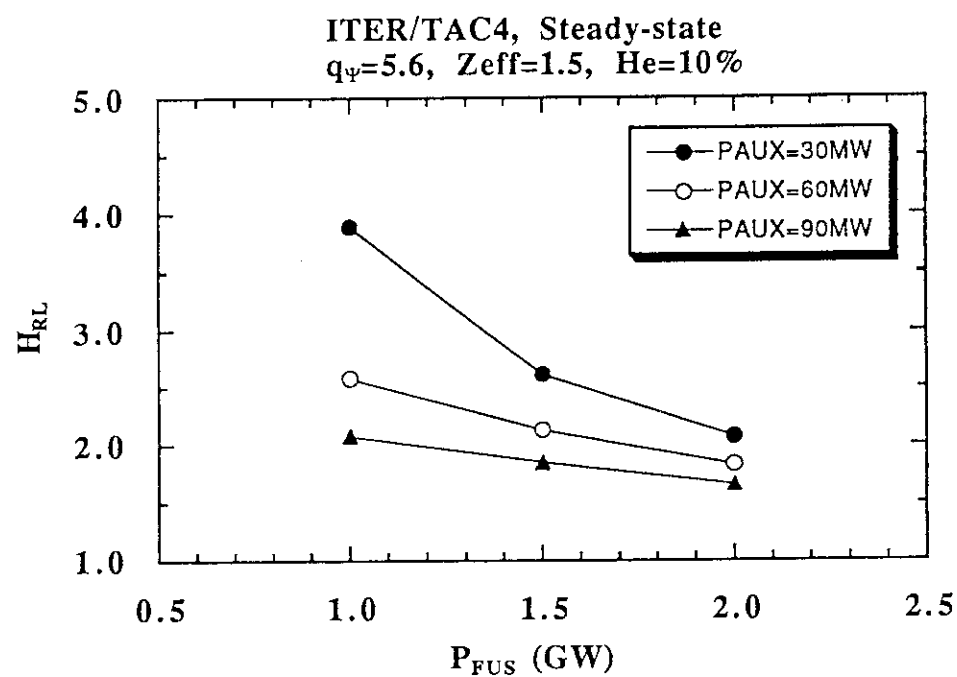
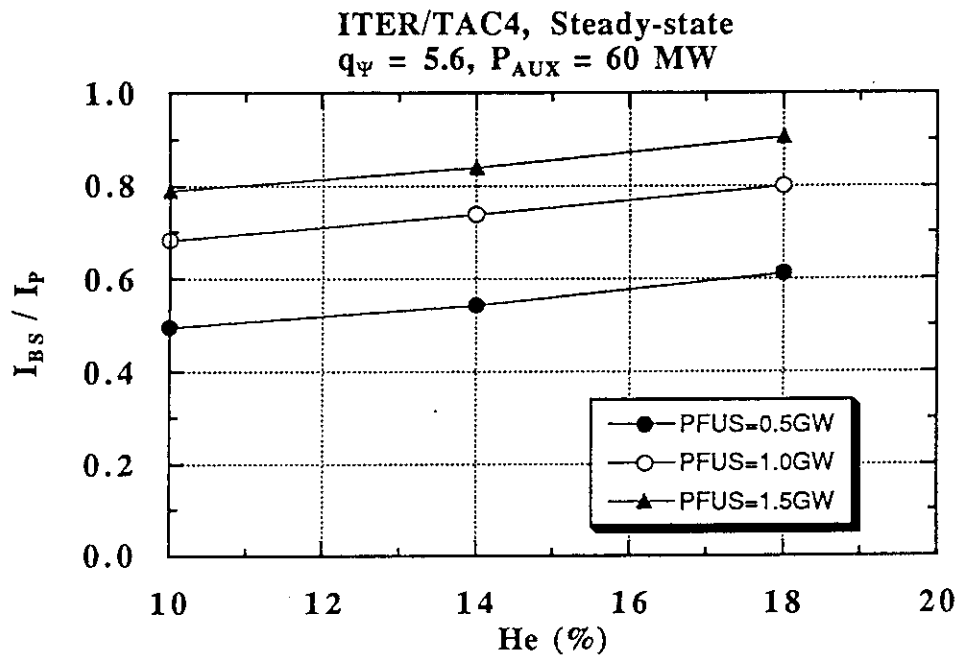


Fig.3.18 (Continued)

a)



b)

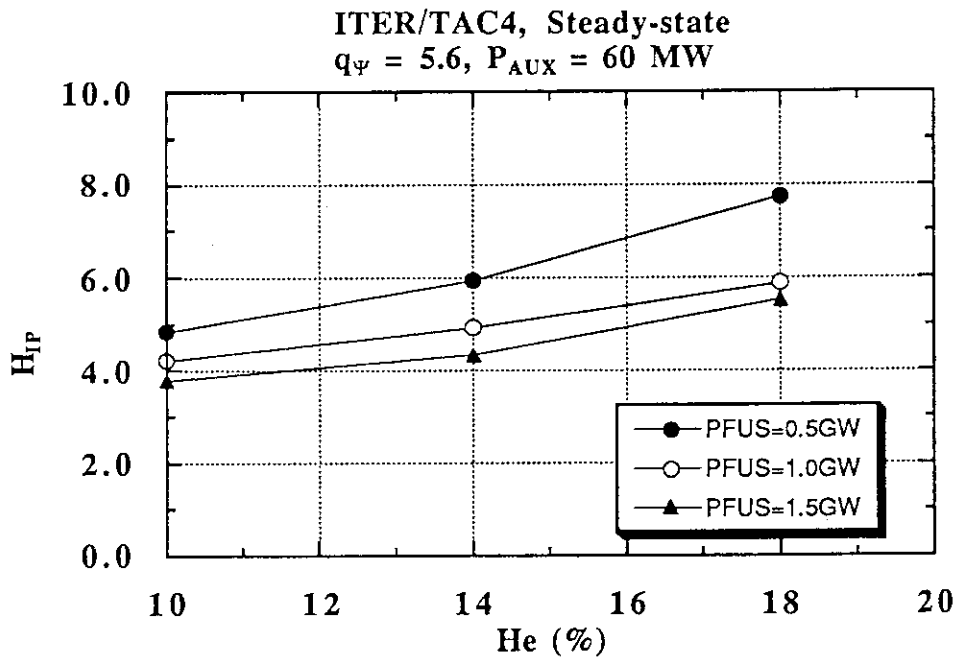
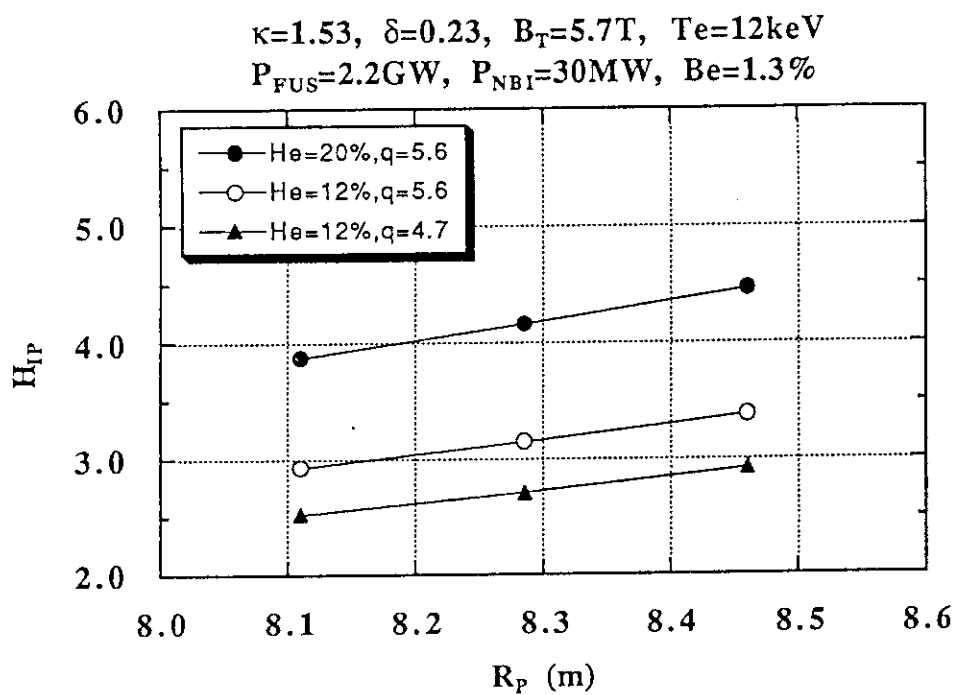


Fig. 3.19 Operation performance of steady-state plasma in high- q_Ψ region as a function of helium accumulation rate. Here, $q_\Psi = 5.6$ and $P_{NB1} = 60 \text{ MW}$.
 a) Fraction of the bootstrap current,
 b) Required H-factor evaluated by ITER89 power scaling law.

a)



b)

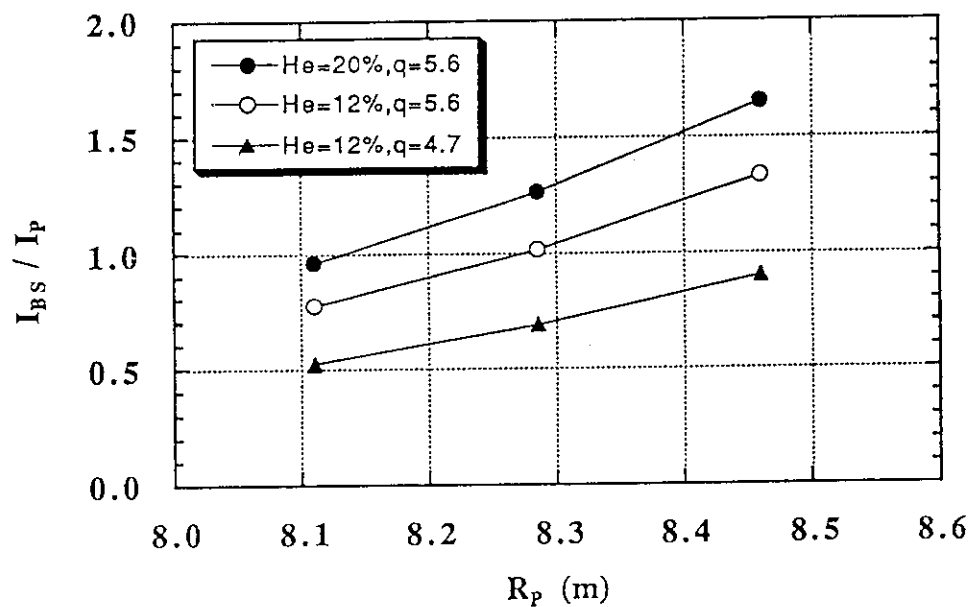
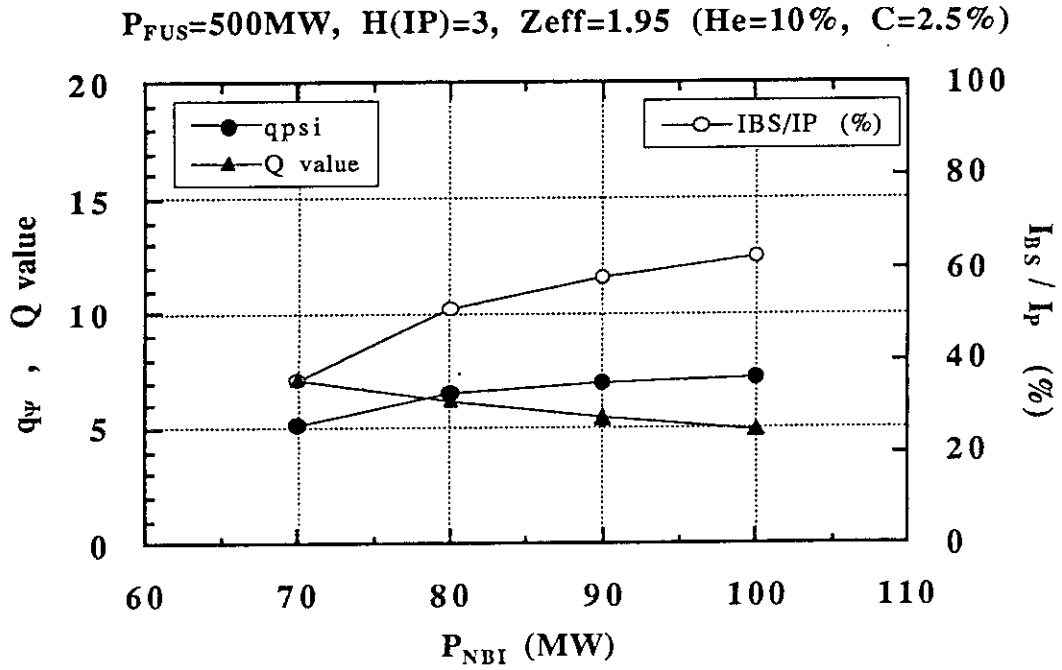


Fig. 3.20 a) Required H-factor and b) fraction of bootstrap current for steady-state plasma as a function of major radius R_P . Here, $\kappa=1.53$, $\delta=0.23$, $B_T=5.7\text{ T}$, $P_{FUS}=2200\text{ MW}$ and $P_{NBI}=30\text{ MW}$.

a)



b)

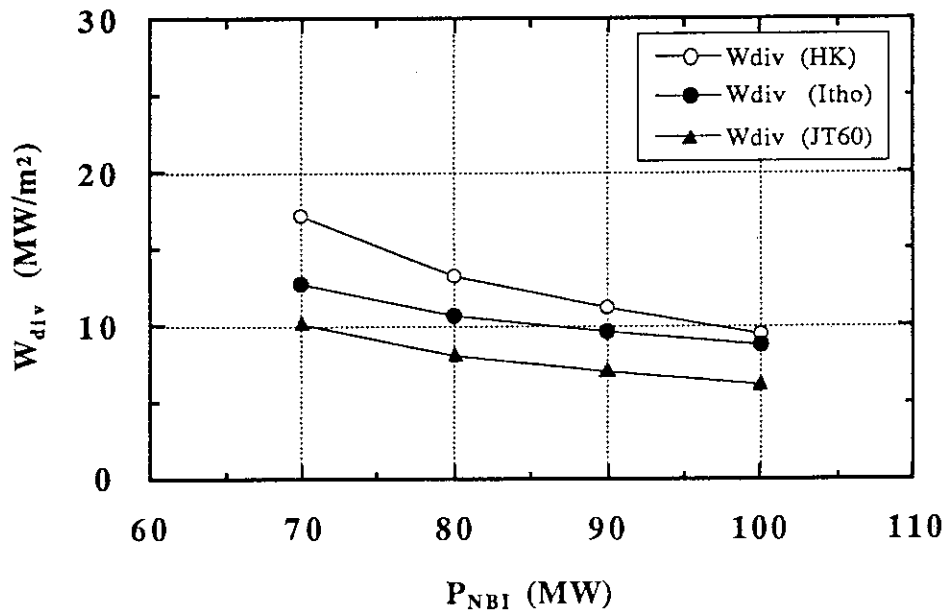
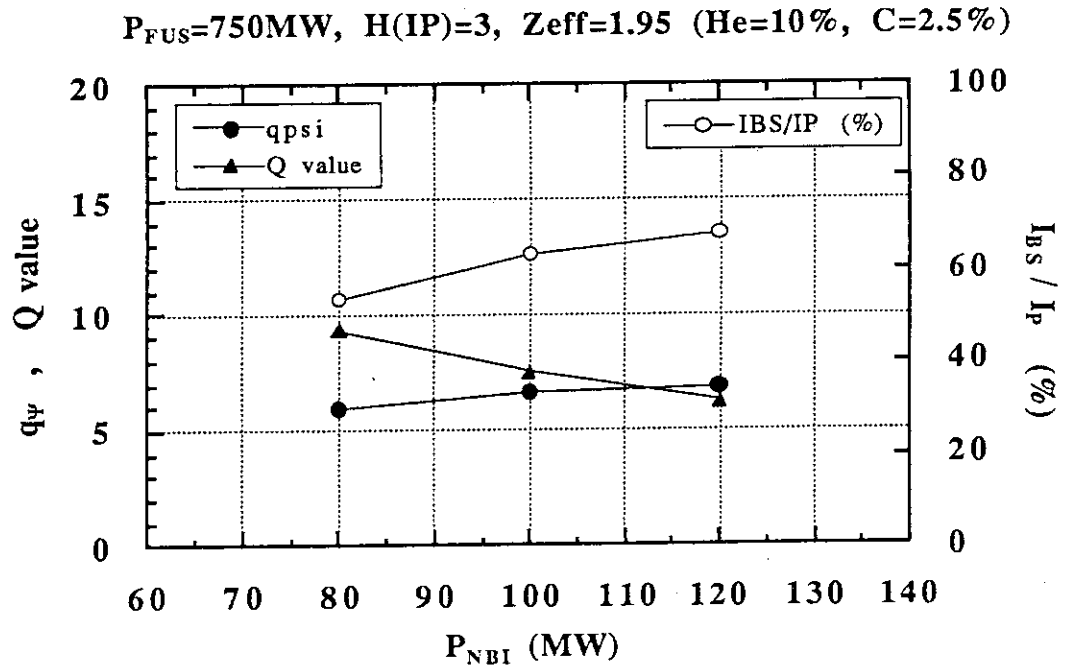


Fig. 3.21 Steady-state operation of EDA-ITER when $H_{IP}=3$, $Z_{eff}=1.95$ and $P_{FUS}=500$ MW.

- a) Achievable fusion gain Q , $q\psi$ and I_{BS}/I_P as functions of the available current-drive power P_{NBI} .
 b) Divertor heat load calculated by 0-D scaling models.

a)



b)

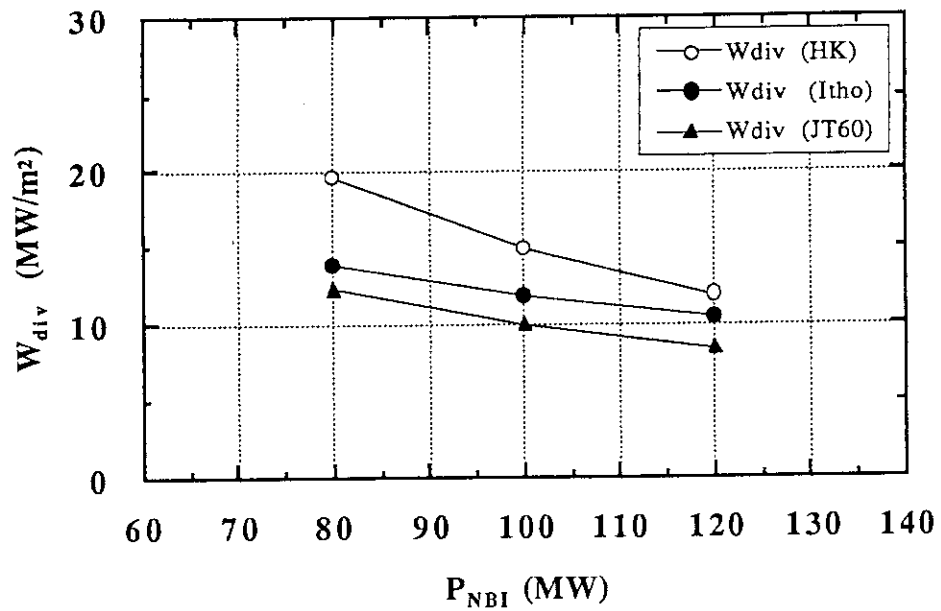
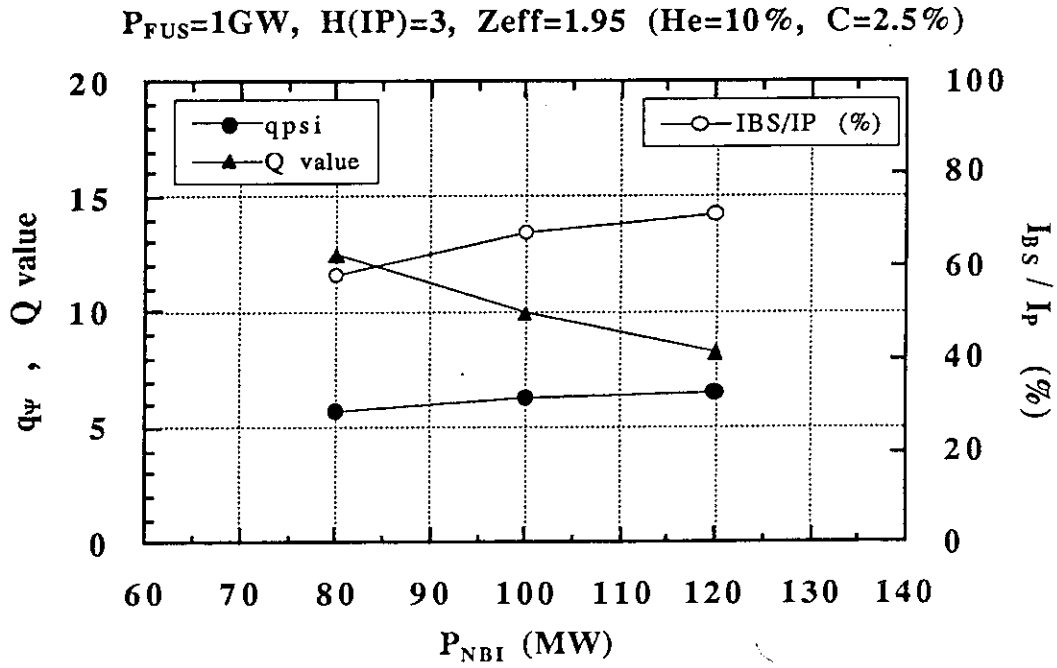


Fig. 3.22 Steady-state operation of EDA-ITER when $H_{IP}=3$, $Z_{eff}=1.95$ and $P_{FUS}=750$ MW.

- a) Achievable fusion gain Q , q_{psi} and I_{BS}/I_P as functions of the available current-drive power P_{NBI} .
 b) Divertor heat load calculated by 0-D scaling models.

a)



b)

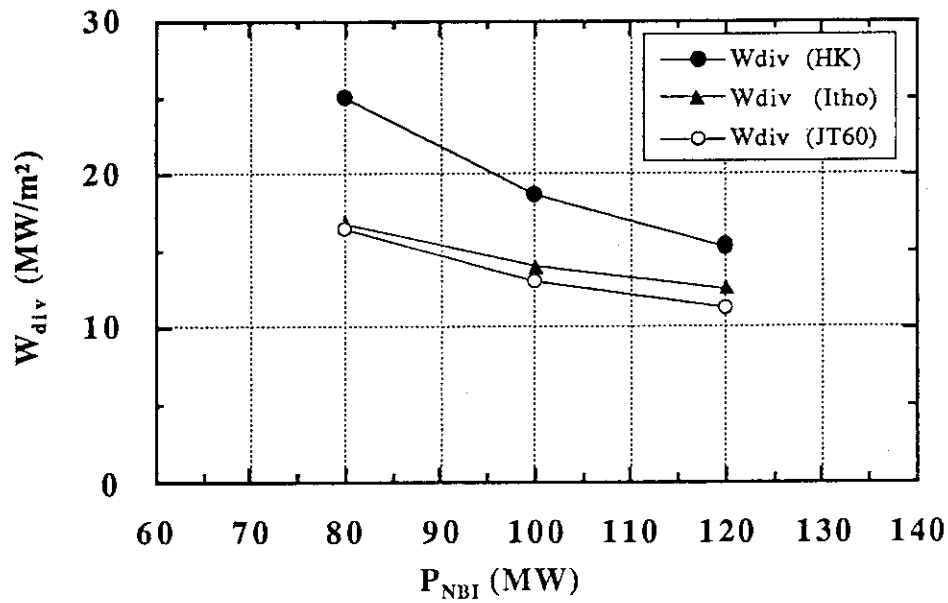
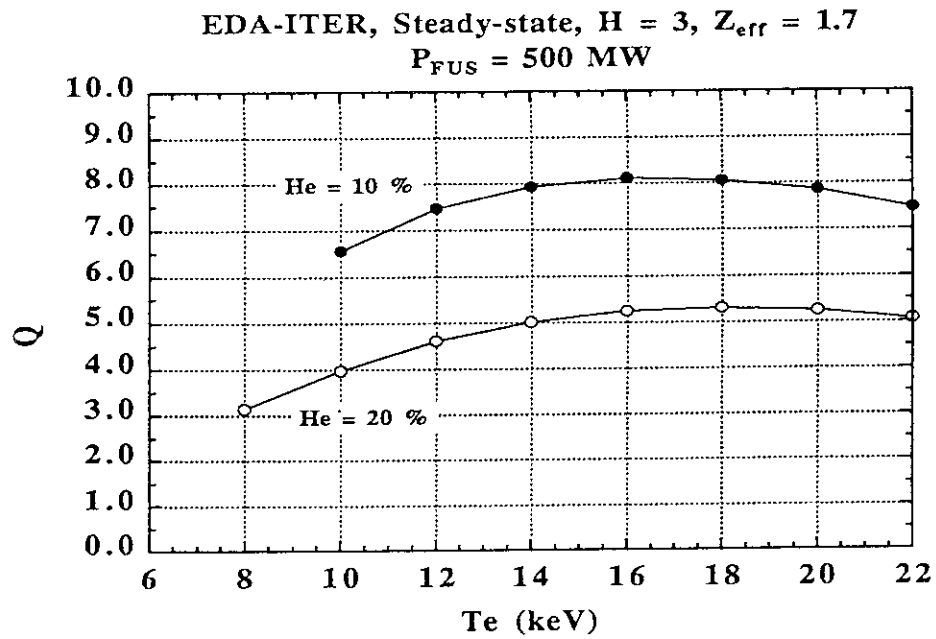


Fig. 3.23 Steady-state operation of EDA-ITER when $H_{IP}=3$, $Z_{eff}=1.95$ and $P_{FUS}=1000$ MW.

- a) Achievable fusion gain Q , q_{ψ} and I_{BS}/I_P as functions of the available current-drive power P_{NBI} .
 b) Divertor heat load calculated by 0-D scaling models.

a)



b)

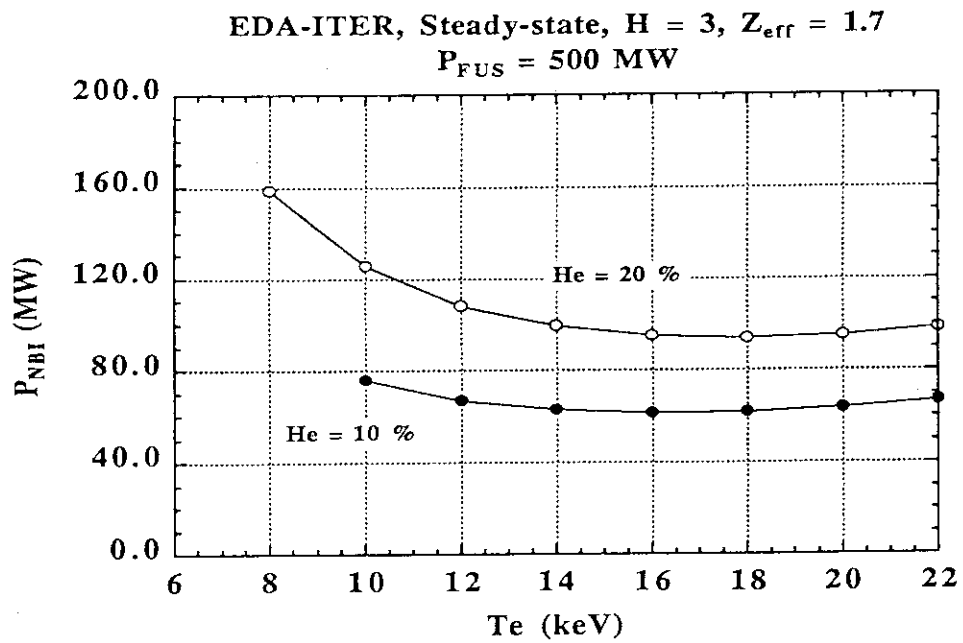
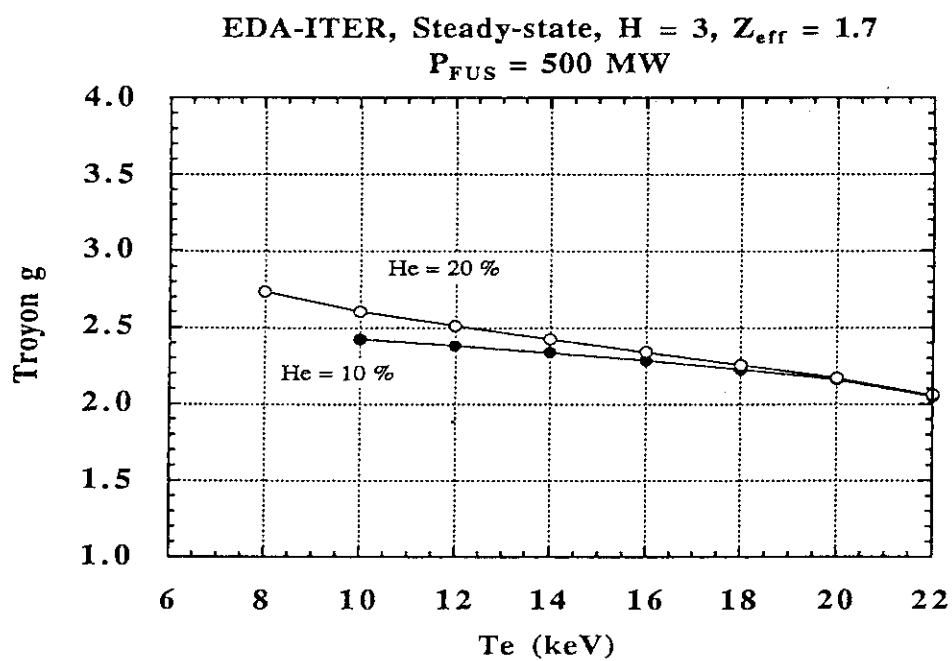


Fig. 3.24 Steady-state operation of EDA-ITER when $H_{\text{IP}}=3$, $Z_{\text{eff}}=1.7$ and $P_{\text{FUS}}=500 \text{ MW}$.

- a) Achievable fusion gain Q as functions of the electron temperature T_e .
- b) Required current drive power P_{NBI} .
- c) Troyon g , d) q_{Ψ} , e) $I_{\text{BS}}/I_{\text{P}}$ and f) n_e .
- g) Divertor heat load (Constant χ model) $W_{\text{div}}^{\text{HK}}$.
- h) Divertor heat load (JT-60U model) $W_{\text{div}}^{\text{JT60}}$.

c)



d)

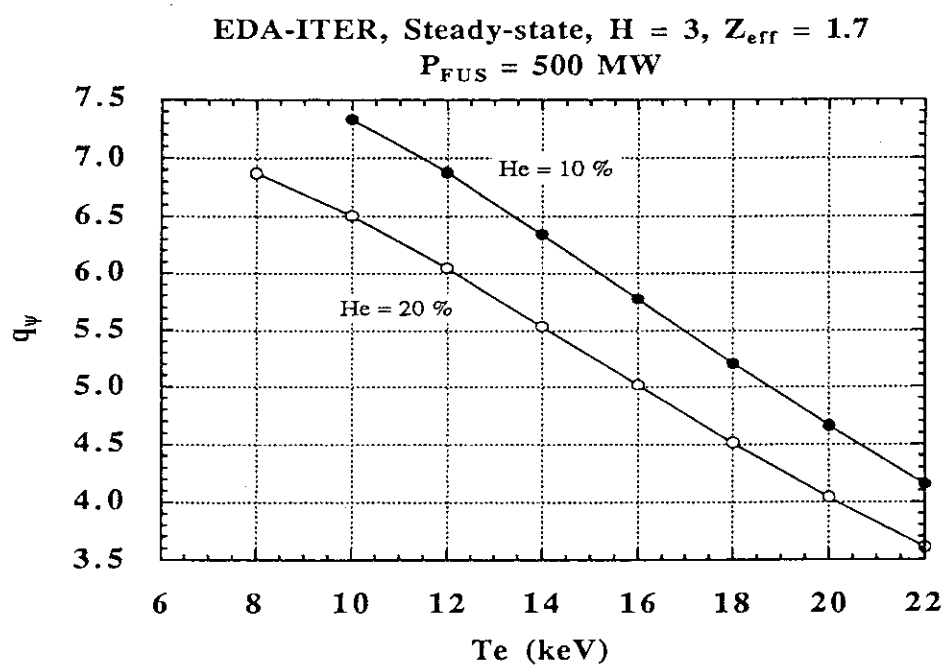
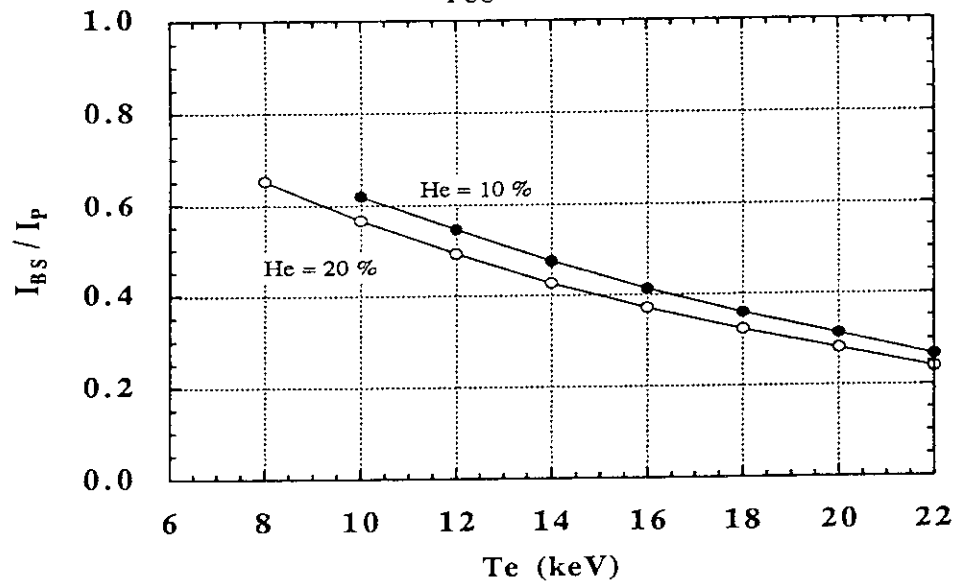


Fig. 3.24 (Continued)

e)

EDA-ITER, Steady-state, $H = 3$, $Z_{\text{eff}} = 1.7$
 $P_{\text{FUS}} = 500 \text{ MW}$



f)

EDA-ITER, Steady-state, $H = 3$, $Z_{\text{eff}} = 1.7$
 $P_{\text{FUS}} = 500 \text{ MW}$

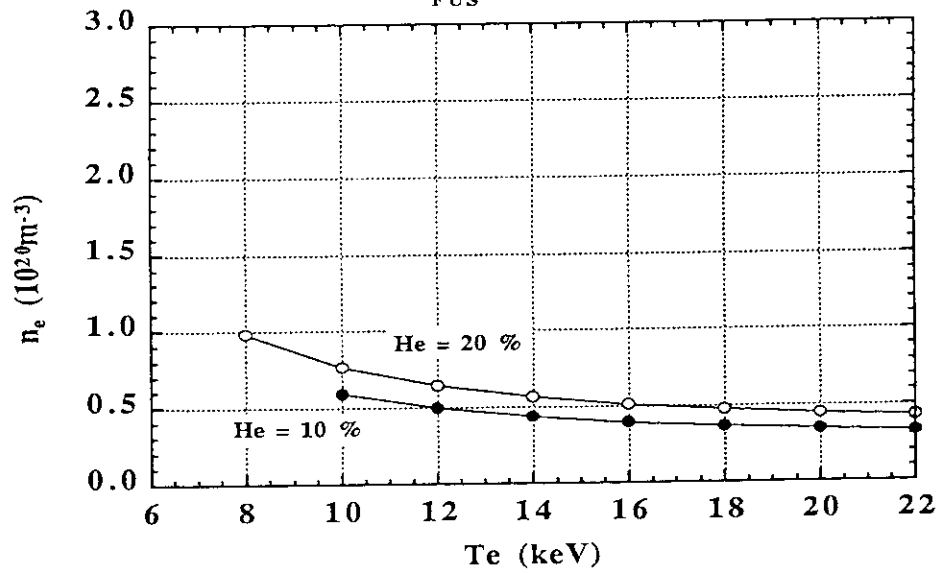
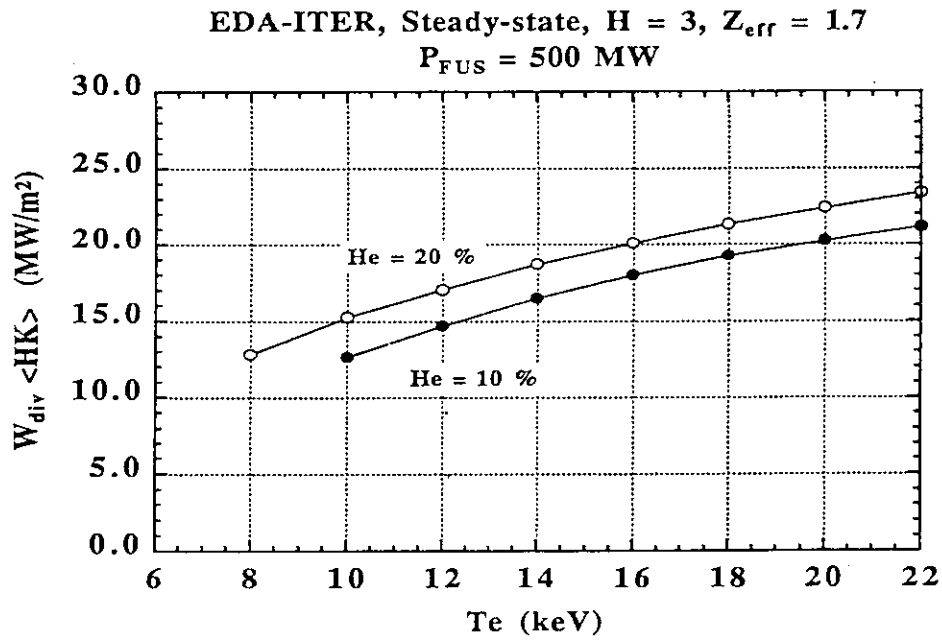


Fig. 3.24 (Continued)

g)



h)

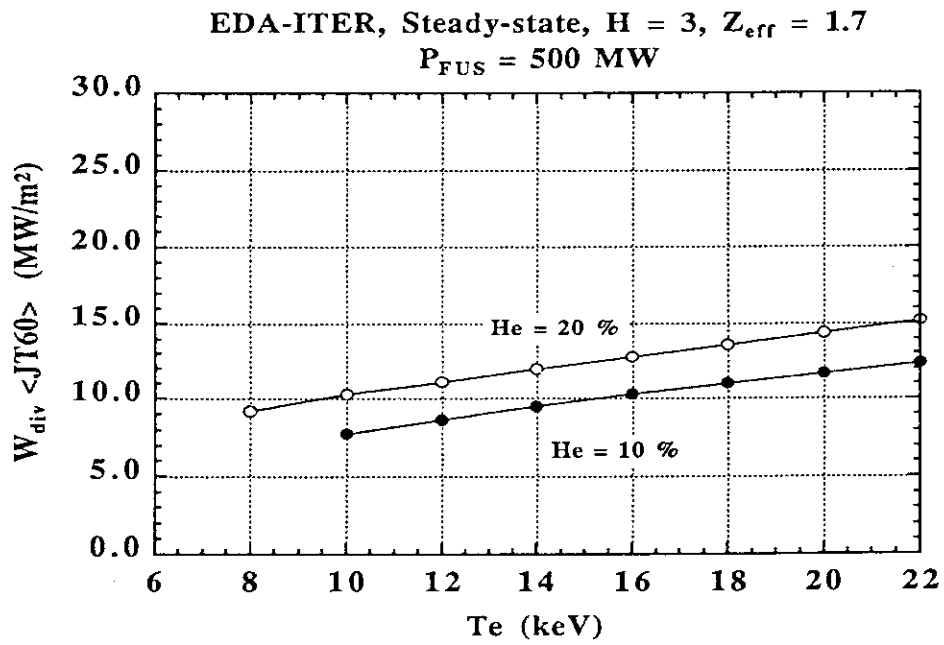
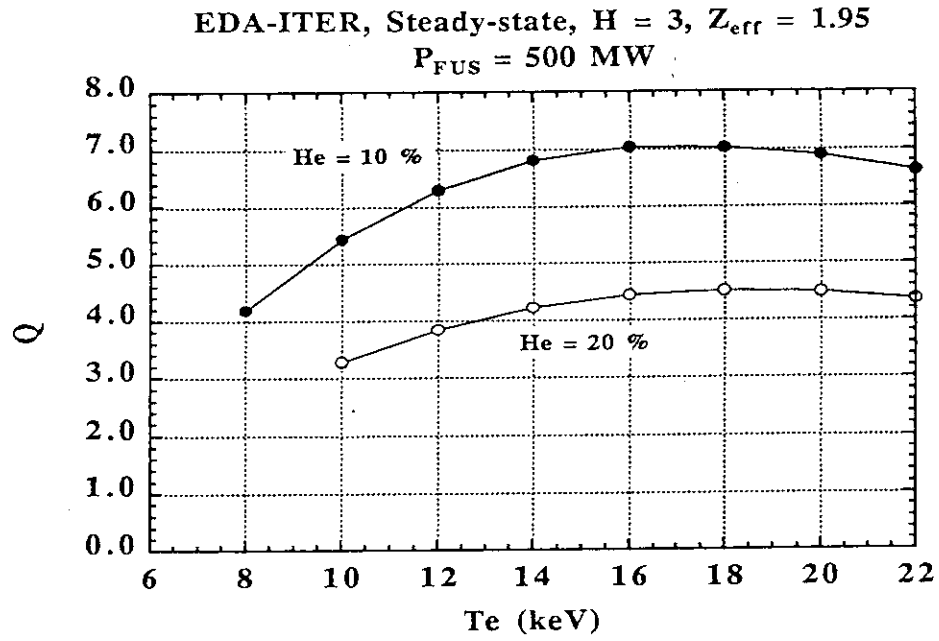


Fig. 3.24 (Continued)

a)



b)

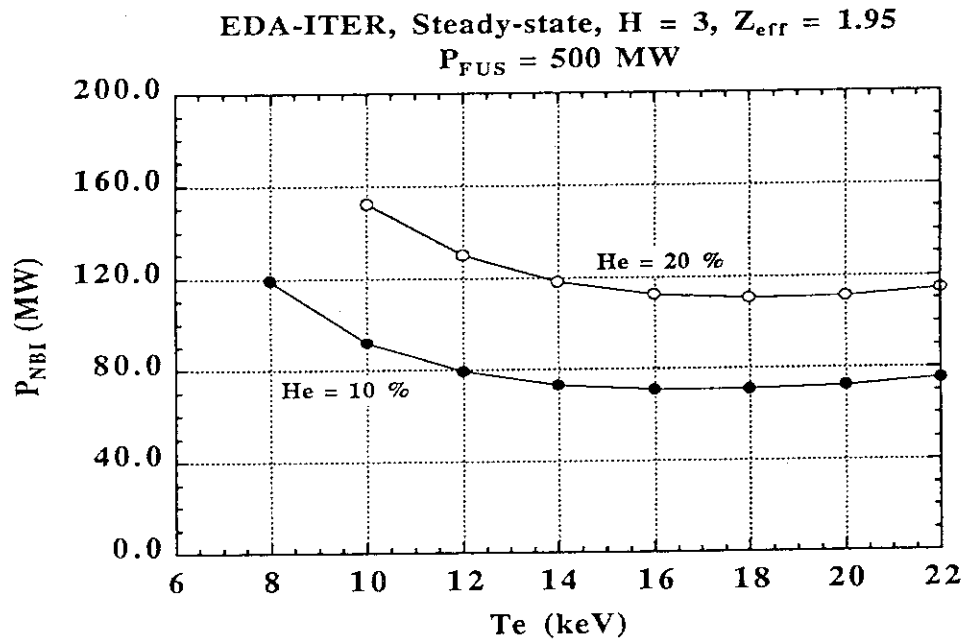


Fig. 3.25 Steady-state operation of EDA-ITER when $H_{IP}=3$, $Z_{eff}=1.95$ and $P_{FUS}=500 \text{ MW}$.

a) Achievable fusion gain Q as functions of the electron temperature T_e .

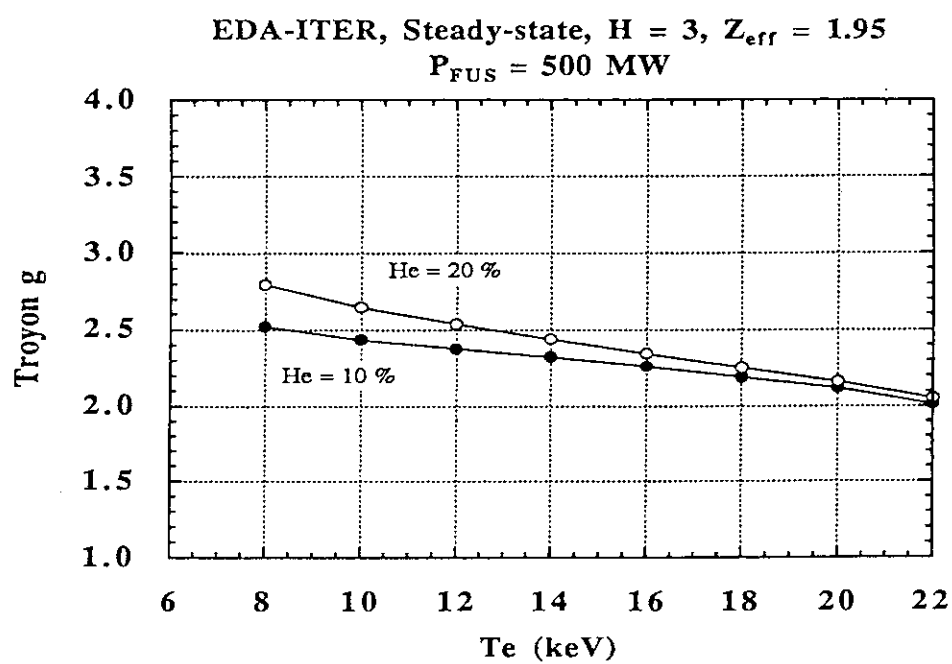
b) Required current drive power P_{NBI} .

c) Troyon g , d) q_{Ψ} , e) I_{Bs}/I_P and f) n_e .

g) Divertor heat load (Constant χ model) W_{div}^{HK} .

h) Divertor heat load (JT-60U model) W_{div}^{JT60} .

c)



d)

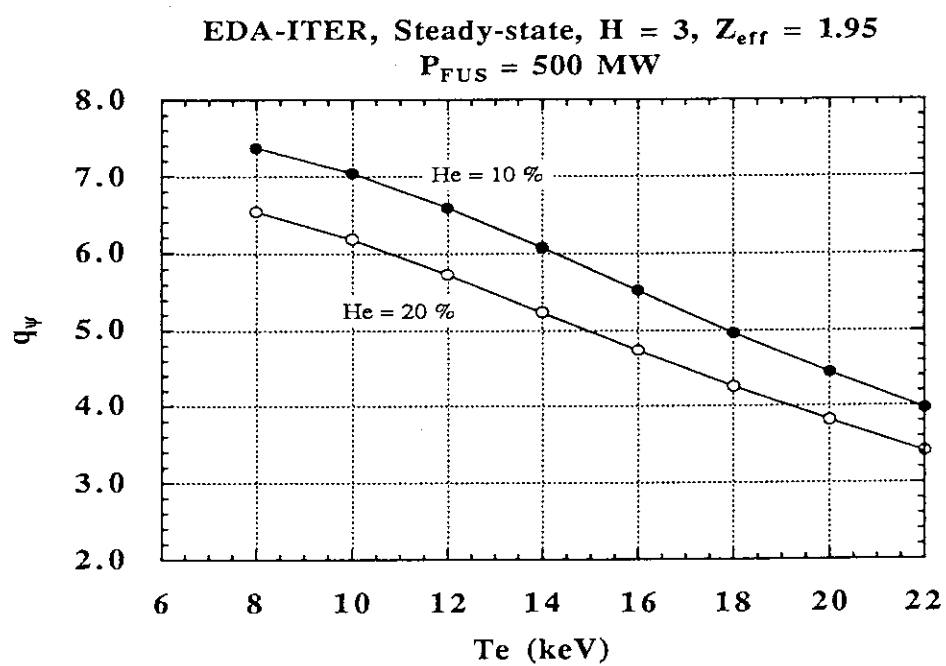
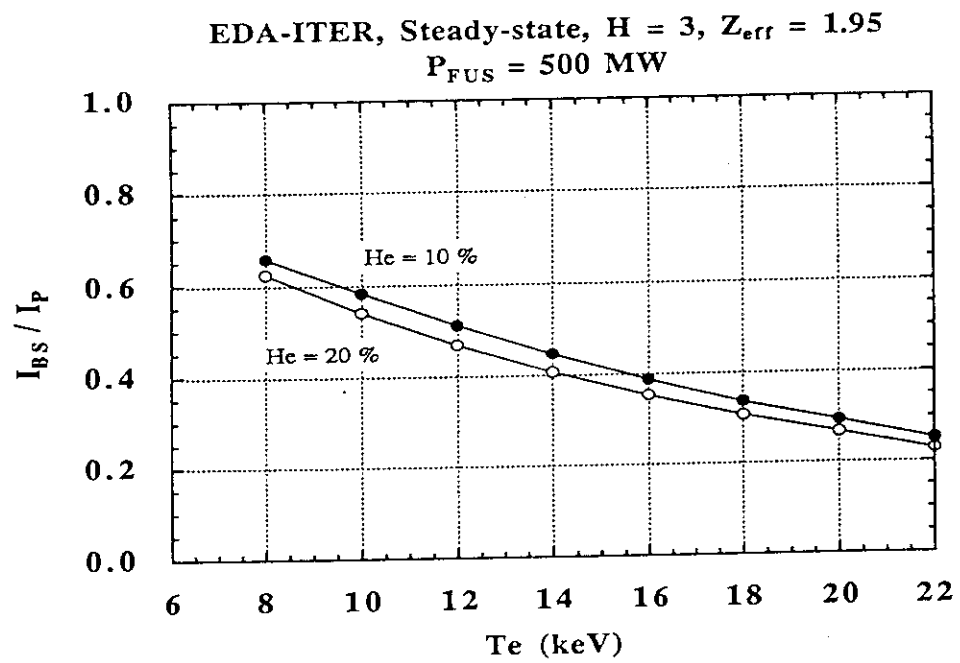


Fig. 3.25 (Continued)

e)



f)

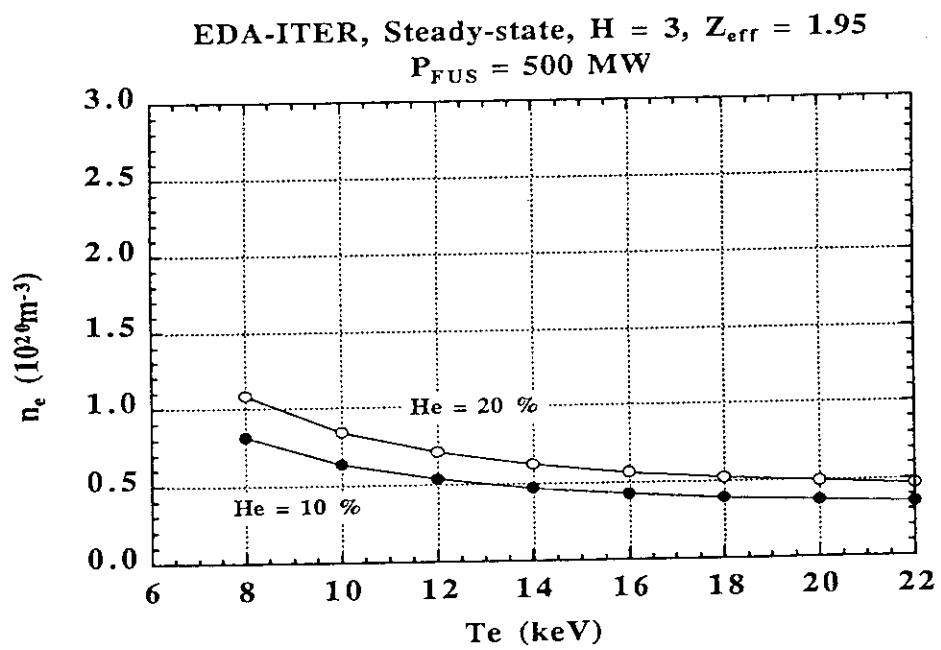
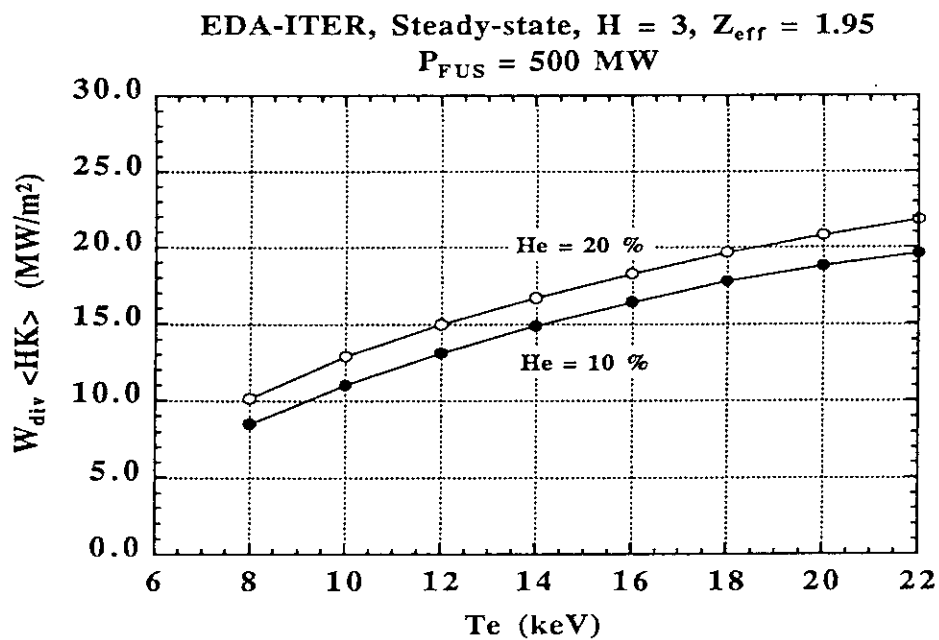


Fig. 3.25 (Continued)

g)



h)

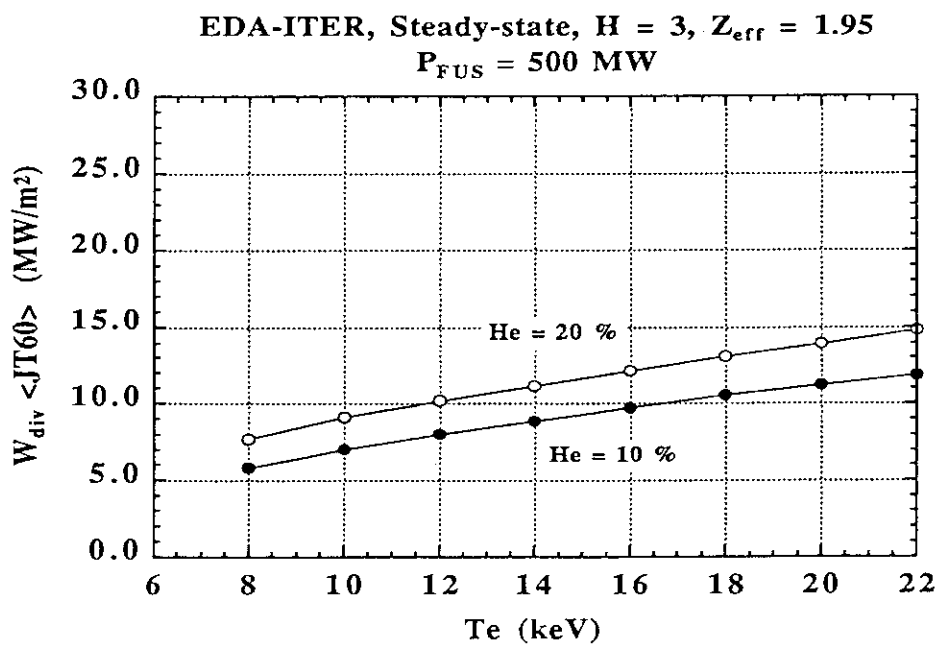
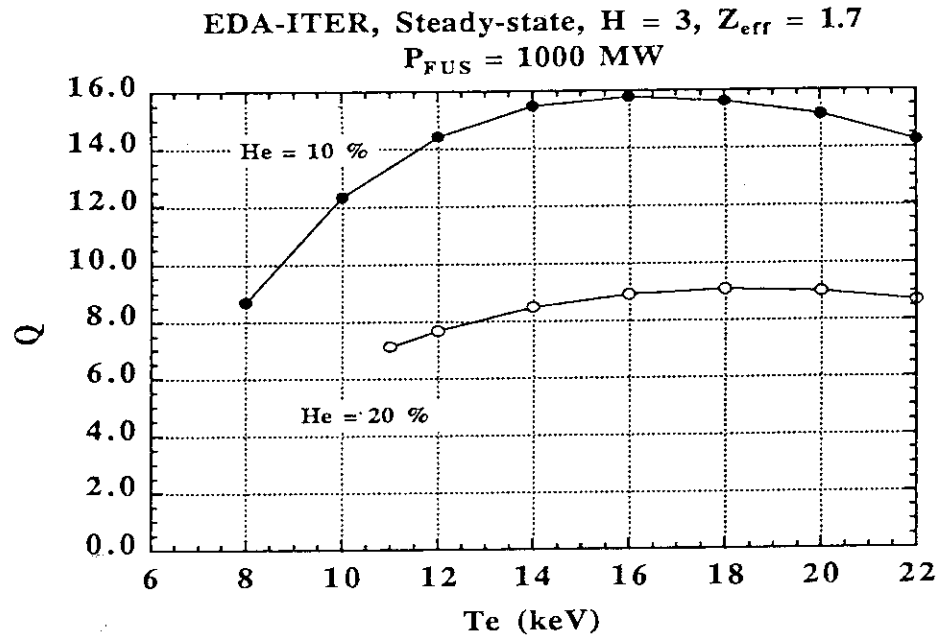


Fig. 3.25 (Continued)

a)



b)

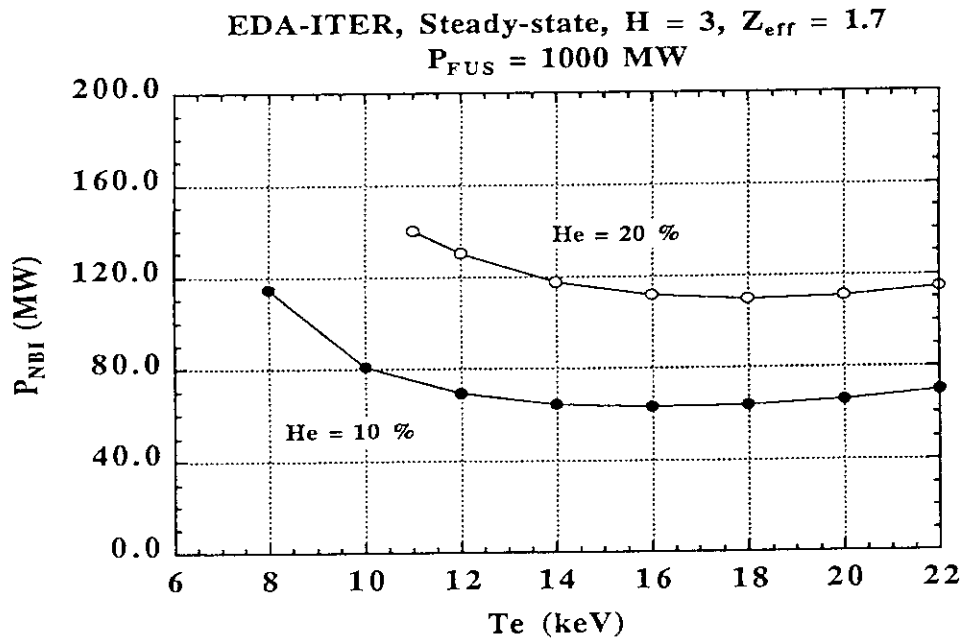


Fig. 3.26 Steady-state operation of EDA-ITER when $H_{IF}=3$, $Z_{eff}=1.7$ and $P_{FUS}=1000$ MW.

a) Achievable fusion gain Q as functions of the electron temperature T_e .

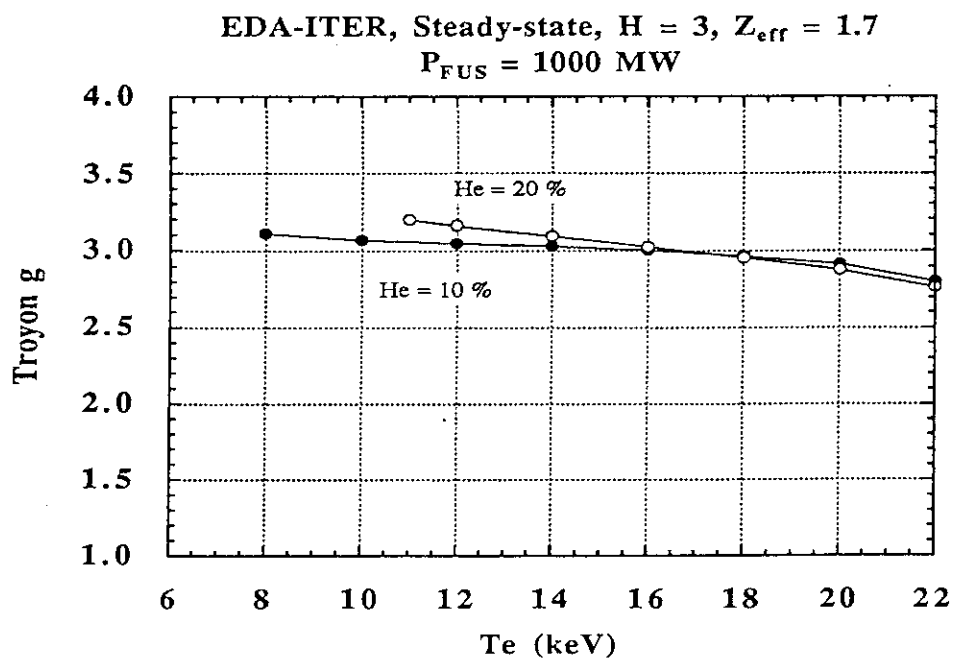
b) Required current drive power P_{NBI} .

c) Troyon g , d) q_{ψ} , e) I_{BS}/I_P and f) n_e .

g) Divertor heat load (Constant χ model) W_{div}^{HK} .

h) Divertor heat load (JT-60U model) W_{div}^{JT60} .

c)



d)

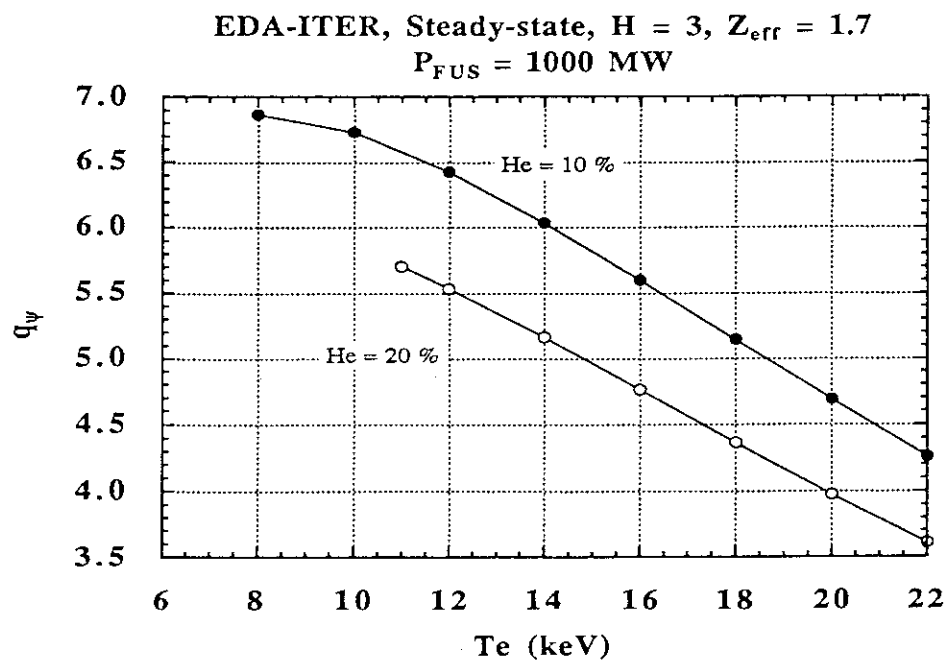
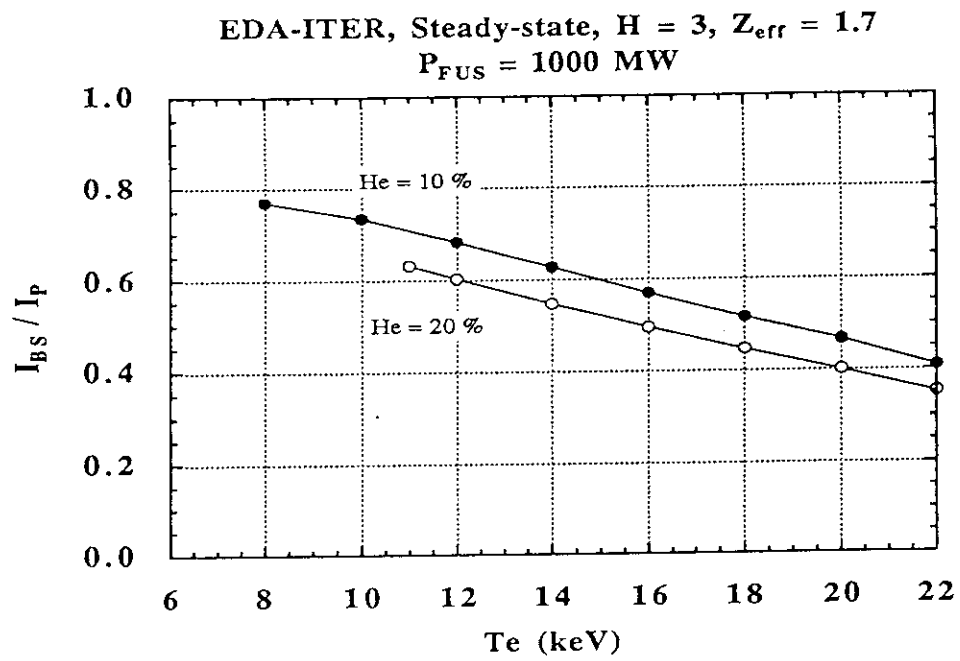


Fig. 3.26 (Continued)

e)



f)

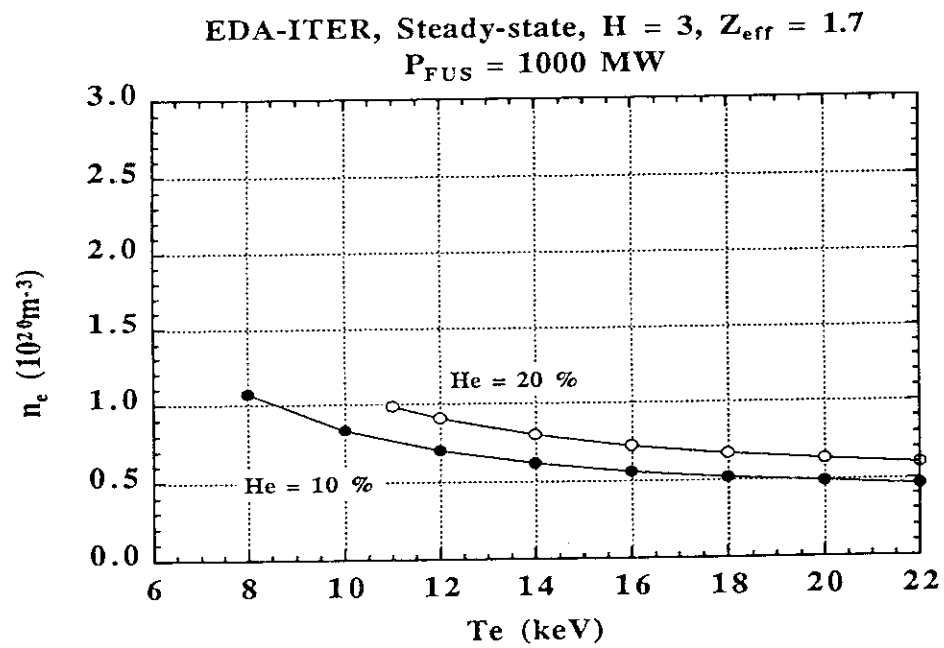
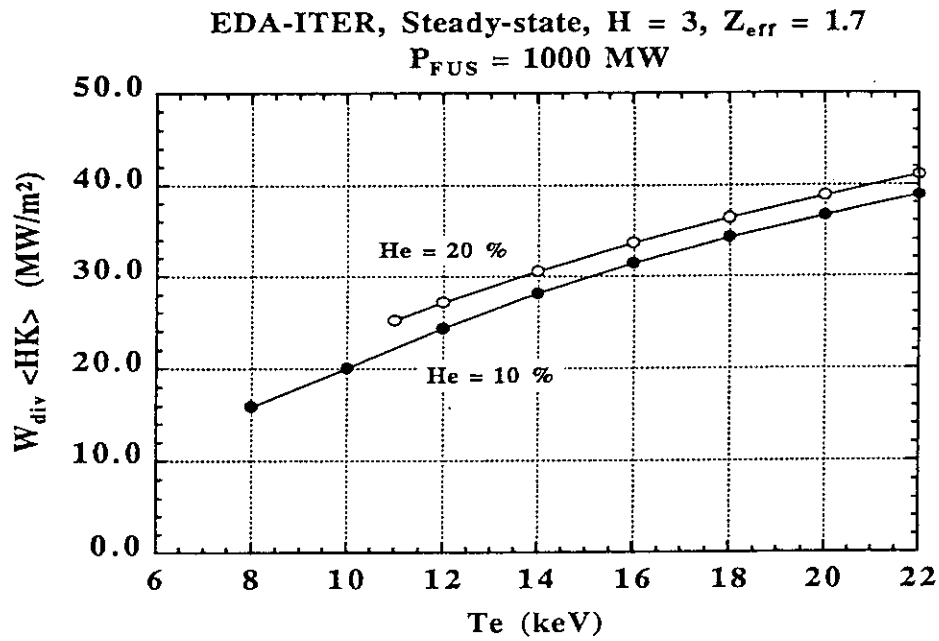


Fig. 3.26 (Continued)

g)



h)

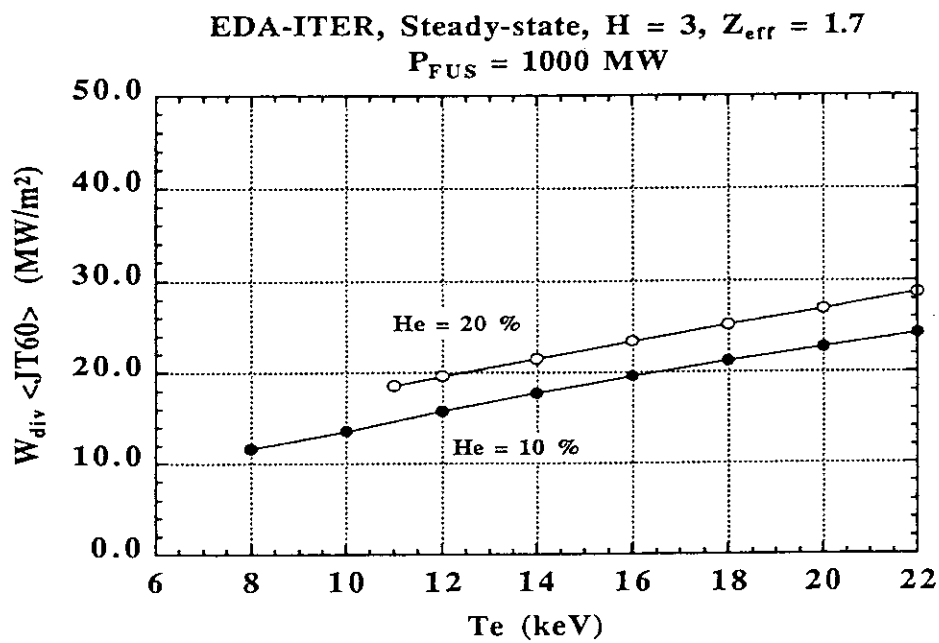
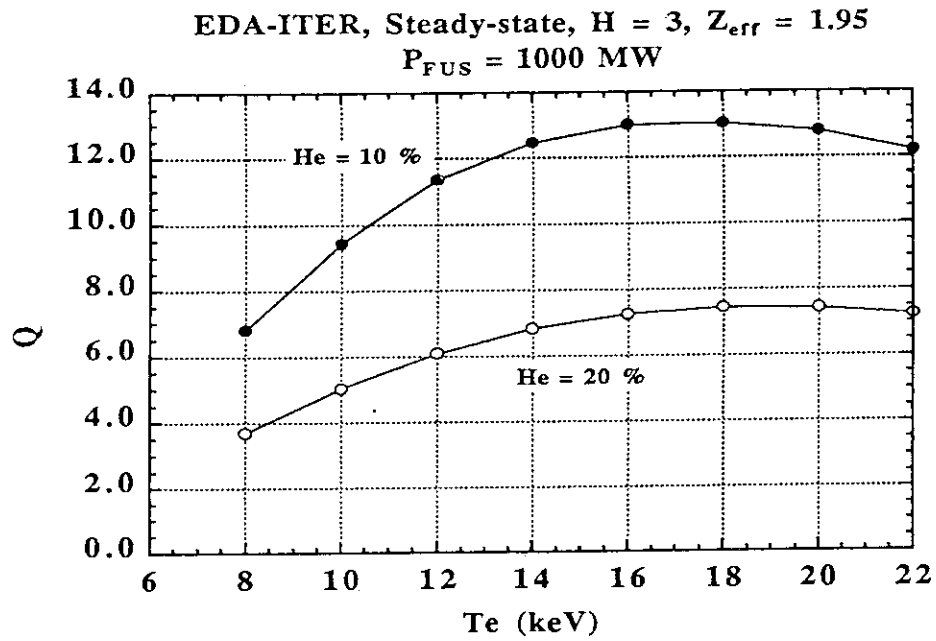


Fig. 3.26 (Continued)

a)



b)

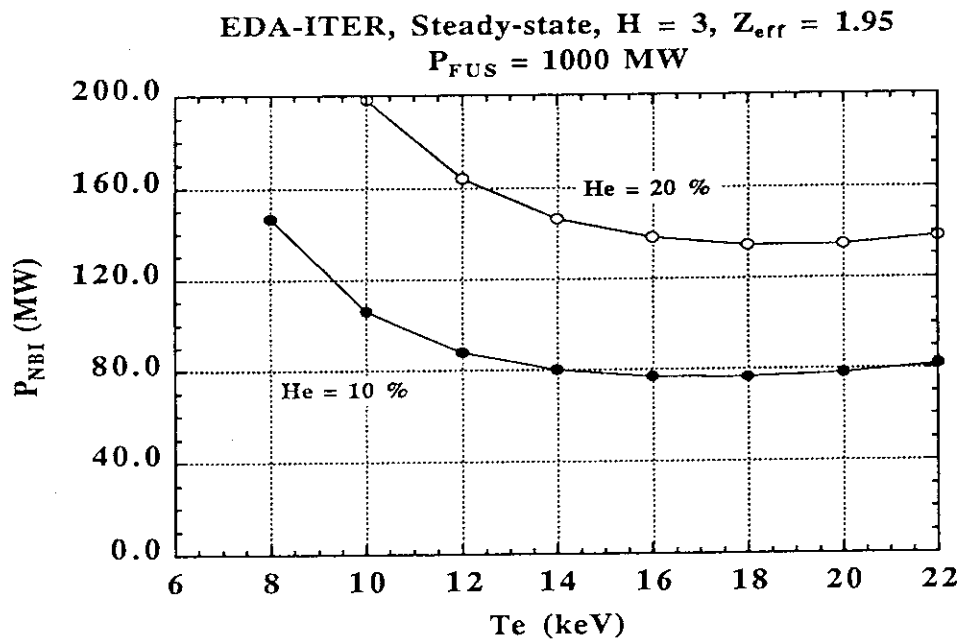


Fig.3.27 Steady-state operation of EDA-ITER when $H_{IP}=3$, $Z_{eff}=1.95$ and $P_{FUS}=1000 \text{ MW}$.

a) Achievable fusion gain Q as functions of the electron temperature T_e .

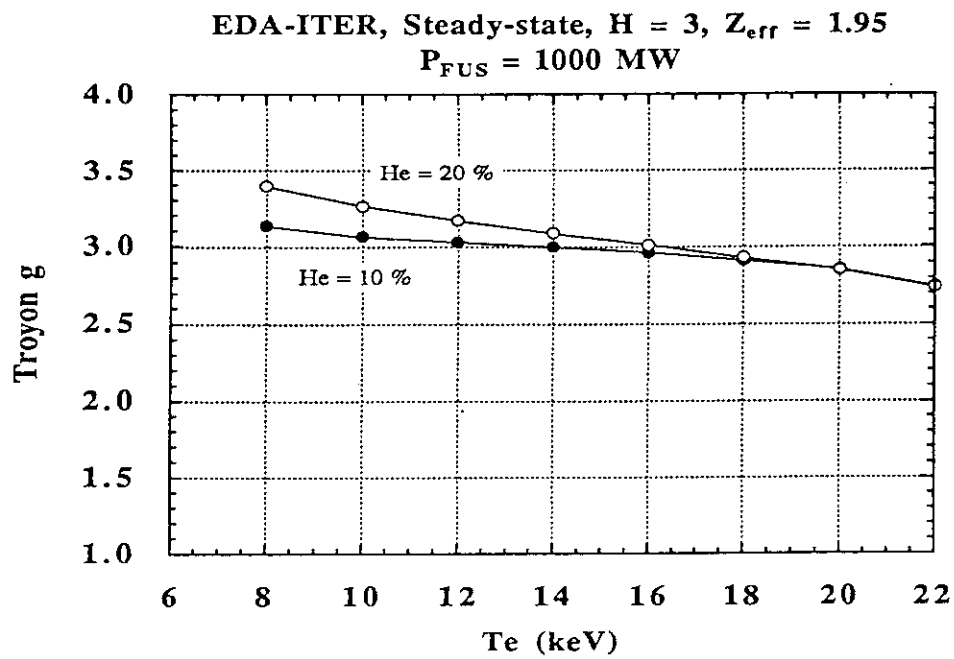
b) Required current drive power P_{NBI} .

c) Troyon g , d) q_ψ , e) I_{BS}/I_P and f) n_e .

g) Divertor heat load (Constant χ model) W_{div}^{HK} .

h) Divertor heat load (JT-60U model) W_{div}^{JT60} .

c)



d)

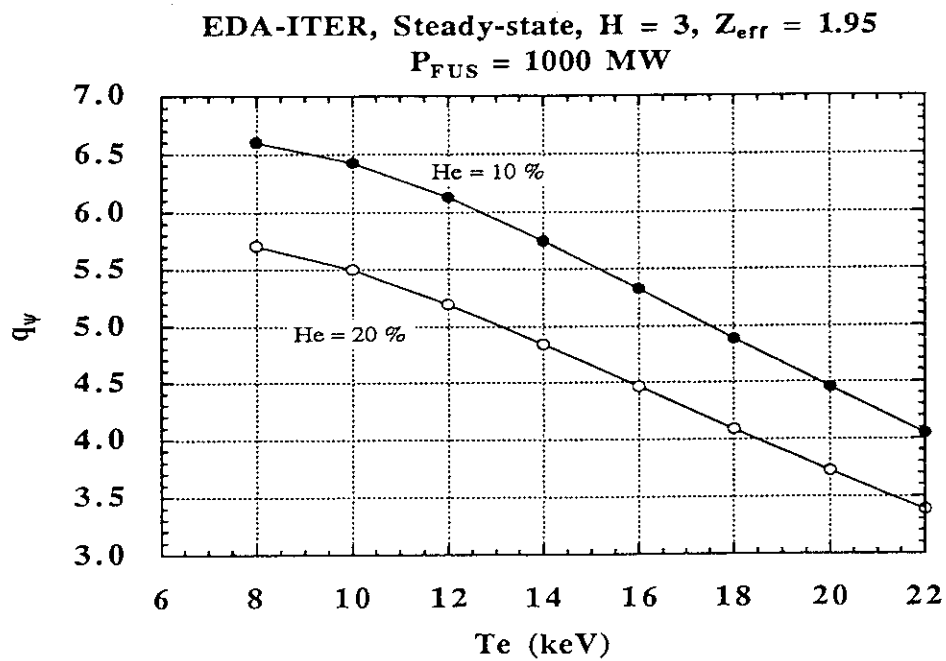
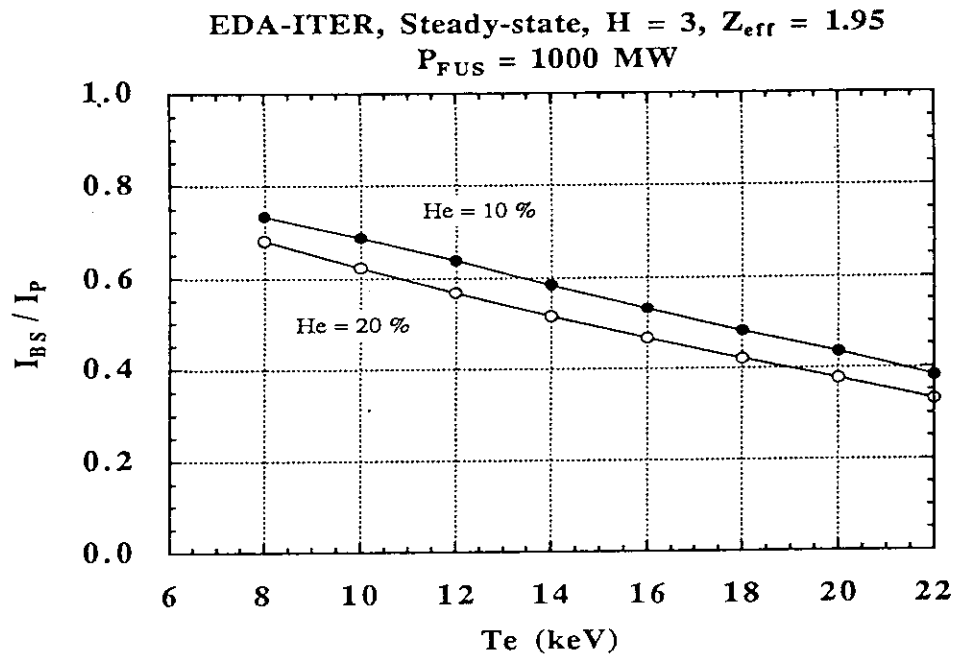


Fig. 3.27 (Continued)

e)



f)

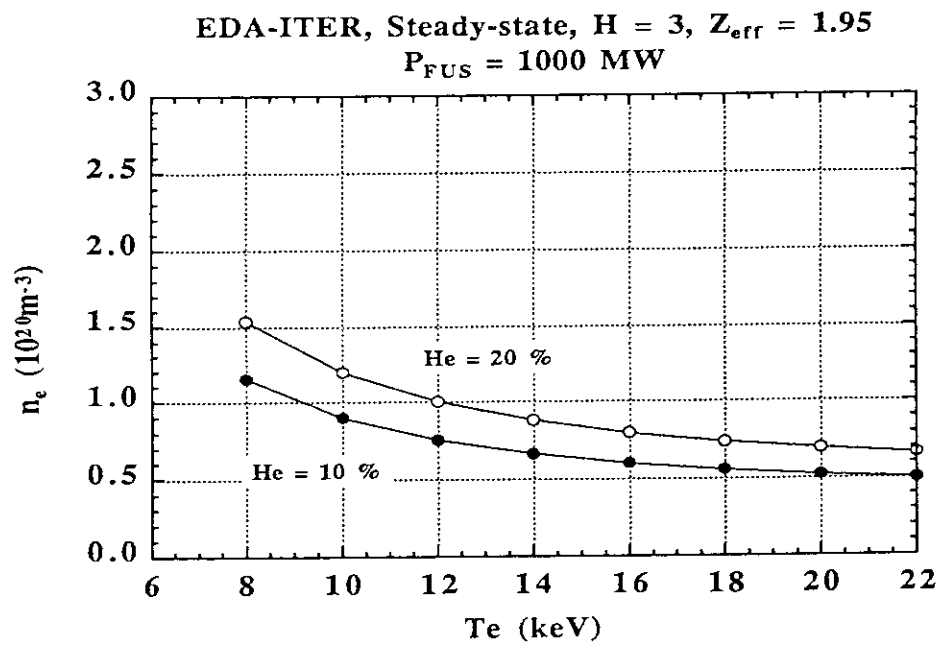
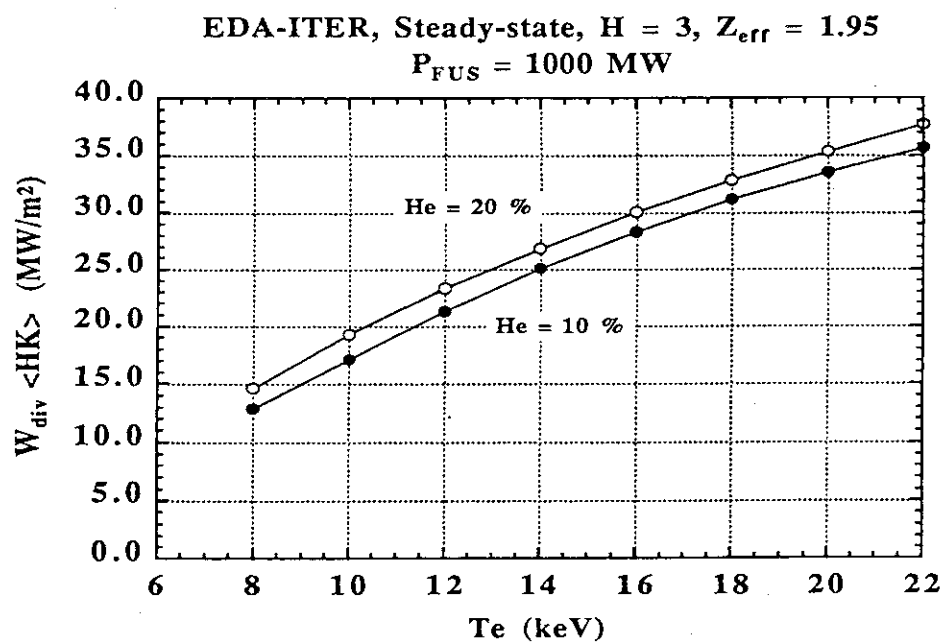


Fig. 3.27 (Continued)

g)



h)

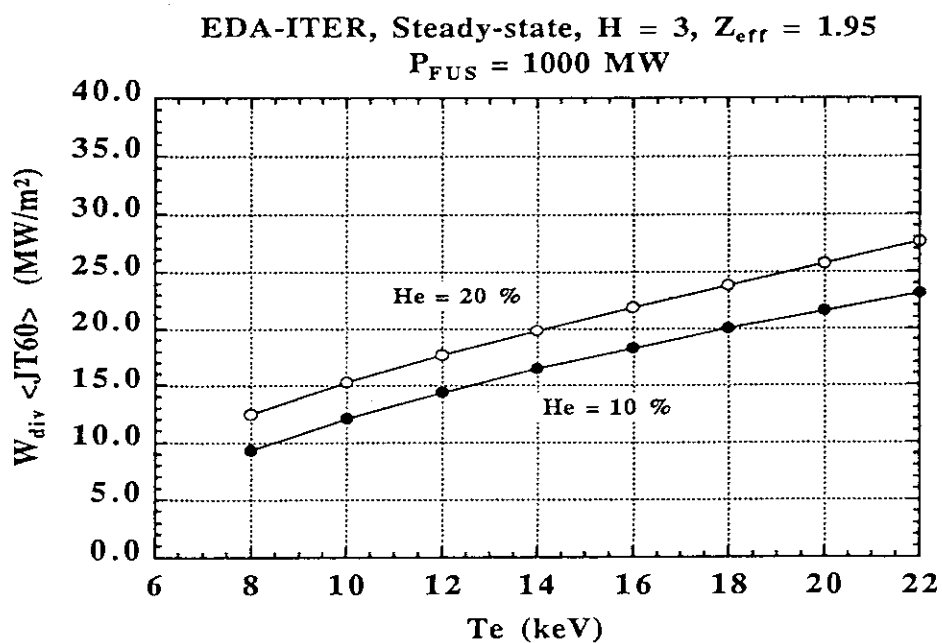
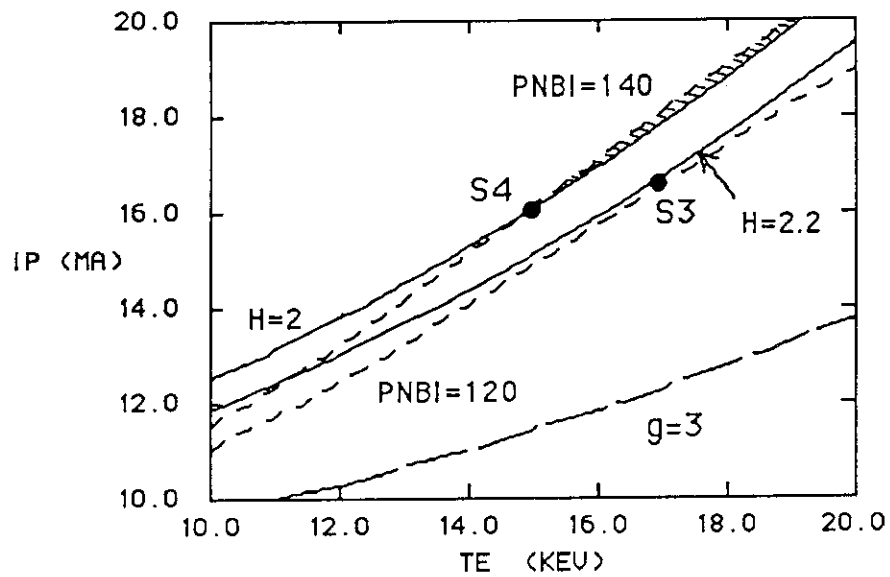


Fig. 3.27 (Continued)

a) $R_p = 7.8 \text{ m}$, $a_p = 2.7 \text{ m}$ (PFUS = 750 MW)



b) $R_p = 7.8 \text{ m}$, $a_p = 2.0 \text{ m}$ (PFUS = 750 MW)

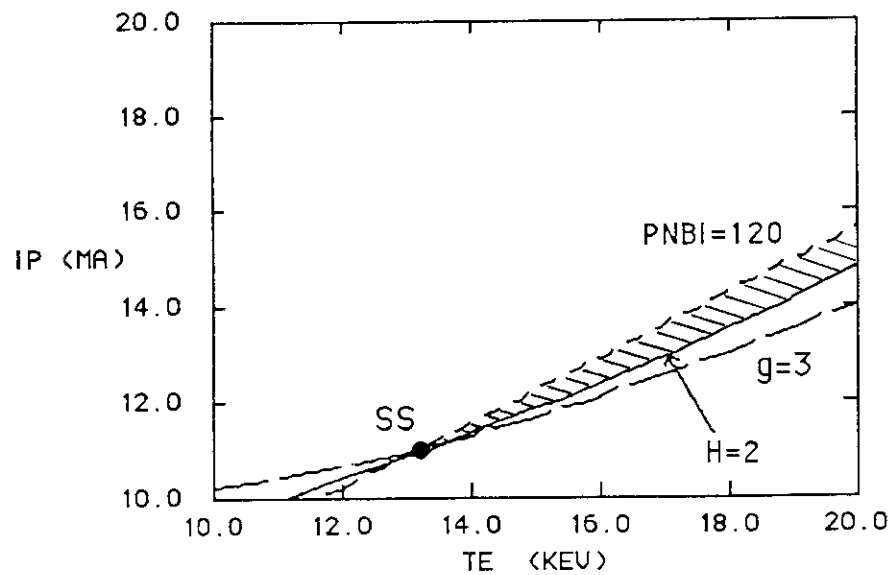


Fig. 3.28 Steady-state operation region for the plasma with different minor radius when $P_{FUS}=750 \text{ MW}$.

a) $R_p=7.8 \text{ m}$ and $a_p=2.8 \text{ m}$, b) $R_p=7.8 \text{ m}$ and $a_p=2.0 \text{ m}$.

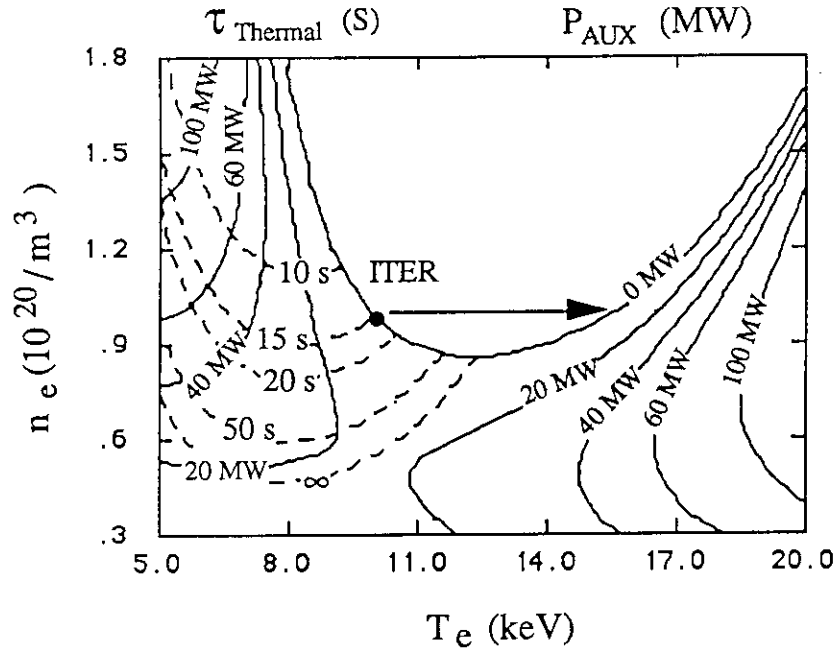


Fig. 4.1 Plasma operation parameter contour (POPCON) plot of EDA-ITER when $H=1.8$ and $Z_{eff}=1.5$ (He=10%, C=1%). Solid lines and dashed lines denote the required heating power and the growth time of the thermal instability, respectively. Here, ITER89 power scaling law is used.

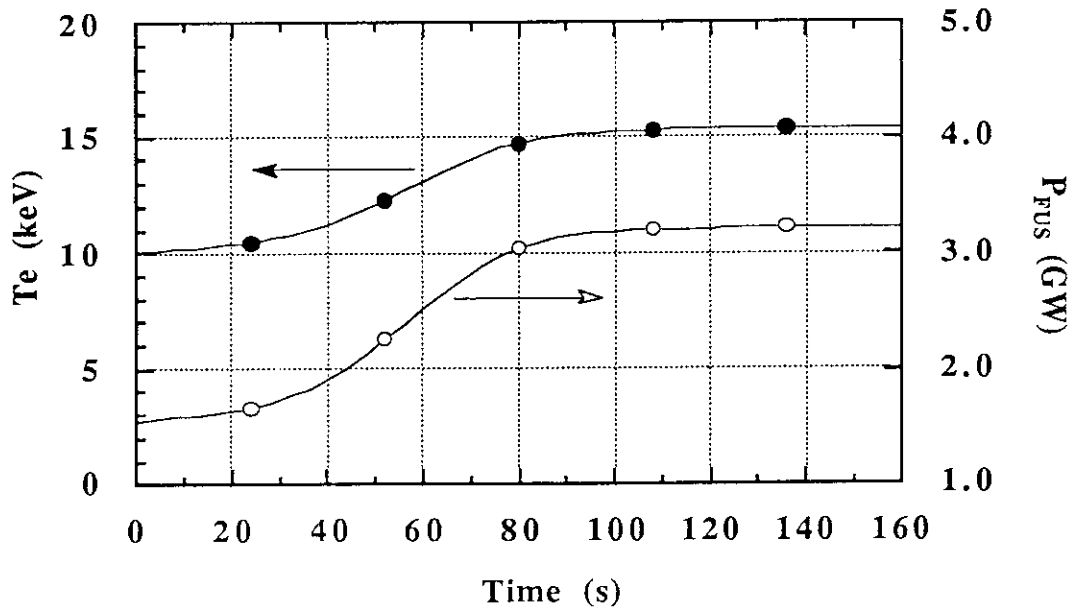


Fig. 4.2 Time development of electron temperature T_e and fusion power P_{FUS} for the reference operation point of EDA-ITER. Here, the electron density is assumed to be constant.